Milky Way-like galaxy simulations in the Gaia era: disk large scale structures and baryonic content

Santi Roca Fàbrega

UNIVERSITAT DE BARCELONA

Departament d'Astronomia i Meteorologia

Milky Way-like galaxy simulations in the Gaia era: disk large scale structures and baryonic content

Santi Roca Fàbrega

Barcelona (Catalonia), November 2014

Programa de Doctorat en Física
Línia de recerca en Astronomia i Astrofísica
2010-2014

Memòria presentada per **Santi Roca Fàbrega**
per optar al grau de Doctor en Física

Directors

Dra. Francesca Figueras Siñol i Dr. Octavio Valenzuela Tijerino

El tutor d'aquesta Tesi Doctoral ha estat

Dra. Francesca Figueras Siñol

Acknowledgments

Per començar vull fer servir aquestes primeres pàgines de la tesi per agrair a tothom qui m'ha acompanyat durant aquest llarg procés d'aprenentatge, tan acadèmic com personal, i que m'ha permès arribar fins aquest moment. Primer de tot vull expressar el meu més profund agraïment als meus directors de tesi. A la Cesca, pel seu suport incondicional, les hores i hores de correccions i els fulls plens de comentaris, que potser sí que en algunes ocasions han estat gairebé incomprensibles però també és cert que sempre han estat encertades, les discussions acalorades i alhora molt productives, els seus valuosíssims consells tan en la vessant personal com en l'acadèmica, i per afrontar-ho sempre tot amb un somriure i no tenir mai un no per resposta. Y también a Octavio, por sus consejos, por compartir sus inmensos conocimientos sobre prácticamente cualquier campo de la ciencia, por su bondad y generosidad y por haberme brindado la oportunidad de conocer una forma distinta de trabajar, una nueva y apasionante cultura y un país maravilloso. Els hi vull agrair també el fet d'haver-me obert les portes al doctorat i d'haver-me acompanyat en tot aquest procés, i és que al cap i a la fi han estat ells els que m'ho han ensenyat tot d'aquest món que és la investigació.

El treball que presento aquí tampoc hauria estat possible sense la col·laboració de molta altra gent. Especialment vull agrair a la Mercè Romero el temps que m'ha dedicat, els seus bons consells i també el fet d'estar disposada a ajudar-me en qualsevol moment. También a Bárbara Pichardo, por su buen humor, por su energía inagotable y por su alegría contagiosa, aunque sobretodo le quiero agradecer el haberme salvado la vida si no hubiera sido así seguro que no habría terminado esta tesis! I també a la resta de gent amb qui he treballat intensament, a la Teresa Antoja, per haver-me acollit en una magnífica i molt productiva estada a Holanda, a Luis Aguilar por sus clases magistrales y por compartir su enorme conocimiento, i també a la resta d'investigadors del Departament d'Astronomia de la UB y del Instituto de Astronomía de la UNAM.

Tot i això aconseguir acabar un doctorat no depèn només de la investigació que un pugui dur a terme sinó també de tenir a prop gent que t'ajudi en les feines del dia a dia de la facultat i del grup d'investigació, així com d'altres que t'ajudin a desconnectar durant els descansos o hores lliures. És per això que també vull agrair l'ajuda de la resta de la gent del Departament d'Astronomia i Meteorologia de la UB, a la Montse, la Rosa i en JR de secretaria per aguantar-me en tots aquells moments de pànic a l'hora de fer papers i més papers, a en Gabi i en Jordi per suportar les nostres ficades de pota amb tots els temes informàtics. Dins del nostre grup d'investigació, el grup de Gaia, també vull agrair l'ajuda i els consells d'en Jordi Torra, la Carme Jordi, l'Eduard Masana, en Xavi Luri, en Josep Manel Carrasco, tota la resta d'enginyers i científics, i sobretot vull agrair a la Lola la feinada i la paciència que ha tingut a l'hora d'entendre els números que li passo després d'un congrés i a en Dani per haver-hi estat sempre per arreglar i instal·la tots aquests programes tan estranys que fem servir els astrònoms. Finalment no puc deixar d'agrair a aquesta espècie tan rara que volta pels departaments d'investigació de tot el món, els becaris, doctorands o post-doctorands, el seu suport i bons moments de desconnexió, rutes, sopars, berenars, descansos tot jugant a cartes o a jocs de taula, discussions de despatx, ... a tots ells, la Maria Monguió, en Pere, la Rosa, la Laia, la Neus, en Xavi, en Benito, l'Ignasi, en Víctor, en Lluís, l'Andreu, la Mar, en Javi, en Josep Maria, la Gemma, l'Àlvaro, la Laura, la Carme, en Jordi, les Mireies, l'Albert, en David, en Roger i a molts d'altres que segur que m'estic deixant, moltes gràcies! También a los becarios del Instituto de Astronomía de la UNAM, en México, con quien he pasado tan buenos momentos, desde los ya famosos "Santitours", a los partidos de fut y a las buenas comilonas, quiero agradecer especialmente a Rut Salazar por hacer que llegara a sentir que México es mi segundo hogar pero también a Eva, los Aldos, Yaxki'n, Alejandro, las Ángeles, Eduardo, Rodrigo, Roberto, Zeus i a todo el resto, y como no también a los investigadores como Toño Peimbert, Jose Antonio de Diego o Erica Sohn con quien volteé mi primer jeep y también al personal de la administración com la señora Maru y el famoso Playa.

Aquesta tesi ha estat l'últim pas d'un llarg camí, en aquest camí molta gent m'ha donat suport i ha posat el seu granet de sorra per fer de mi la persona que sóc avui. Aquí vull aprofitar per agrair-los aquest suport que m'han donat durant tots aquests anys. Començaré doncs des del principi, des del punt en que vaig decidir que volia esser astrònom. Recordo perfectament aquell moment, quan tenia 10 anys, amb les tendes muntades just sobre els prats de la font Tornadissa, camí del Puigsacalm, quan el cometa Hale Bopp es mostrava ben brillant al cel, un moment màgic en uns campaments del GECA, el grup excursionista del meu poble. És a aquesta entitat a qui vull dedicar el meu primer agraïment. Durant tota la meva infantesa i adolescència una profunda curiositat per tot el que passava en el meu entorn, sobretot el natural però també el social, va guiar la meva vida. En aquesta etapa un grup d'esplai que desgraciadament ja no existeix va esser el responsable de respondre les meves incessants preguntes i de construir, en bona part, la persona que sóc ara, alhora que va esser d'on va sorgir la colla d'amics que m'ha acompanyat fins l'actualitat. És per això que necessito dedicar un sincer agraïment a aquest grup, l'esplai de "La Pallofa", així com als seus magnífics monitors. Finalment, d'aquests primers anys de formació personal també vull agrair els anys de consells i acompanyament que em va brindar un gran amic, el Mossèn Joan Boada.
Pel que fa a la meva vida acadèmica vull adreçar també un agraïment als meus professors

de secundària i batxillerat de l'IES Bosc de la Coma que van esser responsables en bona part, de fer-me descobrir la passió pel món científic. Entre d'altres vull fer arribar un agraïment a en Marcos Magallanes, professor de biologia, la Rosa Badosa, professora de química, la Pilar Berga, professora de matemàtiques i en Josep Mata, professor de física. També vull expressar un agraïment a tota la resta de professorat i personal no docent del centre que van fer que la meva etapa d'estudis secundaris fos molt productiva tan acadèmicament com personal. I per acabar amb l'etapa de secundària vull agrair molt especialment a la Dolors Torrent, professora de català i tutora de 4rt d'ESO, la seva dedicació, les seves lliçons morals i sobretot el seu gran cor per entendre'ns en aquells moments tan difícils de l'adolescència. De l'etapa dels meus estudis de la Llicenciatura i màster vull agrair el suport de molts dels professors que vaig tenir els quals fins i tot van esser capaços de fer-me dubtar de si seguir el camí de l'astronomia o d'alguna altra disciplina de la física. Més enllà de les classes vull agrair molt sincerament el suport que em van donar els meus companys de promoció sobretot en els nombrosos moments baixos que vaig tenir durant la llicenciatura, en els quals em vaig arribar a plantejar seriosament de canviar carrera. I és que és gràcies a aquests grans amics que he fet a la universitat, començant per dos d'ells, en Xumeu Planells i l'Enrique Pinto, que de ben segur que no hauria arribat fins aquí, uns grans grans amics. Vull fer extensiu també aquest agraïment, pels bons moments de sopars, dinars, berenars, cafès i excursions a tots els amics de Fisicspelmon.

No puc acabar aquest agraïments sense passar altre cop fora de l'àmbit acadèmic on tanta i tanta gent m'ha acompanyat en aquest camí, tanta que de ben segur que em deixaré algú, així doncs perdoneu si és el cas. Primer de tot, a la gent de l'esbart dansaire Marboleny, bons amics amb qui parlar i amb qui he viscut tantes i tan llunyanes aventures. També a la gent d'un grup que sens dubte ha marcat d'una manera molt especial els meus últims anys i que m'ha canviat completament com a persona, l'Agrupament Escolta Nostra Dona del Tura. És aquí on també hi he fet molt bons amics, gent amb qui sempre he pogut i podré comptar i amb qui he compartit molt i molt bons moments caminant per mil i una rutes, dormint en mil i un llocs amb tendes, llocs moltes vegades no molt legals, improvisant a l'últim moment gimcanes i activitats i suportant llargs consells d'agrupament i on encara no he pogut reeixir en aixecar-los la camisa. Vull agrair tots aquests moments a en Rafel, la Montserrat, la Marta Vila, la Neus, en Guinart, l'Arnau, l'Esther, en Palmero, l'Alba, la Mireia, la Ju, l'Iris, la Lore, la Cris, l'Anna, en Pau, l'Irene, la Sónia, tots els altres caps que han passat per l'agrupament en un moment o altre i també, com no, als nostres magnífics nens.

I ara sí, concloent aquests agraïments vull anar més enllà de la gent que m'ha guiat en els estudis i de totes les persones que m'han acompanyat en les entitats a les que he passat durant aquests anys, un grup de persones que m'han estat acompanyant gairebé des dels meus primers dies. A aquests els vull dedicar aquesta tesi, una dedicatòria seguida d'un profund agraïment per tot el que hem viscut junts, perquè han estat sempre allà, en els moments difícils i en els moments feliços, oferint consells, temps per parlar, per desfogar-me, per cridar, per plorar,.. aquests són la Núria Feixas, la Marta Vila, en Jordi Feixas, la Ceci Roca, la Marta Puigvert, en Miquel Vila , la Laura Gelis, en Marc Valls, en Pau Morchón, l'Esther Massegú, en Jordi Trias, l'Anna Costa, la Laura Pellín, l'Àurea Macias, i molts d'altres bons amics que són i sé que seran sempre al meu costat per quan els necessiti. D'aquests però l'agraïment més especial va cap a la meva família, sobretot al meu germà, l'Albert, amb qui hem compartit molts moments, baralles i fins i tot algunes cicatrius en aquesta vida de poble, i és que de tot se n'aprèn, però també als cosins i tiets, i les àvies que desgraciadament ja no m'han pogut acompanyar en aquest moment tan especial.

Vull acabar amb l'agraïment més sentit de tots, el més profund, sincer i ple d'emoció, i és que ells són els que realment m'han guiat en aquesta vida, els que ho han donat tot perquè jo pogués arribar fins aquí partint d'una senzilla vida de poble, i ho han fet sense dubtar-ho ni un moment, confiant en mi, ajudant a aixecar-me quan he caigut, donant-me ànims i tot el que ha estat al seu abast per fer de mi la persona que sóc, els meus pares. Moltes gràcies mare i pare per tot el que heu fet per mi i per permetre'm d'arribar fins aquí, aquesta tesi no l'he escrita jo, l'heu escrit vosaltres.

Achronims

2D	Two Dimensional
3D	Three Dimensional
ΛCDM	Lambda Cold Dark Matter
APOGEE	APO Galactic Evolution Experiment
ART	Adaptative Refinement Tree
CALIFA	Calar Alto Legacy Integral Field Area Survey
CR	Corotation Radius
DF	Distribution Function
DM	Dispersion Measure / Dark Matter
ELT	Extremely Large Telescope
EM	Emission Measure
ESA	European Space Agency
GC	Galactic Center
IC	Initial Conditions
ILR	Inner Lindblad Resonance
IMF	Initial Mass Function
MANGA	Mapping Nearby Galaxies at APO
MW	Milky Way
OLR	Outer Lindblad Resonance
SDSS	Sloan Digital Sky Survey
SFpFD	Spatial Fourier plus Finite Differences
SFR	Star Formation Rate
TW	Tremaine and Weinberg
TWA	Tight Winding Approximation
WDM	Warm Dark Matter
WKB	Wentzel–Kramers–Brillouin

Resum en català

Antecedents

Ja fa més de 400 anys que Galileo Galilei va fer les primeres observacions del cel nocturn amb telescopi. En algunes d'aquestes observacions l'astrònom italià va apuntar el seu telescopi cap a la banda de llum difusa coneguda com a Via Làctia i va iniciar així els primers estudis d'astronomia galàctica. En les seves observacions amb telescopi de la Via Làctia va descobrir que la llum difusa que s'observava a ull nu eren en realitat un gran nombre d'estrelles molt febles. Un segle i mig després d'aquest descobriment, un astrònom anglès anomenat Thomas Wright va proposar que totes aquestes estrelles podien estar formant part d'un gran objecte en rotació lligat gravitatòriament. Aquest astrònom també va proposar que les estructures nebuloses que s'observaven a través dels telescopis podien esser també sistemes d'aquest tipus però situats molt més lluny. Uns quants anys després Immanuel Kant va anunciar una teoria molt semblant a la de Wright en la qual es deia que la Via Làctia i també algunes nebuloses eren sistemes formats conjunts d'estrelles lligats gravitatóriament i en rotació, enmig d'un univers buit, a aquests sistemes els va anomenar universos illa. Des d'aquells primers passos en l'astronomia galàctica el nostre coneixement dels sistemes galàctics ha millorat molt. Aquest progrés s'ha accentuat en els últims anys gràcies a l'ús de nous i millors telescopis, de nous i més precisos instruments de detecció i, més recentment, a l'aparició de tècniques computacionals que ens han permès simular com les galàxies es formen i evolucionen.

La tècnica computacional més simple que es fa servir per simular l'evolució de sistemes dinàmics sota un camp de força és la tècnica dels N-cossos. En astronomia la força que sol dominar i que per tant dirigeix els processos de formació i evolució de sistemes estel·lars és la gravetat. Les primeres simulacions d'N-cossos que es van fer servir en el camp de la formació i evolució de galàxies van esser els experiments amb bombetes de Holmberg (1941). En aquests experiments en lloc de resoldre les equacions de la força gravitatòria per determinar l'acceleració a la posició de cada una de les partícules de la simulació es feien servir bombetes i fotodetectors. Bàsicament en aquest treball els autors van aprofitar que la llum rebuda per unitat d'àrea des d'una font lluminosa decreix amb el quadrat de la distància, exactament igual com ho fa la força gravitatòria, d'aquesta manera simplement coneixent la quantitat de llum rebuda a la posició de cada fotodetector podien conèixer l'acceleració provocada en aquell punt per la resta de partícules. No va esser fins a la segona meitat del segle XX quan els ordinadors van començar a jugar un paper important en l'astronomia galàctica. Aquest procés que va des dels primers experiments fins passats mitjans de segle es va allargar tan degut al lent avanç de la tecnologia de l'època. De fet en aquells temps, quan van aparèixer els primers ordinadors, aquests només eren capaços de fer simulacions d'un nombre molt petit de partícules (16 en el treball pioner de von Hoerner (1960)). A partir d'aquell moment però, el número de partícules que es podien simular s'ha doblat cada dos anys tot seguint la famosa llei de Moore la qual té en compte les millores tecnològiques. L'aparició de noves tècniques numèriques que permetien resoldre les equacions de la gravetat d'una manera més eficient també va permetre fer més gran el nombre de partícules que es podien simular. La tècnica numèrica més utilitzada en les primeres simulacions era la coneguda com a tècnica de partícula-partícula. En aquesta es tenen en compte totes les interaccions entre totes les partícules. Com a resultat s'obté la força exacta produïda per la presència de tota la distribució de partícules a la posició de cada partícula. Fent servir aquest procés la quantitat de temps de CPU necessari per simular un sistema d'N partícules creix a un ritme de $O(N^2)$, en el passat això impedia simular sistemes amb un número molt gran de partícules ja que la simulació requeria temps de CPU tan grans com dècades o fins i tot segles. Tot i això, com ja s'ha mencionat anteriorment, en l'última dècada les millores tecnològiques han fet possible generar simulacions amb un gran nombre de partícules en un temps raonablement baix, fins i tot fent servir el mètode directe de partícula-partícula. Una de les millores tecnològiques més importants que s'han fet recentment en computació ha estat la introducció del sistema de processament en paral·lel. Aquest nou sistema ha permès generar simulacions que requereixen temps de CPU de desenes o centenars d'anys en temps molt més curts ja que la càrrega de treball es distribueix en diversos processadors. Finalment, la introducció de nous mètodes de truncament o de mètodes de malla, que han substituït els clàssics mètodes directes de partícula-partícula en el càlcul de la força gravitatòria, han reduït també considerablement el número d'operacions necessàries per dur a terme una simulació i així també del temps necessari per completar-les.

En totes les simulacions d'N-cossos que es van fer fins mitjans dels anys 70 l'única component que se simulava era la component estel·lar (p.e. von Hoerner 1960; Hohl 1971; Hohl & Zang 1979). No va esser fins la presentació de les observacions de corbes de rotació planes en galàxies espirals (Rubin et al. 1978) que la comunitat científica es va adonar de la importància d'incloure a les simulacions una component fosca en forma d'halos de matèria fosca per tal de reproduir correctament la dinàmica galàctica. Des d'aquell moment la majoria de simulacions de formació i evolució de galàxies que s'han presentat han fet servir aquesta component de matèria fosca per tal d'obtenir resultats realistes (p.e. Sellwood 1980; Combes & Sanders 1981). Més recentment, gracies a les millores tecnològiques que hem comentat, ha estat possible l'aparició d'una nova generació de simulacions de galàxies aïllades que inclouen discos, halos de matèria fosca i bulbs vius a més de, en alguns casos, la component col·lisional (gas). Aquestes simulacions mostren d'una manera molt realista la formació i evolució d'estructures a gran escala tals com braços espirals o barres (p.e. Athanassoula 1996; Debattista & Sellwood 2000; Valenzuela & Klypin 2003; Kawata & Gibson 2003; Dubinski et al. 2009; D'Onghia et al. 2010; Grand et al. 2012a; Roca-Fàbrega et al. 2013). També en els últims anys diversos projectes han aconseguit generar simulacions realistes de grans volums cosmològics de matèria fosca on aquesta es fa evolucionar des de desplaçaments al vermell molt grans fins a l'actualitat. En aquest context la simulació més famosa és la simulació del mil·leni (Millennium run de Springel et al. (2005)). En aquesta simulació s'hi segueix l'evolució de més de 10 mil milions de partícules dins una caixa cúbica de prop de 2 mil milions d'anys llum per costat. Per completar aquesta simulació va fer falta deixar el superordinador principal del Max Planck Society's Supercomputing Centre a Garching, Alemanya treballant al 100% durant més d'un mes. Des que es va presentar aquesta simulació se n'han presentat algunes d'altres on també s'han simulat grans volums cosmològics (centenars de Mpc per costat) i on s'han fet servir un nombre cada cop més gran de partícules alhora que millors resolucions. Alguns exemples d'aquestes simulacions són la Millennium run II (Springel et al. 2008), la Millennium XXL (Angulo et al. 2012), la Multidark, la Bolshoi que és la que té una resolució més gran (Klypin et al. 2011) i la DEUS-FUR que és la d'un volum cosmològic més gran (Rasera et al. 2014). Actualment les simulacions de grans volums cosmològics que, a més de la matèria fosca i la estelar, inclouen la component col·lisional (gas i pols) i tota la física associada, són molt comunes i assoleixen altes resolucions tan pel que fa a les temporals com a les espacials com també al número total de partícules. Alguns dels primes intents d'incloure la part col·lisional en aquest tipus de sistemes van esser les simulacions presentades per Abadi et al. (2003) i per Sommer-Larsen et al. (2003). En aquests primers casos el que es va simular va esser un petit volum cosmològic amb matèria fosca i partícules de gas, anomenades també partícules d'SPH. Un altre exemple d'aquests primers intents va esser el projecte MareNostrum Universe de Gottlöber et al. (2006). En aquest últim cas es va fer servir el codi anomenat GADGET2 i el que es va simular va esser un volum cosmològic gran amb un nombre també gran de partícules de matèria fosca i de gas. Finalment, en els últims anys alguns autors han aconseguit obtenir sistemes galàctics amb discos estel·lars realistes i semblants al de la Via Làctia. Alguns exemples d'aquests treballs són la simulació ERIS (Guedes et al. 2011) o el projecte Aquari (Springel et al. 2008).

Les simulacions han tingut una importància cabdal en l'estudi de les estructures a gran escala que es formen dins les galàxies. El coneixement de la formació i evolució d'aquestes estructures ha millorat molt en els últims anys gràcies justament a les observacions i també a les simulacions de gran qualitat que s'han estat fent. No obstant això cap de les teories que s'han proposat fins ara ha pogut explicar amb èxit els processos de formació i evolució d'aquestes estructures.

La primera teoria que es va proposar per explicar la formació d'estructures espirals a les galàxies discutia la possibilitat que aquesta es generés a partir d'una estructura radial al disc que es convertiria ràpidament en una estructura espiral degut a la rotació diferencial. Aquesta primera teoria va esser descartada en comprovar que les estructures espirals resultants tindrien una vida molt curta degut al ràpid enrotllament dels braços entorn el disc. El fet que les estructures tinguessin una vida curta contradeia els anàlisis estadístics que s'havien fet a partir d'observacions de galàxies espirals externes, la majoria de les quals tenen estructures espirals en el present, i que concloïen que aquestes estructures havien de tenir temps de vida llargs. Per poder resoldre el problema de l'enrotllament es va proposar una nova teoria. En aquesta nova teoria es va proposar que existeix una pertorbació espiral no material i rígida que recorre el disc en forma d'ona de densitat pertorbant les òrbites estel·lars. En aquesta teoria les estrelles no viatgen sobre del braç espiral sinó que hi passen a través. Els primers a proposar aquesta teoria van esser Lin & Shu (1964) i actualment es coneix com a teoria de l'ona de densitat. Aquesta teoria compta amb una aproximació analítica que és vàlida quan es compleix que la pertorbació espiral té una amplitud i un angle d'enrotllament petits i que les partícules estel·lars del disc tenen dispersions de velocitat també petites i segueixen l'aproximació epicíclica. Tot i les limitacions en la morfologia de les estructures espirals la teoria ha sobreviscut en el temps fins als nostres dies. Actualment aquesta encara és una de les teories més acceptades per explicar com són els braços espirals. Un dels problemes més grans que ha de resoldre la teoria d'ona de densitat és el fet que només explica com són les estructures però no com es van formar. Diverses teories complementàries han aparegut per explicar aquest procés de formació, alguns exemples dels mecanismes proposats són les inestabilitats internes dels discos, la interacció amb sistemes extragalàctics o bé d'altres més complexos com el que es conexi com a "Swing Amplification" o l'acoblament no lineal (Sygnet et al. 1988). En els últims anys s'han proposat d'altres teories que intenten explicar ambdues coses alhora, com són i com s'han format les estructures espirals de les galàxies. Un exemple clar d'aquestes noves teories és la que van proposar Romero-Gómez et al. (2007), on es discuteix que les espirals es poden generar a partir de les òrbites creades pel potencial de la barra galàctica. En aquest escenari apareixen òrbites que parteixen de la barra i que porten les estrelles cap als punts de sella que es generen als extrems de la mateixa seguint després cap a les parts exteriors del disc on segueixen òrbites en forma d'anells o de braços espirals cosa que depèn de la massa i geometria de la barra. Aquesta teoria es coneix amb el nom de teoria de les varietats invariants. Per intentar esbrinar quina de les teories que s'han proposat és la que explica millor la formació i l'evolució de les estructures espirals és necessari recórrer a les simulacions. Tot i això, els resultats obtinguts a partir de les simulacions tampoc són concloents ja que en alguns casos indiquen que la generació de les estructures es dona a través del mecanisme de Swing Amplification / acoblament no lineal (Masset & Tagger 1997) mentre que en d'altres sembla que la generació es produeix a través d'un mecanisme de varietats invariants (Athanassoula 2012). Fins i tot, en treballs més recents s'ha proposat que sota certes condicions els braços espirals generats en simulacions roten a la mateixa velocitat que les partícules del disc. En aquest últim cas l'antic problema de l'enrotllament queda solucionat pel fet que els braços espirals no són permanents sinó que passen per un cicle de creació-destrucció continu (Grand et al. 2012b; Roca-Fàbrega et al. 2013).

L'obtenció d'informació sobre les estructures a gran escala de les galàxies mitjançant observacions a partir de les quals posar a prova les teories, no és fàcil. En observar galàxies externes amb els instruments actuals només som capaços de captar una única fotografia de tot el procés d'evolució del sistema cosa que converteix en pràcticament impossible el seu anàlisi cinemàtic i dinàmic. Els únics estudis que es poden fer directament a partir de les imatges obtingudes de galàxies externes són estudis estadístics. També s'han proposat alguns mètodes indirectes per estudiar propietats concretes de les estructures a gran escala de les galàxies tals com les seves velocitats de rotació, tot i això degut a que en la majoria dels casos es parteix de premisses que prefixen algunes de les propietats d'aquestes estructures el resultat sempre depèn del model que s'ha aplicat (p.e. Martínez-García et al. 2009). D'altra banda existeix un mètode senzill i que no depèn de la imposició de cap model previ. Aquest mètode funciona només assumint tres premisses bàsiques, que el disc és pla, que les estructures del disc tenen una velocitat de rotació ben definida i que la brillantor superficial dels traçadors escollits obeeix les equacions de continuitat, i se'l coneix com a tècnica de Tremaine-Weinberg (Tremaine & Weinberg 1984).
Quan intentem estudiar la nostra pròpia galàxia a través d'observacions ens trobem amb nous problemes diferents als que es presenten en l'observació de galàxies externes. En aquest cas el problema que apareix a l'hora de buscar les propietats de les seves estructures a gran escala és la dificultat d'obtenir informació de les estrelles que es troben dins del disc degut a que la pols i el gas de la nostra pròpia galàxia ens en bloquegen bona part de la llum. Tot i això, en els últims anys s'han proposat diverses tècniques per aprofitar la informació cinemàtica de les estrelles individuals que es troben en l'entorn solar i que ens permeten obtenir informació de les barres i els braços espirals de la galàxia. Un exemple és el descobriment d'unes estructures en l'espai de les fases anomenades grups mòbils que donen informació sobre diverses propietats de les barres i les espirals tals com la seva massa o la seva velocitat de rotació (Antoja et al. 2009). També l'anàlisi dels moments de la funció de distribució de velocitats ha mostrat esser un bon traçador de les estructures de densitat de les galàxies (Vorobyov & Theis 2006; Roca-Fàbrega et al. 2014).

Molt aviat nous i ambiciosos projectes observacionals tals com APOGEE o Gaia, així com noves simulacions de galàxies semblants a la Via Làctia ens permetran discriminar entre les teories de formació i evolució i també sobre com són les estructures a gran escala de les galàxies. Estem entrant en l'època daurada de l'estudi de la galàxia i dels seus components.

Objectius de la tesi i metodologia

La formació i evolució de les estructures espirals en galàxies de disc és un procés que encara no s'entén del tot. Algunes propietats d'aquestes estructures tals com el perfil de densitat, les freqüències de rotació o el seu efecte sobre les estrelles del disc tampoc estan ben determinades. Aquesta falta de coneixements és deguda a que un estudi detallat a partir d'observacions encara no ha estat possible. El problema es troba en que les galàxies externes es troben tan lluny que només ens permeten veure-les com a objectes estàtics, i per tant ens és impossible estudiar-ne l'evolució directament. En aquest cas l'única opció que ens queda és fer estudis estadístics amb els quals posar límits a algunes de les seves propietats, un exemple d'això n'és l'estudi de temps de vida dels braços espirals. En el cas de l'estudi de la nostra pròpia galàxia el problema esdevé encara més complex ja que el que intentem és observar-ne les estructures des de dins mateix. Els problemes principals en aquest cas són l'absorció deguda a la pols i el gas, els efectes de projecció i la degeneració dels resultats degut a la presència de múltiples estructures de densitat. Tot i això, estudiar les estructures de la nostra pròpia galàxia també té alguns avantatges com per exemple el fet que podem analitzar la cinemàtica d'estrelles individuals o fer anàlisis estadístics de les propietats de grups d'estrelles que es troben en regions concretes dins la galàxia, cosa que actualment és impossible de fer en galàxies externes. L'anàlisi estadístic de la cinemàtica d'estrelles que es troben dins la Galàxia ha resultat esser una font important d'informació sobre les estructures no axisimètriques. Recentment s'ha confirmat que la presència de grups d'estrelles movent-se a velocitats semblants, o també coneguts com a grups mòbils, pot donar-nos informació sobre les propietats de les barres i dels braços espirals. D'altres paràmetres tals com les mitjanes de velocitats o els moments de segon i tercer ordre de la funció de distribució de velocitats també han mostrat esser bons traçadors de les propietats d'aquestes estructures.

Degut als problemes que es presenten quan s'intenten utilitzar les observacions amb l'objectiu de determinar els processos de formació i evolució dels braços espirals i quines són les seves propietats, s'han presentat diverses teories que intenten explicar-ho des d'un punt de vista teòric. La majoria d'aquestes teories proposen que aquestes estructures tenen temps de vida llargs i que no són ones materials sinó ones de densitat que passen a través del disc tot rotant rígidament. Molt poques d'aquestes teories però proposen mecanismes de formació. D'altres teories han proposat d'altres escenaris on els braços es formen a partir del potencial de barres centrals o bé de braços espirals que corroten amb les partícules de disc. Tot i la manca d'observacions que ens permetin fer un anàlisi profund d'aquestes estructures, sí que n'existeixen algunes que apunten cap a l'existència de braços amb temps de vida curts, d'altra banda els anàlisis estadístics d'observacions de galàxies externes donen suport a la hipòtesis dels braços espirals amb temps de vida llargs. Fins que no s'obtinguin observacions de qualitat suficient per dur a terme aquests estudis l'única manera de provar les teories sobre formació i evolució de braços espirals serà l'ús de les simulacions.

En l'última dècada diversos grups han començat a fer servir simulacions numèriques per posar a prova les teories que intenten explicar les propietats dels braços espirals de les galàxies. Tot i això els resultats que s'han obtingut fins ara no han estat concloents ja que les diferents simulacions que s'han fet servir han acabat donat suport a gairebé totes les teories. Una possible explicació a aquest fet és que els braços espirals no s'originin per un únic procés ni amb unes propietats úniques sinó que sota certes condicions i medis ambients es formin estructures que s'ajusten més o menys a una o altra teoria. Com hem detallat en els paràgrafs anteriors queda clar que encara queden moltes preguntes per respondre sobre la formació, evolució i propietats dels braços espirals, a continuació en detallem algunes:

- Quins són els mecanismes que porten a la formació de braços espirals a les galàxies?
- Sota quines condicions actuen aquests mecanismes?
- Els braços espirals són estructures amb temps de vida llargs o curts?
- Com roten? Depèn això del mecanisme a partir del qual s'han format?
- Són ones de densitat o estructures materials?
- Existeixen propietats cinemàtiques de les estrelles del disc que ens permetin determinar propietats de les estructures a gran escala?
- Quina és la relació entre les barres i les estructures espirals? Per què els braços espirals solen estar connectats als extrems de les barres en les galàxies de gran disseny?
- El gas o el camp magnètic juguen un paper important en la formació d'aquestes estructures?

Per donar resposta a totes aquestes qüestions és necessari dur a terme una recerca molt més profunda que la que presentem aquí. Tot i això, gràcies al recent increment en la qualitat de les simulacions, els grups de recerca han pogut començar a investigar les propietats de les estructures espirals amb molta més precisió i fins i tot han pogut començar a respondre a algunes de les qüestions que hem proposat anteriorment. En aquesta tesis ens hem proposat d'aconseguir generar simulacions d'una qualitat semblant o superior a les que s'estan fent servir en aquest camp de recerca i així respondre també a algunes de les qüestions obertes que queden en aquest camp.

En aquesta tesis doncs hi estudiem els codis d'N-cossos que en permeten generar simulacions realistes de formació i evolució galàctica. També hi analitzem propietats globals i locals de les estructures a gran escala i de les estrelles, amb l'objectiu de trobar mètodes que ens permetin distingir entre les diferents naturaleses i mecanismes de formació que s'han proposat. Els objectius específics del nostre treball són:

1. Obtenir models N-cossos realistes que ens permetin analitzar la cinemàtica, la dinàmica i l'estructura interna de les components no axisimètriques de les galàxies.
2. Aprendre com es controlen els efectes numèrics en les simulacions i a distingir-los dels efectes físics reals.
3. Detectar traçadors cinemàtics i dinàmics que ens puguin donar informació sobre la formació, evolució i propietats generals de les estructures a gran escala de les galàxies.
4. Desenvolupar mètodes basats en l'estudi de les propitats cinemàtiques locals i de les propietats globals de les estructures galàctiques a gran escala que siguin útils per distingir la naturalesa dels braços espirals en galàxies reals.

Paral·lelament a aquests objectius principals també esperem aprendre a fer servir els codis que inclouen la hidrodinàmica i també entendre com aquesta s'afegeix als codis d'N-cossos purs, tot amb l'objectiu final d'obtenir un sistema semblant a la nostra pròpia Galàxia. Finalment, ja que, un cop obtingut, un model realista de la Via Làctia ens oferirà l'oportunitat d'estudiar molts altres processos a part dels referents a les estructures espirals, esperem poder fer-lo servir justament per estudiar d'altres propietats de la galàxia que actualment no s'entenen prou bé.

Per dur a terme la recerca presentada en aquesta tesis hem utilitzat diverses tècniques de simulació numèrica. Per començar, hem fet servir simulacions d'N-cossos pures que ens han permès simular sistemes galàctics aïllats, més endavant hem fet servir simulacions de partícules test imposant diversos tipus de potencials no axisimètrics, finalment hem generat simulacions de galàxies tipus Via Làctia en un context cosmològic fent servir un codi d'N-cossos on s'han incorporat els processos hidrodinàmics.
El codi ART ha estat el nostre codi d'N-cossos bàsic i l'hem fet servir tan per les simulacions pures com per les que contenen també la part hidrodinàmica. També hem fet servir el codi anomenat GADGET3 amb l'objectiu de demostrar que els nostres resultats són independents del codi que s'ha fet servir per simular els sistemes aïllats d'N-cossos purs. Els primers models d'N-cossos purs que hem generat han estat models simples de galàxies tipus Via Làctia, aïllades. Aquests models s'han iniciat a baixos desplaçaments al vermell i a partir d'unes condicions inicials que ja contenen discos, halos de matèria fosca i en alguns casos també bulbs, tots vius (no analítics). A partir de la generació d'aquestes primeres simulacions hem après a fer servir de manera adequada els codis d'N-cossos, a fer-ne l'anàlisi i també a reconèixer quins resultats són conseqüència d'errors numèrics i per tant no es poden aprofitar amb objectius científics. Un cop hem adquirit un bon coneixement sobre els codis hem començat a aprendre com es generen sistemes més complexes

tals com volums cosmològics que s'inicien a alts desplaçaments al vermell i que utilitzen les fluctuacions primordials de l'univers com a condicions inicials. Aquests últims models han esdevingut els models més realistes de galàxies tipus Via Làctia que hem aconseguit i podem dir que han estat la culminació del treball dut a terme en aquesta tesis.
Més enllà dels models d'N-cossos també hem fet servir d'altres simulacions en entorns més controlats que ens han permès provar que els nostres resultats són correctes. Hem analitzat simulacions de partícules test imposant diferents potencials analítics tan de barres com de braços espirals i fent servir diferents condicions i paràmetres inicials. En el cas de les estructures espirals hem fet servir el potencial de TWA que ens ha servit per a simular els nostres models bàsics els quals hem comparat amb d'altres on hem canviat d'un en un alguns paràmetres del potencial tals com l'amplitud, la freqüència de rotaciò o l'angle d'enrotllament o alguna de les condicions inicials ja siguin les dispersions de velocitat o el temps d'integració. Aquestes comparacions ens han permès determinar de quina manera els nostres resultats depenen d'aquests paràmetres. També hem fet servir un altre potencial per als braços espirals, un potencial que és una mica mès realista i que es coneix amb el nom de PERLAS (Pichardo et al. 2003). Pel que fa als de potencials barrats hem analitzat dos models diferents, un model clàssic del barra quadrupolar i un altre amb una barra de tipus Ferrers. Amb l'objectiu de simplificar els anàlisis en aquesta tesi no hem utilitzat cap model mixta que uneixi potencials de barra i de braços espirals.
Finalment pel cas de braços espirals tipus TWA hem estat capaços de desenvolupar una expressió analítica que ens ha permès determinar com les simulacions s'allunyen dels models teòrics.

Tots els models que hem generat en aquesta tesi s'han analitzat fent servir codis escrits en FORTRAN i en Python i que hem generat a mesura que ens han estat necessaris en els nostres estudis. També hem fet servir eines de visualització tals com Topcat i TIPSY que ens han permès controlar les propietats globals de les simulacions.

Resultats i conclusions

En aquesta tesi hem estudiat la cinemàtica i la dinàmica de galàxies semblants a la Via Làctia en diversos models teòrics i simulacions. Els models que hem fet servir, en ordre creixent de realisme i complexitat són: models analítics, simulacions de partícules test, simulacions N-cossos pures de galàxies aïllades i finalment simulacions de volums cosmològics que tenen en compte tan la part dels N-cossos com la de la física de les components hidrodinàmiques. Tots els models que hem generat en aquesta tesi queden ara disponibles per a nous estudis.
Les primeres simulacions que hem fet servir per dur a terme el treball que presentem aquí són els models N-cossos purs de galàxies tipus Via Làctia, aïllades. Al Capítol 4 detallem tots els anàlisis que hem dut a terme a partir d'aquests models i que estan relacionats amb

l'estudi del perfil radial de la velocitat de rotació de les estructures espirals. Els resultats principals que hem obtingut són:

- El mode de densitat dominant en simulacions de galàxies barrades és el mode de Fourier m=2, que correspon a la barra en la part més interna i a uns braços espirals bisimètrics a la part externa del disc. Aquest mode està connectat a la barra la major part del temps. Quan la connexió amb la barra es trenca l'estructura espiral es dilueix i s'integra al disc. Poc temps després de al desconnexió es genera un nou mode espiral d'm=2 des de la barra.
- Aquest mode espiral de densitat rota a la mateixa velocitat que la barra i té perfil radial de rotació semblant al d'un sòlid rígid quan aquesta és forta (té una amplitud gran).
- El perfil radial de rotació de l'estructura espiral s'allunya de la rotació rígida quan la barra és feble i tendeix a la corrotació amb les partícules del disc.
- En els models barrats, a més del mode dominant, existeixen d'altres modes subdominants amb perfils de velociat diferents al de l'estructura principal. Un dels nostres models mostra una estructura d'm=2 present a radis grans i que rota molt més lenta que la principal.
- Les partícules que es troben dins els braços espirals dominants, en els models barrats, es mouen seguint l'estructura del braç i cap a les parts externes del sistema, una situació que és compatible amb l'escenari de formació de braços espirals anomenat de varietats invariants.
- Per obtenir models amb barres fortes és imprescindible fer servir simulacions amb discos de matèria fosca vius (no analítics) cosa que permet el lliure intercanvi de moment angular entre les diferents components de la galàxia.
- En els models no-barrats no existeix un mode de Fourier que domini clarament i que tingui un temps de vida llarg. Diversos modes espirals competeixen en les nostres simulacions essent els més importants el 3 i el 4.
- Tal com caldria esperar en un cas barrat on l'amplitud de la barra tendeix a zero, en els casos no-barrats les estructures espirals dominants presenten un perfil radial de rotació que coïncideix amb el de les partícules del disc, és a dir ambdues components corroten. Aquests braços corrotants són altament transitoris i presenten temps de vida de l'ordre de desenes de milions d'anys.
- El moviment de les partícules en els models no-barrats és l'esperat per un cas on els braços són corrotants. Si analitzem en detall l'evolució de les partícules que es troben distribuïdes dins un braç veiem com amb el temps aquestes s'enrotllen entorn del disc galàctic tal com ho fan les partícules del disc galàctic degut a la rotació diferencial.

- Els braços espirals corrotants també indueixen a les estrelles del disc a migrar radialment.

Per tal d'assegurar que es pot confiar en els resultats que presentem aquí hem fet diversos tests de convergència del codi. Amb aquests tests hem demostrat que aquests no estan afectats per problemes numèrics i que no depenen del codi utilitzat per obtenir les simulacions.

En el segon estudi que presentem aquí, a més de les simulacions d'N-cossos pures, hem utilitzat una aproximació analítica per braços espirals de tipus TWA i diversos models de patícules test on hem imposat, a part del potencial axisimètric, diversos potencials de barra o de braços espirals. Els resultats d'aquest estudi els presentem al Capítol 5 i responen a l'anàlisi de la funció de distribució de velocitats de conjunts d'estrelles que hem agrupat en petites regions distribuïdes per tot el disc galàctic. A continuació resumim els resultats principals:

- Confirmem que la posició de les regions amb valors no nuls de la desviació del vèrtex (l_v) són un bon indicador de la presència d'estructures de densitat en les galàxies.

- En tots els casos de braços espirals no corrotants que hem analitzat el signe de la l_v canvia en creuar els pics de densitat de l'estructura espiral i també a la regió inter-braç. Aquest resultat s'observa en l'aproximació analítica i també en les simulacions de partícules test i N-cossos.

- El canvi de signe que es produeix en creuar el pic de densitat o la regió inter-braç és diferent depenent de si la regió es troba dins del radi de corrotació de l'estructura amb el disc (CR), entre la corrotació i la resonància externa de Lindblad (OLR) o fora de la OLR. En la regió compresa entre el radi de CR i el radi de la OLR els valors de la l_v passen de negatius a positius quan se segueix la direcció de rotació galàctica, mentre que en la resta de regions el canvi és de valors positius a negatius.

- En el cas corrotant no existeix una correlació directa entre els valors de la l_v i les sobredensitats. No obstant això és necessari un estudi més profund per tal d'entendre si existeixen relacions d'algún altre tipus.

- Fent servir simulacions de partícules test on s'han variat d'un en un alguns paràmetres inicials de la component axisimètrica i dels potencials no axisimètrics hem demostrat que els nostres resultats no depenen de les condicions inicials ni dels potencials imposats.

- Per primera vegada s'ha fet un anàlisi complet de la l_v en simulacions d'N-cossos. Els resultats que hem obtingut coïncideixen amb els dels models de partícules test i també amb els de l'aproximació analítica.

- El fet que el gradient de la l_v que s'observa quan es creuen els braços espirals es pugui utilitzar com a indicador de la posició de la CR fa que també sigui útil per discriminar quina és la naturalesa dels braços espirals. Un exemple d'això és el fet que de la teoria dels braços de tipus ona de densitat en surten uns braços que es troben dins la CR mentre que de les varietats invariants en surten uns que es troben fora.

- A part dels efectes dominants presentats anteriorment s'observen també diferències de segon ordre en la forma i la magnitud dels patrons de l_v segons el model que s'analitza. Aquestes irregularitats poden esser una conseqüència directa de les diferències en els camps de força generats pels diversos potencials. Estudiar aquestes diferències, tot i que requereix un anàlisi molt més profund, ens pot servir per trobar un mètode que ens permeti caracteritzar el potencial de l'estructura espiral en galàxies reals.

Finalment, després de passar els primers anys d'aquesta tesi entenent el funcionament dels codis i buscant unes condicions inicials idònies, hem estat capaços de generar models realistes de galàxies tipus Via Làctia en un context cosmològic, fent servir codis d'N-cossos amb hidrodinàmica. Els models que hem obtingut estan descrits amb tots els detalls al Capítol 6. Aquests models que inclouen la component hidrodinàmica (gas i pols) , així com diversos procesos físics relacionats amb la seva evolució, són molt més realistes que els que s'han fet servir en els estudis que hem presentat anteriorment i és per això que també el seu anàlisi és molt més complex. En l'últim any d'aquesta tesi n'hem iniciat el procés d'anàlisi i els primers resultats que hem obtingut han estat molt interessants. No obstant això, serà necessari molt més temps per poder analitzar, entendre i treure el màxim profit d'aquesta nova simulació. A continuació detallem alguns d'aquests primers resultats que hem obtingut i que presentem al Capítol 8:

- Els canvis en l'agressivitat del refinament de les components de matèria fosca i de gas no tenen un impacte important en les propietats generals del model. D'altra banda, sí que s'observa una disminució de la massa total de gas fred a mesura que l'agressivitat augmenta. Aquesta disminució de la quantitat de gas fred es deu al fet que se'n consumeix una quantitat major en la formació estel·lar. Noves regions de formació estel·la apareixen en llocs on amb una agressivitat menor aquesta no es produïa. Aquesta manca de gas fred a z=0 també es tradueix en una disminució del ritme de formació estel·lar (SFR).

- A la regió central dels nostres sistemes galàctics principals, i a partir de les partícules del disc, es forma una barra jove. La seva longitud d'escala és de 2 kpc i és molt densa.

- L'origen del sistema galàctic principal dels nostres models es troba en la fusió de dues galàxies el·líptiques a z=3. D'aquesta fusió n'ha sobreviscut una estructura en forma de barra amb una població estel·lar molt vella. Aquesta barra vella té una longitud d'escala de 7 kpc, és molt menys densa que la barra jove i el seu semieix major es troba desfasat 90 graus respecte a la primera.

- Ambdues barres roten a una velocitat molt semblant, cosa que, juntament amb la baixa densitat de la barra vella, permeten que aquesta configuració es mantingui estable durant diversos milers de milions d'anys.
- La distribució de gas calent en els halos foscos dels nostres sistemes principals és altament anisotrópica. En el cas que aquest resultat es presenti també en els sistemes reals pot portar a importants biaixos en la determinació de la seva massa total de gas si s'utilitzen les tècniques observacionals habituals. Això és degut a que habitualment es fan servir un nombre molt petit d'observacions en direccions diferents del cel per determinar una mitjana de la densitat columnar de gas calent i a partir d'aquesta mitjana, assumint una distribució homogènia de gas en tota l'esfera celest, calcular-ne la massa total. Hem constatat que fent servir aquesta tècnica es necessiten un mínim de 50 observacions a punts diferents del cel per recuperar el valor mig real de la distribució, mentre que actualment se n'estan fen servir de l'ordre de 10 o menys.
- El gas calent de l'halo es troba en un estat altament turbulent, de fet hem observat que existeixen regions amb valors de metal·licitat molt diferents en continu moviment. Hem vist com gas de baixa metal·licitat cau cap al disc galàctic des del medi intergalàctic mentre el gas ric en metalls parteix del disc empès pels vents estel·lars i les explosions de supernova. Observem també una clara anisotropia entre els hemisferis galàctics nord i sud en la metal·licitat del gas. Hem comprobat que aquesta anisotropia és deguda a l'acreció de petites galàxies satèl·lit entorn a z=0.
- La quantitat de gas calent que hi ha a l'halo pot explicar en bona part la massa dels coneguts com a barions perduts tot i això aquesta no és suficient per resoldre del tot el problema. Resultats molt semblants s'han obtingut en d'altres simulacions i també en algunes observacions.
- Finalment, un altre resultat interessant que hem obtingut és que la massa total de les galàxies pot estar directament relacionada amb la seva massa total de gas calent. Si això es confirmés la determinació de la masa total de gas calent ens permetria posar nous límits a la massa total d'aquests sistemes.

Concloent, en aquesta tesi hem analitzat diverses propietats de les estructures a gran escala de les galàxies tipus Via Làctia fent servir diverses aproximacions, des de models analítics fins a simulacions de volums cosmològics que inclouen partícules N-cossos i també la hidrodinàmica del gas i de la pols. Obtenir i analitzar tots aquests models ens ha permès aprendre el funcionament de grans infraestructures de computació, a treballar amb grans bases de dades, a distingir entre els efectes numèrics i els efectes reals en les simulacions i a programar en diversos llenguatges, entre d'altres. Els resultats que hem obtingut aquí seran molt útils en un futur proper quan les dades de noves missions i projectes observacionals tals com APOGEE i Gaia es facin públiques. Aplicant els nous mètodes que hem desenvolupat a les dades reals podrem obtenir nova informació sobre les estructures a gran escala tan de la nostra pròpia Galàxia, la Via Làctia, com de galaxies externes.

Abstract

Simulations have shown to be one of the best tools to study properties of large scale structures and their effects on to the local kinematics of stars in in galactic systems. The aims of this thesis are: i) To obtain realistic N-body models that allow us to analyse kinematics, dynamics and internal structure of non-axisymmetric components in galaxies, ii) to learn how to control numerical effects and how to distinguish between them an the proper physical ones, iii) to find observational kinematical or dynamical tracers that can give us information about formation, evolution and nature of the large scale structures in galaxies and, iv) to develop methods that from the observed local kinematic properties of stars or from the global properties of galactic large scale structures give us information about the nature of the spiral structures in real galaxies. Using high resolution simulations obtained with different codes and initial condition techniques we find that exist two different behaviours for the rotation frequency of transient spiral arms like structures. Whereas unbarred disks present spiral arms nearly corotating with disk particles, strong barred models (bulged or bulge-less) quickly develop a bar-spiral structure dominant in density, with a pattern speed almost constant in radius. We have also mapped the kinematics of stars in the simulated galaxy disks with spiral arms using the velocity ellipsoid vertex deviation (l_v). For this study we have used both test particle, high resolution N-body simulations and analytical approaches. We have seen that for all barred models spiral arms rotate closely to a rigid body manner and the vertex deviation values correlate with the density peaks position bounded by overdense and underdense regions. In such cases, vertex deviation sign changes from negative to positive when crossing the spiral arms in the direction of disk rotation, in regions where the spiral arms are in between corotation (CR) and the Outer Lindblad Resonance (OLR). By contrast, when the arm sections are inside the CR and outside the OLR, l_v changes from negative to positive. We propose that measurements of the vertex deviations pattern can be used to trace the position of the main resonances of the spiral arms. Finally we present a new cosmological Milky Way like galaxy simulation including N-body and the hydrodynamical component, that has been obtained using the adaptive mesh refinement (AMR) code ART (Kravtsov 2003). This MW like system has been evolved inside a 28 Mpc cosmological box with a spatial resolution of 109 pc. At z=0 the system has an $M_{vir} = 7.33 \cdot 10^{11} M\odot$. We have observed how a well defined disk is formed inside the dark matter halo and the overall amount of gas and stars is comparable with MW observations. Several non-axisymmetric structures arise out

of the disk: spirals, bars, warp and also two disk components, a thick and a thin disks. The most interesting structure that has appeared inside the simulated disk is a system of two misaligned bars. These two bars are misaligned 90 degrees and have a completely different origin. The first one is young and has been formed from disk particles, the second one is a fossil of a major merger that occurred at z=3 and because of that it is much older. Both bars rotate at the same pattern speed what would explain why the system remained stable for the last Gyrs. In this work we have also studied the hot gas component that is present in the galactic halo. We have observed that a huge reservoir of this gas is present at large distances from the disk, embedded in the dark matter halo region. Gas column density, emission and dispersion measures have been computed from the simulated disk at a position of 8 kpc from the center, resembling Suns' position, and in several directions. Our preliminary results reveal that the distribution of hot gas is non-isotropic what agrees with recent observations (Gupta et al. 2012; **?**). This anisotropy can become a problem when using a low number of observations to compute the total gas mass in galaxies. We demonstrate that when it is used the most common technique to compute the total gas mas in galaxies from observations more than 50 observations of different positions in the sky are needed to recover the real value.

The author was supported by the Predoctoral Fellowship of Ministerio de Economia, Ciencia y Deporte (MECD) 2009FPU AP-2009-1636 and by the GREAT-ESF Short Visit Grant with reference number 5121. This thesis has been carried out at the Departament d'Astronomia i Meteorologia (Universitat de Barcelona) and at the Instituto de Astronomía (Universidad Nacional Autónoma de México. This study was supported by the MINECO (Spanish Ministry of Economy) - FEDER through grant AYA2009-14648-C02-01, AYA2010-12176-E, AYA2012-39551-C02-01 and CONSOLIDER CSD2007-00050. The simulations were run at the Pakal, Abassi, Abassi2 and Atócatl clusters at the IA-UNAM, Miztli cluster in the DGSCA/UNAM, Obacs and Pirineus at CESCA supercomputing center in Barcelona, CATON cluster (Sol), centzonmimixcoa and bonaigua at the DAM/UB and at the HTCondor in the Kapteyn Astronomical Institute.

Contents

1
Introduction

1.1 Background

It was more than 400 years ago when the first telescope observations of night sky were done by Galileo Galilei. It was also Galileo Galilei who made the first observation of our Milky Way Galaxy using a telescope. With these first observations he discovered that the diffuse band of light that can be observed by naked eye is in fact a large group of faint stars. These first observations became the beginning of the study of galactic systems. One century and a half after these first discoveries an English astronomer called Thomas Wright suggested that all those stars that could be observed by telescopes might be bounded together by gravitational forces and may be a part of a large rotating body. This astronomer, after looking carefully other diffuse light structures known as nebulae, also purposed that some of them could be similar systems as the Milky Way but far away. Some years later Immanuel Kant proposed the final idea that the Milky Way and some external nebulae could be isolated stellar systems inside a mostly empty universe, he called these systems island universes. From these first works in galactic astronomy, our knowledge have improved a lot by using new and better telescopes and also new and more precise instruments. Recently by using computer techniques our understanding of galaxies have gone one step further as they allow us to make simulations of how such systems form and evolve.

The most basic computer technique used to simulate systems that evolve under a force field is the so called N-body technique. In general, in astronomy, the main force that drives the evolution of systems is the gravity. First N-body simulations in galaxy formation and evolution date back to the very first light-bulb experiments of Holmberg (1941) in where it were used, instead of equations representing gravitational force, light detectors. This experiment was possible as the received light per unit area decreases with the square of distance, what makes the problem the same as when using gravity. However, it was not until second half of XX century when computers started to play an important role in galactic astronomy. This delay was a consequence of that first simulations could only deal with a low number of particles (16 in von Hoerner (1960)) due to computational restrictions. Since then, the number of particles was doubled every two years in accordance with Moores' law that takes into account the technological improvements. Also the use of new techniques to compute and solve gravity equations improved a lot the number of particles that could be used. In the first simulations it was used a technique known as particle-particle computation in which all interactions between each one of the particles are taken into account. This method gets the exact force produced by the presence of all particles in the system, at each particle position. In this case the amount of computational work required increases as $O(N^2)$ what makes impossible to simulate systems with a large number of particles as it can require decades or centuries of CPU time, to be completed. As we mentioned before, in the last decade technological improvements have made possible to obtain results from simulations with a large number of particles with reasonable computation times also using the particle-particle approach. One of the most important technological improvements in computation was the usage of parallel computers. Finally the introduction of new truncation or mesh techniques to compute gravitational forces also reduced the number of operations needed to complete the simulations and then the total time required.

In first N-body simulations only the stellar component of single galactic systems was modelled (e.g. von Hoerner 1960; Hohl 1971; Hohl & Zang 1979). It was not until the observation of galactic flat rotation curves were presented by Rubin et al. (1978) that the importance of dark halos in galactic dynamics arose. Since then most of simulations of galaxy formation and evolution have used a dark matter component to obtain realistic results (e.g. Sellwood 1980; Combes & Sanders 1981). More recently thanks to technological improvements it has been possible to obtain a new generation of isolated galaxy simulations that include live disks, dark matter halos, bulges and some of them the collisional component too. These simulations show the formation and evolution of realistic large scale structures such as bars and spiral arms (e.g. Athanassoula 1996; Debattista & Sellwood 2000; Valenzuela & Klypin 2003; Kawata & Gibson 2003; Dubinski et al. 2009; D'Onghia et al. 2010; Grand et al. 2012a; Roca-Fàbrega et al. 2013). Also in the recent years several projects succeeded in generating simulations of huge cosmological boxes in where dark matter evolve from high redshifts to the present days in a realistic way. In this context the most famous simulation is the Millennium run (Springel et al. 2005) that used more than 10 billion particles to trace the evolution of the matter distribution in a cubic region of the Universe over 2 billion light-years on a side. To simulate it it kept busy the principal supercomputer at the Max Planck Society's Supercomputing Centre in

Garching, Germany for more than a month. From this first case new large cosmological box simulations (hundreds of Mpc per side) with higher number of particles and/or better resolutions have been presented. Some examples are Millennium run II (Springel et al. 2008), Millennium XXL (Angulo et al. 2012), Multidark, Bolshoi that is the one with higher precision (Klypin et al. 2011) and the DEUS-FUR that is the larger one (Rasera et al. 2014). Simulations of cosmological volumes including not only collisionless particles but also lot of new physics mainly related with hydrodynamical processes are commonly used today and are reaching very high spatial and temporal resolutions with large number of particles. Some of the first attempts to include the collisional component in such systems were simulations presented by Abadi et al. (2003) and Sommer-Larsen et al. (2003). In these first cases it was simulated a small cosmological box with both dark matter and SPH gas particles. Another example of these first attempts was the MareNostrum Universe project (Gottlöber et al. 2006). In this case it was used GADGET2 code and it was simulated a large cosmological volume with a large number of both, dark matter and gas particles. Finally some recent works succeeded into obtaining realistic disk galaxies, this is the case of the ERIS simulation (Guedes et al. 2011) or the Aquarius project (Springel et al. 2008).

Far from the study of formation and evolution of galaxies using simulations, several authors focused their studies in the large scale structures of such a systems. Also in this field, the knowledge of formation and evolution of these structures improved a lot in recent years due to the high-quality observations and simulations available. However no one of the purposed theories to explain the processes of their formation and evolution and also to understand their nature, have succeeded. In the first theories of formation of spiral arm structures in galaxies it was proposed that a radial perturbation in the disk can be quickly converted into a spiral structure due to disk differential rotation. This first theory was discarded when it was demonstrated that such structures should have a much smaller lifetime than the one derived from observations due to that the winding is too efficient in differently rotating disks. Arising from this winding problem a new theory was proposed. In this new theory the spiral perturbation is an immaterial rigid spiral density structure that passes through the disk perturbing stellar orbits. This theory was first proposed by Lin & Shu (1964) and is known as the density wave theory. An analytical approach was presented to support the theory, however the approach only can be used if several assumptions are considered. Some of these assumptions are that the spiral perturbation have to has small amplitudes and pitch angles, and disk particles have to has small stellar velocity dispersions and follow the epicyclic approximation. Although there are several problems that need to be solved to fit this theory with observations, it survived across the decades up to our days. Nowadays it is one of the most accepted theories to explain the nature of spiral structures. One of the biggest problems of density wave theory is that it only explain what kind of object are the spiral structures (its nature) but not its origin. Several complementary theories have been proposed to explain such origin, for instance internal disk instabilities, the interaction with external galactic systems, or also more complex scenarios like the so known as Swing amplification or the non-linear coupling (Sygnet et al. 1988). In the recent years new theories that try to explain both, the origin and the nature of spiral structures have appeared. A clear example of these new theories is the one proposed by Romero-Gómez et al. (2007). In Romero-Gómez et al. (2007) the authors propose that spirals can be generated by the bar non-axisymmetric potential as orbits departing from sail points at the end of the galactic bar. This theory is known as the Invariant Manifolds theory. When trying to distinguish between which one of the present theories for the formation and evolution of spiral structures is correct it is common to use simulations. However results obtained from simulations are non conclusive as some of them point to a Swing Amplification / non-linear coupling generation (Masset & Tagger 1997) while others to Invariant manifolds (Athanassoula 2012). More recently several works purposed that in fact, under some conditions, spirals can be corotating with disk particles. In these works the initial winding problem is avoided by a recurrent spiral arm generation-destruction (Grand et al. 2012b; Roca-Fàbrega et al. 2013).

To obtain information about large scale structures from observations is not an easy task. When looking to external galaxies with the available instruments we can only observe them as an unique snapshot of its evolution what makes virtually impossible to analyse its kinematic properties. The only studies that can be made in a direct way with external galaxies are statistical studies. Some indirect techniques have been proposed to study large scale structure properties such as pattern speeds, most of them departing from assumptions that makes them model dependent (e.g. Martínez-García et al. 2009). However, it exists a simple model independent technique that under only three small conditions finds pattern speeds of spirals in external galaxies. This method is called Tremain & Weinberg technique (Tremaine & Weinberg 1984) and the only assumptions it makes are that the disk is flat and has a well defined pattern speed, and that the surface brightness of the tracer obeys the continuity equations.

When studying our own Galaxy the real problem to find properties of large scale structures is the amount of gas and dust that makes difficult to obtain data from stars that are far and inside the galactic disk. In recent years some techniques have been proposed to study properties of galactic large scale structures such as bars and spirals using kinematic data from individual stars in the solar neighbourhood. It was discovered that structures in the kinematic space called moving groups can give information about several properties of both, bars and spirals. With these techniques it will be possible to constrain the pattern speed, amplitude and also pitch angle of such structures (Antoja et al. 2011). Also the analysis of moments of the velocity distribution function have shown to be good tracers of galactic density structures (Vorobyov & Theis 2006; Roca-Fàbrega et al. 2014).

In the near future new and very ambitious surveys like APOGEE and GAIA and also very realistic high resolution MW like simulations will be available to test all the proposed theories for the galaxy formation and evolution an for the nature of its large scale structures. We are now entering to the gold age of the study of galaxy and its components.

1.2 Thesis aims and methodology

The formation and evolution of spiral arm structures in disk galaxies is a process that is not well understood. Properties of these structures like rotation frequency profiles, density structure or its effect over disc stars remain unclear. To study such structures from observations is not easy. External galaxies are so far that we can only observe a single picture of its structures and not the evolution. In this case what we can do is to make statistical studies to constrain properties such as the lifetime of these structures. The case of our own Galaxy is much more complicated as we are looking these structures from inside. The main problems we face when looking for structures in the MW are the dust absorption, projection effects and the degeneracy of the results due to the presence of multiple density structures. Nonetheless to study structures in our MW has some advantages too, for instance we can analyse kinematics of single stars or statistical properties of such stars in small regions inside the Galaxy, something that nowadays it is impossible for external galaxies. These kinematic statistical analysis of stars in small regions inside the Galaxy have shown to be a source of information about the none axisymmetric structures. It has been confirmed that the presence of groups of stars moving at similar speeds, known as moving groups, can give us information about spiral arm and bar structures. Other parameters like velocity means, second and third order moments have shown that can be other good tracers of the properties of such structures.

Due to the problems with observations several theories have been proposed to solve the problem of the formation, evolution and properties of spiral arm structures. Most of these theories argue that these structures are long lived density waves passing through the disk in a rigid body rotation, however only few of them purpose possible formation scenarios. Furthermore, observations do not agree with the spiral life times as they are based only in statistical studies. Until now the only way to test these theories is to use realistic simulations of formation and evolution of galaxies.

In the last decade several groups have started using simulations to test spiral arm theories obtaining results that confirms most of the theories. It is possible that in the real world spirals have not a single origin or nature, it may happen that under different assumptions or environments the spiral arms fit better within one or other theory. Nowadays still there is a long list of unresolved questions about spiral arms formation, evolution and nature and here we summarize some of them:

- Which are the mechanisms that drive the formation of spiral arms in galaxies?
- In which circumstances each one of these mechanisms act?
- Are spiral arms long or short lived structures?
- How these structures rotate? It depends on the triggering mechanism?
- Are spirals density waves or material structures?
- Can some kinematic property of local stars disentangle between spiral arm natures?
- It exist some large scale observable property that can give us information about formation and nature of such structures?
- Are all spiral structures producing shocks with disk material and triggering star formation?
- Are great design spirals generated in a different way than floculent ones?
- In which degree bars are related with spiral structures? Why they usually show to be connected in great design structures?
- Is the gas or even the magnetic field important for the formation and evolution of these structures?

To answer all these questions further research is required. The increasing quality of simulations let to research groups to start investigating deeper all properties of spirals and to start solving some of the previous questions. In this thesis we plan to obtain simulations that can reach the level of the ones used in the community and try to solve some of the open questions in the field.

In this thesis we study the N-body codes that let us generate realistic simulations of galaxy formation and evolution. We also analyse the global and local properties of large scale structures and stars to find a method that helps us to distinguish between different natures and formation mechanisms. The specific aims of this research are:

1. To obtain realistic N-body models that allow us to analyse kinematics, dynamics and internal structure of non-axisymmetric components in galaxies.
2. To learn how to control numerical effects and how to distinguish between them an the physical ones.
3. To find kinematical or dynamical tracers that can give us information about formation, evolution and nature of the large scale structures in galaxies.

4. To test which of the methods obtained from the study of simulations can be used to distinguish between spiral arm natures in real galaxies.

In parallel with these main goals we also expect that in this thesis we learn how hydrodynamics are implemented in N-body models and which are the key parameters that drives to the obtention of realistic galactic systems. Finally, as a realistic MW like model will give us much more information than only the one of spiral arm structures, we expect that we will be able to use them to study other properties of galaxies that nowadays are not well understood.

To undertake the research entailed in this thesis we have used several simulation techniques. To begin with we have used a collisionless N-body code to simulate isolated galactic systems, later we have analysed test particle simulations with different imposed non-axisymmetric potentials and finally we have generated simulations using an N-body plus hydrodynamics code.
The ART code has been our basic N-body code both for collisonless and cosmological N-body plus hydrodynamics simulations. The code called GADGET3 has been used to test the independence of our results on the code. The first N-body models we have generated are simple models of isolated MW like systems starting from recent epochs and with all components alive (halo, disk and in some cases bulge). With these first simulations we have learned how to use properly N-body codes, how to analyse them and how to avoid numerical problems. After acquiring a good knowledge about N-body codes we have started to learn how to simulate more complex systems such as ones in fully cosmological boxes that start at high redshift, just from primordial density fluctuations. These last models have become the most realistic MW like Galaxy models and with higher resolution we have obtained and culminate the work that we undertook in this thesis.
Apart from N-body models, we have used other simulations to test our results in more controlled environments. We have analysed test particle simulations with different bar and spiral imposed potentials and with different initial conditions and parameters. For the spirals we have used the classical TWA potential with changing their intrinsic parameters such as amplitude, rotation frequency, pitch angle, velocity dispersions or integration time to test the dependence of the results on the parameters of the spiral. We have also used PERLAS spiral arm potential model (Pichardo et al. 2003) that is a specific potential model for the MW that is consistent with several recent observational constrains. For the bar we have analysed two sets of models, ones with quadrupole and the others with Ferrers potentials. We have not mixed bar and spiral arm potentials to simplify the analysis.
Finally for spiral arms TWA approach it has been possible to develop an analytical expression to test how far the theory is from the simulations.

All models have been analysed using FORTRAN and Python codes that we have generated according to our needs. We have also used visualization tools such as Topcat and TIPSY to control the global properties of simulated systems.

1.3 Thesis outline

This thesis is structured as follows. After this first chapter where we introduce the reader to the field of study of this work follows Part I in where we detail the numerical N-body codes we used for the analysis we present in Part II. Finally, summary and conclusions and also future work and perspectives are shown in PART III. In the next paragraphs we detail the content of each one of the parts and also of its chapters.

Part I presents the codes and the methodology used to obtain the N-body models that we have analysed to undertake the work presented here. In Chapter 2 we describe ART and GADGET3 collisionles N-body codes and the process we have followed to obtain isolated galaxy models. In this chapter we also detail the strength and weaknesses of using such simulation method as so the tests that are necessary to ensure that results are not dominated by numerical effects. Chapter 3 is devoted to describe the hydrodynamical implementation used here to obtain a realistic model in a fully cosmological environment. All implemented physics are fully described in this chapter and also, as for the collisionless codes, the strength and limitations of using this technique are pointed out.

Part II reports the main results of this thesis. In Chapter 4 we present the collisionless N-body models of isolated galaxies we have used both in this chapter and in the next one. First results on the rotation frequency profile of spiral arms and its dependence on the galactic model are also presented in this chapter. Chapter 5 describes the results of analysing local kinematics of stars in several analytical, test particle and N-body models in where different spiral arms potential, i.e. natures, are present, both because have been imposed or they have naturally arisen. Finally in Chapter 6 we describe our final N-body plus hydrodynamics cosmological models of a realistic MW like galaxy. In this chapter we show the general properties of the model and we compare them with the observations. To finish with we present some first results on the analysis of the hot gas component present in the galactic halo and also of several large scale structures embedded into the galactic system.

Finally Part III summarises the main outcomes of the whole thesis and purposes the future work and perspectives that arise from it. In Chapter 8 we give the general conclusions of the thesis and in Chapter 9 the future work that need to be undertaken to answer the new questions that arise from the results obtained here. At the end of the thesis we present the bibliography and three appendixes. Appendix A is where we show how we generate the toy models we have used to test in which situations the methods used to compute spiral arm rotation frequency work and in which not. Also the results of such analysis are presented here. Appendix B contains the analytical development we have followed to obtain the analytical vertex deviation expression that describes how this parameter behaves in a system with an TWA spiral arm potential. In Appendix C we describe the methodology used to find the galactic center an to set the galactic disk plane in our fully cosmological N-body plus hydrodynamics simulations.

Part I

Numerical tools

2

Collisionless N-body simulations

2.1 Introduction

The use of simulations to study galactic dynamics and kinematics has a long tradition since systems with non-axisymmetric structures like spiral arms and bars became too complex to be studied analytically. A first kind of simulations that can be used to undertake these studies are the so called test particle simulations. In these simulations an axisymmetric potential is imposed and then it can be superimposed a non-axisymmetric one. Once having the analytical potential a distribution of N particles are evolved under it without self-interaction. Using these simulations one can study orbits and statistics of particles moving under similar potentials, nonetheless them have also some limitations. One important limitation is the difficulty of imposing a potential that evolves in time, evolution that actually happens in real galaxies. Other is the lack of self-consistency as particles are not seeing each other. On the other hand a strength of the method is that it is not as computationally expensive as other methods like N-body models. Also important to mention is that test particle models are highly parallelizable what allows to simulate lots of particles at once.

However, as mentioned, if we want to study a time evolving system that has a highly non-lineal nature and we also want that it evolves self-consistently, we need a new method. This new method can be N-body simulations. The simplest N-body simulations are those that compute positions and velocities of particles only under its own gravitational field by solving Poisson and Boltzmann equations. In these simulations interactions between particles are taken into account and the global potential is generated by the whole particle distribution. However, although they are a good tool to analyze a great variety of systems, it is important to be aware of the range of physical scales where the simulation is well behaved to detect which results are real and which ones can be created by numerical effects. These physical scales are defined by what is called resolution. One example is the temporal resolution that is given by the minimum time step between two computations of the gravitational force and that puts a limit in the temporal scale as particles move from its previous position to the next one without taking into account what happen in the way. Other example is the spatial resolution that is the minimum distance between two points where the force is computed exactly, in the intermediate positions the force is interpolated. Some other examples are the softening, i.e. the minimum distance from the gravitational source in where the gravitational force take real values, or the mass resolution that is the minimum mass of particles.

As we said, the most simple N-body simulations are the ones where only gravity is taken into account, we will refer to them as pure N-body simulations or collisionless. Although their apparent simplicity this pure N-body simulations are a powerful tool to study first order effects of galactic dynamics and kinematics as gravity plays the main role in the galactic evolution. Using the collisionless N-body simulations we are able to study processes like bar formation and evolution and spiral arms dynamics, without forgetting that there are some limitations given by resolutions and by the lack of physical processes.

Here we present pure N-body codes used in this work, the generation of initial conditions and finally some convergence test we made to ensure that our results are not affected by numerical issues and also the limitations that we have when using this technique.

2.2 Adaptive Refinement Tree code (ART)

In this section we describe the Adaptive Refinement Tree code (ART) (Kravtsov et al. 1997) that is an Eulerian collisionless N-body code. As a summary, the code follows the main steps we numerate here, after the initial conditions have been provided:

1. Generation of a regular cubic grid covering the whole computational volume.
2. Addition of refinement cells where they are required. This addition happens in regions where the density is above some imposed threshold.
3. Density computation at each cell taking into account the mass and position of particles.
4. Solution of Poisson equation using the FFT gravitational solver at each cell through all refinement levels.
5. Update of particle positions and velocities.
6. Start again the process, modifying the mesh hierarchy.

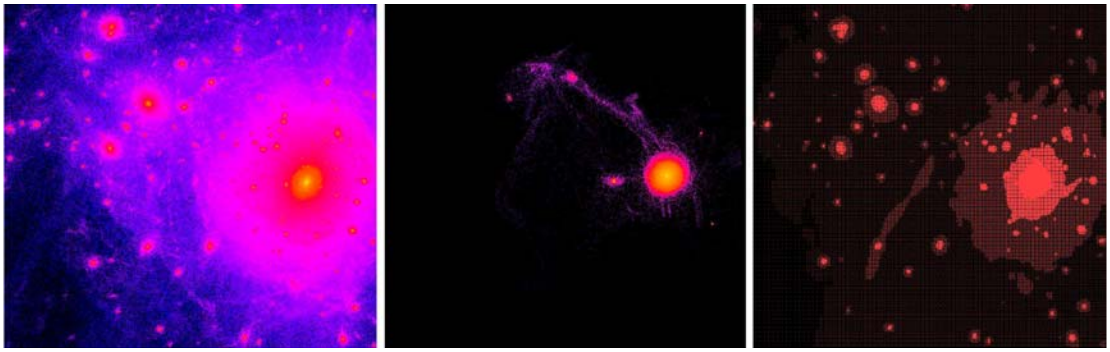

Figure 2.1: Left: Dark matter density field. Center: Stellar density field. Right: corresponding AMR grid.

In the next sections we go in more detail on each one of the simulation steps and on the used procedures.

2.2.1 Adaptive mesh refinement (AMR)

ART uses an Adaptive Mesh Refinement (AMR) technique for solving the Poisson differential equations (PDE, Equation 2.1). In this code the simulation box is divided in a first coarse grid of cells where the PDE are solved meanwhile the AMR is applied. AMR is a method of changing the resolution of the mesh (grid spacing) where the equations are being solved, when the properties in the region change somehow (see right panel in Figure 2.1). In the case of galaxy formation and evolution simulations equations that are solved are the PDE. The resolution changes depend on density limits imposed before starting the simulation, as denser is the region, smaller becomes the grid spacing. The use of AMR approaches reduces by a large factor the CPU time required for a simulation. In ART the AMR approach used is the one that divides the computational volume into regular cubic cells. This approach could be problematic when dealing with complex boundaries in which case the best choice could be to use irregular cells, however in astronomy, as it is the case here, it is usual to have simple boundaries then this approach is the best as is the less CPU consuming.

$$\nabla^2\phi = 4\pi G\rho \tag{2.1}$$

As previously pointed in this code each cell is split in eight when a density threshold is reached (more than N particles reside inside the volume). Also if at some point the threshold is not reached anymore the cells are joined together again.

2.2.2 Tree system and refinement process

In ART cells are organized in a tree system to form a multigrid hierarchy. Cells are treated as individual units organized in refinement trees. Each tree has a root that is a cell belonging to a base cubic grid that covers the entire computational volume. From the root, if the cell is refined (split) there are eight children that are smaller and non-overlapping that will reside in this volume. The child cells can be refined in their turn and so on up to the maximum refinement level allowed. This structure is called octal rooted tree. All cells in a given refinement level are organized in linked lists and form a refinement mesh. The tree data structures make mesh storage and access in memory logical and simple, while linked lists allow for efficient mesh structure traversals. In this code the information about the parent cell and the first child is maintained for each cell, also the information about the six adjacent cells. With all these information it is possible to avoid problems derived from heavy jumps (more than one refinement level) in resolution between cells. When a parent cell is refined the code check if its six neighbours are of the same refinement level as the parent or coarser, if not, the neighbours are refined. When the neighbours are refined, again the refinement level of the neighbours of the neighbours are checked and so on. With this system two cells with a difference of more than 1 refinement level are never contiguous. The refinement process can be split into two major parts. First all cells that need to be refined are marked creating a refinement map that is smoothed by marking additional cells so that any cell that was originally marked is surrounded by a buffer of at least two other marked cells. Second, when the map is completed, it is used to make the actual splitting. This refinement procedure is used both to construct the mesh from scratch and or to modify the existing meshes from a previous simulation step. Once generated the mesh for the first time it is never destroyed, only modified at each step. Modifying the mesh is much less CPU consuming than rebuilding it all at each step.

2.2.3 Density computation and PDE solver

Once the mesh is completed, the correct density have to be assigned to each cell from the particles distribution. Before computing density it takes place a process that distributes the mass from individual particles to cells that is where the computations take place. The process used here is a method known as cloud-in-cell (CIC) (Hockney & Eastwood 1981), and it takes place starting at the finest level and then up to the zeroth level. The CIC assumes the particle is not anymore placed at its initial position as a point source of gravity but in a “cloud of mass” all around it. This cloud of mass usually fills partially more than one cell, in this case what the code does is to assign to the cell all the mass that falls inside it (see a simple 2D example in Figure 2.2). In this way the particle mass is split to the contiguous cells according to its distance. In the ART code it is used a Triangular Shaped Cloud (TSC) what ensures the continuity of first derivatives. As the particles only belong to the finest cells enclosing them, to compute density at all levels they are passed

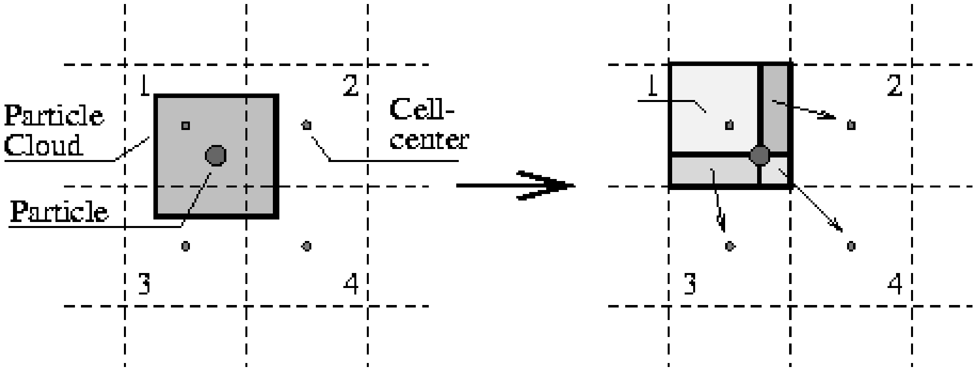

Figure 2.2: 2D CIC mass assignment.

from children to their parents. In this way all particles contribute to density of all levels.

After finishing the previous process a multigrid method is used to compute the potential at each position of the grid. This method works as follows: PDE are solved in the coarser or zeroth refinement level using a standard Fast Fourier Transform (FFT) method with periodic boundary conditions. This solution is then interpolated from the coarser onto the finer fist-level mesh to get the boundary values and first-guess solution. Once the boundary problem is defined, an iterative method (e.g. Press et al. 1992) is used to solve the Poisson equation on this level of the mesh , this process is a Gauss-Seidel relaxation scheme with Successive Overrelaxation (SOR) and with Chebyshev acceleration (Hockney & Eastwood 1981). Since the process starts from an initial guess that is already close to the final solution, the iterative procedure converges quickly, only 2 or 3 iterations are needed. After the convergence at the first refinement level, the same procedure, i.e. obtaining boundary values and an initial guess by interpolation from the previous coarser level, is repeated for the next level, and so forth. Using this process, the convergence is so fast that it is not needed to come back from the finest grid to the coarser one to obtain the proper potential values (i.e. a full-multigrid method is not necessary). At the end of this process the potential at each cell is obtained and it is interpolated to the original particle location using again the CIC method (Hockney & Eastwood 1981).

2.2.4 Update of particles position and velocity

Once computed the total potential at the particles position, new particle positions can be integrated from the Newtonian equations of motion in an expanding cosmological framework (e.g. Peebles 1980). These equations are expressed in terms of comoving coordinates $\mathbf{x}$ related to the proper coordinates as $\mathbf{r}$=a(t)$\mathbf{x}$, where a(t)=$(1+z)^{-1}$ is the expansion factor and z the redshift:

$$\frac{d\mathbf{p}}{dt} = -\nabla_{\mathbf{x}}\phi, \quad \frac{d\mathbf{x}}{dt} = \frac{\mathbf{p}}{a^2}, \tag{2.2}$$

,$\mathbf{p}$ is the momentum of the particle and $\nabla_{\mathbf{x}}\phi$ is given by the Poisson equation relating the potential ϕ to deviations of density from the background ($\bar{\rho}$):

$$\nabla^2_{\mathbf{x}}\phi = 4\pi G a^2(\rho - \bar{\rho}) \tag{2.3}$$

The above equations are integrated numerically using dimensionless variables:

$$\mathbf{x} = x_0\tilde{\mathbf{x}}, \quad t = \tilde{t}/H_0, \quad \phi = \tilde{\phi}(x_0 H_0)^2, \tag{2.4}$$

$$\mathbf{p} = \tilde{\mathbf{p}}(x_0 H_0), \quad \rho = \tilde{\rho}\frac{3H_0^2}{8\pi G}\frac{\Omega_M}{a^3}, \tag{2.5}$$

where x_0 is the length of a zeroth-level mesh cell, H_0 is the Hubble constant, G is the gravitational constant and Ω_M is the present-day (z=0) contribution of matter to the total density of the universe. We also use the expansion factor a instead of the time, so that the equations can be rewritten:

$$\frac{d\tilde{\mathbf{p}}}{da} = -f(\Omega_M, \Omega_\Lambda, a)\tilde{\nabla}\tilde{\phi}, \tag{2.6}$$

$$\frac{d\tilde{\mathbf{x}}}{da} = -f(\Omega_M, \Omega_\Lambda, a)\frac{\tilde{\mathbf{p}}}{a^2}, \tag{2.7}$$

$$\tilde{\nabla}^2\tilde{\phi} = \frac{3\Omega_M}{2a}(\tilde{\rho} - 1). \tag{2.8}$$

Ω_Λ is the contribution of vacuum energy to the total density of the universe (measured by the cosmological constant). The function f is specific to a given cosmological model. f general form is:

$$f(\Omega_M, \Omega_\Lambda, a) = \frac{1}{1 + \Omega_M(1/a - 1) + \Omega_\Lambda(a^2 - 1)}. \tag{2.9}$$

The integrator used in the code is a standard second-order leapfrog (Yoshida 1993). The integration is done in a quasi-symplectic process as, although the time step depends on the resolution element, it is made slow enough to ensure that energy and volume in phase space are highly conserved. Next we detail the integration process. For a step n corresponding to a time step $a_n = a_{init} + n\Delta$a, the momenta and positions of particles are updated as follows:

$$\tilde{\mathbf{p}}_{n+1/2} = \tilde{\mathbf{p}}_{n-1/2} + \frac{d\tilde{\mathbf{p}}_n}{da}\Delta a, \tag{2.10}$$

$$\tilde{\mathbf{x}}_{n+1} = \tilde{\mathbf{x}}_n + \frac{d\tilde{\mathbf{x}}_{n+1/2}}{da}\Delta a, \tag{2.11}$$

where indexes n, n+1 and n±1/2 refer to quantities evaluated at times a$_n$, a$_{n+1}$ and

$a_n \pm \Delta a/2$ respectively. The time step is constant for all particles of the same level and it is reduced by a factor 2 per level from zeroth level to maximum refinement level.
It is important to take in mind that some complications arise from the integration method if the movement of particles across the level boundaries is not controlled. The resolution gradients, for example, may induce unwanted force fluctuations and anisotropies that need to be quantified (Jessop et al. 1994; Anninos et al. 1994). Also the momentum conservation, achieved by exact cancellation of numerical terms in the Cloud in Cell (CIC) method is not guaranteed on that cases. To avoid as much as possible this effects, in this code the force interpolation that uses both coarse and fine boundary cells is prohibited, interpolating instead on the coarse level. In this way particles are driven only by the coarse force until they move sufficiently far into the finner mesh where boundary cells will be of a higher refinement level. The same is true for particles moving from the finner to coarser mesh.

2.2.5 Set up and initial conditions

The generation of the initial conditions of a simulation is a key point to obtain results with a right physical meaning. These generation can lead to final results highly influenced by numerical effects if the process is not carefully done. Specially important is to take into account both, the effects of statistical fluctuations in the force representation and density distribution, the finite precision of computers and the truncation of high order therms when converting analytical equations into numerical expressions.
In this work we used two approaches for the initial conditions of N-body particles: evolution of an isolated galactic system and simulations of galaxy formation and evolution in a cosmological context. As the code allows the user to start the simulation from an arbitrary redshift we started the first ones at z=1 and the seconds at z=60. The former group of simulations starts from an axisymmetric disk galaxy distribution (stellar disk + dark matter halo) while the second one starts from the primordial density fluctuations of the universe.

Isolated galaxy initial conditions

To make the initial conditions of an isolated galaxy is a complex process that starts with the selection of the simulation box limits and ends with giving to all particles the velocities and positions that make the system stable after the simulation starts.
To undertake this process is important to know that in general the structure and evolution of a system with many particles (N-body) is described by the Boltzmann-Vlasov differential equation (von Roos 1960). This equation is a continuity equation in the phase space (coordinates and moments space) and its solution is a distribution function ($f(\mathbf{r}, \mathbf{v})$) that tells us the amount of particles per volume unit that are at a certain position, for a given velocity and moment ranges. If this distribution function can be obtained analytically

then it is simple to give to particles the positions and velocities that makes the initial system self-consistent (i.e. is solution of Poisson and Boltzmann equations at the same time).

In our work we used the RODIN code created by Dr.Octavio Valenzuela (IA-UNAM) for the initial conditions generation. This code uses the method proposed by Hernquist (1993) for the generation of positions and moments. Hernquist method is based in a theorem that ensures that a distribution function (f) can be expressed as a series of its moments (μ_{ijk}). The moments expression is defined in Equation 2.12 where U,V,W are the galactocentric velocity components and N the total number of particles in the system. In this method first the moments of the Boltzmann equation are computed, then some observed properties of galaxies are used to simplify the problem and cut the series at the order that minimizes the truncation error (e.g. stellar orbits assumed to be circular also called epicyclic approximation). This method can be used to generate all kind of structures from bulges and halos to disks, however it is important to take into account that some approximations are used to cut the series of moments that gives the distribution function.

Next we summarize how RODIN generates the initial conditions using the moments method.

$$\mu_{ijk} = \frac{\int\int\int_{\inf} U^j V^k W^l f(\mathbf{r},\mathbf{v}) dU dV dW}{\int\int\int_{\inf} f(\mathbf{r},\mathbf{v}) dU dV dW} \equiv \frac{F(U^j, V^k, W^l)}{N} \tag{2.12}$$

RODIN: Positions

The first step to generate the initial conditions with Hernquist method is to generate positions according to a density function. RODIN generates this distribution in spherical shells of width dr putting inside each of them a number of particles that depends on the theoretical density value for the shell and of an imposed threshold for the total number of particles that need to be placed inside it. Each one of particles positions (x,y,z) are obtained randomly using a Monte Carlo method. The width of the shell (dr) and the total number of particles inside it is determined establishing a limit on the difference between the theoretical density value and the value obtained from the distribution generated with this method. If the system has enough particles it is better to have smaller dr to reduce the possible effects of shell modulation, otherwise we need to take care on the Poisson fluctuations due to low number of particles that may affect the final distribution. As can be inferred from the previous discussion dr is a key parameter as gives us a limit in our spatial resolution, first because we want resolutions that do not resolve the shell distribution, i.e. the resolution has to be at least two times dr, and second because we also want Poisson fluctuations much smaller than spatial resolution. The second point is important to avoid as much as possible the contribution of Poisson noise to the generation of large scale fluctuations in our simulation, somehow we can stay that dr controls the Poisson fluctuations when the total number of particles is fixed. Here it is important to mention that Poisson fluctuations are one of the main issues in N-body simulations of galaxy evolution as usually became the seeds of the large scale structures observed in them. D'Onghia et al. (2013) showed that about 10^8 disk particles are needed to avoid completely the effect of these fluctuations. In our simulations as we are not interested in the origin of spiral arms or bars (i.e. internal or external perturbations) but in their properties and evolution, we are not much concerned about this problem, nonetheless we maintain Poisson fluctuations much below of our spatial resolution. For our models we used the theoretical density distributions that follows:

$$\rho_{disk} = \frac{M_d}{4\pi z_0 R_d^2} \exp \frac{R}{R_d} \mathrm{sech}^2 \left(\frac{z}{z_0} \right), \text{ cut-off at } R = 5R_d \text{ and } z = 3z_0 \tag{2.13}$$

$$\rho_{halo} = \frac{\rho_s r_s^3}{r\left(r_s + r\right)^2}; \quad \rho_s = \frac{M_{vir}}{4\pi r_{vir}^3 \left[\ln\left(1 + C\right) - \frac{C}{1+C}\right]}; \quad C = \frac{r_{vir}}{r_s} \tag{2.14}$$

$$\rho_{bul} = \frac{\rho_0 r_H^4}{r\left(r_H + r\right)^3}; \quad \rho_0 = \frac{M_{vir}}{4\pi r_H^3 \left(\frac{C_H}{1+C_H}\right)}; \quad C_H = \frac{r_{vir}}{r_H} \tag{2.15}$$

where M_d is the disk mass, z_0 the disk scale height, R_d the disk exponential length, r_s the halo scale radius, M_{vir} the virial mass, R_{vir} the virial radius and r_H the bulge scale radius.

The mass of each particle is constant for disk and bulge components, otherwise for the halo component RODIN uses a multi-mass method that places particles with low mass, that is the same mass as the one for disk and bulge particles, in the inner regions and increases it for particles at larger distances. As initial parameters the number of DM species is selected and also an equal number of limiting radius from where each specie begins or ends to be placed. The mass assigned to each particle is doubled when a limiting radius is reached. It is important in this process to ensure that not much high mass particles interact with the inner regions of the simulation. It have been well tested that for MW like sized models the region covered by small mass particles has to be at least ∼40 kpc, much larger than the size of the disk (O. Valenzuela PhD thesis). This method is used to reduce the total number of particles and then the required CPU time.

Rodin: Velocities

After positions generation the next step is to obtain the velocities of each particle, according to a velocity distribution function. For disk particles we obtain the vertical and radial dispersions using the following equations:

$$\sigma_z^2(R) = \pi G z_0 \Sigma(R), \tag{2.16}$$

$$\sigma_R^2(R) = A \exp^{-\frac{R}{R_d}}, \tag{2.17}$$

where $\Sigma(R)$ is the surface stellar density, z_0 the vertical scale height that is constant all over the disk, and A is a constant. The first expression corresponds to the solution of an hydrostatic problem when assuming constant velocity dispersion in the vertical direction. To obtain the second expression we assume that at some reference radius the radial random velocities are equal to Q (Toomre parameter) times the critical value needed to stabilize a differentially rotating disk against local perturbations:

$$A = \sigma_R(R_{ref}) = Q\frac{3.36G\Sigma(R_{ref})}{\kappa(R_{ref})}, \tag{2.18}$$

where κ is the epicycle frequency. In our MW like models we used an R_{ref}=8 kpc, however the result is very insensitive to this value as we use a constant Q parameter all along the disk. The Q or Toomre parameter is a quantity that measures the stability of a differentially rotating disk of matter against gravitational collapse and it is expressed as:

$$Q = \frac{c_s\kappa}{\pi G\Sigma}, \tag{2.19}$$

where c_s is the sound speed. The disk is stable (it will not develop instabilities like bars or spirals) when Q>>1.5 while it is linearly unstable if <1.5.
From dispersions velocities are obtained with a random Monte Carlo generation of a Gaussian distribution centered at 0 and with a dispersion that is one of the ones we obtained from equations.
Azimuthal dispersions are obtained by using the asymmetric current, epicyclic approximation and thin disk approximation:

$$V_\phi^2 = V_c^2 - \sigma_R^2\left|\left(\frac{2R}{R_d} + \frac{\kappa^2}{4\Omega^2} - 1\right)\right|, \quad \sigma_\phi^2 = \sigma_R^2\frac{\kappa^2}{4\Omega^2}, \tag{2.20}$$

V_c is the total circular velocity (disk+halo+bulge). In this case we give the azimuthal velocity to particles also in a random Monte Carlo generation but now with a Gaussian distribution centered at $V_\phi(R)$ and with σ_ϕ as the dispersion.
In all our generations we use the thin-disk approximation, i.e. all particles at the same radius have the same velocity distribution independently on the height.

For the spheroidal components, if we have a previous knowledge of $M(r)$ distribution (Equations 2.14 and 2.15) we obtain their velocity distribution integrating the Jeans second equation (see Equation 2.21 to see the example for the halo component). With this integration we obtain directly velocity dispersions. Velocities are then computed using the same methodology as the one used for the disk components.

$$\sigma_{r,h}^2 = \sigma_{\phi,h}^2 = \sigma_{z,h}^2 = \frac{1}{\rho_h}\int_r^{\inf}\rho_h\frac{GM(r)}{r^2}dr, \quad M(r) = M(r)_{disk} + M(r)_{bulge} \tag{2.21}$$

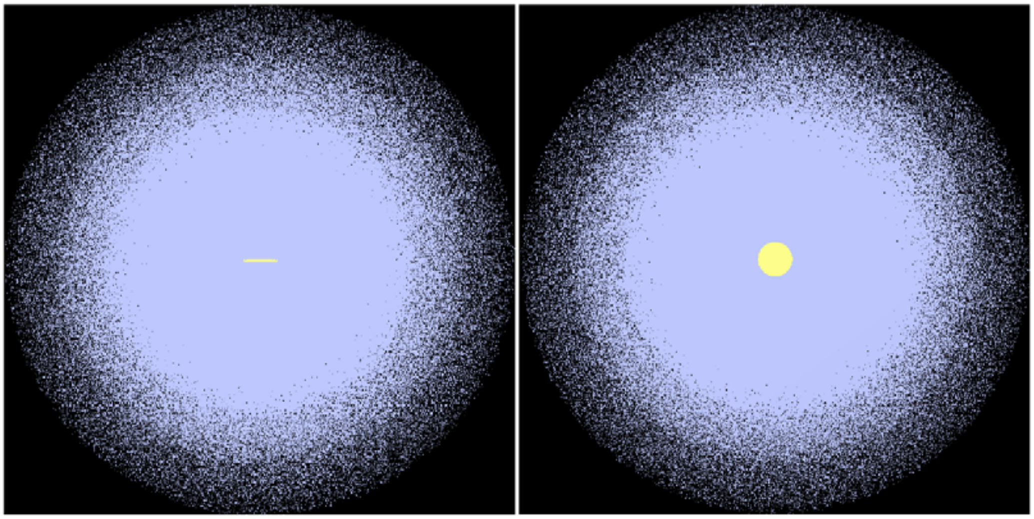

Figure 2.3: Initial conditions for stars (yellow) and dark matter (grey) in an isolated MW like simulation.

It is important to mention that in all processes of velocity generation we cut the velocity distributions at the scape velocity. RODIN have a function that cuts the higher halo velocities as it was well tested that it overestimates the number of particles with high velocities. It was also well tested that making this cut the system evolve, in the first simulation steps, to a stable and realistic state.

As the reader can notice, some of the assumptions we make in the initial condition generation are very strong. Due to these approaches the final distribution we obtain is only an approximate solution for the equilibrium velocity distribution. However it was well tested that the system initially adjust to compensate such approximations and that the final values of some parameters, as for example Q parameter, quickly evolves in the first time steps to end in a realistic distribution (see Figures 2.4 and 2.5).

From equations it is clear that a large number of free parameters are required to generate initial conditions for an isolated disk galaxy system. In this work we selected all of them to fall near a Milky Way like system (see Section 4.2.1 for a detailed description of the used parameters).

The last step of initial conditions generation is to check that the result obtained is the one expected. First, every time initial conditions are generated we need to be sure that Poisson noise is under the required spatial resolution. We check that computing the radial density curve and ensuring that the wavelength of these fluctuations is under the expected resolution. It is also important to check that the shells width (dr) used in the

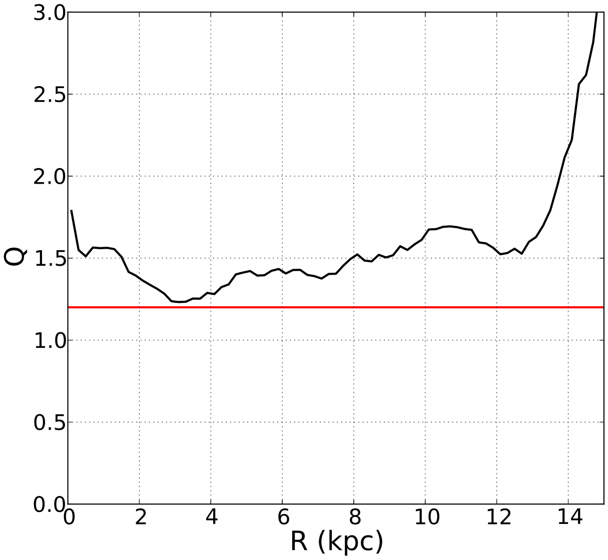

Figure 2.4: Toomre parameter as function of radius in the initial conditions (red) and after 1 Gyr of evolution (black).

density generation are under the resolution. Finally other important tests are to check that the generated velocity dispersion curves are correct and that the Toomre parameter is the one expected all over the disk.

Although after all the steps presented here the initial conditions can be generated easily, it is important to control that in the first time steps of the simulation the system became relaxed and no strange features appear.

Cosmological initial conditions

To generate the initial conditions of cosmological N-body simulations presented here we used the so called zoom-in technique. This technique is a powerful tool to simulate highly resolved structures within a cosmological context while keeping the computational costs reasonably low. In this technique we first generate initial conditions at high z for a big cosmological box with a resolution of 128^3 particles. These high z initial conditions are generated following the primordial density fluctuations in a specific universe (ΛCDM, WDM, ...) and with imposed cosmological parameters such as the present-day Hubble constant (H_0), the baryonic matter density ($\Omega_{b,0}$), the matter density ($\Omega_{m,0}$) and the vacuum density ($\Omega_{\Lambda,0}$). There are several methods to generate Gaussian random fields that follow a prescribed power spectrum and act as source terms for density and velocity perturbations in Lagrangian perturbation theory. Here we use the convolution kernel based approach

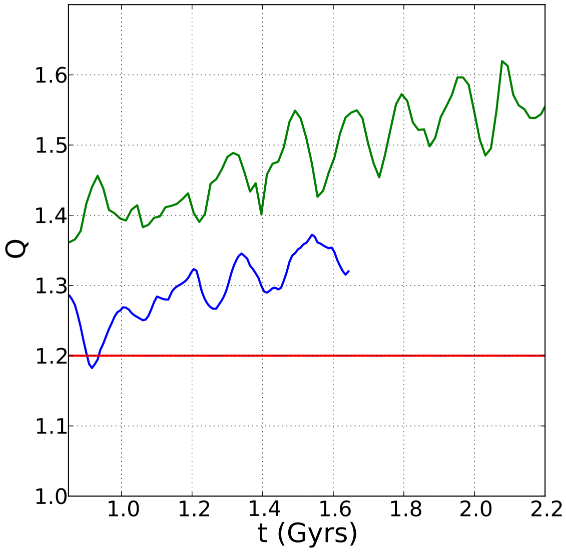

Figure 2.5: Evolution of mean Toomre parameter between 5 and 8 kpc in radius. We show the evolution of this parameter in two simulations with a different number of disk particles. In blue a model with $5{\cdot}10^6$ particles in the disk, in green with 10^6 and in red the initially imposed Q=1.2.

described in Hahn & Abel (2011).

Once generated we run the simulation with these initial conditions up to z=0. At this point (z=0) we select the region that is of our interest and we put the simulation back in time to the initial z. Now the first initial conditions are changed increasing locally the effective resolution up to 1024^3 or 2048^3, depending on the computer architecture, only in the selected region. In this region particles are split into some others with lower masses. To assign the mass a multi-mass method is used. With this method a number of new mass species is added, only limited by the computer structure. Each new specie has half of the mass of the previous one being the less massive the one that is in the selected region and the more massive the one far away and well inside the low resolution region. In terms of initial parameters it is something commonly done to fix a minimum resolution level for the low-resolution region and a maximum for the high-resolution one.

Is also at this point of the generation when the hydrodynamics can be initialized by adding a mesh that also have the finest grids in the selected region.

When the new initial conditions are ready the new low-resolution + high-resolution region (zoom-in) simulation can be started.

2.3 GADGET

In this work we used not only ART code but also GADGET code to ensure that our results are not code dependent.

Here we used GADGET3 code (private collaboration) that is a modification of the original code GADGET2 last described in Springel (2005). The modifications included in GADGET3 affect the hydrodynamical part of the code and its parallelization.

GADGET is a Lagrangian collisionless N-body code. In it, gravitational forces are computed with a hierarchical multipole expansion, commonly named a tree algorithm, which can optionally be applied in the form of a TreePM algorithm. In the tree scheme the particles are arranged in a hierarchy of groups i.e. when the force of a particular particle is computed, the force exerted by distant groups is approximated by their lowest multipole moments. In this way the computational cost for a complete force evaluation can be reduced to order O(NlogN) as instead of requiring N-1 partial forces per particle, as needed in a direct-summation approach, the gravitational force on a single particle can be computed with just O(logN) interactions. The forces become more accurate if the multipole expansion is carried out to higher order but eventually the increasing cost of evaluating higher moments makes it more efficient to terminate the multiple expansion and rather use a larger number of smaller tree nodes to achieve a desired force accuracy. The code uses the Barnes-Hut tree construction (Barnes & Hut 1986) that is a technique that uses a tree-structured hierarchical subdivision of space into cubic cells, each of which is recursively divided into eight subcells whenever more than one particle is found to occupy the same cell.

Forces are then obtained by walking the tree and summing up appropriate force contribution from tree cells, starting at the root cell. At each tree node a decision is made whether or not the multipole expansion is considered to provide an accurate enough partial force (which will in general be the case for cells that are small and distant enough). If it is considered the multipole force obtained for the tree node is used all along the branch of the tree, if it is not the daughter cells are considered in turn and so on to the smaller cells. The criteria to go deeper into the tree can be modified taking into account that if it is soft (we let the code go deeper inside the tree) the resulting force will be more accurate but the computation will be less efficient.

TreePM method is an hybrid method consisting of a synthesis of the PM method and the tree algorithm. The potential in this case is explicitly split in Fourier space into a long-range part and a short-range part. The long-range potential can be computed then very efficiently with mesh-based Fourier methods. The short-range part of the potential can be solved in real space easily. With this method the tree only needs to be walked in a small spatial region around each target particle, and no corrections for periodic boundary conditions are required. In addition, one typically gains accuracy in the long-range force, which is now basically exact, and not an approximation as in the tree method. The

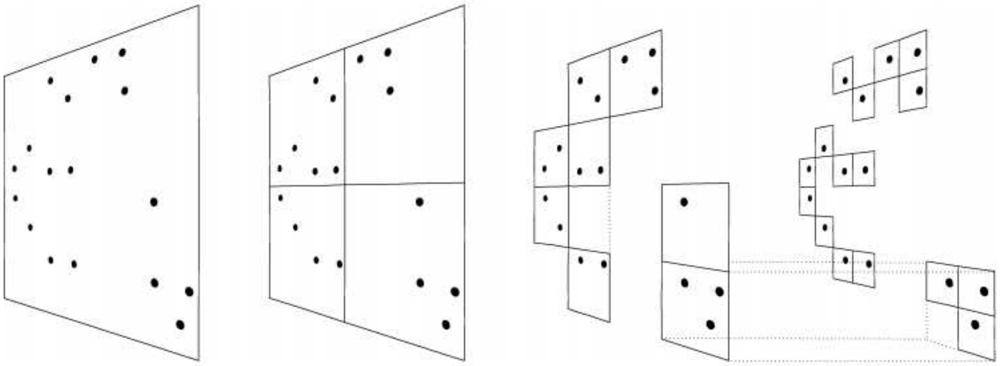

Figure 2.6: Barnes and Hut oct-tree in 2-D.

TreePM method maintains all of the most important advantages of the tree algorithm, namely its insensitivity to clustering, its essentially unlimited dynamic range and its precise control about the softening scale of the gravitational force.
Finally the integration in GADGET is done by using a KDK leapfrog integrator, where K referees to a Kick operator and D to a Drift operator (Quinn et al. 1997). For the time step one can select to use the same minimum time step for the whole simulated box or to use an adaptive time-step. The adaptive time-step scheme deals better with a simulation of the nature as the ones we deal in this work, simulations with regions with high density and regions basically empty.

2.3.1 Set up and initial conditions

To make the initial conditions for the GADGET simulations a different approach than the one for ART is used. Here analytical axisymmetric distribution functions (*df*) that describes separately each one of the galactic components (disk, halo and bulge) are superposed in a direct summation. To obtain the global *df* of the system the work hypothesis used here is that the final distribution function can be approximated as a sum of the individual ones. The resulting *df* can or can not fall near the real one, because of that, some additional tests are needed to ensure that the result will not suffer important numerical effects. First of all, after obtaining the final *df* is needed to ensure that it is solution of both, Boltzmann equation and a Poisson equations, i.e. it describes a self-consistent system. To ensure the self-consistency of the initial conditions we apply an iterative method. This method works as follows: first we test analytically that the resulting *df* is solution of Boltzmann equation, once tested that we distribute the particles according to it. Second, we change the density structure to make it consistent with Poisson equation. Finally, we recompute particle positions and velocities using the new potential and the original *df*

(integrating *df* for all velocities), and we repeat the process until positions and velocities converge, when that happens the system is solution of both equations.
Using this system we are able to reproduce a large variety of systems. This process is also well described in Widrow & Dubinski (2005); Jarvis & Freeman (1985).
It is important to mention that a problem that one can suffer when using this method can appear if the final distribution function is far away from the one resulting from the direct summation. In this case the required number of iterations to get the wright *df* can be very big or, in extreme cases, the iterations would not converge, in this last case it would be necessary to change the individual *df* or to use another method.

2.4 Convergence tests

In Kravtsov et al. (1997); Colín et al. (2003); Valenzuela & Klypin (2003) several tests have been done to ensure that ART code has a correct energy conservation and a good force computation. In these works they also tested the convergence of global parameters when using different initial conditions, computers and compilers, and the influence of the refinement density threshold in the results (in our simulations the limit density for the refinement is used as a free parameter). Also in Springel et al. (2001); Springel (2005) similar tests have been done for GADGET code.

Here we have done additional tests for our specific ART isolated disk galaxy models. We have tested the convergence of general parameters such as bar length and strength, velocity dispersions and disk density profiles under changes in the number of particles and resolutions. We also made simulations changing only the minimum time step to find effects of this change on the final results. With these tests we could determine the parameters we need to use to obtain results as less affected by numerical effects as possible.
An important result we have obtained from these tests is that the global properties of the bar are not strongly affected by changing the number of disk particles from $2{\cdot}10^5$ to $5{\cdot}10^6$. We also saw that to increase the number of particles has only important effects in global parameters after ∼2.5Gyrs of evolution. On the other hand we have found that the number of density structures that appear in the disk are much higher when the number of disk particles increases. This last effect can be explained as more disk internal modes can be populated if the system has more particles. Also the presence of these new density structures may be the cause of the small changes observed in the growth rate or pattern speed evolution of the bar after several Gyrs of evolution as they self-interact gravitationally. Other possible consequence of these increase on the number of density fluctuations is a faster increase of the Toomre parameter. This is due to that all density structures become heating agents as when they pass through the disk give energy to stars making their velocity dispersions higher. This increase of velocity dispersions makes the system more stable what also means a system with higher values of Q (see Figure 2.3).

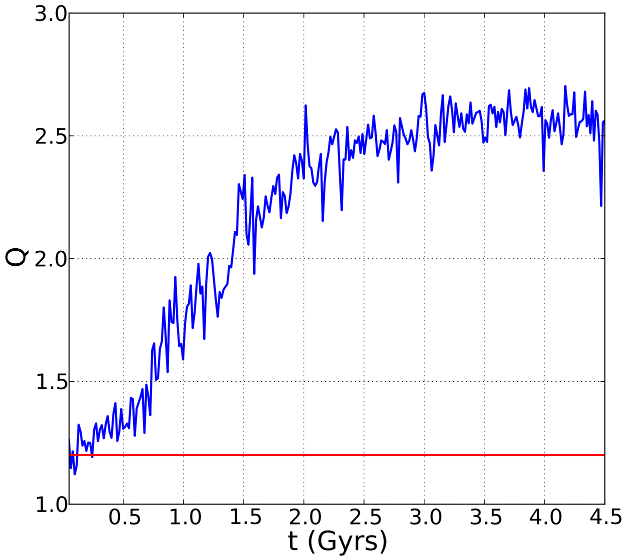

Figure 2.7: Blue: Evolution of Toomre parameter (Q) in a simulated galactic disk with a presence of bar and spiral arms. Red: Initial Q value.

The same effects we observe when increasing the number of particles are observed when increasing spatial resolution. To increase spatial resolution makes the system resolve smaller density fluctuations what lets them to grow and interact with others. However in the case of changing resolutions it is important to take into account that there is a limit in the maximum resolution that is the level of Poisson fluctuations due to the finite number of disk particles. To have higher resolutions will make the system resolve these Poisson fluctuations and then they will grow.
Other important result we found when changing the minimum time-step is that both using a time step too big or too small has similar effects: the system does not conserve the angular momentum. This process makes particles to fall into the central region of the simulated galactic system generating a high concentration of particles that can destroy the bar if there are one (Athanassoula et al. 2005), as can be seen in Figure 2.4.

2.5 Limitations

To use N-body simulations let us study the formation and evolution of systems as complexes as galaxies. However these models suffer from some important limitations that the user need to keep in mind when using them.

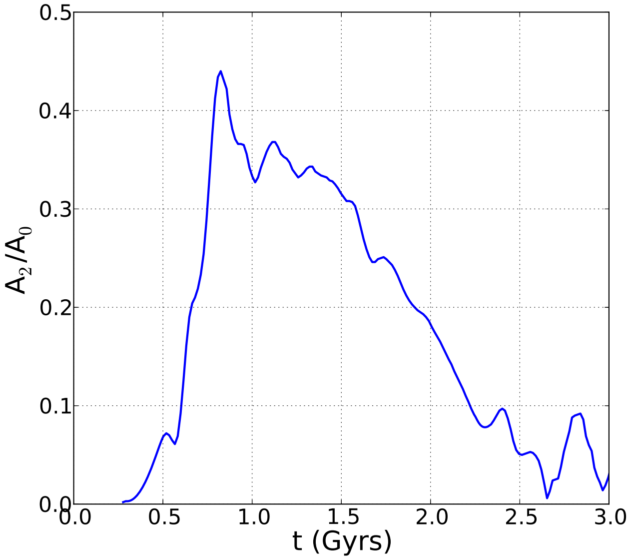

Figure 2.8: Evolution of bar amplitude in a simulation with $5{\cdot}10^6$ disk particles with a too small time step.

2.5.1 Resolutions

A critical point in N-body simulations is to be aware about the limitations the simulation has due to spatial, temporal and mass resolutions. Each simulation has an specific physical range where the user can work and be sure that results he will obtain will not be affected by numerical effects, this physical range is determined by resolutions. The analysis of simulations out of its physical limits can drive to wrong results and conclusions what had happened several times in the past (e.g. angular momentum catastrophe in Navarro & Steinmetz 2000).

2.5.2 CPU time

The most important limitation in N-body simulations is imposed by the high computational resources needed for each one of them. As discussed in previous sections the CPU time required for a simulation can grow as $O(N^2)$, where N is the number of particles, in the worst case, or in some cases as O(logN) depending on the code. Also to get better spatial or temporal resolutions implies to use much higher number of CPU hours. The required CPU time puts a limit in mass, spatial and temporal resolutions of our simulations.

Parallelization

To use parallelized codes is mandatory when simulating huge systems as the ones presented here. Be able of using as many CPU as possible for each simulation is a key point to reach high resolutions and then competitive models. Both codes used here work in parallel but GADGET is the one with a better parallelization; an improved ART version is being developed. ART code uses a parallelization scheme that just divides the simulated space in cells of equal volume and then it sends each one of these cells to a different CPU to be computed. This simple scheme works well when the operations needed in the simulation are distributed homogeneously on the entire volume, however when exists a region with larger computational charge it becomes inefficient very fast. This last point is a problem we deal with in isolated galaxy simulations as there we have a central region with high density, and then high number of operations, while in the borders there are only few particles what means a small number of operations. In this case we will have some CPUs that will need lot more time to finish their computations than the others. In this situation the last CPUs will be waiting since the others finish their computations making the process very inefficient. Otherwise, in the case of cosmological simulations this scheme works well and the performance o the code is much better as inside the cosmological box there is a roughly homogeneous density distribution. However in the zoom-in technique we use in our simulations the efficiency decreases again as we add a high-resolution region where the number of operations is much higher than in the low-resolution places. We have made some tests to find which is the more efficient number of processors we can use with ART code (see Figure 2.5) and we have obtained that the optimal number of CPUs to be used in isolated disk galaxy models is 8 while it is 16 in the cosmological + zoom-in technique ones.

To solve these problems of inefficiency there are other parallelization schemes that can be used, e.g. adaptive schemes or non geometrical divisions. An example of non-geometrical divisions is to take into account the number of operations per region and then distribute the operational charge to the CPUs equitatively.

2.5.3 Memory and analysis

Other problem we need to face when using N-body simulations is that we need of lot of space to save data. As an example simulations of isolated galaxies with $5{\cdot}10^6$ disk particles generate files of 5 Gbytes for each snapshot while biggest cosmological simulations generate files up to 12 Gbytes each.

Also to have such huge files adds another complication that is we require much more to process time and analyze data. This puts limits on the computers that can be used for such a work in terms of RAM memory, too.

2.5.4 Effect of gas and environment

Pure N-body simulations are useful for a large variety of problems. First simulations we studied in this work are collisionless N-body simulations of isolated galaxies. In his simulations we are avoiding at least two important processes, the effect of the collisional

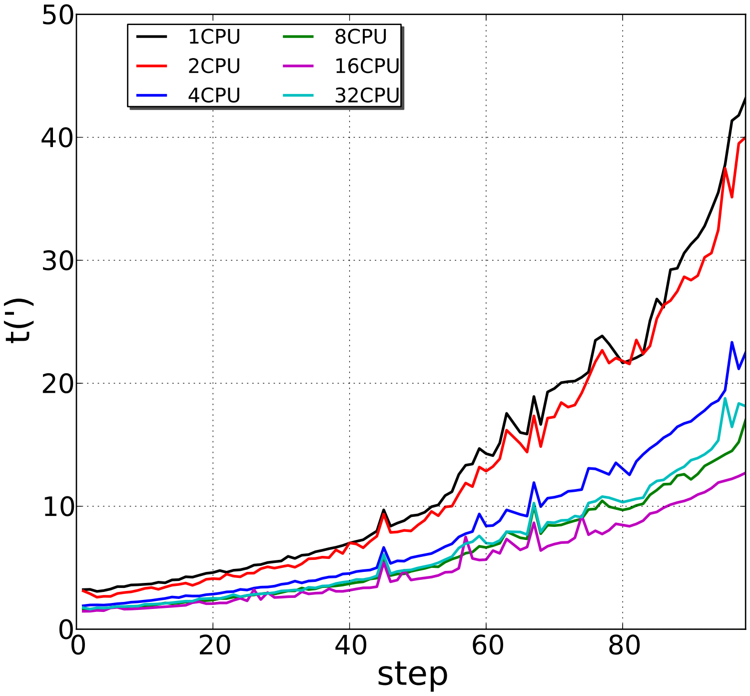

Figure 2.9: Total time required to complete a time step calculations as function of the time step in a cosmological + zoom-in simulation. We show results when using 1, 2, 4, 8, 16 and 32 CPUs.

component and the effect of the environment (i.e. interaction with other galaxies, gas flows, ...). For our purpose of studying general parameters of a well isolated galaxy we argue that these processes are not necessary in a critical way. However, other parameters as for example the spiral arms and bar live times are highly affected by them. It was well studied that cold gas flows let the disk to maintain bar and spiral structures for a long period of time as from it new stars with lower velocity dispersion form what keeps Q parameter low (Sellwood & Carlberg 1984) and then the disk unstable. In Figure 2.3 it can be observed the effect of disk heating (increase of Q parameter) in a simulation with spiral arms and bar. As it is also clear from the figure, at some point the heating agents (spirals and bars) disappear. The last is a consequence of that the disk has become too stable due to the lack of cold gas inflows and then the formation of young stars with lower velocity dispersions.

To ensure that results obtained from collison-less N-body simulations of isolated galaxies do not depend on the presence of collisional component (gas) and the environment, we have made a second set of simulations (see Chapter 3). These simulations are the simulations of galaxy formation and evolution in a cosmological context presented in this chapter but where we have also added the hydrodynamical component. In the next chapter (Chapter 3) we present all physical processes included in these N-body + hydrodynamics simulations.

2.6 Advantages

The main advantage of using collisionless N-body simulations is that the resolution that can be reached is much larger with much less CPU time. Is due to this situation that the first kinematical analysis of stars in simulated disk galaxies have been done using this kind of simulations.

Other important strength of the method is that it can be studied the formation and evolution of large scale structures both in the universe or in individual galaxies, from a much larger sample of simulations, again because of these simulations require much less CPU time. On that cases as gravity is the main force that drives the formation of these structures and then the effects of collisional component can be neglected, although being very careful on selecting processes where these effects can be truly avoided.

3

Cosmological N-body + Hydrodynamics simulations

3.1 Introduction

The collisionless approach presented in the previous chapter has been very useful to study the formation and evolution of large and small structures in the universe. For instance, dark matter only cosmological simulations (such as the Millennium runs Springel 2005; Boylan-Kolchin et al. 2009) have been able to reproduce the observed clustering properties of matter in the Universe, and have been of decisive help in establishing the current ΛCDM cosmological paradigm. Collisionless simulations have also become an important tool for studying how galaxies and their large scale structures form and evolve, what is an important goal of this thesis.

Although collisionless simulations have shown to be very useful, it is needed to add the collisional component to study processes that are highly affected by the presence of the hydrodynamical components, both at large and small scales. These simulations let us to study new large scale properties such as stellar age distribution in galaxies with different morphologies, their chemodynamical evolution and the interstellar gas distribution and its interaction with galactic systems, an ingredient that has an important impact on galaxy formation evolution processes. At galactic and sub-galactic scales, the study is much more complex as a big amount of physical processes need to be taken into account. It is at these scales where the general picture of galaxy formation is still fraught with uncertainty.

Much of the current simulation work in the field is attempting to clarify the role of these complex physical processes operating on galactic and sub-galactic scales, and their interplay within the cosmological context. Although several of these processes acting at sub-galactic scales are still under study and not well implemented, nowadays simulations of N-body plus hydrodynamics or plus SPH (Smooth Particle Hydrodynamics) are successfully reproducing the large scale structure of the universe and they are starting to succeed into simulate the formation of Milky Way like galaxies (e.g. Guedes et al. 2011; Bird et al. 2013; Mollitor et al. 2014).

In all these simulations the starting point, both for collisional and for collisionless components, is an imposed spectra of initial density fluctuations derived from the observed microwave background radiation (Spergel et al. 2007). The simulation runs under an initially adopted cosmology that is defined by the Hubble constant, the cold dark matter spectrum and the components of the total density of the universe. When it starts, the initial density overdensities collapse due to self-gravity and form cosmological walls, filaments, voids, and at smaller scales, dark matter halos. Later on, when the universe cools down, baryons start to follow the implemented physical processes falling down into dark matter halos. This infall of baryons occurs at different rates depending on the mass of the DM halo. Also, depending on the environment (i.e. interactions with other systems), these baryons may fall in a disk shaped distribution due to the angular momentum conservation, or end in a spheroidal distribution if the system suffers strong interactions (Baugh et al. 1996). Following the imposed prescriptions stars begin to form. When star formation begins also feedback processes and chemical evolution starts following the implemented physics for SNeIa, SNeII and stellar winds. As a consequence, galactic chemical evolution starts. It is in these processes that lies one of the most important keys to obtain realistic galaxy systems.

As we have mentioned above some authors have successfully started to reproduce Milky Way like systems but only in terms of large scale properties such as rotation curves, total masses or disk to bulge mass ratios, while for others like the number of satellite galaxies or the gas distribution they are not. When analysing properties of these models like star formation rates and chemical and stellar age distributions, strongly affected by internal physical processes, the agreement with MW observations is not so clear. To better fit the observations and to follow the theoretical predictions, a deeper knowledge about these internal physical processes and its correct implementation is required. In addition, it has to be taken into account that some of these processes occurs in a smaller scales than the resolution what makes necessary to use approximated processes that mimic the effects at larger scales. This is the case for the star formation, the cooling processes and several kinds of feedback mechanisms. Obtaining such models is one of the most challenging goals that we plan to address in the present work.

In the present work we have used the adaptive mesh refinement N-body+hydrodynamics code presented in Kravtsov et al. (1997) and Kravtsov (1999). The code is based on the collisionless ART N-body code (Chapter 2) adding the hydrodynamics, that are computed using an Eulerian method, and all physical processes we have mentioned above. To use an hydrodynamical mesh code instead of SPH particles to simulate the collisional component has advantages but also presents some drawbacks. An advantage of using mesh codes is that they does not need to add an artificial viscosity term to avoid strong interactions as it is in SPH. The introduction of this artificial viscosity term makes classical SPH codes unable to properly reproduce shocks and contact discontinuities (Tasker et al. 2008), as so instabilities like the Kelvin-Helmholtz one (Agertz et al. 2007). More recently new SPH implementations successfully reproduced these processes but with a high CPU time consumption (Kawata et al. 2013). Also the multi-phase gas can not be correctly simulated due to the use of the kernel that softens the gravitational force around SPH particles. On the other hand a clear strength of using SPH is its Lagrangian nature that ensures better energy and angular momentum conservations when a single time step is used what can not be easily done in mesh codes. Also SPH describes in a simpler way the high density regions. Hydrodynamical codes, both SPH and mesh-based, are continuously under development as new physical mechanisms are discovered and better understood. The code used here have been updated several times since its creation and all new implementations have also been properly tested. Some examples of these updates and tests, like new star formation recipes, stellar feedback and cooling processes, can be seen in Kravtsov (1999, 2003); Kravtsov et al. (2005); Colín et al. (2010); Avila-Reese et al. (2011). Tests of the collisionless part of the code have been well described in Section 2.4. This thesis has not been devoted to improve the code but to deeply analyse and test how changes into the parameters describing the implemented physical processes conduct to models that are able to reproduce Milky Way like systems. Our final goal is to obtain a model that fits with several of the observed parameters for our MW galaxy.

3.2 The collisionless component

As mentioned, the code we have used to simulate the collisionless component both on the galactic formation and evolution and on the formation and evolution of its large scale structures is based on the ART code (fully described in Chapter 2). Thus dark matter and stellar particles in this code follow the ART collisionless computations.

3.3 Hydrodynamics in the code

The code we have used here to compute the evolution of the collisional component is an AMR (Adaptive Mesh Refinement) code that uses an Eulerian method to solve the gas hydrodynamical equations. In practise an adaptive mesh is superposed into the collisionless system initial conditions following the primordial density fluctuations. In the collisionless mesh only gravity acts while in the hydrodynamical mesh also hydrodynamics are considered.

3.3.1 Physical processes

In this section we detail the physical processes included in the code. First we detail the implemented cooling and heating mechanisms that drive to a multiphase gas environment. These mechanisms also regulates global properties such as the star formation rate or the baryonic fraction in the DM halos. Secondly we describe the star formation approach that is supported by observations and need to mimic the effects of physics that acts at smaller scales than the resolution we are able to reach. These are the so called subgrid physics. Finally we describe how the stellar evolution, the SNe feedback and the advection of metals are included.

Cooling and heating

The cooling and heating rates in this code incorporate a large variety of processes: compton heating/cooling, atomic, molecular hydrogen and metal-line cooling and UV heating from the cosmological background radiation modeled by Haardt & Madau (1996). All these processes are tabulated for a temperature range of 10^2 K $<$ T $<$ 10^9 K, a grid of densities from n=0 to n=50 cm^{-3}, a range of metallicities from $Z/Z/\odot$=-3.0 to $Z/Z/odot$=1.0 and also a range of redshifts from $z=z_{ini}$ to z=0, using the CLOUDY code (Ferland et al. 1998, , version 96b4).
Cooling processes are very important as they are the ones that drive the formation of cold compact dense clouds where among other processes the star formation takes place. On the other hand it has been demonstrated that UV heating is important to avoid early star formation by delaying the primordial gas infall into dark matter halos (Machacek et al. 2001).

Subgrid physics: Star Formation (SF)

Star formation is an important physical process that needs to be well understood and implemented to obtain realistic systems. In order to find a suitable model of star formation it is needed to turn towards observations. Many observational studies show that star formation rate (SFR) across entire galaxies, both local and at high-z, depend actually on the total mass of very dense gas (n>10^4 cm^{-3}, where n is the gas number density) within molecular cloud complexes, being this gas typically confined to sub-parsec narrow filamentary structures and compact cores (Lada et al. 2012, 2010). As these authors remark, the key point to understand what ultimately controls the SF is to know how the local processes that produce the dense and cold gas component of the interstellar medium

(ISM) work. From observations, Krumholz & Tan (2007) showed that at scales of 1-100 pc galactic molecular clouds form stars at a rate that is proportional to the gas density (ρ_g) divided by the free-fall time (t_{ff}) where $t_{ff}=\sqrt{3\pi/32G\rho_g}$. The proportionality term is known as the star formation efficiency per free-fall time (ϵ_{ff}). The authors also mention that for reasons that are yet not fully understood, this SF process is very slow, with only about 1-3 per cent of the gas consumed in one free-fall time, i.e. $\epsilon_{ff} \sim$ 1-3. For the most active star-forming complexes in the Milky Way - which are responsible for one third of the total star formation - Murray (2011) find that ϵ_{ff} may be as high as 8 per cent.

Commonly SF is modeled as taking place in the coldest and densest collapsed regions, defined by $T < T_{SF}$ and $n_g > n_{SF}$, where T and n_g are the temperature and number density of the gas, respectively, and T_{SF} and n_{SF} are the temperature and density SF threshold. Our simulations resolve regions an order of magnitude larger than the size of typical molecular clouds that is tens of parsecs. Unfortunately under these circumstances a realistic density threshold of $n>10^4$ cm^{-3} or more cannot be used because structures with this density are not resolved. Values we use, in combination with values of other subgrid parameters, are suitable for used resolutions and result in reasonable ISM properties at scales larger than the resolution as well as realistic structural and dynamical properties of the whole galaxies (see Colín et al. 2010; Avila-Reese et al. 2011). These values are close to the value estimated for he giant molecular clouds in the Milky Way by Krumholz & Tan (2007).

When the conditions in temperature and density are simultaneously satisfied stars are formed at a rate of

$$\frac{d\rho_*}{dt} = \epsilon_{ff}\frac{\rho_g}{t_{ff}} \tag{3.1}$$

When created, the resulting stellar particles of mass $m_\star$ are placed in the corresponding grid cell and the total mass of stellar particles is removed from the gas mass in the cell. Particles subsequently follow collisionless N-body dynamics. No other criteria is imposed. The stellar particle mass, $m_\star$, is calculated by assuming that a given fraction (SF local efficiency factor ϵ_{SF}) of the cell gas mass, m_g, is converted into stars; that is, $m_\star = \epsilon_{SF} m_g$, where ϵ_{SF} is treated as a free parameter. The value for ϵ_{SF} needs to be high enough for the thermal feedback to be efficient in regions of dense, cold, star-forming gas and not as large as to imply that most of the cell gas is exhausted.

High resolution simulations require a way to limit the number of produced star particles to relieve the computational burden of N-body calculations. This is typically done both by creating star particles stochastically with low probabilities and by limiting the minimum mass that a star particle may have. In most high resolution simulations star particles are created by stochastically sampling the Equation 3.1, defining a probability of star formation (P_{SF}) and a minimum mass for the star formation (M_{min}) (e.g. Stinson et al. 2010; Guedes et al. 2011; Christensen et al. 2012; Governato et al. 2012; Brook et al. 2012; Calura et al. 2012; Munshi 2013; Ceverino et al. 2014). By construction, as SFR is maintained, this approach produces individual star formation events with large ratios of stellar mass to gas mass to compensate for the events where no stars are allowed to form. Only in the limit of high probability for each star formation event (i.e. P_{SF} ∼1), does this ratio approach the observed value, with ϵ_{ff} = 1-8 per cent. Resulting high M_{star}/M_{gas}, that can be understood as an artificially enhanced star formation efficiency, sometimes requires to adjust ϵ_{SF} by a factor of two in order to obtain stellar masses that fall on the Moster et al. (2013) stellar-mass-halo-mass relation (Brook et al. 2012). Moreover, unrealistically high ratios have also the effect of increasing the strength of the stellar feedback and enhancing gas blowouts from star-forming regions. This increase of stellar feedback is also traduced in an increase of the total energy released by SNe events. As a consequence, the energy release will be highly inhomogeneous and concentrated in a few high efficiency regions. To avoid these issues a solution is to remove the lower mass limit for star particles and to control the mass solely by the observed efficiency of star formation for each star formation event, ϵ_{ff}. Unfortunately, using low deterministic star formation efficiencies at the typical densities and resolutions of current simulations is prohibitively expensive since the long gas consumption times yield particles with very small masses.

Also to avoid the problem of high M_{star}/M_{gas} ratios, Christensen et al. (2012) adopted a model of star formation where 33% of the local gas mass is converted into stars at all SF events (P_{SF}=1). More recently, Brook et al. (2012) used a similar recipe, converting about 20 per cent of gas mass into star in each event. Although leading to realistic results, these ϵ_{SF} numbers are a factor of ∼ 2-3 larger than the average observed efficiency of star clusters in the Milky Way that is ϵ_{SF} ∼8 per cent (Murray 2011).
In our models we have used a similar approach with P_{SF}=1, i.e. no a stochastic but a deterministic method, and with a high star formation efficiency. The typical initial star particle masses in our runs is, in a 99 percent cases, between $1.18{\cdot}10^3$ and $1.2{\cdot}10^6$ $M_\odot$ when we have imposed a minimum mass limit of $10^3 M_\odot$. The density-based deterministic SF and thermal-driven feedback implementations we use here are discussed in detail in Colín et al. (2010) and Avila-Reese et al. (2011). As demonstrated by the authors this approach in general agree with the common schemes applied to this kind of simulations in order to obtain present-day “realistic” galaxies (see for a recent review and comparison among several schemes and codes Scannapieco et al. 2012).

Subgrid physics: Stellar evolution, SNe feedback and advection of metals

Since stellar particles are much more massive than the mass of a single star, typically 10^4–10^5 M⊙, once formed, each stellar particle is considered as a single stellar population, within which the individual stellar masses are distributed according to the Miller & Scalo (1979) IMF (the code has as an option to use Chabrier IMF, too). Stellar particles eject metals and thermal energy through stellar winds and Type II and Ia SNe explosions following the IMF prescriptions. Each star that is more massive than 8M⊙ is assumed to dump into the ISM, instantaneously, $2{\cdot}10^{51}$ erg of thermal energy: 10^{51} erg coming from the stellar wind, and the other 10^{51} erg from the SN explosion. Moreover, the star is assumed to eject to the ISM $1.3M\odot$ of metals in the SNe explosion. In this code only two species of metals are released in such explosions, i.e. iron and alpha elements, the proportion of each one solely depends on the SNe type. As an example, for the assumed Miller & Scalo (1979) IMF, a stellar particle of 10^5 $M\odot$ will produce 749 Type II SNe. For a more detailed discussion of the processes implemented in the code, see Kravtsov (2003); Kravtsov et al. (2005); Colín et al. (2010); Avila-Reese et al. (2011).

3.3.2 Overcooling problem

An important drawback related to the lack of understanding and the approximated and simplified recipes applied for the subgrid physics is the so called overcooling problem. As a summary, the overcooling problem is the process by which the energy released in SNe explosions is too efficiently lost by radiation processes. As we describe below, these too efficient radiation losses are caused by unrealistically high gas concentrations around SF regions. The consequence of this process is that most of the SNe energy can not be converted into kinetic energy, what would retain the energy into the galactic system. This has important consequences in the galaxy formation and evolution as it drives to a continuous loss of systems' energy and angular momentum, making a large number of particles to end in the central regions of the system. Systems with an unsolved overcooling problem are characterized by rotation curves that are unrealistically peaked in the inner regions (see Figure 3.1).

Describing it in more detail, this overcooling problem begins with stellar particles dumping energy in the form of heat due to SNe explosions into the cells in which they born. At this moment, due to the lack of subgrid star formation physics, if resolution is not high enough and/or n_{SF} is too high, most of this thermal energy injected to the cell is radiated away too fast, i.e. gas is overcooled. As we have mentioned above, this process is a consequence of the presence of a too high amount of gas around the region where the energy is released. As larger is the amount of gas in the SF region, smaller the SNe energy released per gas unit mass, and thus, the gas reaches lower temperatures. In this situation of lower gas temperatures, cooling processes are more efficient and the energy is radiated faster. From a physical point of view what happens is that in this situation cooling time t_c is similar or smaller than the crossing time t_s (Stinson et al. 2006; Dalla Vecchia & Schaye 2012). As pointed before, under this circumstances most of the dumped energy is radiated away and not converted in kinematic energy, a process that would disperse the cloud.

It is a common practice to avoid the overcooling by artificially delaying the cooling in the star-forming regions (e.g. Stinson et al. 2006; Colín et al. 2010; Agertz et al. 2011; Hummels & Bryan 2012). To do that the cooling is turned off some time (t_{off}) in the cells where stellar particles form. This turning off mechanism along with a relatively high value of ϵ_{SF} and a relatively small value for n_{SF} makes both, the gas concentration in the

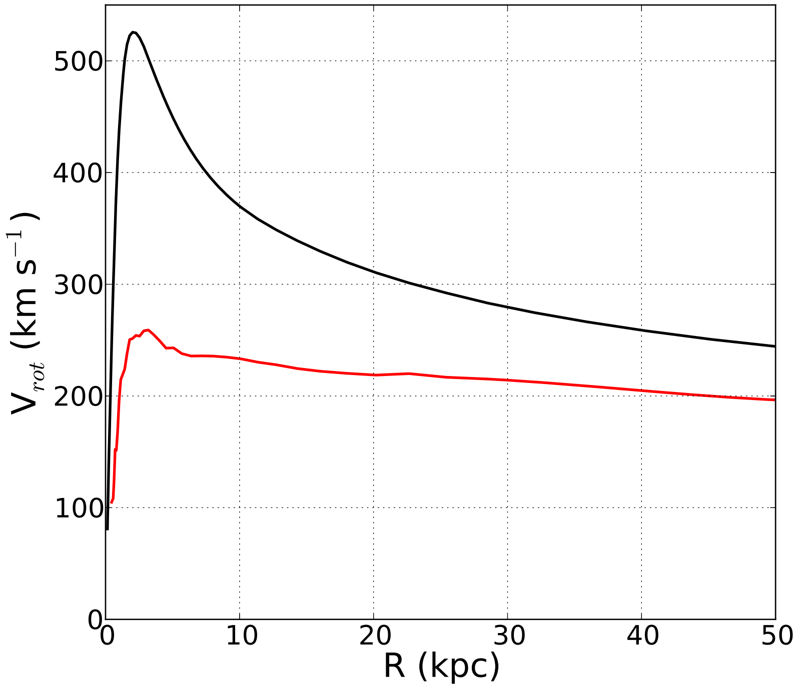

Figure 3.1: Total rotation curves of simulation HART321 (see Chapter 6), in red, and the same simulation but only changing ϵ_{SF} parameter, in black. HART321 simulation has a high star formation efficiency (i.e. 65%) while it is lower in the other simulation (i.e. 60%).

region to became lower and after supernovae explosions to expand it and move away from the star-forming region. This t_{off} parameter is directly linked to the crossing time in the cell at the finest grid, thus it depends on the resolution: as high the resolution is, smaller its value. However, the selection of this parameters' value is not critical as tests show that the large scale structure of simulated galaxies is not sensitive when changing it in a factor of two (Colín et al. 2010).

Recently several works have confirmed that in simulations with high enough resolutions the overcooling problem disappears and it is no longer needed to turn off the cooling (Dalla Vecchia & Schaye 2012). Some other authors suggested that even when the resolution is not sufficiently high, the artificial cooling turn off become unnecessary if new subgrid physics like radiation pressure are implemented (Hopkins et al. 2012).

In the simulations we present here we are still turning off the cooling to avoid the overcooling problem. The t_{off} value we have used is fixed at 40 Myrs. However, we are running new simulations where radiation pressure is implemented and then this process is not longer needed.

3.3.3 Oncoming update of the code: The radiation pressure and the photoionization from UV potons

As we have mentioned, several new processes are being implemented in a new version of the code (Colin et al. in preparation). In this section we give a general description of one of them, the radiation pressure (RP).

One of the first works that used a RP scheme was Murray et al. (2010). In this work they analyzed the theoretical effects of several forms of stellar feedback on parent molecular clouds. On their models they included momentum input form ionized gas in HII regions, shocked stellar winds, hot gas pressure, protostellar jets and cosmic rays. They concluded that radiation pressure (RP) on dust grains is likely to be the dominant form of feedback in star-forming galaxies. Later on a variety of other studies have reached the same conclusion, placing the combination of RP and photoionization of gas by massive stars as the dominant mechanism for disruption of molecular clouds and internal regulation of the star formation process (e.g. Krumholz & Matzner 2009; Murray et al. 2010; Andrews & Thompson 2011; Lopez et al. 2011; Pellegrini et al. 2011; Hopkins et al. 2011). In addition, recent numerical work by Krumholz & Thompson (2012) shows that RP fully accounts for the large gas velocity dispersions measured in young star clusters in the MW. Also observations support the fact that RP is an essential ingredient of the galaxy formation and evolution processes. In fact, observations show that molecular clouds begin to disperse shortly after the O stars form and before the first supernovae explode and deposit their energy into the gas (Kawamura et al. 2009). Also from observations it has been concluded the total energy output of a stellar cluster is dominated by radiation. The rate of radiative energy output by O and B stars is ~ 200 times larger than the average power injected by supernovae and stellar winds during the lifetime of the most massive stars. Finally, another observational work suggest that it is difficult to explain the large gas turbulence values observed in star-forming regions without including the momentum input by radiation (Murray et al. 2010).

In a recent paper Ceverino et al. (2014) include the effect of RP and photoionization from UV photons in cosmological simulations of high-redshift MW progenitor, using an AMR code. Their simulations with RP show a reduction of the star formation rate by a factor of $\sim$ 2-3 at z=3 compared to a simulation with supernovae feedback alone, with RP playing the dominant role and gas photo-heating having only a secondary effect. With this processes the authors have started to solve another important problem of numerical simulations of galaxy formation and evolution that was the high star formation rate at high redshifts what generate galaxies with too many old stars and with no enough fuel to support the observed SFR at z=0.

These works point toward a new paradigm of galaxy formation, where radiation from massive stars is responsible for regulating star formation and powering galactic winds, while the properties of the inter-stellar medium (ISM) are controlled by the energy from supernovae. We are running new simulations that include such mechanisms and in where approximations like the usage of a t_{off} are not longer needed to obtain realistic galactic systems.

3.4 Simulation method

As pointed in the previous chapter to obtain simulations with high spatial and temporal resolution (i.e. tens of parsecs and thousands of years) it is necessary to use techniques that reduce the CPU time required. With this purpose we use the "zoom-in" technique (see Figure 3.2). This method begins with a first cosmological low-resolution run that has a single mass population of dark matter particles (DM). Once finished the low resolution simulation (z=0) the user selects the region in which is interested. In our work we select a region where there are an isolated DM halo with a mass and a maximum of the velocity density curve of the DM component that are similar or a little smaller than the ones of the MW. Finally the region of interest is picked up and re-simulated with high resolution, lower dark matter particle masses and with the hydrodynamical treatment included. In the rest of the simulated box the low-resolution state is maintained.
This method enable us to reach high resolutions in simulations in where the cosmological environment effects are also included. Under these circumstances and if using a high enough number of particles we are allowed to better study small systems like satellite galaxies and also kinematics and dynamics of density structures formed inside Milky Way like systems.

3.4.1 Low resolution simulation

Initial parameters

In our work the low resolution simulations are run with 128^3 particles inside a box of $10h^{-1}$ Mpc, per side, i.e the box is initially covered by a mesh of 128^3 cells (zeroth level cells). Most simulations presented here have run in a ΛCDM cosmology with $\Omega_0 = 0.3$, $\Omega_\Lambda = 0.7$, $\Omega_b = 0.045$, and h = 0.7, following (Colín et al. 2010). The CDM power spectrum is taken from Klypin & Holtzman (1997) and it is normalized to $\sigma_8 = 0.8$, where σ_8 is the rms amplitude of mass fluctuations in 8 h^{-1} Mpc spheres. The initial redshift is set to z=60 and the final at z=0.

3.4.2 Selection of an appropriate dark matter halo

Once finished the low resolution simulation, at z = 0, we look for halos with the proper properties to undertake our analysis. In this work we have selected halos with masses between ($2{\cdot}10^{11} < M_h/M_\odot < 1.4{\cdot}10^{12}$), inside or slightly under the mass ranges obtained for our MW. The lower mass range is inferred by stellar kinematics (see e.g. Kafle et al. 2012; Bovy et al. 2012; Deason et al. 2012), and the higher mass one by kinematics of

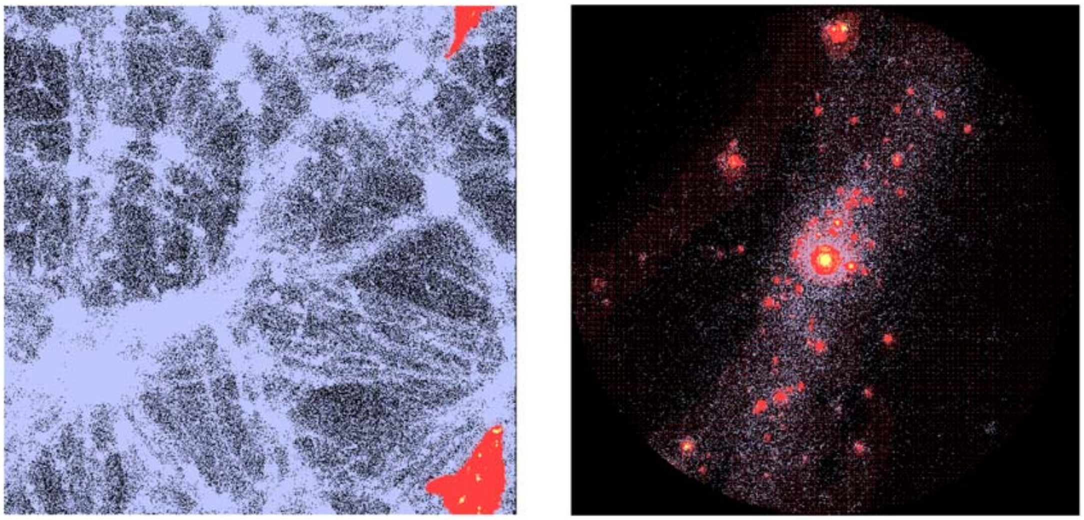

Figure 3.2: Left: Snapshot the simulated cosmological box of model HART321. The high resolution region is highlighted in red by the hydrodynamical mesh. Right: Zoom to the high resolution (109 pc per cell) region. In soft blue we show DM particles, in yellow stellar particles and in red the hydrodynamical mesh (gas).

satellite galaxies or statistics of large cosmological DM simulations (see e.g. Busha et al. 2011; Boylan-Kolchin et al. 2013). A deep discussion about MW virial mass range can be found in Piffl et al. (2014) and in Kafle et al. (2012). The selection of halos with slightly smaller masses than the ones we want for our final systems is motivated by the fact that mass can increase when adding the baryonic component. Other restriction when selecting our DM halo candidates was to chose only halos without major mergers since z=1.5 and up to z=0, defining major mergers as the fusion with halos more massive than $M_{vir}/10^3$. We have also checked that all halos merged before z=1.5 are well mixed within the system at z=0. However, the major mergers condition does not ensure that in the resimulation process a major merger between z=0 and z=1.5 will not occur. A new major merger at low redshifts can appear due to changes in positions and velocities of satellites produced by the introduction of baryons and the increase of resolution. To avoid this problem the systems we have chosen have no satellites more massive than 0.1 times the mass of the main system inside 5-10 times R_{vir}. This condition ensures that none of them will fall inside the main system causing an unplanned major merger in the resimulation process. Finally we have only selected halos that do not belong to a void or a knot (galaxy cluster) but belong to a wall or a filament, and also that they evolved far away from the borders of the simulated cosmological box. Due to our selection process in most of the cases our main system has a neighbour halo of similar mass at around 1 Mpc.

3.4.3 High resolution re-simulation

After selecting the region of interest the high resolution simulation can be started. In our work, to generate high resolution initial conditions, we identify a Lagrangian region of 2 or 3R_{vir} centered at the selected halo from the initial snapshot at z=60, and we have resampled it with additional small-scale modes and with the baryonic component (Klypin et al. 2001). All the initial conditions generation process is well detailed in Section 2.2.5. It is important to mention that the virial radius, R_{vir}, used here is defined as the radius that encloses a mean density ($\bar{\rho_h}$) equal to Δ_{vir} times the mean density of the universe ($\bar{\rho_u}$), where Δ_{vir} is a quantity that depends on Ω_0, Ω_Λ, and z. For example, for our cosmology $\Delta_{vir}(z = 0) = 338$ and $\Delta_{vir}(z = 1) = 203$. This definition is borrowed from structure growth theory, and its use is not appropriated when one wants to define a physically meaningful halo edge (Cuesta et al. 2008; Zemp 2013). To avoid ambiguity and to simplify comparisons are usually used two new definitions in where Δ_{vir} value is imposed. In the first one a Δ_{vir}=200 is imposed, a value that is commonly used in the literature. In the second case Δ_{vir} is fixed to 97, a value derived from the spherical top-hat collapse model for ΛCDM (Bryan & Norman 1998) at z=0 for our cosmology.
When the high resolution simulation starts from the initial conditions, all physical processes described in Sections 2.2 and 3.3 for the collisionless and hydrodynamical components respectively, start working and drive the evolution of the DM and the baryons which are initially embedded within it.

Next we describe the initial parameters that need to be fixed in our cosmological + hydrodynamics simulations. In Chapter 6 we detail the values we have used for our main models.

Initial parameters: Dark matter species

As described in Section 2.2.5, in the high resolution simulation we use a multi-mass method with the most massive particles in the low resolution regions and the less ones in the high resolution regions (see Section 2.2.5). The number of 1rst specie DM particles, that is the less massive, in the high resolution region, depends on the total number of DM species and on the total mass of the halo. The mass of the most massive DM specie is fixed from the critical density of the universe. Particles belonging to each new specie has half of the mass of the previous one. As a consequence, as more species are used, smaller the mass of the lightest DM particles and bigger the number of particles needed to account for the total halo mass. Then, to have a larger number of DM species improves the mass resolution but increases the CPU time needed for simulation. Also the architecture of computers shall be taken into account when choosing the number of dark matter species as a higher number of species requires much more internal memory.

Initial parameters: Refinement criteria

In the ART plus hydrodynamics code the same mesh is used for both, the collisionless and the collisional component. Criteria chosen to refine such mesh are based on density also for both components. The cell is refined when the mass in DM particles exceeds $1.3(1\text{-F}_{b,U})\text{m}_p$ or the mass in gas is higher than $13.0\text{F}_{b,U}$ m_p, where $\text{F}_{b,U}$ is the universal baryon fraction and $\text{m}_p = \text{m}_{dm} + \text{m}_g = \text{m}_{dm}/(1\text{-F}_{b,U})$ being m_{dm} and m_g the mean DM and gas masses in the box. In our models $\text{F}_{b,U} = 0.15$ for the cosmology we have imposed and the mean DM and gas densities in the box are assumed to be equal to the corresponding universal averages. For the simulations presented in this work the grid is always unconditionally refined to the third level, corresponding to an effective grid size of 512^3. A limit also exists for the maximum allowed refinement level and it is what will give us the spatial resolution, i.e. the spatial size of the finest grid cells (R_{max}). Here we allow the refinement to go up to the tenth refinement level.

The refinement criteria, both for gas and DM, can be changed making it softer (i.e. less cells will be refined) or more aggressive. As we show in Chapter 6 we have used different criteria to obtain simulations with higher or smaller number of stars what is also translated in more or less computationally expensive simulations. Changes on these criteria have not a strong impact in the general parameters of the simulation (see Figure 3.3). However, as described in Section 6.4.3, significant changes are observed when analysing the total gas component. A direct consequence of using a more aggressive refinement is the generation of a more extended high resolution region what lets us to resolve fainter structures like stellar streams or satellite galaxies.

Initial parameters: Star formation and evolution

As we have pointed in Section 3.3.2 star formation and feedback approaches have an important impact on the global parameters of cosmological simulations. One of the most relevant effects consequence of the wrong treatment of these ingredients is the formation of a dense bulge in the central region of the simulated galactic systems, seen as a cusp in rotation curves, due to the so called overcooling problem (see Section 3.3.2). In this work we have seen the clear correlation that exists between the presence of big cusps in the rotation curve and the low ϵ_{SF} and/or n_{SF}. We have seen that high density thresholds have a similar effect as having high star formation efficiency that is to avoid the high efficiency of cooling processes due to a high gas density in SF regions when the SNe explosions occur. This is due to that in the first case the gas needs to be more concentrated before the star formation begins and when it happens a higher amount of gas is converted to stars consuming a bigger part of the surrounding gas. In the second case, as high is the star formation efficiency more gas is converted into stars and then, again, less gas is left in the region. As described before, when the gas density around the SF region is low, feedback is able to give kinetic energy to this gas. In this case the whole system become less concentrated as the material does not cool down due to energy looses in form of

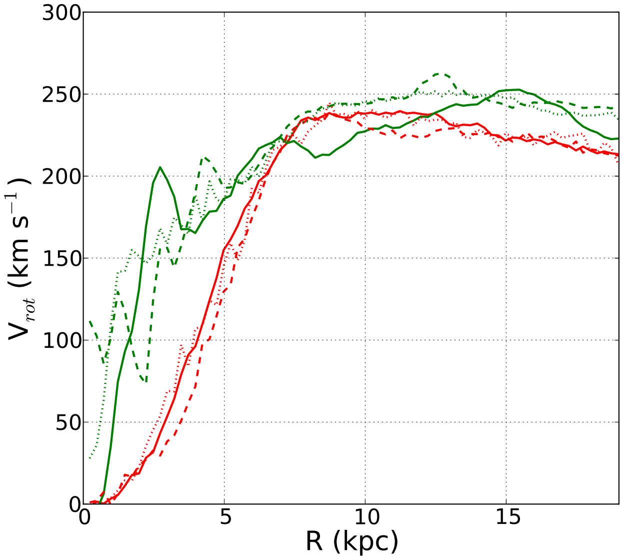

Figure 3.3: Red: Stellar rotation curve at z=1 of the simulated system HART32X but changing the gas and DM refinement criteria to be aggressive (solid line), intermediate (dashed line) and soft (dotted line). These models, namely HART322, HART323 and HART321, are analysed in Chapters 6 and 8. Green: Same as red lines but for the gas component.

radiation (see Figure 3.1).

Although to use higher ϵ_{SF} and/or n_{SF} seems to be a good approach to obtain realistic systems other consequences of this parameter selection need to be contemplated. First, it is important to take into account that when ϵ_{SF} is too high all gas in the region would be converted into stars what also will drive to a non physical situation where the SNe energy can not be released and distributed to the surrounding environment in a realistic way. Second, it is also important to know that as high ϵ_{SF} and/or n_{SF} are, higher will be the number of stellar particles that will be created and then also higher the CPU time required.

The final choice of parameters need to take into account all points to obtain a realistic rotation curve with a reasonable CPU time.

Initial parameters: Others

Some other parameters need to be set in order to start the simulation. In this work we have fixed all of them following (Colín et al. 2010). Some of these parameters are for example the gas pressure floor, the amount of energy released by SNe, the used IMF, the minimum stellar mass allowed when the star formation occurs, the UV ionizing background spectra and the total time in which cooling is switched off after SNe explosions, among others.

3.5 Strengths and weaknesses

Although N-body + hydrodynamics codes are much more complex than the pure N-body ones most weaknesses are common in both approaches. Basically these weaknesses are the CPU time requirements and the resolution problems that have been well described in Section 2.5.

It is true that using simulations that include hydrodynamics, some important processes related to the collisional component (gas and dust), that have an important impact on galaxy formation and evolution, can be well studied. However, new limitations concerning hydrodynamics appear, for instance, due to the limitation of resolution some important processes can not be implemented (see Section 3.3.1) and then the only solution is to use approximations. Other limitation that arises in these kind of simulations is that physical processes like turbulence or star formation in molecular clouds are not yet well understood so they can not be properly implemented. Turning it around it is also true that these simulations help the researchers to understand better these processes when testing the effects they have when they are implemented. Then there is a feedback between improving physics and improving simulations both helping each other to reach a final better understanding.

In our models we have some extra weaknesses in the implemented physics. Some of them are the lack of radiation pressure, the lack of a realistic molecular cooling, what implies that the gas can not be cooled down 200K, and the existence of only three different chemical species, i.e. alpha and iron elements and the rest of gas that has the same composition as primordial gas in the universe. These processes are being gradually implemented in new versions of the code. In Section 3.3.1 and in Chapters 6 and 8 we discuss how the the lack of these processes have been solved by using strategies that allow us to minimize the impact in the studies presented here.

Finally we shall mention that in our models we have turned off the AGN feedback as it has been checked that this process is not well implemented in the code. This drawback have not an strong impact in our results as our model is a MW like system, and the AGN in the MW has low activity.

Part II

New methods to trace spiral arms' nature

4

On galaxy spiral arms' unraveled by rotation frequencies

4.1 Introduction

Since the early seventies, it has been suggested that the dynamics driven by bars and spirals have profound consequences on the kinematic and structural evolution of galactic disks (e.g. Miller et al. 1970; Hohl 1971; Athanassoula 1980; Sellwood & Athanassoula 1986; Friedli & Benz 1993). More recently, stellar radial migration in disk galaxies has been recognized as a critical component of disk galaxy evolution. This process may drastically alter our view of the connection between the present-day phase space and chemical distributions of stars and the processes of disk formation and evolution. Sellwood & Binney (2002) set up the dynamical framework of this process through the effects of transient spiral structure, which seems to be a crucial process to understand the solar neighborhood observations as suggested originally by Wielen et al. (1996). Authors such Roskar et al. (2008), Schönrich & Binney (2009), Roskar et al. (2011) and Minchev et al. (2012), among others, revived the study of spiral arms and bars as triggers of stellar radial migration. Despite these numerous studies, fundamental questions arise such as: what is the nature of the spirals? or, how is their pattern speed related to the motion of the stellar component? Several models have been proposed up to now, from the classical Tight-Winding Approximation (TWA, e.g. Binney & Tremaine 2008) to the mechanisms proposed to account for self-excited spiral patterns (Toomre 1990; Bertin & Lin 1996; Sellwood 2000; D'Onghia et al. 2013), or the manifold theory (Romero-Gómez et al. 2007; Tsoutsis et al. 2009; Athanassoula 2012).

In the quest of dynamical models not limited to quasilinear approximations or steady state, N-body simulations have been used to understand the origin and evolution of spiral structures. After pioneering studies like Miller & Smith (1979), Sellwood & Sparke (1988) and Rautiainen & Salo (1999), only recently appeared another boom of papers likely as a result of progress in the computational resources and codes. This re-ignition of simulations based studies opened-up an interesting debate about the possible corotating nature of spiral patterns with disk particles (e.g. Quillen et al. 2011; Grand et al. 2012a,b; Minchev et al. 2012; D'Onghia et al. 2013; Baba et al. 2013). As an example, Grand et al. (2012a,b) computed collisionless N-body and smoothed particle hydrodynamics (SPH) simulations of disk galaxies and illustrated that transient spiral features appear to corotate with the disk. Comparetta & Quillen (2012) also suggested that some short lived features arising from constructive interference between longer lived modes, i.e. fast bar and slowly moving spiral pattern modes, can be nearly corotating with the disk. This corotating nature would have consequences on the stellar radial migration mechanisms (Grand et al. 2012a).

From the observational point of view, the nature of spiral arms is also far from being clear (Sheth & Rossi 2010; Foyle et al. 2011; Ferreras et al. 2012). Nowadays, only weak observational constraints are available to answer these questions. Some constraints come out from direct measurement of the rotation frequencies radial variation in external galaxies (e.g. Meidt et al. 2009), a method with a strong potential but currently applied only to a handful of galaxies, or from indirect measurements as the one proposed by Martínez-García et al. (2009). Other constraints to spiral arms' nature are based on small scale stellar kinematic substructure analysis in the Milky Way (MW) disk (e.g. Antoja et al. 2011, 2012). Furthermore, although it is now commonly accepted that the MW is a barred galaxy, it is not clear how the arms and bar are related or if they are connected at all. The rotation frequency of both, bar and spiral arms, seem to show different values, none in mutual corotation or in corotation with galactic disk material, leaving unclear spiral arms' nature (Martos et al. 2004; Gerhard 2011). It is fair to say that currently, galactic arms' pattern speed estimations are mostly model dependent (Martos et al. 2004). The situation is also not clear for external galaxies (Buta et al. 2005). The interpretation of observational results is based on previous theoretical studies and also on numerical simulations (Sellwood & Sparke 1988; Rautiainen & Salo 1999). Some of these studies adopted simplifications like 2D N-body models and a rigid halo or no halo at all. It is not clear if such assumptions may affect the generality of their conclusions as is suggested by Athanassoula (2002) for the case of bar growth. It is also not obvious if the corotating nature of spiral arms recently suggested by Grand et al. (2012a) is valid also in models with different structure (i.e. models with strong/week bar and/or bulge). Furthermore, classical methods to estimate disk modes' rotation frequencies like time Fourier Spectrogram applied to simulations, have been claimed to suffer from biases in models with multiple or week spiral arms, hampering estimations of arms' pattern speeds (Grand et al. 2012a).

In this chapter we analyze collisionless N-body models simulated using the codes presented

in Chapter 2, with different stellar/dark structure, using live halos and with enough mass, force and time resolutions to accurately describe the internal disk kinematics. We performed some testing on the results dependence on codes and initial conditions techniques. Although here we do not analyse simulations with the hydrodynamical component, it became clear from the first attempts to simulate gas in barred galaxies (Sanders & Huntley 1976) that gas influences disk stellar dynamics, by even changing the life time of bars and spirals (Bird et al. 2012; Di Matteo et al. 2013). Gas makes disks to show more complicated and well-defined morphologies. As an example, inner rings, such the Galactic Molecular Ring observed in our MW (Clemens et al. 1988), have been the subject of numerous observational (Buta et al. 2004) and theoretical investigations (e.g. Byrd et al. 2006; Romero-Gómez et al. 2011). The influence of the gaseous component and its subgrid physics in our simulations is now under investigation using the ART code in the hydrodynamic version presented in Chapter 3.
The aim of the study presented here and reported in Roca-Fàbrega et al. (2013) is to revisit the possible correlation between spiral arm kinematics and their nature using the purely stellar component.

4.2 Methodology

4.2.1 Simulations: Collisionless models

Here we present three sets of collisionless fully self-consistent models, all of them with a live exponential disk and live dark matter halo with a NFW (Navarro et al. 1997) density profile. All models have been obtained using one of the codes described in Chapter 2. In Table 4.1 we show the most significant parameters we used for each one of the main models we analyze here. The use of live halo is one of the key points in this work and that differs from others that has not. As mentioned above, to have a live halo is important to obtain barred spiral galaxies because it ensures disk-halo angular momentum exchange. This exchange of angular momentum plays an important role in the formation and evolution of bars as discussed by Athanassoula (2002).

ART Barred and Unbarred models

Using ART code we have simulated barred (B) and unbarred (U) models with the aim to compare spiral arms potentially triggered by a bar against arms triggered by other mechanisms. To generate initial conditions of these models, as we have described in Section 2.2.5 we have used the Jeans equation moments method as introduced by Hernquist (1993). We have also used a multi-mass method to sample the halo particle distribution, which allows us to obtain similar results as using a higher number (N_{eff}) of particles, minimizing two body scattering as discussed in Valenzuela & Klypin (2003) (see Section 2.2.5 for a detailed

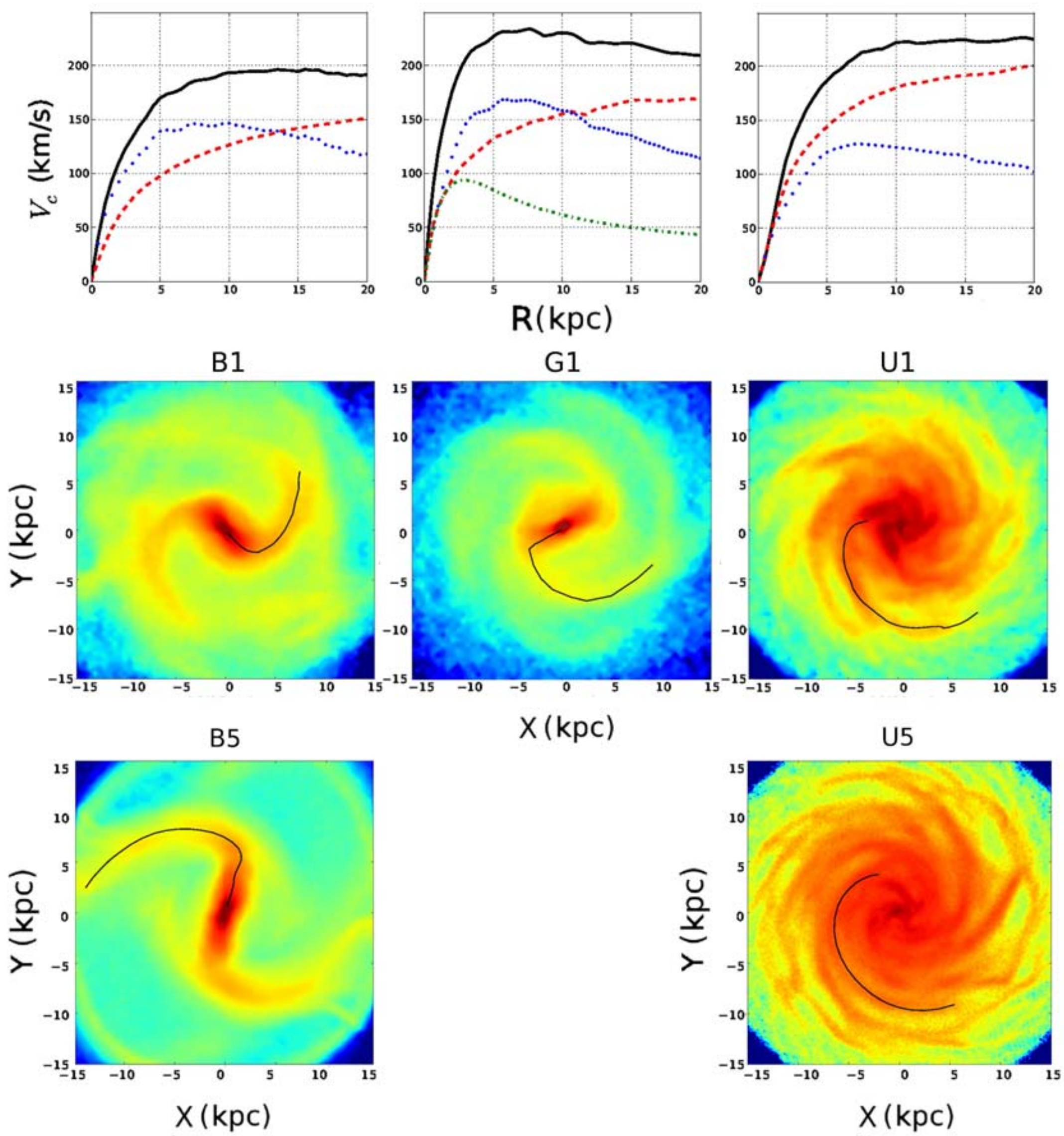

Figure 4.1: Structure of main models of this work. Top: Initial circular velocity of models B (left), G (center) and U (right) , computed from the potential field gradients using TIPSY package. We show the total rotation curve (black solid), disk (blue dotted), halo (red dashed) and bulge (green dot-dashed) contributions. Center: Density distribution of the models B1 (left), G1 (center) and U1 (right) after 900 Myr of evolution. Bottom: Density distribution of the models B5 (left) and U5 (right) after 900 Myr of evolution. The black solid line shows the locus of the spiral arms derived using Fourier analysis ($m = 2$ for B and G models, $m = 4$ for U). Spiral structure rotates clockwise in all models.

description of the multi-mass method). Barred models have a stellar disk and total mass similar to the one observed for the MW with additional initial parameters as proposed by Colín et al. (2006) (model K_{cb}), see Table 4.1. As discussed in (Klypin et al. 2002), the final properties of this model, after rescaling, can reproduce the observed quantities for the MW. This rescaling process has not been applied in this work since it does not affect the disk kinematic properties we analyse. Unbarred models have a smaller disk and a massive and highly concentrated halo. The number of disk particles in our models range from one to five million particles (see Table 4.1).

As expected (e.g. Ostriker & Peebles 1973), the models with a relatively dominant disk rapidly generate a bar with trailing spiral arms while unbarred models do not, at least in the first ∼ 3Gyrs. In the first case, we have a similar halo and disk contribution to the circular velocity inside a radial exponential length and, as described in Valenzuela & Klypin (2003), the self-gravity of disk density fluctuations (disk modes) dominates making the instability grow and generate a bar (Figure 4.1, left and middle panels). This bar mode induces the formation of a bisymmetric spiral structure apparently connected to the bar ends (e.g. Binney & Tremaine 2008, and references therein). There is still controversy on the nature of these bisymmetric spirals (resonant coupling, manifolds, or others), but what is evident in all our models is that these structure dominates in density. For the unbarred model (Figure 4.1, right) the halo contribution to the potential is higher and the disk modes cannot grow so easily. Although in both cases the initial velocity dispersion is low ($Q = 1.2$), the higher halo mass concentration in the unbarred model prevents disk from having a dominant bisymmetric mode in the first Gyrs of evolution, i.e. other modes grow forming a trailing 3-4 armed structure. Some other structures with lower density appear in the external regions of these simulations (both barred and unbarred). In Section 4.3.2 we discuss their imprints on the frequency space. As expected for MW like galaxies, we also note that rotation curves in our set of simulations are rather flat (see top panels of Figure 4.1).

We see that dominant spiral modes have a recurrent nature with periodicities of less than one galactic rotation. The amplitude of the spiral arms in the unbarred case is significantly lower than in the barred models.

In Figure 4.1 we observe that some parameters of the bar and spirals are different from B1 (one million disk particles) to B5 (five million) models. These differences are arising from the fact that the number of particles, spatial and time resolution in B5 model are much better than in B1, i.e. we are resolving smaller wavelength disk modes in the B5 case than in B1. These modes interact with the disk and then, due to the high non-linearity of the system, lead the evolution to a slightly different configuration (e.g. bar length and speed). However global quantities like circular velocity and density profiles are more robust to such effects. The situation is well known and it has been reported in previous works (Sellwood & Debattista 2009; Klypin et al. 2009). A convergence study of this and other models is presented in the Section 2.4, however, as will be seen in next sections, the main results of our simulations are robust across changes in numerical parameters.

Halo evolution

Dark matter halos in models analyzed here have been generated using density and velocity profiles presented in Section 2.2.5. In Figure 4.1 we show their initial rotation curves while their initial parameters are shown in Table 4.1. The rotation curve and density profiles does not change significantly during the simulation, although it exists a redistribution of mass and energy when non-axisymmetric structures forms in the galactic disk. As can be seen in Table 4.1, we used 6 or 7 dark matter species for the generation of the halo. The election of the number of DM species depends on the mass of the lightest specie, that in its turn depends on the total number of disk particles inside the model as disk particles have the same mass as the lightest DM specie. So, we have used more DM species when the disk particles are lightest (i.e. has more particles) to ensure that DM particles in the last specie are not too massive.

We have tested that during the simulation only few particles of other species than the less massive interact with the disk region. It is important to ensure small number of halo massive particles interact with inner regions as the more massive ones can perturb significantly the disk evolution, even resembling the interaction with a satellite.

Disk evolution

Initial parameters used to generate disks of our main models can also be seen in Table 4.1.

In all models, disk initial parameters change when the simulation evolves. In Figures 4.2, 4.3 and 4.4 we show, as an example, the evolution of velocity dispersions, density profile and rotation velocity curve in model B1. As expected, all velocity dispersions increase with time due to disk heating driven by non-axisymmetric structures (see Section 2.4). This increase is more evident in the central region where the bar is placed. The formation of the non-axisymmetric structures conducts to a redistribution of mass along the disk (see Figure 4.3). In barred models a large amount of material moves to the central regions to form the bar while spirals form in region between 1 and 10 kpc, depending on the model. Finally, rotation velocity of disk particles also changes with time mainly due to the redistribution of matter and the consequent change in the potential. However, as we can see in Figure 4.4 changes in this parameter are small. As we show in previous sections Toomre parameter also varies with time (see Figure 2.5), these changes are a direct consequence of the increase of velocity dispersions.

In the evolution of simulations from initial conditions it is important to mention that it exists a small period of time when the system goes through a transient state. This

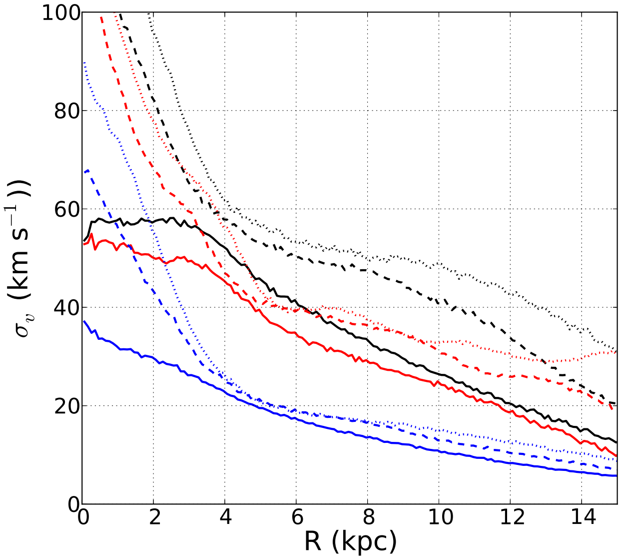

Figure 4.2: Velocity dispersions (black=σ_r, red=σ_{phi}, blue=σ_z) as function of radius and time (solid line = 0.02 Gyrs of evolution, long dashed = 1.1 Gyrs, and short dashed = 2.6 Gyrs) for simulation B1.

short time at the beginning of the simulation is characterized by the formation of several spurious density structures as multiple low amplitude spiral arms or also rings. The origin of this transient state is in the generation of initial conditions. When we generate initial positions and velocities we get a system that is not in a perfect equilibrium what means that it is not fully self-consistent. In this short period of time the system accommodates to the nearer stable self-consistent state. We have analysed all of our simulations after this period.

ART complementary models

To complement and reinforce our results we have simulated additional systems. Models like model M shown in Table 4.1 develop bars with intermediate amplitude and give us information about the influence o bar strength to the spiral arm dynamics. Other models we have generated have the same parameters as models B or U but with a smaller number of disk particles, different Toomre parameter value or smaller resolution. These models have been used to test how dependent are our results on these parameters and also the convergence of the code. All these models are not being presented here but are available for new studies.

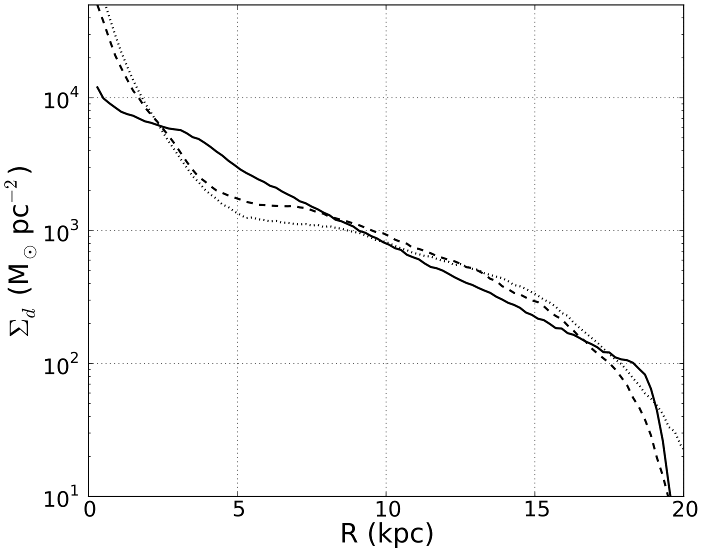

Figure 4.3: Disk surface density profile for three different time steps of simulation B1. Solid line = 0.02 Gyrs of evolution, long dashed = 1.1 Gyrs, and short dashed = 2.6 Gyrs.

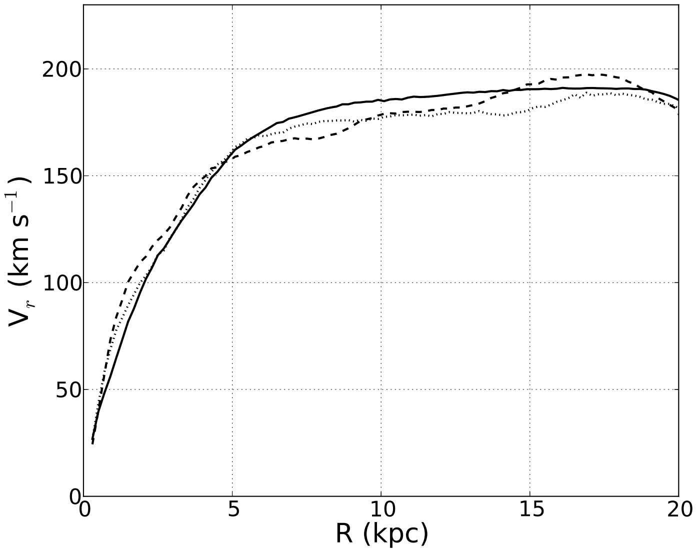

Figure 4.4: Rotation velocity of disk stellar particles for three different time steps of simulation B1. Solid line = 0.02 Gyrs of evolution, long dashed = 1.1 Gyrs, and short dashed = 2.6 Gyrs.

Parameter	B1/5	G1	U1/5	M5
Disk mass (10^{10} $M_{\odot}$)	5.0	6.01	3.75	4.29
Halo mass (10^{12} $M_{\odot}$)	1.38	0.66	1.5	1.4
Disk exp. length R_d (kpc)	3.86	3.0	4.0	3.96
Disk exp. height Z_d (kpc)	0.2	0.2	0.2	0.2
Halo NFW R_d (kpc)	29.19	14.4	16.61	20.91
Halo concentration	10	10.4	18	14
Halo DM species	6/7	1	6/7	7
$\mathrm{N}_{*disk}(+\mathrm{N}_{*bulge})$ (10^6)	1.0/5.0	0.5(+0.5)	1.0/5.0	5.0
N_{eff} (10^7)	2.86/13.8	0.15	4.1/20.0	16.3
Min. time step (10^4 yr)	3.2/1.6	4.4	7.9/3.1	3.1
Spatial Resolution (pc)	44.0/11.0	35.0	11.0/11.0	11.0
Total integration t (Gyr)	4.6/2.8	1.4	3.2/2.8	2.8
Total CPU time (10^3 h)	4.1/13.8	2.8	3.9/11.8	12.7

Table 4.1: Parameters of the simulations: Column indicated by B1/5 presents the parameters for models with 1 million (B1) and 5 million (B5) star particles in the disk, simulated using ART code, idem for unbarred models U1/5 in the third column and for the model with a small bar (M5) in the last one. Parameters for the barred model G1, using GADGET3 code, are shown in the second column.

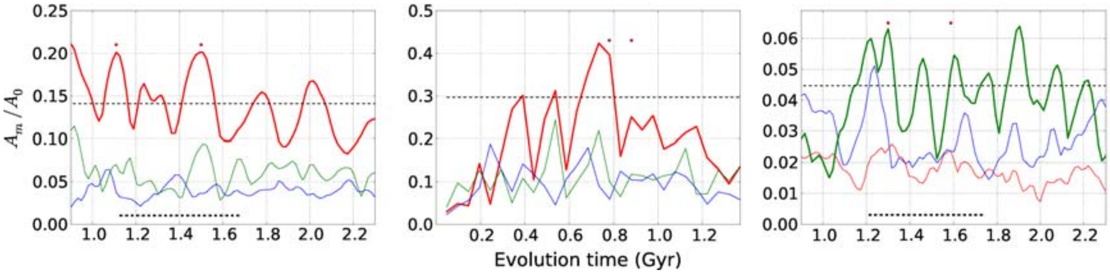

Figure 4.5: Amplitude evolution of disk modes. Fourier amplitude for modes 2 (red), 3 (blue) and 4 (green) as a function of time, averaged for radius between 4 and $10\mathrm{kpc}$ of the barred (B1, left), the bulge-barred (G1, center) and the unbarred (U1, right) models (notice change in vertical scale). Thin black dashed lines indicate a threshold in amplitude used to compute Figure 4.8 using SFpFD method. The black dots indicate the snapshots for which the kinematic analysis is shown in Figure 4.9 using SFpFD method, and thick black dashed lines indicate the temporal range used to compute Spectrogram in Figure 4.10.

GADGET3 Barred models

In this work we have used the GADGET3 code to simulate some barred models, labeled G, that also include a bulge component with a Sersic profile ($R_b = 1.75$ kpc, $M_b = 8.57 \cdot 10^9$ $M_\odot$). As we detail in Section 2.3.1 the generation of the initial conditions was made using the code described in Widrow & Dubinski (2005). G models, like in the ART barred case, are disk-dominated and have live dark matter halos. Parameters of the main G model can be seen in Table 4.1.

To have models obtained using different N-body codes and methods to generate their initial conditions allows us to ensure the independence of our results on these two variables. To better characterize the effects of using different codes, we have new models with exactly the same initial conditions as the ones for models B and U but simulated using GADGET instead of ART. The comparison between B and U models and the new ones is now work in progress.

4.2.2 Analysis tools

To undertake the study of spiral arms and their kinematics in our pure N-body simulations we have needed to develop new analysis tools and techniques. In this section we present them, as well as those commonly used in the bibliography. Most of the techniques commonly used for the study of spiral arms density perturbations are based on the Fourier transform techniques, both spatial and temporal (see Equations 4.1 and 4.4).

The initial analysis of our models have been done using the visualization tool TIPSY from the Washington University, and their internal scripts.

Fourierograms or SFpFD

We have called fourierograms a technique that uses spatial Fourier analysis to trace the spiral arms density peak and finite differentiation to compute the pattern speed of this structure.

To compute the pattern speed of galactic structures we have two major challenges, the first one is to find properly its exact position, the second one is to compute its rotation frequency. To reach the first goal this technique uses spatial Fourier analysis azimuthally averaged to trace the density peak of the spirals and the bar (Valenzuela & Klypin 2003), working in cylindrical shells equally spaced in galactocentric distance. Equation 4.1 shows how we compute the amplitude of mode m (A_m) and the angular position of its maximum (Φ_m). These two parameters are computed at each radial ring using the angular positions of each particle (ϕ_i). Figure 4.1 shows an example of how well the spatial Fourier method traces the peak overdensities up to the end of the dominant structures (m=2 for barred cases and m=3,4 for unbarred ones). Once the locus of the spiral is derived, we have used here finite differentiation among three consecutive snapshots to compute the rotation frequency (see Equation 4.2 and Figure 4.6).

When using Spatial Fourier plus Finite Differentiation (hereafter SFpFD) we have observed that if several density fluctuations are present in disks the method gives not the proper position of spiral structures. To test in which cases SPpFD drives to wrong conclusions due to a false detection of the spiral structures we made several toy models where to apply the method and see if it works or not (see Appendix A.1). The conclusion we have obtained from using synthetic models is that SFpFD does not work when two structures of the same Fourier mode coexist at the same radius, independently of having two or more spiral arms. When this happens the method results in an unique structure placed at the average angle of both structures. Due to this problem we have needed to control how the system is before applying the method to avoid errors in the derived rotation frequency.
The strength of using SFpDF is that it allows us to compute the rotation frequency of a single known mode m structure and for a single time instant, something that other methods can not do. As a consequence, this method is able to show us how the structures evolve with time.

$$\begin{aligned} a_m(r) &= \sum_{i=1}^{N} \sin(m\phi_i) \\ b_m(r) &= \sum_{i=1}^{N} \cos(m\phi_i) \\ A_m(r) &= \sqrt{a_m^2 + b_m^2} \\ \Phi_m(r) &= \mathrm{atan}\left(\frac{a_m}{b_m}\right) \end{aligned} \tag{4.1}$$

$$\Omega = \frac{\Phi_{i+1} - \Phi_{i-1}}{2 \cdot \Delta t} \tag{4.2}$$

Spectrogram

Spectrogram technique used to compute rotation frequencies of galactic large scale structures is a well known and long used classical method (Sellwood & Athanassoula 1986). In this case, as in SFpFD the density structures are found by using a spatial Fourier technique (see Equation 4.1). The difference with the method described in the last section is the way of computing rotation frequencies once found the exact position of the structure. Spectrogram use also a Fourier analysis to find the rotation frequencies but now temporal Fourier instead of spatial. In Equation 4.4 we show the analytical expression used to compute the amplitude of rotation frequencies ($\tilde{A}_m(\Omega, r)$) at each radial bin.
As for SFpFD method here we have used synthetic models to test the method when it is applied to models with different configurations and number of structures (see Appendix A.2).

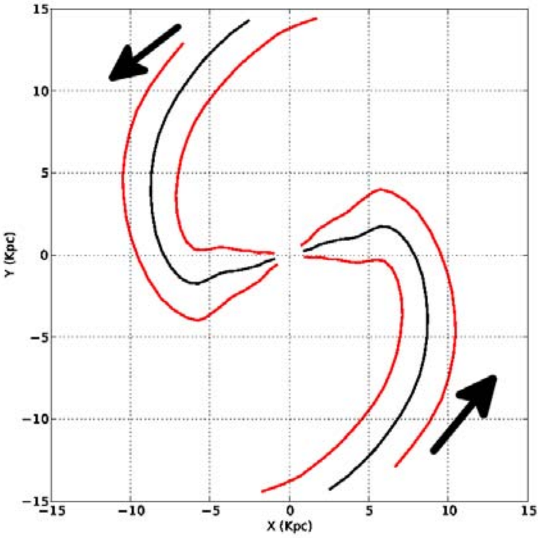

Figure 4.6: Identified spiral structure in three consecutive snapshots of model B5 using spatial Fourier method.

From these tests we confirm that Spectrogram allow us to find discrete rotation frequencies from structures coexisting at the same radius differently from SFpDF. However we also found a caveats of using this technique, that is it needs to be applied to a large time interval or to very close snapshots due to the Nyquist frequency limitation. This limitation arises when using discrete samples to analyse processes that present periodicities. In these cases it exists a limiting frequency that defines which processes can be studied and which ones not. This frequency is known as Nyquist frequency (see Equation 4.3). Finally other problem that appears when using Spectrogram method is that results may be contaminated by recurrent arms sequences with low or negligible spiral amplitude as a consequence of transient nature of the structures. This drawback is already discussed by Grand et al. (2012a).

After carefully weighting the pros and cons we state that none of the two methods presented here (SFpFD and Spectrogram) is perfect for our analysis , nonetheless they are complementary.

$$\nu_{Ny} = \frac{\nu_{samp}}{2} = \frac{N}{2\Delta t} \tag{4.3}$$

where N is the number of samples and Δt the total analysed interval.

$$\tilde{A}_m(\Omega, r) \quad = \quad \sum_{T_1}^{T_2} e^{i\omega t}[b_m(r,t) + i \cdot a_m(r,t)]\Delta t \tag{4.4}$$

Density peak technique

Using both methods detailed above we ensure that results of computing rotation frequencies are method independent. However, as they use the same technique to find the density structures, we can not ensure these structures are found properly without any dependence on the method used. As a consequence we have decided to use another technique, only to find the density structures, called density peak method and that has also been used in Grand et al. (2012a,b). This density peak method starts with the generation of a full galaxy density map. When the map is completed we subtract the mean exponential disk density profile and then we cut it at an imposed density threshold. From this we obtain an overdensity map from where, using a clustering algorithm, we can find the density structures we are interested in. Once selected we look for the upper density regions to trace the exact position of the maximum density that will be the position of the density structure for us.

FORTRAN programs

Several FORTRAN programs have been developed to analyse the data and convert it from internal code format to a readable one. We have programs to compute the position and velocity of spiral arms but also to fully analyse disk kinematic parameters as Q, σ, $\bar{v}$ and to obtain density profiles. All these software is now available under a single big analysis package.

4.3 Discussion and results

4.3.1 Theories of spiral arms nature

Nearly about 80-90 percent of galaxies in the nearby universe are characterized by a disk with spiral arms. Some of them have strong spirals and are defined as great design spirals while others have less defined structures. Although the number of spiral galaxies is so large our understanding of the origin of formation, evolution and nature in general of these patterns is incomplete even after decades of theoretical study (e.g. Toomre 1977; Athanassoula 1984; Romero-Gómez et al. 2007; Binney & Tremaine 2008; Sellwood & Carlberg 2014).

Several ideas have been proposed to explain their formation and nature. One of the first theories that is even nowadays accepted by a large part of galactic astronomers community is the density wave theory (Lin & Shu 1964; Bertin & Lin 1996). This theory was born to solve the so called winding problem, that is the impossibility of maintaining a spiral mass density perturbation in a disk with differential rotation for a long period of time. In particular, density wave theory argues that a density wave without any mass associated to it is continuously propagating in the disk passing through the material and compressing or expanding it. In this model the perturbation can be maintained for a long period of time. However in this model the density wave remains at least quasi-stationary in a frame of reference rotating around the center of the galaxy at a fixed angular speed, identified with the pattern speed of the spirals, and do not give a answer to the its formation process.

An alternative theory proposes that spiral arms are stochastically produced by local gravitational amplification in a differentially rotating disk (Goldreich & Lynden-Bell 1965; Julian & Toomre 1966). The mechanism behind this process is known as swing amplification and it can be seeded either by preexisting leading waves, by the response of a disk to the presence of a corotating overdensity, such as a giant molecular cloud or by the continuous infall of substructures in the dark matter halos (Gauthier et al. 2006; Purcell et al. 2009). This dynamical response takes the form of wavelets in the surrounding medium, each amplified by its own self-gravity through the swinging of leading features into trailing ones owing to the shear. Complementary to the swing amplification, which came from the linear study of formation of density waves in disks, recent works suggested that a more complex mechanism can be present in galactic disks. They studied larger order effects and found that starting from the swing amplification (or from external perturbations like satellite galaxies) other disk density modes can develop and produce complex structures like multiple-spiral systems. This mechanism is known as non-linear coupling (Sygnet et al. 1988).

According to this second theories, spiral arms in a purely stellar system would fade away in one or two galactic years when the driving perturbations are removed by the disk heating (Toomre & Kalnajs 1991), in contrast to the quasisteady nature of the arms in the model proposed by Lin and Shu. However when introducing the infall of cold intergalactic gas it reduces the disk heating as new stars with cold orbits can be produced, then, the structures can be maintained for a longer periods of time (Sellwood & Carlberg 1984).

More recently, another theory that accounts for the formation and evolution of spiral density waves is the invariant manifolds theory (Romero-Gómez et al. 2007). This theory suggests that bisymmetric spirals can be formed by stars departing from unstable Lagrangian points at the galactic bar edges. In this case the spirals are not only a density wave but a material wave with the particles traveling along the spiral. This mechanism can be maintained as long as the bar is well formed, however it is not clear if the amount of particles that will follow these spiral orbits can be high enough to form the observed spiral structures.

It is important to remark that all models presented previously accounts for spirals that are density waves and are based on analytic theory with several assumptions and simplifications needed to find analytical solutions. For example, the swing amplification analysis involved linear approximations to the equations of motion or the classical density wave theory is only valid when spirals have low amplitude, velocity dispersions, pitch angle and follows the epicyclic approximation. The real galaxies are more complex than all these models. Some observations show that spiral arms might be density waves , however in other cases the spiral arms seems to rotate at the same speed as disk particles (e.g. Meidt et al. 2008, 2009; Speights & Westpfahl 2012), however from observations it is difficult to obtain temporal information and then to infer the evolution of these structures. In the case of N-body experiments, where we can study their formation and evolution, it was not possible until now to produce long-lived spiral structures, as predicted by the stationary density wave theory. Simulations of cool, shearing disks always exhibit recurrent transient spiral activity and this situation has not changed over the past several decades as computational power has increased (Sellwood 2000; Grand et al. 2012a; Roca-Fàbrega et al. 2013; Sellwood & Carlberg 2014), or when including cold gas flows. Also using simulation it became clear that interactions with massive galaxies drive to the formation of grand-design spirals like what is observed for M51 while some works suggest that tidal effects of small satellites are much smaller and can not seed the formation of spiral structures (D'Onghia et al. 2010). Other studies have been done in the way of finding which method is able to create spiral structures in disk galaxies, an example is the one of (D'Onghia et al. 2013) where they suggest that density inhomogeneities orbiting within the disk (globular clusters, molecular clouds, ...) can drive the formation of spirals and also have the same effect as cold gas flows allowing the formation of long lived structures.

Here also using N-body simulations we study differences on the rotation frequency of spiral structures. This study can provide us a tool to distinguish between the nature of these structures. We performed a first kinematical analysis on the dominant modes in density shown in Figure 4.5, $m = 2$ for barred (bisymmetric spiral) and $m = 4$ for unbarred models (4 armed structure). In both models the spiral arms are recurrent transient structures and this can be clearly seen in Figure 4.7 where we show the amplitude of cosenoidal Fourier component of m=2 mode of model B1 (left) and m=4 of model U1 (right), as function of time (see b_m in Equation 4.1). For the B1 model the bar is shown as a straight structure up to $R = 5$ kpc and spirals as structures that depart from the bar and disappear and appear again from the bar, periodically. In the U1 case the spiral structures appear spontaneously from the disk and they are much more spurious and with shorter life. Also in both models, as can be seen in Figure 4.1, the dominant density structures extend up to $10 - 11$ kpc. In Figure 4.8 we present the rotation frequency curves for the three models with one million disk particles computed using the SFpFD method. It includes all timesteps where we can ensure the spiral arm is well formed. We empirically establish that a spiral is well formed when the amplitude of the dominant mode is above 0.7 times the maximum value of this mode in the range we study (see thin black dashed lines in Figure 4.5). These density maps are constructed from the superposition of all the

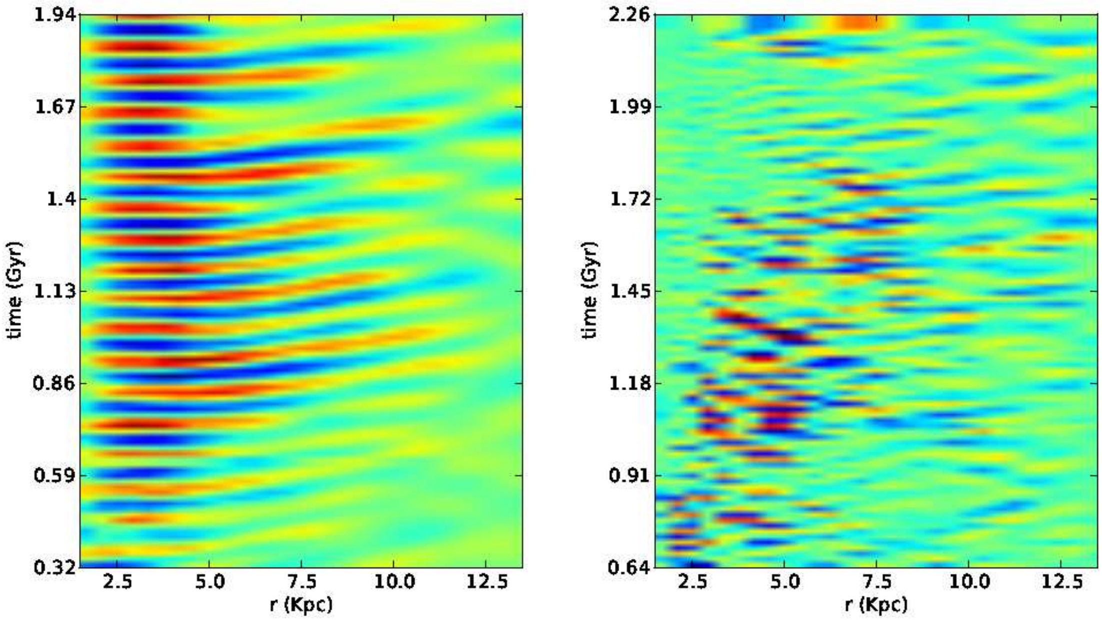

Figure 4.7: Left: Amplitude of m=2 Fourier cosenoidal component (b_m) as function of evolution time for model B1. Right: Same as in the left but for m=4 mode and for model U1.

rotation frequency curves at timesteps when the amplitude of the mode is above the mentioned threshold. As we present in next sections these figures show significant differences between barred and unbarred morphologies indicating a difference on their nature.

4.3.2 Pattern speed in barred models

Here we present the results of analysing barred models (B1 and G1, computed using ART and GADGET3, respectively). In Figure 4.8 we show that in these barred cases the spiral pattern rotates almost as a rigid body what is compatible with a density wave or also with an invariant manifold. To distinguish between these two theories it is necessary to study the motion of particles when being nearby the spiral arm perturbation as in the first case all particles will follow disk rotation with low or no perturbations while some particles will travel along the arm in the second case. We study the particles motion in Section 4.3.4. A more exhaustive analysis on the rotation frequencies is shown in Figure 4.9, considering models with a higher number of disk particles and a different technique for the detection of the spiral structure. Instead of working with density maps, here we plot single timestep curves computed using SFpFD for models with both one and five million disk particles. As it can be seen in the figure we avoid the central part where the bar is placed and also the external regions where the number of particles is too low. The red-dashed lines

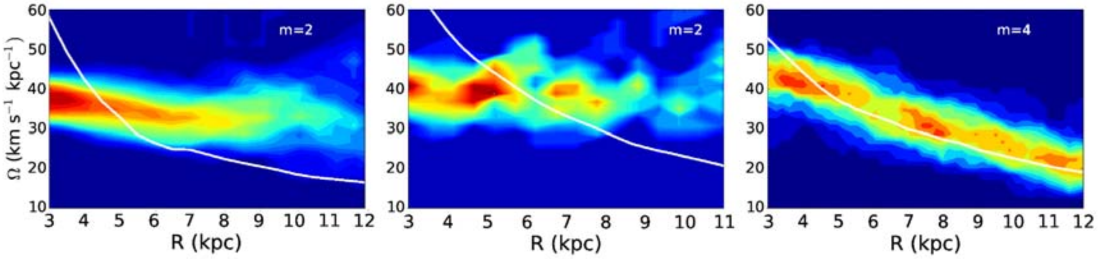

Figure 4.8: Rotation frequencies as a function of radius calculated using SFpFD method for dominant mode across time in models B1 (left, G1 (center) and U1 (right) (see Figure 4.5). Here we plot the frequency density map of the rotation frequencies computed using all time instants when the spiral arms' amplitude is above 70% of the maximum mode amplitude (dashed line in Figure 4.5). Circular frequencies of disk particles are indicated as solid white lines and have been computed in an intermediate instant of the analyzed time interval. The length of the bar is $\sim 4.5\mathrm{kpc}$ and $\sim 5\mathrm{kpc}$ for B1 and G1 models respectively.

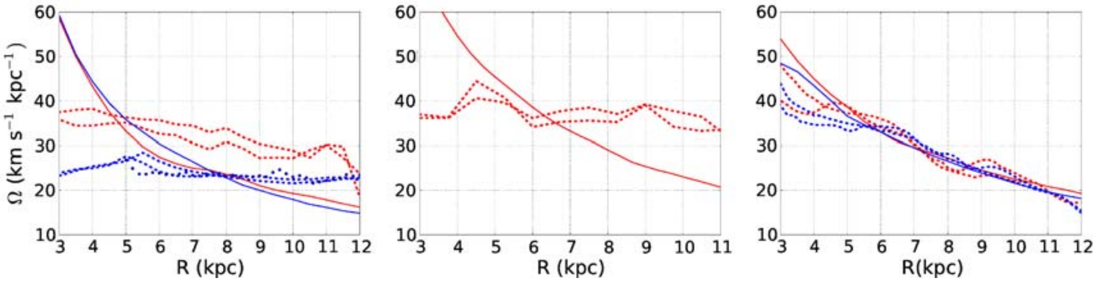

Figure 4.9: Rotation frequencies as a function of radius calculated using SFpFD method for selected time instants when the amplitude of spiral arms is maximum (black dots in Figure 4.5). All the rotation frequencies analysis of barred (B1, and B5 left), the bulge-barred (G1, center) and the unbarred (U1, right) has been computed taking cylindrical shells of $0.5\mathrm{kpc}$ width. In red dashed we show results obtained for models with 1 million disk particles. In blue dashed, those of the ART models, with 5 million disk particles (left and right panels respectively, for models B5 and U5) when the amplitude of the spirals arms is maximum (0.75 and 1.12 Gyr). Circular frequencies of disk particles are indicated as solid lines (red for models B1 and U1 and blue models B5 and U5). Additionally, blue dots in the left panel show the results of applying a density peak method similar to one used in Grand et al. (2012a) to B5 simulation, to find the spiral structure. The dispersion on rotation frequency profiles due to its computation at several time steps when the amplitude of the dominant mode and its behaviour can slightly change, is shown at Figure 4.8. The length of the bar is $\sim 4.5\mathrm{kpc}$, $\sim 7.0\mathrm{kpc}$ and $\sim 5.0\mathrm{kpc}$ for B1, B4 and G1 models respectively. The differences in bar properties between models B1 and B5 are discussed in Section 4.2.1.

correspond to two instants of the one million disk particle models (included in the density plot of Figure 4.8) shown as red dots in Figure 4.5. More important, the blue-dashed lines correspond to models with five million disk particles integrated using ART. Furthermore, the blue-dotted line corresponds to the barred ART five million model for which the spirals have been detected using the density peak method (similar to the one in Grand et al. (2012a,b). Note how the conclusions reached in Figure 4.8 are well corroborated. We can see spiral patterns rotating almost as a rigid body in all our barred models, both using ART and GADGET3, using different techniques for the spatial detection and considering a different number of particles. We have also verified that simulations with $2 \cdot 10^5$ disk particles show the same behaviour (not included here). A slightly decreasing rotation frequency with radius is observed only for the ART model with one million disk particles (B1).

To ensure that our results are not dependent of the method used to compute the rotation frequencies, in Figure 4.10, we perform one last test using, in this case, the classical spectrogram method in B1 model with a Nyquist frequency of $\sim 100 - 150$ km s^{-1} kpc^{-1}. The panels framed in red correspond to the dominant modes discussed above, and they are to compare with the left and right panels of Figure 4.8. Note that, again, the barred model presents a dominant mode that rotates as a rigid body. A feature observed in this dominant mode deserve special attention. A well defined structure is observed at a radial range of $11 - 14$ kpc (only the beginning of the structure is shown in the figure). It rotates slower than the disk with a frequency of about 8 km s^{-1} kpc^{-1}. As mentioned in Section 4.2.2, here we note one of the advantages of the Spectrogram, i.e. they are able to detect multiple spiral patterns at a given radius. Later on using SFpFD we have checked that the low frequency structure corresponds to one of this lower density structures observed in the outer radii of the center-left panel of Figure 4.1. We have made a first analysis of this structure and we find that it is compatible with having its origin in a non-linear coupling interaction with the dominant structure, however this deserves for a deeper study. As it is known, these multiple pattern speeds are common in spiral barred galaxies both in simulations and observations (e.g. Masset & Tagger 1997; Buta & Shang 2011).

Finally it is important to point to that we have analysed other barred models with smaller bars (e.g. model M in Table 4.1) and we find that as weaker is the bar nearer to disk rotation is the spiral arms rotation frequency.

4.3.3 Pattern speed in unbarred models

We have made the same analysis as for barred cases to models U1 and U5 computed using ART code. In Figure 4.8 we show how differently from barred cases in the unbarred cases the spiral pattern rotates at the same rotation frequency as the disk particles, i.e. corotates with the disk. In this case no one of the theories presented in Section 4.3.1 is valid. Again results are clearer in Figure 4.9, where we have analysed the spiral arms

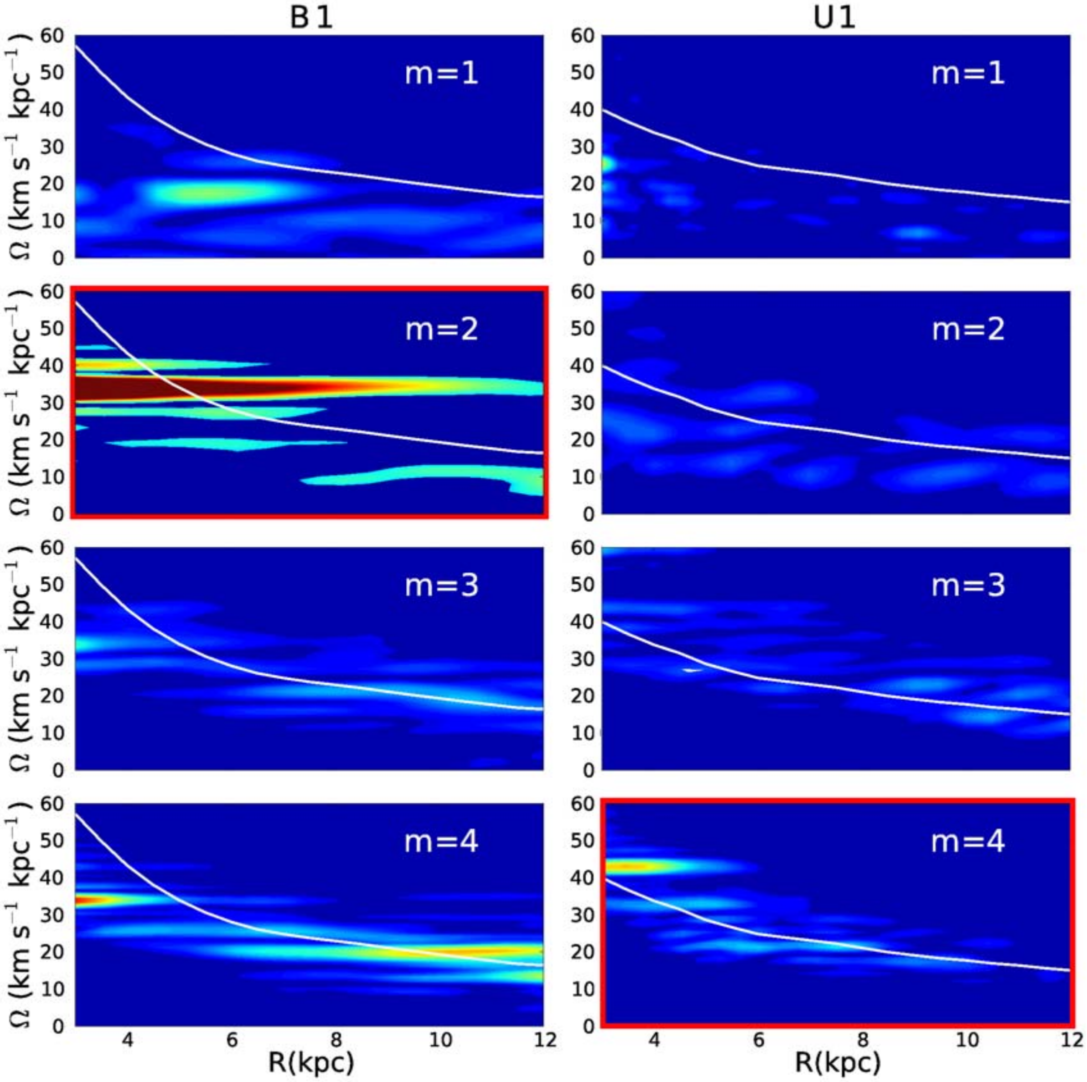

Figure 4.10: Spectrogram for the barred model B1 (left) and unbarred U1 (right) obtained using Sellwood & Athanassoula (1986) method. We show the Fourier component for the m=1,2,3 and 4 modes in a window spanning 0.5 Gyr centered at 1.4 Gyr (left) and 1.45 Gyr (right), (see dashed dark lines in top panels of Figure 4.5), and with a Nyquist frequency $\sim 100 - 150 \mathrm{kms}^{-1}\mathrm{kpc}^{-1}$. The y axis is the angular frequency in $\mathrm{kms}^{-1}\mathrm{kpc}^{-1}$ and the x axis is radius in kpc. Overplotted in white we show the rotation curve of disk particles computed for an intermediate instant of the analyzed time interval.

rotation frequency at two time instants and in two simulations with different number of disk particles. In the analysis of these unbarred cases we have avoided the central complex region where the 3-4 armed structure converges and also the external region where the number of particles is too low, as we have done in barred cases. Here as for the barred cases the red-dashed lines correspond to two instants of the one million disk particle model U1 (included in the density plot of Figure 4.8) shown as red dots in Figure 4.5 and the blue-dashed line corresponds to the same two time instants but in the model with five million disk particles U5. Note how the conclusions reached in Figure 4.8 are well corroborated, spirals in unbarred models have a completely different behaviour from all our barred models, both using one million and five million disk particles.

Again and also to ensure the independence on the method used to compute the rotation frequencies, in Figure 4.10 we show the results of applying the spectrogram method in U1 model with a Nyquist frequency of $\sim 100 - 150$ km s^{-1} kpc^{-1}. As we have mentioned in the last section the panels framed in red correspond to the dominant modes discussed above, and they are to compare with the left and right panels of Figure 4.8. In Spectrogram it is also evident that spiral structure in U model has not a rigid rotation but a number of structures at different radii ever overlapped with disk rotation frequency curve. The interpretation of this diagram is not straightforward. Several authors observed similar trends on other unbarred models and some of them pointed not to a single corotating spiral structure as in Grand et al. (2012a) but to several spiral structures with a rigid rotation interacting between them and highly transients (Sellwood 2013). Here we have not a deep study of the nature of these structures as we only point to the difference on the rotation frequency when the system has a central strong bar.

Some important consideration about Figure 4.10 is that the flat structure in the rotation frequency that can be appreciated in the central region of unbarred model (R $<$ 4 kpc, bottom right panel) and which could remind the signature of a weak bar it is not. And it is clear as it corresponds to a $m = 4$ mode, and, actually, the amplitude of the $m = 2$ mode in this region is less than 2% (see Figure 4.5). To make this point clearer we show, in left panel of Figure 4.11, how really looks like the radial profile of B1 Fourier amplitudes when a strong bar is present compared with the right panel where we show same profiles but for U1 unbarred model.

As in barred case we have made a first attempt to find non-linear coupling interactions between the structures of different modes presents in Spectrogram (Figure 4.10). We have not succeed with these attempts and we asses that a deeper analysis like the one done in a similar model by Minchev et al. (2012) (Figure 8) is needed.

4.3.4 Particles motion

From the analysis of the rotation frequencies of spiral arms we have realized that individual particles, not only large scale structures, have a different behaviour depending on the

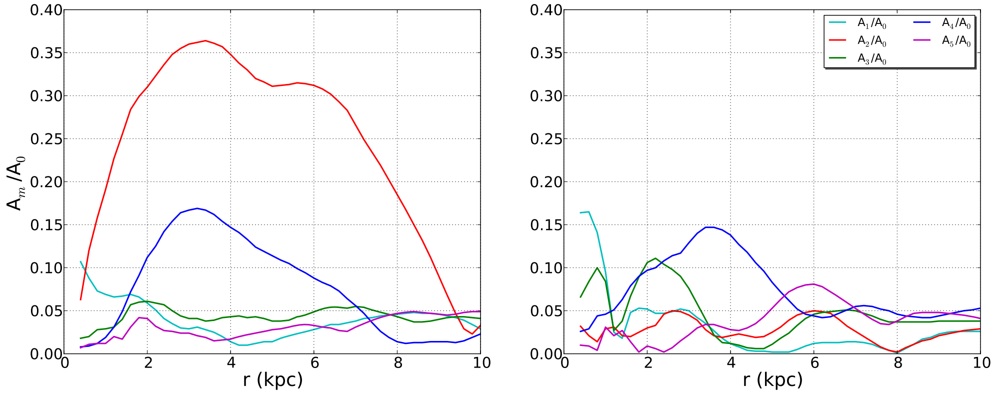

Figure 4.11: Amplitude of m=1 to m=5 Fourier modes as function of radius for a single time instant. The amplitudes have been computed for modes B1 (left) and U1 (right).

presence of a bar. In this section we make a first approach to analyse the particles motion, their relation with the presence of a bar and also if it exist radial migration as detected in works like the ones of Grand et al. (2012a,b). All these processes can give us information about the nature of the spiral arms in our models.

To analyse the particles motion in spiral arms and inter-arm regions in barred and unbarred models we have marked particles that belongs to one of those regions and we have followed them in time. In Figures 4.12, 4.13 and 4.14 we show how particles move in model B5 and in Figure 4.16 in model U1. All figures presented in this section have to be deeply analysed as lot of physical processes are involved in what we observe. To begin with we analyse particle motions in barred models (B1).

Motions in barred models

When we observe carefully Figure 4.12 we see how, as expected, spiral arms are moving faster than disk particles. We state that this happens in our simulations because when new spiral structures appear and marked particles are in the inter-arm region (e.g. panels 13 to 15) these new spiral structures quickly reach their position. Also interesting is that in the time instants when spirals are strong enough (e.g. panels 1-10 and 19-26), some particles seem to be associated with them. When the spirals became fainter and disappear, particles fall into the inter-arm region. One important point here is that the strength of spirals seems to be strongly associated with the bar. Observing the evolution of spirals carefully we see that they seem to grow from the bar. After its formation, at some point, spirals break the connection with the bar and are disrupted within the disk. Next, new ones begin to form again from the bar region. This process of growth of spirals from the bar and also the fact that some particles seem to be trapped into the spirals induces us to think that the mechanism that generates these kind of structures can be, at least in part, the invariant manifolds proposed by Romero-Gómez et al. (2007). Something that also supports the invariant manifold hypothesis is that, when spirals are strong, particles trapped in them mostly move inside their density structure from inner to outer regions . We also observe that disk particles can be captured by spirals and once it happens they also start moving inside (see panels 19-26). Also in accordance with invariant manifold theory some particles may have not the proper kinematic conditions to be trapped by the manifolds although the spirals reach them they continue following the disk rotation. To study deeply this possible connection with manifolds theory we show Figures 4.13 and 4.14. In Figure 4.13 we selected all particles that are placed in the spiral arm region at t=1.125 Gyrs and that according to the manifolds theory they may belong or not to the spiral structure. In this case what we would expect to see when time passes is that some particles, the ones that truly belongs to the spirals, follow the spiral structure, and a second one that is disk population, does not. This is just what we observe in the first panel of Figure 4.13 that shows the origin of particles that are placed in spirals in the central panel. In this panel we distinguish clearly two populations, one associated with the spirals in the central region and other with a high spread all over the disk. The same trend is observed when looking to the last panel that is forward in time, a population that followed spiral arms to the external regions and other that passed through them. In Figure 4.14 we selected particles that truly belong to the spiral arms at t=1.125 Gyrs and we followed them back and forward in time. What we see in this last figure is that without any doubt these particles follow the spiral arm structure from the bar region (first panel) to the external regions of the system (last panel). Similar results as the ones presented here were obtained by Athanassoula (2012). A last test we have done to study particles motion in barred models is shown in Figure 4.15. In this figure we show the mean velocity of particles in the spiral arms reference frame overplotted to density maps and there it is easy to find the bar Lagrange points, that are the ones that drive the manifolds that generates spiral arms. After all our analysis we conclude that there is a great chance that the spiral arms in barred models presented here have a manifold origin. It is important to mention that in such manifold driven mechanism it arises naturally a radial migration of disk particles. What remains unclear from this scenario is which process make the spiral arms break their connection with the bar and makes then the spirals highly transients.

Motions in unbarred models

In unbarred cases where spiral arms corotate with disk particles, we expect a much simple scenario than the one observed for barred models. What we would expect is that if we mark particles spanning a large range in radius they will became winded due to disk differential rotation, ending in a ring like distribution. However this scenario is not taking into account particles velocity dispersions and the presence of spiral arms. In Figure 4.16

we show what happens in reality and it is similar to what we said we would expect. We see that after 1.141 Gyrs of evolution the selected population in panel 1 have been spread at all angles ending in a ring shaped distribution. Moreover, superposed to this general effect we observe how particles also suffered a smaller spread in radius due to radial dispersion and also radial migration as the minimum and maximum radius are far from the original ones. Effect of corotating spiral arms in the radial migration of disk particles has been well studied in Grand et al. (2012a).

4.4 Conclusions

The rotation frequencies of the spiral modes in barred and unbarred models, integrated with different N-body codes (ART and GADGET), and analysed with different techniques (Spectrogram and finite differences), present a well defined different behaviour. Whereas unbarred models show transient arms corotating with disk particles, in good agreement with those recently reported by Grand et al. (2012a) and Baba et al. (2013), barred models deserve further comments. As shown in Figures 4.8 and 4.9, barred models present a spiral pattern speed almost constant in radius for all the range where the spiral structure is dominant in density. These results are consistent with those of models I, II and III in Rautiainen & Salo (1999), computed using a simplified 2D model and with rigid or no halo. We want to emphasize that whereas in those early models it is difficult to detect spiral structures in the configuration space, particularly in the external regions, in our simulations with 1 and 5 million disk particles, the spiral structure is clearly identified (see Figure 4.1), allowing us to use the arm phase in order to test claimed biases in the derivation of the rotation frequencies using Spectrogram (see Section 4.2.2).

It is important to compare our results with those recently obtained by Grand et al. (2012b). The authors have analyzed N-body/SPH simulations of isolated barred galaxies concluding that, spiral arms' pattern speed decreases with radius, closely in corotation with disk particles. Grand et al. (2012b) computed the rotation frequencies averaging the values obtained for several snapshots over two time intervals during spiral arm evolution, one when the bar is well defined in their images ($\sim$ 1 Gyr of evolution, see their Figure 9) and the other when the bar has significantly weakened ($\sim$ 1.5 Gyr, Figure 10). In both cases, the spirals pattern speed is almost corotating with disk particles. The previous result is at odds to what is obtained in our study. However they also noticed a small offset of the spiral arms' rotation frequency profile from being corotating with disk particles, particularly when the bar is stronger, suggesting that further analysis is required. Here we have analyzed the correlation between the strength of the bar and the spiral rotation frequency in our B1 ART model, a Milky Way like simulation. With such a purpose, we have computed arms' rotation frequency during the first evolutionary stages, when the bar is still growing and weak ($A_2/A_0 < 0.1$) at about 0.3 Gyr of evolution. Only when the bar

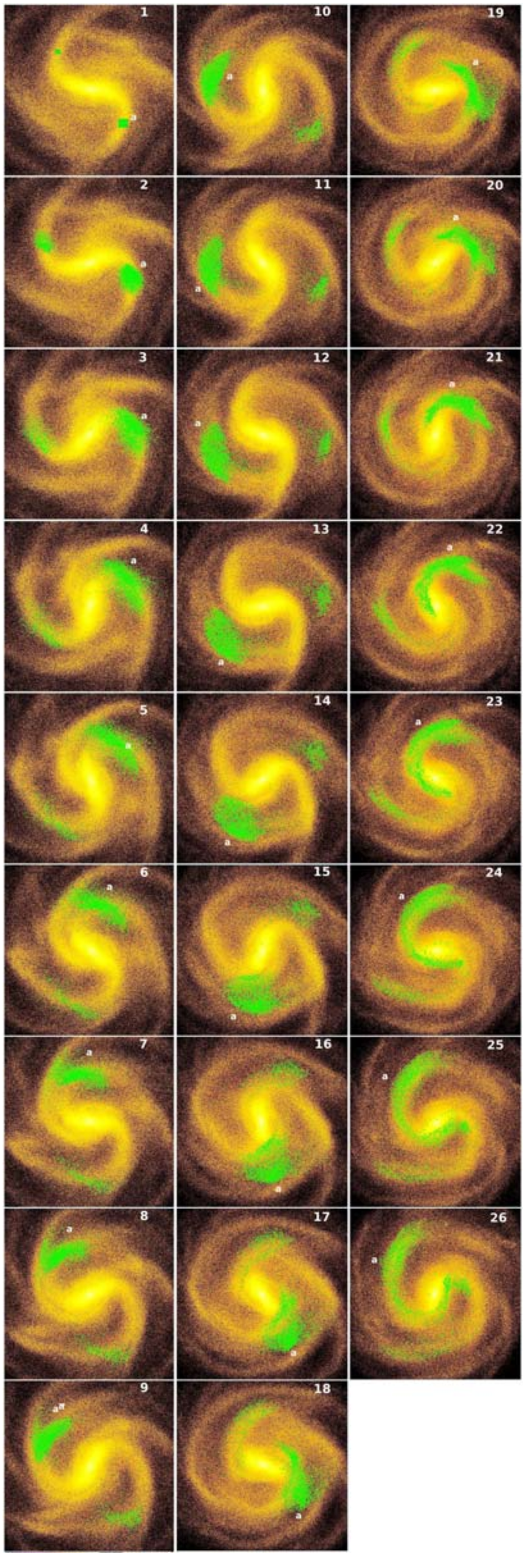

Figure 4.12: Evolution of particles (green) in B1 simulation during 0.725 Gyrs. In orange all disk particles of the simulation. The region named as "a" is the one that best traces the evolution of particles in the simulation.

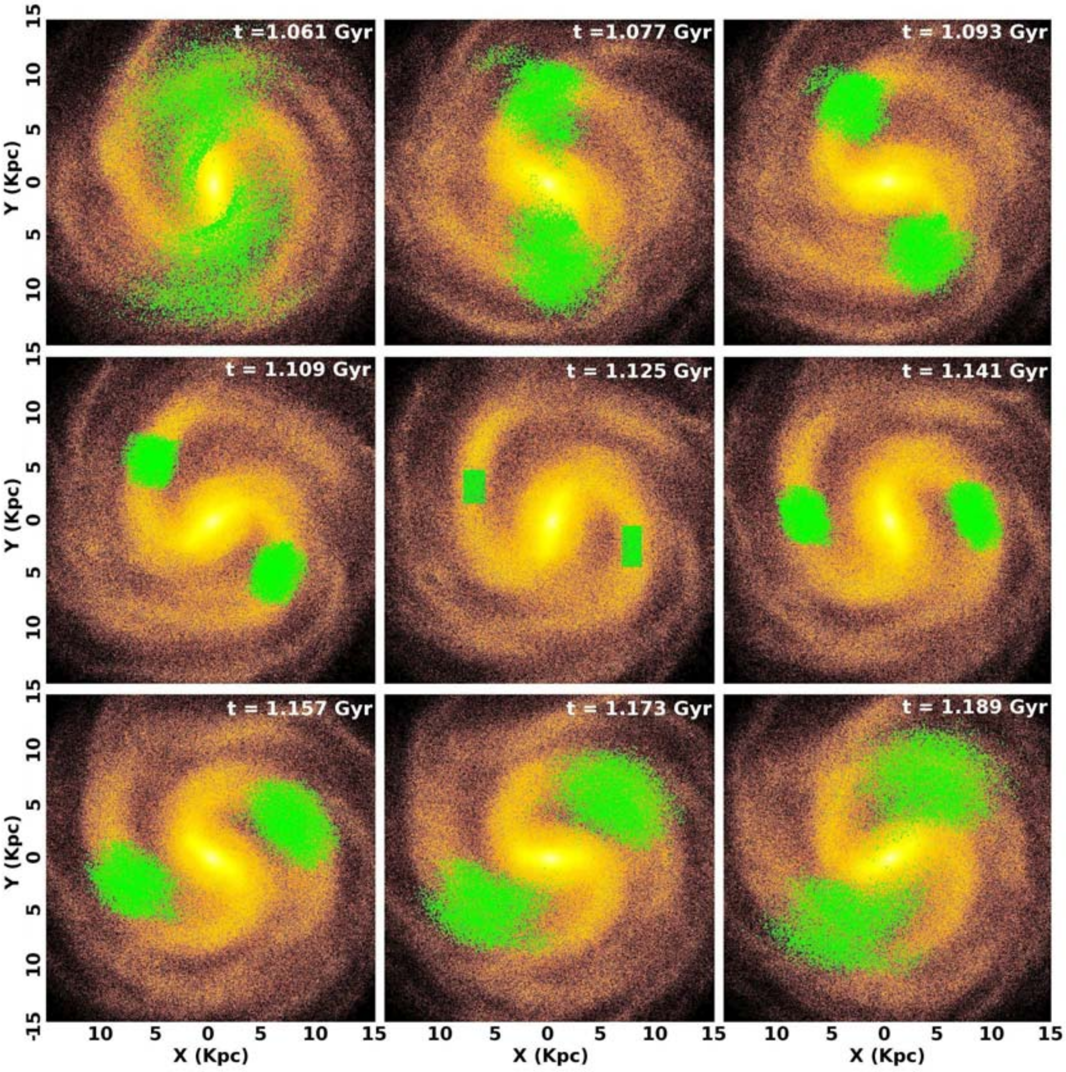

Figure 4.13: Same as in Figure 4.12 but now following particles backward and forward in time, with initial time being at t=1.125 Gyrs (center panel).

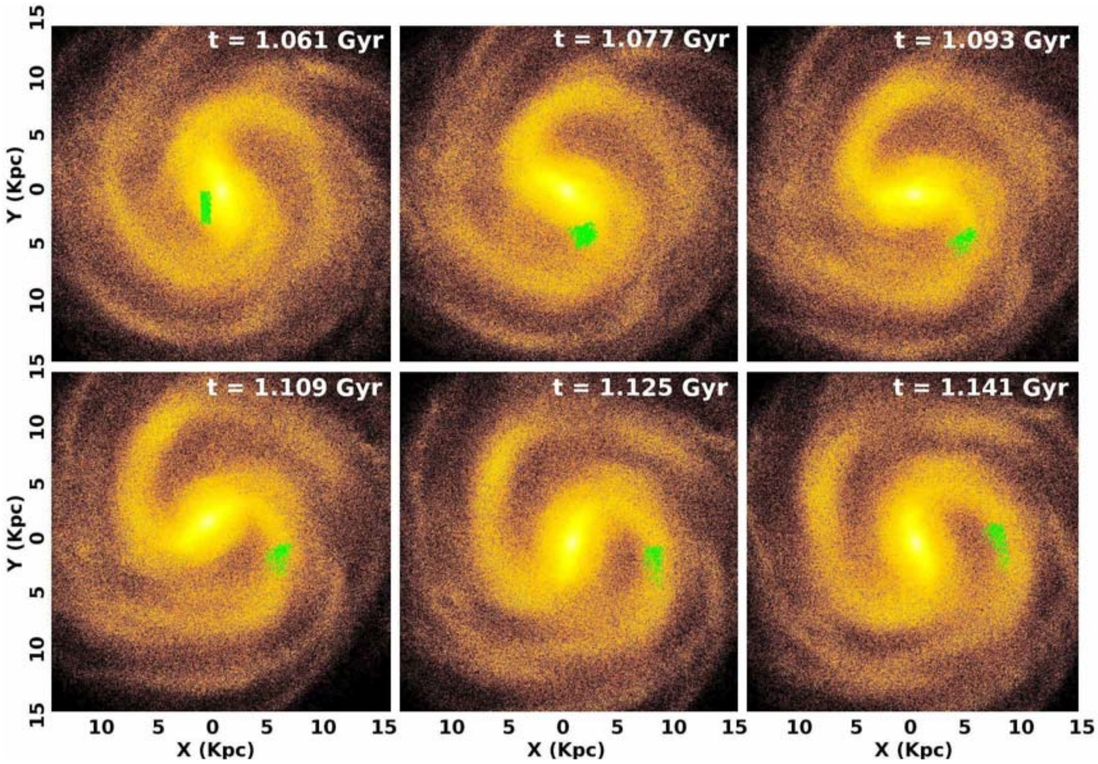

Figure 4.14: Same as in Figures 4.12 and 4.13 but now only for particles selected to be inside the spiral arms at t=1.125 Gyrs as shown in Figure 4.13.

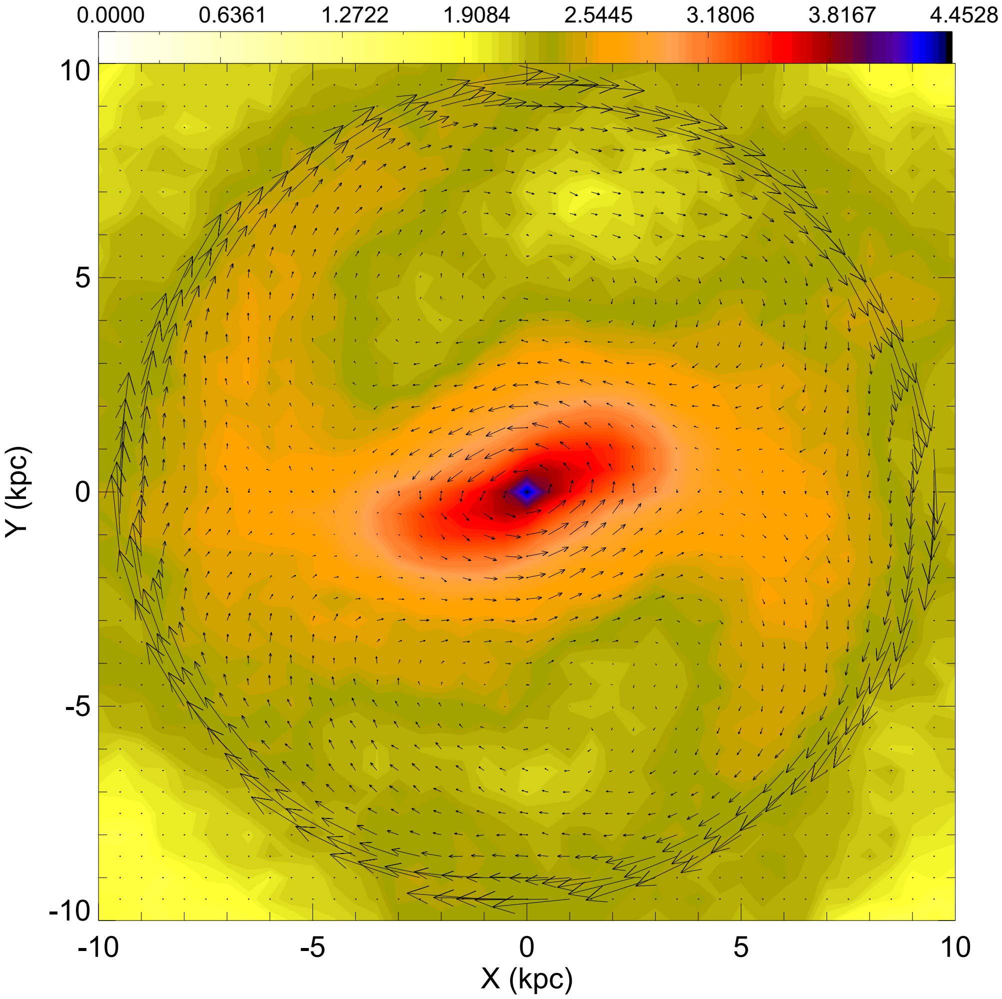

Figure 4.15: Density and velocity map of disk particles in the spiral arms reference frame for model B1 at 1.73 Gyrs of evolution.

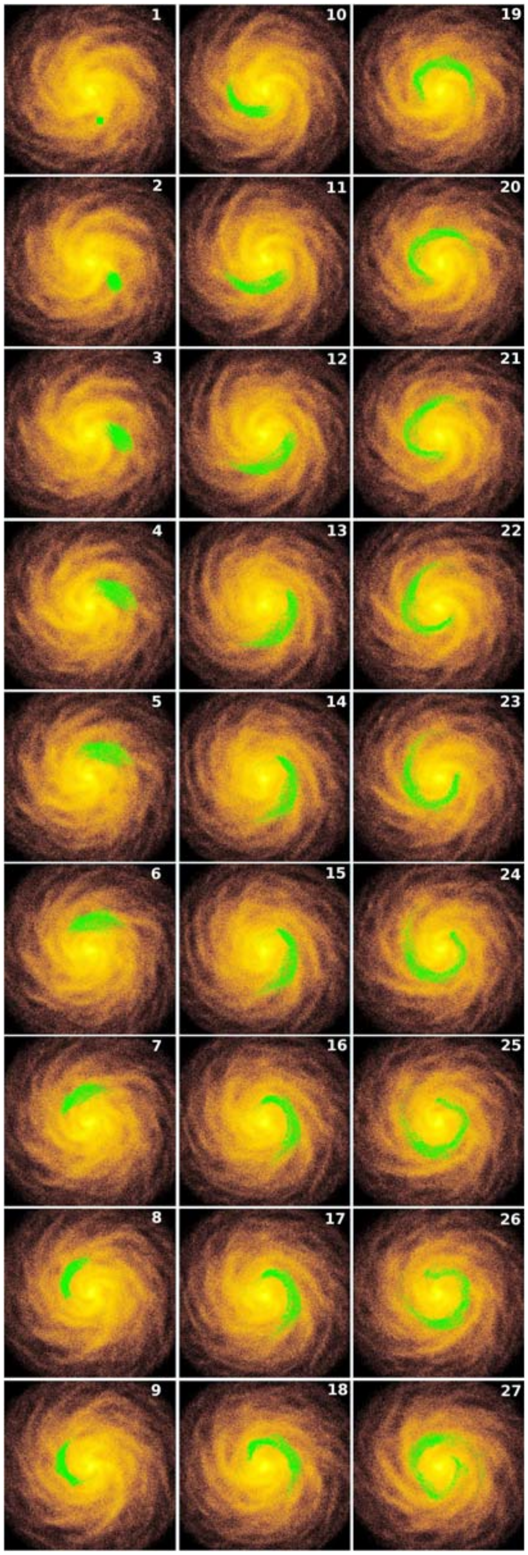

Figure 4.16: Evolution of particles (green) in U1 simulation during 1.141 Gyrs. In orange all disk particles of the simulation.

is weak we observe that the external m=2 mode (bisymmetric arm) rotation frequency is close to disk corotation. After few galactic rotations, when the bar has fully formed ($A_2/A_0 > 0.4$) (as shown in Figure 4.5 left panel), the rotation frequency becomes almost constant, approaching the bar rigid body rotation, if any with a small decrement in radius (see Figure 4.8 and 4.9, left and central panels). This result is qualitative in agreement with the statement discussed by Grand et al. (2012b), unfortunately we do not have information of bar amplitude in Grand et al. (2012b) simulations, and their models assume a gas component making harder a further comparison. We conclude that in barred models the spiral rotation frequency approaches the bar rigid body rotation with the increment of bar strength.

Furthermore, our simulations, with a high number of disk particles, allow us to analyze the behaviour at larger radii $\sim 12-14$ kpc. As can be seen in Figure 4.10 (m=2 mode, left panel second row), the Spectrogram method applied to the B1 bar model shows an external structure, at radii larger than R= 11 kpc, that rotates slower than the density dominant mode. This external structure has a lower amplitude, lower rotation frequency (less than 10 km s^{-1} kpc^{-1}), it is tightly wound, and it is recurrently connected/disconnected with the inner and faster spiral (see movie[1]). Other authors (i.e Sellwood & Sparke 1988) have reported similar structures but apparently they detected them only in the frequency space, probably due to the statistical fluctuations given by their number of particles (see however figure 16 in Rautiainen & Salo (1999)). The lack of detection in configuration space led the authors to conclude that inner fast rotating structures correspond only to the bar structures while the slower and external ones to the entire and unique spiral mode. Here we confirm the detection and the rotation frequency in configuration space (see Figure 4.1) for all these structures, and that the inner fast rotating structure includes both: a bar and an inner spiral structure apparently connected. The slow rotating mode is an external spiral mode. We stress that we also find both structures using the SFpFD method in configuration space. In conclusion, at large radii, and for m=2, we do see the external slow and low amplitude arm coexisting with the dominant spiral mode which is most of the time connected to the bar.

The results presented here for the barred case are also compatible with the observations recently reported by Meidt et al. (2009). They derive rotation frequencies in four spiral galaxies: two strong barred, one unbarred and one with rings. They find that in the two strong barred cases the inner bisymmetric spirals rotate with the same frequency as the bar. Furthermore, one of the barred cases present an external armed structure rotating with a much lower frequency (see their Figures 8 and 12) as it is observed in our B1 barred model. For the other cases they find multiple pattern speeds that can be or not in a resonance coupling situation. It is important to mention that at least one of their barred galaxies is likely in interaction (M101). As discussed by the authors, the limiting

---

[1] This movie can be downloaded from http://www.am.ub.edu/∼ sroca/Nbody/movies/B1.mpeg and it shows the density evolution of model B1, spanning from 0.1 to 3.1 Gyrs. High density regions (~ 3.7 $\mathrm{M}\odot/\mathrm{pc}^3$) are shown in dark-blue colors while zero density ones are in white.

observational accuracy - precision in the radial binning and frequency sampling - do not allow them to confirm or refute the small radial decrement in rotation frequency shown in our Figure 4.8, therefore they conclude that arms in their study are rigid body rotators. Further observations will be required to confirm this tendency.

The study of the motion of individual particles shed some light on the nature of the spiral arms in our models. We observed that in barred models particles move in a way that is highly compatible with an invariant manifold origin for spirals. Moreover the high transient nature of them do not fit well inside the theory and then its origin deserves a further investigation. In the unbarred case particles become winded around the disk due to differential rotation, as expected. We also observe in this last case that corotant spiral arms induce radial migration, result that is in agreement with what was observed by Grand et al. (2012a,b).

From the simulations we have performed it is clear that a difference in the spiral arm kinematics exists between ones triggered by a bar or others by another mechanism, and also that barred models seem to show at least two kinds of spiral arms. Further analysis of the arm nature, and numerical convergence will be undertaken in a future work.

As a summary we confirm that:

- The dominant spiral mode (m = 2) in strong barred models is most of the time connected to the bar. Its rotation frequency is near to the bar solid body rotation, with a small decrement with radius which is more important as the bar amplitude decreases. Arms are corotating with disk particles only for very weak bars.
- Although the dominant spiral disk mode in barred simulations is the one connected with the bar, we observe at least one subdominant slow and winded mode at large radii, using either SFpFD, Spectrogram (see Figure 4.10) and density maps.
- Particles in barred models that are placed inside spiral arms move such a way that is compatible with spirals being induced by invariant manifolds. A solid body rotation for the spirals is also compatible with the one expected from spirals originated by this invariant manifold process.
- In unbarred models the spiral structures are corotating with disk material, in agreement with previous results Grand et al. (2012a).
- Motion of particles in unbarred models also support the fact of having corotant spiral arms and also show that corotant spirals induce radial migration.
- Our results are robust to changes in numerical parameters (time step, spatial resolution, number of particles), mode analysis techniques (SFpFD, Spectrogram, density peak) and also to changes in numerical codes (ART and GADGET3).

In Figure 4.17 we summarize the main results discussed in this section.

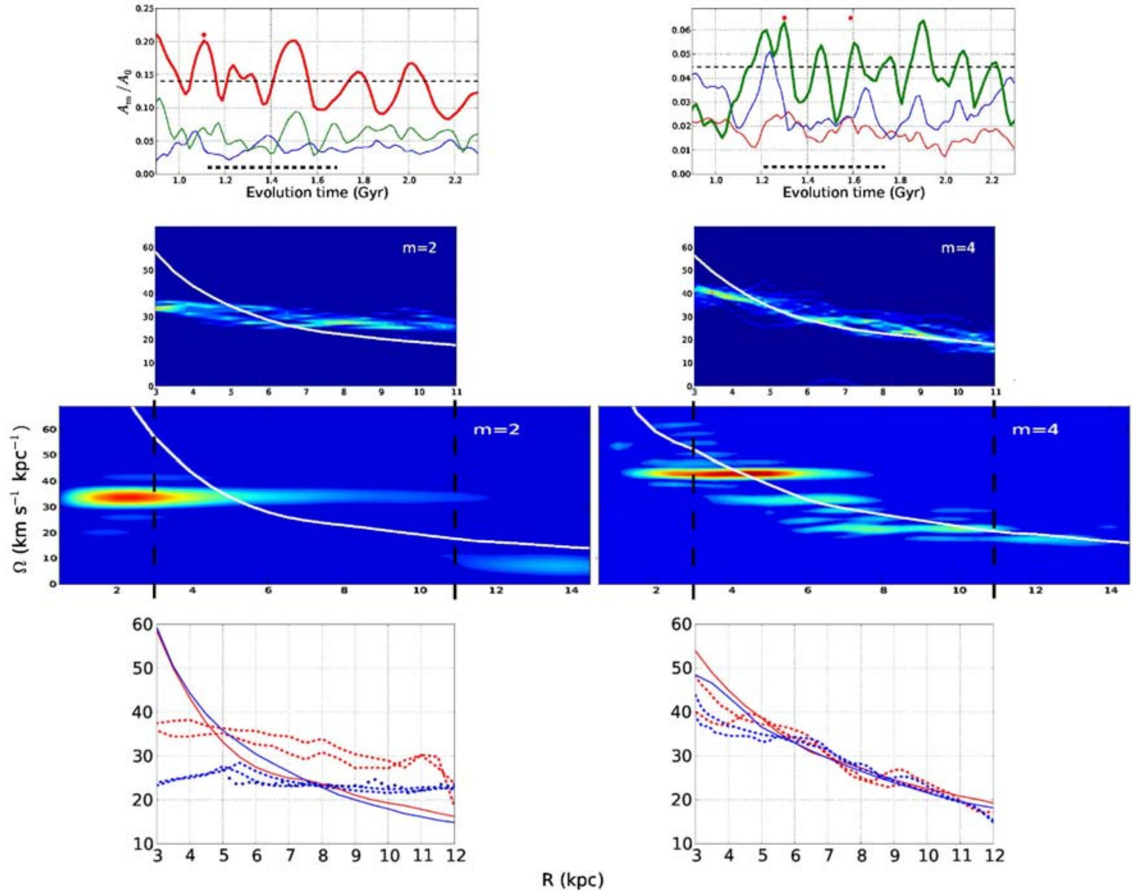

Figure 4.17: Top: Amplitude of Fourier modes m=2 (red), m=3 (blue) and m=4 (green) as function of time for B1 (left) and U1 (right) models. Thin dashed lines indicate the threshold imposed to compute the rotation frequency of spiral arms using SFpFD shown in top-center panels, all time instants above the line have been used. Thick dashed line indicates the temporal range where Spectrogram have been used to obtain the bottom-center panels. Upper dots indicate the time instants from where spiral arm rotation curves plotted in red in the bottom panels have been obtained. Top-center: Rotation frequencies obtained using SFpFD method for B1 (left) and U1 (right) models. White line indicates values of disk rotation frequency. Bottom-center: Rotation frequencies obtained using Spectrogram method for B1 (left) and U1 (right) models. White line indicates the values of disk rotation frequencies. Bottom: Rotation frequencies obtained using SFpFD in B1/U1 and B5 models (red and blue long dashed lines, respectively) and GADGET models (green long dashed lines). Blue dots indicate the spiral arms rotation frequency obtained using Fourier + density peak method for B5 model. Disk rotation frequencies are shown as short dashed lines.

4.4.1 Limitations of the models and future work

The models used in this section are collisionless N-body models of isolated galaxies. As we have mentioned in Section 2.5.4 some processes related to the presence of the collisional component are not being considered here. Also processes related to the interaction of galactic systems with extragalactic medium or with other systems can not be studied in these models. Moreover results obtained in this section have been confirmed in works where the collisional component is implemented in the SPH approach (Grand et al. 2012a,b).

From the work presented here a lot of new question arise. For instance the formation and the transient nature of the spiral arms is still misunderstood. Next step after finishing this work will be to study processes that lead spiral arms in barred models to break their connection with the bar. Another interesting study we deserve for the future is to deeply analyse Spectrogram obtained for all Fourier modes presented in Figure 4.10, looking for possible scenarios of non-linear coupling.

In this work we have generated a set of high quality N-body models that can be used for a large variety of studies. Some of them can be used to reinforce our conviction that our results are code independent or to answer questions such as: What happens with spiral arms that are originated by the interaction with other systems like satellite galaxies? Are they similar to the unbarred, to the barred systems or it depends on the properties of both systems? How many of these interacting systems develop a bar and later on spiral arms from it? How is their rotation frequency? Is the ratio between disk mass and halo mass important in such scenario of interactions in therms of bar formation? We hope that also from sharing these models we will be able to establish new collaborations in where squeeze them the maximum.

Finally, a natural question that arises is to ask which is the situation for the MW: Do the traditional spiral arms correspond to the mode coupled with the bar? or instead correspond to the modes we observed at larger radii? or both? Planned and current surveys measuring stellar kinematics and distances inside our Galaxy as Gaia (ESA) or APOGEE (SDSS) will open up the possibility of direct estimation through methods like the one proposed by Tremaine & Weinberg (1984). Spectroscopic high resolution surveys of external galaxies like CALIFA (Sánchez et al. 2012) or MANGA(AS3/SDSSIV) will contribute to test our predictions using stellar kinematics.

5

A novel method to bracket resonance radius

5.1 Introduction

It is well known both from simulations and observations that the large scale structures in galaxies such as bars and spiral arms strongly affect the stellar kinematics of their disks. One of the properties of such structures that is most relevant for the disk dynamics is their pattern speed which sets the position of the resonance radius. Rautiainen et al. (2008) have exhaustively reviewed the methods usually applied to external galaxies to derive this information. Some of these methods are model independent techniques such as the so-called Tremaine & Weinberg (1984) method, whereas others are parametric - they fit several given analytical potential components to observations (i.e. Zhang & Buta 2007) - or based on the relation of various morphological or photometric features with resonances (e.g. Martínez-García et al. 2009). The model dependent methods are based on several assumptions, being one of the most critical the adoption of a model for the spiral arm kinematics (the density wave theory is usually imposed). In addition to these methods, and thanks to the new detectors available, kinematic methods based on the analysis of the residual pattern in the velocity field, have been used by Canzian (1993) and recently by Font et al. (2011). With these methods, a residual velocity map allows the exploration of the resonant structure of the galactic disks but, again, they require the removal of circular velocities (previous knowledge of the galactic rotation curve) and, up to now they have been applied only to the gas component.

Focusing in our Milky Way galactic disk, the corotation radius (CR) of the spiral pattern is still a controversial parameter. Without intending to be exhaustive, CR has been

estimated, for example, by applying techniques such as the Ogorodnikov-Milne Model to the Local Stellar System Kinematics of young Hipparcos stars (Fernández et al. 2001) or by evaluating the change of the kinematic substructures of the velocity field (usually named as moving groups) in test particle simulations (e.g. Chakrabarty 2007; Antoja et al. 2011). Related to this, the distribution of the fine structure in the velocity space has been used to study bars and spiral arms morphology and dynamics both from solar neighbourhood observational data (e.g. Dehnen 2000) and from more extended RAVE data (Antoja et al. 2013; Monari et al. 2014). All these methods require, again, the adoption of a model for the bar or spiral arm potential.
At the eve of the Gaia era, new methodologies have to be set up for such analysis in our Galaxy. Our aim here is to analyze deeply the connection between resonant radius and the moments of the stellar velocity distribution function. This link will open up new avenues for a model independent kinematic method to determine CR. In this context, Vorobyov & Theis (2006, 2008) demonstrated, from simulations, how second order moments of the stellar velocity distribution can be potential tracers of large scale structures such as the spiral arms in galactic disks (see Figure 5.1). As known, the velocity ellipsoid in axisymmetric systems is oriented with the radial and azimuthal axis of the galaxy. The misalignment of this ellipsoid, known as vertex deviation (l_v, see Equation 5.2), provides important information on the non-axisymmetric components. Following that pioneer work, in this chapter we will focus on the analysis of the l_v all through the galactic disk, postponing for further investigations the use of higher order moments or even the reanalysis of first order moments, that is the mean residual velocities. This results have been reported in Roca-Fàbrega et al. (2014).

The misalignment of the velocity ellipsoid in the solar neighbourhood was initially reported by Strömberg (1946). The determinations of the l_v in the solar neighbourhood from Hipparcos data are around 30 deg for early-type stars and 10 deg for old-disk stars (Dehnen & Binney 1998). More recent measurements give values around 20 deg, using late type stars from SDSS (Fuchs et al. 2009). Several possible causes for this non null l_v have been proposed, most of them related, as mentioned, to the non-axisymmetric components (bar and spirals). These non-axisymmetric components can create patterns in the velocity field that change the shape and orientation of the velocity ellipsoid. Furthermore the existence of fine kinematic substructure (moving groups) may also change the moments of the velocity distribution function (Binney & Tremaine 2008). This kinematic substructure can consist of groups of young stars still following similar orbits from the time when they were born or can be caused by the resonances of the non-axisymmetries of the Galaxy for example through mechanisms such as resonant trapping or scattering (e.g. Antoja et al. 2009).

The possible connection of l_v with the spiral structure was early discussed by Woolley

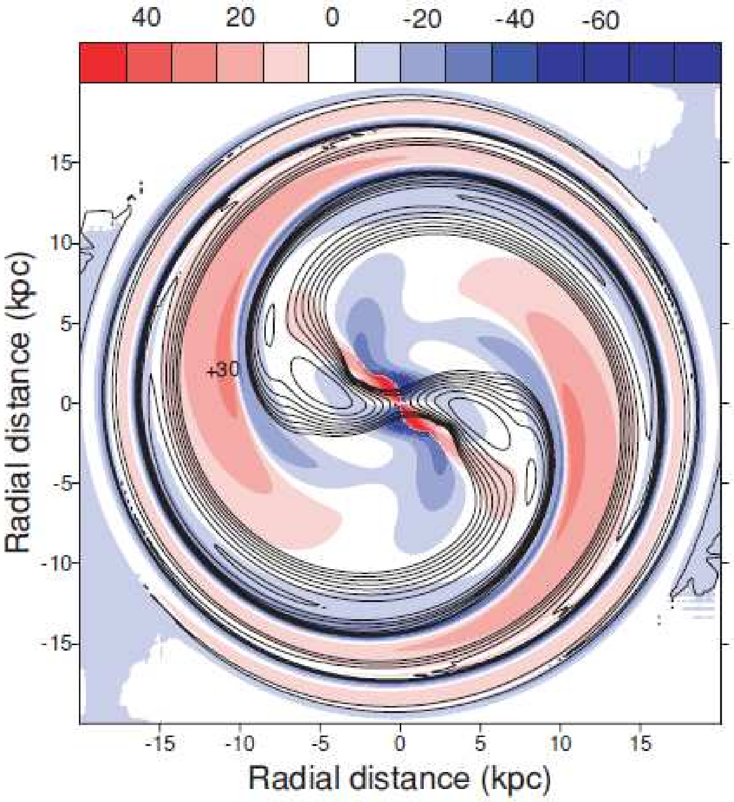

Figure 5.1: Vertex deviation color map from the semi-analytical model presented in Vorobyov & Theis (2006). Red colors indicate positive and blue negative l_v values. Contour lines indicate the position of density structures.

(1970) and Mayor (1970). The former concluded that l_v is a remnant of the conditions of stars when they were formed, mostly based on the fact that l_v is observed in young stars but not so clearly in the old populations. The latter used the analytical expressions of the density wave theory from Lin et al. (1969) to quantify this effect in the solar neighbourhood. He derived analytically the second order moments of the velocity distribution function by considering a Galactic system composed of an axisymmetric part and a spiral perturbation and using the zero and first order moments computed by Lin et al. (1969). In particular, the Tight Winding Approximation (TWA hereafter) was imposed. As described by Binney & Tremaine (2008), the TWA spiral arms model is the result of using the WKB approximation used in quantum mechanics. In Mayor (1970), the epicyclic approximation was adopted and velocity dispersions were assumed to be small (valid for a young and cool population). Furthermore, his analytical approach required a small amplitude and pitch angle of the spiral pattern (i.e. the TWA shall be fulfilled). Later on, Hilton & Bash (1982) reproduced the observed l_v sign and magnitude for young stars with a model where dense molecular clouds are launched from spiral arms at post-shock velocities, and as a consequence, the forming stars move at the same velocities. Coming back to the analytical approach, Kuijken & Tremaine (1994) found how elliptical potentials could also lead to a non-vanishing l_v and tested their results using orbital integrations. Muhlbauer & Dehnen (2003) and Monari et al. (2013) showed that a barred potential induces different l_v, depending on the position with respect to the bar and its main resonances. They also found that the l_v increases with decreasing velocity dispersion.

As discussed above, Vorobyov & Theis (2006, 2008) computed the moments of the velocity distribution function across the disk in both test particles simulations, imposing a spiral arms' potential, and in spiral arms' semi-analytical models (with the so called BEADS-2D code). In this study they found a clear correlation between the position of the density structures (i.e. the spiral arms) and the change of the sign of the l_v. They saw that large regions with positive l_v are present in front of the spiral arm (following the spiral rotation), while negative l_v were found behind the arms. In their analysis, however, only cases where the spiral structure is located outside CR were considered.

Here we map the l_v caused by the spiral arms in the whole galactic disk. To undertake our study we use: i) an analytical approach, ii) test particle simulations imposing a fixed 2-armed galactic potential or a bar; and, iii) self-consistent N-body simulations. First, in our analytical development, we extend the modelling of Mayor (1970) to analyse the expression for the l_v in the TWA model not only locally, as he did, but across the whole disk. Second, the use of test particle simulations allows us to control the parameters of the imposed potential and to explore the parameter space and its influence on the results. For example, we can fix the position of the spiral pattern resonances at our convenience and monitor the behaviour of the l_v inside or beyond CR, which was not addressed in previous studies. Besides, we also use simulations where the spiral arms are formed as a response to an imposed barred potential. Finally, N-body simulations, used here for the first time

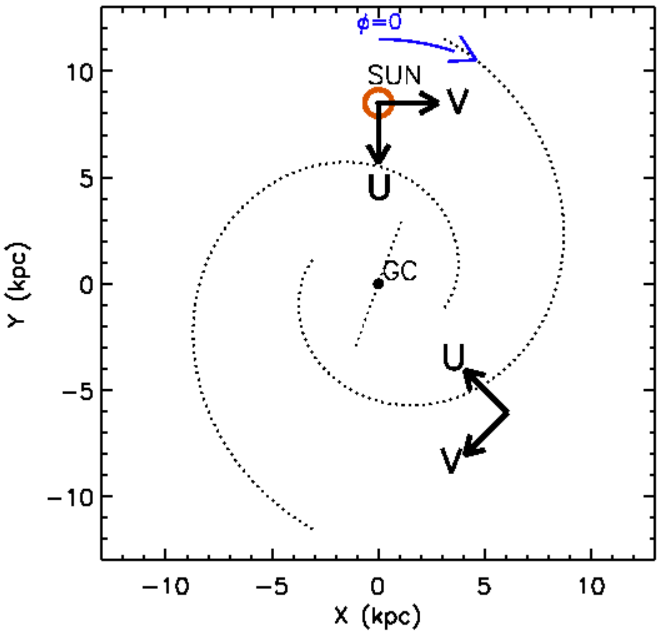

Figure 5.2: Definition of U, V galactocentric velocities used in this work.

to map the l_v, provide a more realistic framework because they are fully self-consistent. These simulations also allow us to analyse the evolution in time of l_v.

5.1.1 Moments of the velocity distribution function

The velocity distribution function of a system of particles can be well characterized by its moments. In this section we give the analytical expression of these parameters and also show how from them we obtain the vertex deviation. In all this work we use the radial galactocentric velocity U as the velocity component that is directed towards the galactic center, the tangential galactocentric velocity V as the one that is positive in the direction of rotation (see Figure 5.2) and the vertical galactocentric velocity W as the one perpendicular to the plane and directed to the north galactic pole.

Moments

The velocity dispersion tensor that defines the (p, q, r)th centered moments of the velocity distribution at position $\mathbf{x}$ and time t is defined as:

$$\mu_{pqr} = \frac{1}{\mu_{000}} \int d^3\mathbf{v}\, (u - \bar{u})^p\, (v - \bar{v})^q\, (w - \bar{w})^r\, f, \tag{5.1}$$

with $\mathbf{v} = (u, v, w)$ where u, v and w denote, respectively, the radial, azimuthal and vertical velocity components and $f = f(\mathbf{x}, \mathbf{v}, t)$ is the velocity distribution function.

Vertex deviation

The vertex deviation (l_v) is the angle that measures how the velocity ellipsoid, in the U-V plane, is tilted with respect to the orientation of an axisymmetric configuration (see Figure 5.3); it is related to a non null value of the cross correlation coefficient μ_{110}. Here we use the extended definition presented in Vorobyov & Theis (2006) that includes the possibility of having large l_v (Equation 5.3), which happens when breaking the epicyclic approximation locally in regions where the spiral gravitational potential is strong:

$$\tilde{l}_v = \frac{1}{2}\mathrm{atan}\left(\frac{2\mu_{110}}{\mu_{200} - \mu_{020}}\right) \tag{5.2}$$

$$l_v = \begin{cases} \tilde{l}_v & \text{if } \mu_{200} > \mu_{020} \\ \tilde{l}_v + \mathrm{sign}\left(\mu_{110}\right)\frac{\pi}{2} & \text{if } \mu_{200} < \mu_{020} \end{cases} \tag{5.3}$$

We computed the error on l_v (denoted by ϵ_{l_v}) as the propagation of errors in the second and fourth order moments (Nunez & Torra 1982):

$$\begin{aligned}
\epsilon_{l_v} &= \left| a_4 \sqrt{b_1 + a_1 b_2 + b_3 \left[\frac{\mu_{220}}{N} + \mu_{110}^2 a_2 + \mu_{200}\mu_{020} a_3\right]}\right| \\
a_1 &= 2\left(N-1\right)^{-1} - 3N^{-1} \\
a_2 &= \left(N-1\right)^{-1} - 2N^{-1} \\
a_3 &= \left(N-1\right)^{-1} - N^{-1} \\
a_4 &= \left(\mu_{110}\left(a_1 + 4\right)\right)^{-1} \\
b_1 &= \left(\mu_{400} + \mu_{040}\right) N^{-1} \\
b_2 &= \left(\mu_{200}^2 + \mu_{020}^2\right) \\
b_3 &= \left(\mu_{200} - \mu_{020}\right)^2 \left(\mu_{110}\right)^{-2}
\end{aligned} \tag{5.4}$$

This expression takes into account the fact that the error is larger both, when the number of particles is low - due to Poisson noise - and when the velocity ellipsoid is nearly circular so the major axis of the velocity ellipsoid is not well defined.

5.2 Methodology

Here we present our analytical development as well as the characteristics of the simulations we have used in our analysis.

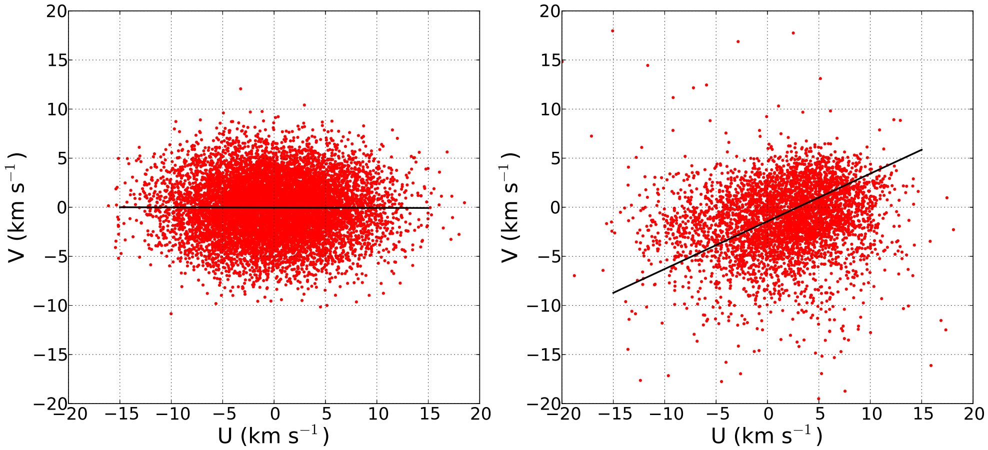

Figure 5.3: Left: U-V velocity plane of an axisymmetric distribution of particles. Right: The same as at left panel but for a non-axisymmetric distribution. Black line show the position of the semimajor axis of the velocity ellipsoid. The tilt on this semimajor axis with respect to the horizontal line is the so named vertex deviation parameter.

5.2.1 Analytical approach

We have derived the analytical expression for the vertex deviation $l_v(r, \theta)$ of the velocity distribution function proposed by Lin et al. (1969). This consists of a perturbed classical Schwarzschild distribution, where the perturbation is the result of a m-armed Lin & Shu (1964) spiral arm. The final expressions are a generalization of the expressions by Mayor (1970). We use these expressions to map the l_v values across the whole galactic disk.
As input parameters we have used a spiral arms' rotation frequency of 35 km s^{-1} kpc^{-1}, a pitch angle of 8 deg, a mass of 5% of the disk mass, a radial velocity dispersion of 20 km s^{-1}, constant with radius, and a disk rotation curve derived from the axisymmetric Galactic model of Allen & Santillan (1991). The CR in this model is placed at 6.2 kpc and the OLR at 10.2 kpc, while the ILR does not exist. The amplitude of the spiral arms potential declines in radius as $\propto$ r exp$(-r/R_\Sigma)$ with a radial scale length of R_Σ=2.5 kpc. We use an amplitude normalization (A_{sp}) of 850 km^2 s^{-2} kpc^{-1}. The locus of the spiral is an m=2 logarithm that starts at 2.6 kpc.
The assumptions we have used to obtain the final expression are:

- The velocity distribution is a Schwarzschild distribution plus a small perturbation.
- The spiral arms have low amplitude.
- The spiral arms have small pitch angle.
- Velocity dispersions are low.

- Epicyclic approximation can be used.

In Appendix 2 we detail computations we have made to obtain the expression for the vertex deviation shown in Equation 5.5.

$$
\begin{aligned}
\frac{1}{2}\tan\left(2l_v\right) &= \frac{\tilde{\mu}_{110}}{\tilde{\mu}_{200}-\tilde{\mu}_{020}} = \\
&= \frac{\frac{Re(i\vartheta_1)}{\gamma}D_\nu^{(1)}(x) - V_\varpi V_\theta \frac{\sigma_*}{\sigma_*^0}}{\left(\sigma_\varpi^2 - Re(\vartheta_1)\right)\left(1-\frac{1}{\gamma^2}\right) + Re(\vartheta_1)\left(D_\nu^{(2)} - \frac{D_\nu^{(3)}}{\gamma}\right) - \left(V_\varpi^2 - V_\theta^2\right)\frac{\sigma_*}{\sigma_*^0}}
\end{aligned}
$$

where:

$$
\begin{aligned}
D_\nu^{(1)}(x) &= x\frac{\nu\pi}{\sin\left(\nu\pi\right)}\frac{1}{2\pi}\int_{-\pi}^{\pi}\sin\left(\nu\alpha\right)\sin\alpha\left(1+\cos\alpha\right)\exp^{-x(1+\cos\alpha)}\,d\alpha \qquad (5.5)\\
D_\nu^{(2)}(x) &= \frac{\nu\pi}{\sin\left(\nu\pi\right)}\frac{1}{2\pi}\int_{-\pi}^{\pi}\cos\left(\nu\alpha\right)\left(1-x\sin^2\alpha\right)\exp^{-x(1+\cos\alpha)}\,d\alpha\\
D_\nu^{(3)}(x) &= \frac{\nu\pi}{\sin\left(\nu\pi\right)}\frac{1}{2\pi}\int_{-\pi}^{\pi}\cos\left(\nu\alpha\right)\left(1-x-2x\cos\alpha-x\cos\alpha^2\right)\exp^{-x(1+\cos\alpha)}\,d\alpha
\end{aligned}
$$

5.2.2 Simulations: Test particles

We have run test particle simulations using several galactic potentials. Potentials used here are the result of a superposition of an axisymmetric part plus spiral arms or bar components. In all cases, the axisymmetric component is the one described in Allen & Santillan (1991) and consists of the superposition of analytical and time independent bulge, disk and halo potentials. Here we analyze separately the non-axisymmetric components of the potential (imposed bar or imposed spirals) to avoid a more complex scenario when interpreting the connection of density structures with the l_v.

Parameters of our basic models and characteristics of our simulations are presented in Table 5.1. In this table we show for each model some of the main properties of the potential, the number of particles and the total integration time. The number of particles in all cases is around or much higher than $5{\cdot}10^6$ and the integration time from about 5 to 20 rotations of the non-axisymmetric structure. Whereas with large integration times the test particles have reached approximately total statistical equilibrium with the galactic potential, for shorter times the particles may not be completely relaxed or face-mixed. Nonetheless, by analysing snapshots with higher and lower evolution times, we tested that results presented in Section 5.3 are independent on the integration time.

Spiral arm potentials

We use two different types of spiral arm potentials, namely the TWA (Lin et al. 1969; Binney & Tremaine 2008) and the PERLAS (Pichardo et al. 2003) models, which are both described in Antoja et al. (2011). These simulations are for 2D disks. As initial conditions we have used an axisymmetric Miyamoto-Nagai disk density profile. The initial velocity field has been approximated using the moments of the collisionless Boltzmann equation, simplified by the epicyclic approximation with a local normalisation of $\sigma_u(\mathrm{R}_\odot)$=20 kms^{-1} (for more details see Antoja et al. 2011). According to Aumer & Binney (2009) this value corresponds to a young population of late B, early A type stars. We refer to these initial conditions as ICMN20. In some cases we have used a set of simulations that were generated for other purposes (see Antoja et al. 2011). In this simulations an initial 2D exponential density distribution as in Hernquist (1993) was used, and we have named this initial conditions as IC2. Finally, to test the independence of results on the initial conditions we have made some models changing only the radial velocity dispersion at Suns' position, we have named them ICmys10.

The simulations named TWA1, TWA2 and TWA3 are our basic models. The non axisymmetric component of the potential have been introduced abruptly from the beginning. Particles have been then integrated during 5 spiral arm rotations. We have also produced experiments increasing adiabatically the spiral arms and we have noticed that for the pitch angle and spiral arms mass ratio employed here, the effect of introducing the arms impulsively (from t=0) or adiabatically, is negligible. The parameters that fix the TWA potential are the amplitude of the cosine perturbation $A(R) = -A_{sp} R \exp(-R/R_\Sigma)$, the radial scale length R_Σ, the number of spiral arms m, its initial phase ϕ_0, its locus $g(r)$, which in turn depends on the pitch angle i, and the radius at which the spiral arms begin R_{sp} (see Antoja et al. 2011). Here we have used A_{sp}=850 km^2 s^{-2} kpc^{-1}, R_Σ=2.5 kpc, m=2, ϕ_0=0, R_{sp}=2.5 kpc, and $g(r) = -2/\tan(i)\ln(r/R_{sp}) + \phi_0$. The pattern speed for TWA1 (TWA2 and TWA3, respectively) is fixed to 20, (35 and 50, respectively) km s^{-1} kpc^{-1} and it is assumed to be constant at all radii. As known a change on this parameter directly produces a change in the CR. This lets us study differences on the l_v values inside or outside CR. Note that TWA2 has very similar parameters to the ones set in our analytical approach of Section 5.2.1.

Apart from the main models (TWA1, TWA2 and TWA3) we have performed several more simulations only changing one of the parameter each time (see boldface parameters in Table 5.1). This is to test the independence of our results on the most critical parameters: spirals amplitude, pitch angle, initial velocity dispersions of the test particles, angular speed of the pattern and total integration time are the parameters we have changed in these test models. In particular, we have scanned the values of 8 to 15 deg for the pitch angle, 600 to 1300 km^{2}s^{-2}kpc^{-1} for the TWA amplitude, 10 to 40 kms^{-1}kpc^{-1} for the radial velocity dispersions and 2 to 7 spiral rotations for the integration time.

The PERLAS model is a density distribution based potential for the spiral arms. In this case, unlike the very simple spiral arms mathematical approximation represented by the TWA model, PERLAS is formed, like bricks in a building, by inhomogeneous oblate spheroids, simulating beads on a necklace (from there the acronym). This model presents

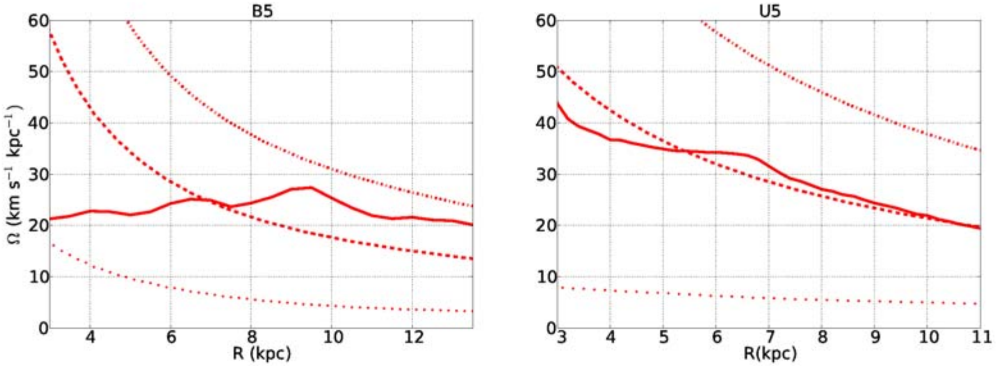

Figure 5.4: Disk (red dashed) and bar and spiral pattern (red solid line) rotation frequency as a function of radius for the N-body model B5 (left) and U5 (right). The ILR and OLR curves are shown as red dotted and red dot-dashed, respectively.

more abrupt gravitational potential and forces (see figures 7 and 8 in Antoja et al. 2011). We have run two PERLAS models. Model PER1 has a set of parameters selected so that the spiral arms are comparable to TWA2 in terms of pitch angle (8 deg) and pattern speed (35 $\mathrm{kms}^{-1}\mathrm{kpc}^{-1}$). However, they produce a smaller force. This can be quantified with the parameter $Q_t(R)$ which measures the maximum azimuthal force in a given radius scaled to the axisymmetric force at that radius. While at a characteristic radius of 8 kpc this parameter is 0.005 for PER1, it is 0.017 for TWA1, TWA2 and TWA3. For model PER2 we used the same initial parameters as in PER1 but a pitch angle of 15.5 deg. instead of 8 deg. and the pattern speed is fixed to 20 $\mathrm{kms}^{-1}\mathrm{kpc}^{-1}$. Because of the larger pitch angle, the torque produced by PER2 is higher than for PER1 and it has a parameter Q_t at 8 kpc of 0.020, which makes it more similar in terms of force to the previous TWA models.

Barred potentials

We have selected barred potentials that generates a spiral arm structure as a response. Several tests have been performed using Ferrers and Quadrupole bars. As initial conditions we have used a 3D axisymmetric Miyamoto-Nagai density profile with a radial velocity dispersion at the Suns' position of $\sigma_u(\mathrm{R}_\odot)$=30 kms^{-1} and a scale height value of h_z=300pc. According to Binney & Tremaine (2008) and Robin & Creze (1986), these values would correspond to a hot population of Red Clump K giants. We refer to this set of initial conditions as ICMN30.

The characteristics of the bar potential presented here (FBar) can be found in Romero-Gómez et al. (2011). As this model has been developed to be compared with the Milky Way its main parameters are fixed within observational ranges for the Milky Way bar (see Romero-Gómez et al. 2011). The model is a superposition of two bars in order to obtain a boxy/bulge type of bar. For the COBE/DIRBE bulge we set the semi-major

Model	i (deg)	Initial Conditions	N (10^6)	Ω_b ($\mathrm{kms^{-1}kpc^{-1}}$)	R_{CR} (kpc)	t_{int}
TWA1	8	ICMN20	5	**20**	**10.2**	5 rot.
TWA1.1	**15**	ICMN20	5	20	10.2	5 rot.
TWA1.2	8	ICMN20	5	20	10.2	**2 rot.**
TWA1.3	8	ICMN20	5	20	10.2	**3 rot.**
TWA1.4	8	ICMN20	5	20	10.2	**6.67 rot.**
TWA2	8	ICMN20	5	**35**	**6.2**	5 rot.
TWA2.1	8	**IC2mys10**	5	35	6.2	5 rot.
TWA2.2	8	ICMN20	5	35	6.2	5 rot.
TWA3	8	ICMN20	5	**50**	**4.04**	5 rot.
TWA3.1	8	**IC2mys10**	5	50	4.04	5 rot.
PER1	8	ICMN20	4.3	35	6.2	5 rot.
PER2	**15.5**	IC2	4.8	20	10.2	5 rot.
FBar	-	ICMN30	80	50	4.04	18 rot.
B5	-	-	5	22	7.7	1.2 Gyr
U5	-	-	5	-	-	1 Gyr

Table 5.1: Parameters of test particle and N-body simulations. TWA, PER and FBar are test particle models with imposed cosine spiral arms, PERLAS spiral arms and Ferrers' bar potential, respectively (see Section 5.2.2). B5 and U5 are two snapshots from different N-body simulations (see Section 5.2.3). The i values refer to the pitch angle of the imposed spiral structure, Ω_b the pattern speed of the perturbation, R_{CR} its CR and t_{int} the integration time of the simulation. Bold faced highlights parameters that departs from the three TWA main test particle models (i.e. TWA1, TWA2 and TWA3).

axis to $a = 3.13$ kpc and the axes ratios to $b/a = 0.4$ and $c/a = 0.29$. The mass is $M_{bul} = 6.3 \times 10^9\, M_\odot$. The length of the other bar, that is a Long bar, is set to $a = 4.5$ kpc and the axes ratios to $b/a = 0.15$ and $c/a = 0.026$. The mass of the bar is fixed to $M_b = 3.7 \times 10^9\, M_\odot$. This bar is introduced adiabatically and its mass is subtracted from the one of the Allen & Santillan bulge (Romero-Gómez et al. 2011). The total mass is, therefore, $M_b = 10^{10}\, M_\odot$. In this case, the bar rotates at a constant pattern speed of 50 $\mathrm{kms^{-1}kpc^{-1}}$.

5.2.3 Simulations: Collisionless models

The N-body simulations we use here are the ones presented in Chapter 4 as B5 and U5 models. All of them include a live disk and live halo but not a gas component (Valenzuela & Klypin 2003). B5 model has an effective number of particles of nearly 400 million, 5 of them in the disk. We built the model ensuring the formation of a strong bar and a bisymmetric spiral associated to it. U5 model is similar to B5 but has a heavier disk and a smaller halo, which inhibits the bar formation. As a consequence, in the U5 simulation a multi-armed structure dominates, and resembles a late type galaxy with transient high m spiral waves. Simulations like the ones used here have been long tested to avoid numerical effects (see Valenzuela & Klypin 2003; Avila-Reese et al. 2005; Klypin et al. 2009).

Figure 5.4 shows the rotation frequency of the disk particles and the spiral arms dominant mode (red dashed and red solid line, respectively), and the ILR and OLR curves (red dotted and red dot-dashed, respectively). The rotation frequency has been computed using the method described in Chapter 4. Basically we find the spiral density structures using Fourier analysis and later on we compute the rotation frequency from a finite differentiation of three consecutive snapshots of the simulation. In the B5 model a strong bar is present up to 7.7 kpc that is where the spiral arm structure begins. Figure 5.4 left panel shows how the bar (that ends at CR$\sim$7.7 kpc) and the spiral arms rotate at the same nearly flat rotation frequency ($\Omega = 24 \pm 3$km s^{-1} kpc^{-1}). In the U5 model the dominant mode is the m=4 and as it can be seen in right panel of Figure 5.4 spirals nearly corotate with disk particles.

The high temporal and spatial resolutions and the large number of disk particles makes U5 and B5 models one of the best available simulations to measure kinematic quantities in the entire galactic disk with enough resolution.

5.3 Results

In this section we show the behaviour of l$_v$ across the galactic disk in our different models. For that we split the disk in cylindrical sectors (integrated for $|z| < 0.5$ kpc). We select each region to have a Δr=200 pc and a $\Delta\theta$=6 deg. Each region overlaps 100 pc and 3 deg with the contiguous ones. The expressions used for the computation of l$_v$ and its error are given in Section 5.1.1 and 5.2.1.

In the polar plots of this section the disk rotates from left to right. In all plots we overplot the locus of the bisymmetric spiral structure as a thick solid black line. In the analytical analysis, this is given directly by the equation of the density perturbation of the TWA. In simulations we show the Fourier m=2 mode locus computed by applying a spatial Fourier analysis in radial bins (Roca-Fàbrega et al. 2013). For simulations we also show density contours of regions with density above the mean. We computed the overdensity value of each region by subtracting the mean radial density to the local value. We mark the spiral CR with a thick solid horizontal black line and the OLR radius with a thick dashed horizontal black line, if those are well defined. Note that for U5 model there is no CR as the material is corotating with the spiral pattern and also that we do not plot the m=2 Fourier mode as this does not represent the spiral structure (in this case we have a four armed spiral instead). The white regions in the l$_v$ plots correspond to regions where the relative error in l$_v$ is above 50%.

5.3.1 TWA analytical approach

The results of our analytical development are presented in Figure 5.5. This map clearly shows that l_v follows periodic patterns related to the position of the spiral arms. In particular, it changes the sign when moving from behind to in front of the spiral perturbation. Additionally, positions with maximum or minimum spiral arm potential correspond to regions with almost null l_v. This result confirms the correlation between the mass density distribution and the l_v, which was already pointed out by Vorobyov & Theis (2006).

Besides, we notice here a novel result when studying the second order moments of the velocity distribution. We see that when crossing the spiral arms overdensity in the direction of rotation, the sign of the l_v changes from positive to negative if we are inside the CR, but the other way around between CR and OLR radius, and again from positive to negative outside OLR radius. Note here that Mayor (1970) computed l_v values only at the Solar neighbourhood in a model where the Sun was placed inside CR. Therefore, he could not notice these patterns. In next sections we use this analytical result as a framework to understand the kinematics observed in our test particle and N-body simulations.

A question that arises from the results presented in this section is what the origin of the l_v sign changes is. We deeply analyzed the analytical expression for the l_v (see Equation B.19) presented in Appendix B to answer this question. We have found that these sign changes are driven by the term $\mathrm{Re}(i\vartheta_1)\mathrm{D}_\nu^{(1)}(x)$ in the numerator. The part $\mathrm{Re}(i\vartheta_1)$ drives the change that occurs when crossing the density peak and it corresponds to the imaginary term of the spiral arm potential, that is shifted $\pi/2$ from the spiral arm density. $\mathrm{D}_\nu^{(1)}(x)$, which is a function of ν=m$(\Omega_p$-$\Omega)/\kappa$, drives the change at CR and is related to the fact that the rotation frequencies of stars are larger or smaller than the patterns' rotation. This is a quantitative explanation, but a qualitative physical origin of these sign changes remains unclear.

5.3.2 Results from test particle models

Here we discuss the patterns of l_v we obtained for all test particle models presented in Section 5.2.2 and its connection with the analytic results we show in Section 5.2.1.

TWA spiral arms potential

Figure 5.6 shows the density distribution (top) and the l_v values (bottom) in polar coordinates across the whole disk for models TWA1 (left), TWA2 (middle) and TWA3 (right) that differ only by their spiral pattern rotation frequency. When we compare these plots with Figure 5.5 we see that the l_v structures are not so sharp. We also see that due to both, the Poisson noise and that the velocity ellipsoid is so rounded, the l_v has a large uncertainty in some regions. As explained before, these regions with a high error in the l_v appear in white.

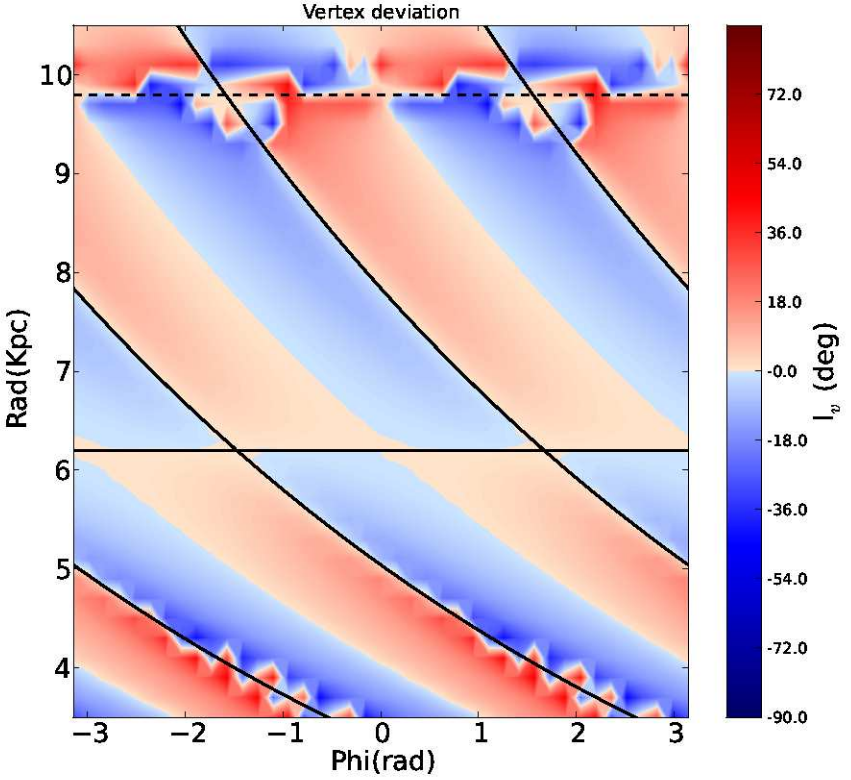

Figure 5.5: Vertex deviation polar plots in a color scale (red for positive values, blue for negative) for the TWA analytical solution (see Section 5.2.1). The solid and the dashed horizontal black lines show the position of CR and OLR radius, respectively. The curved black solid lines show the position of the spiral arms locus. The galaxy rotates from left to right.

Here, we see the same behaviour of l_v as seen in the analytical expressions of previous section. This is consistent and expected because the underlying spiral arm potential model is the TWA in both cases. However, here we did not impose a certain distribution function but compute the real orbits of particles in this potential. In particular, we can clearly see this for TWA2 which is a test particle simulation with similar initial conditions and parameters as the analytical approach potential. For the other two cases, TWA1 and TWA3, where most of the disk is either inside or outside CR we observe that the behaviour is the same as inside or outside CR, respectively, in TWA2. Note also the reverse of l_v sign beyond OLR for TWA3.

To see all these results in more detail we plot in Figure 5.7 (top panels) the l_v and the overdensity (black) values, as a function of angular distance to the spiral arm overdensity peak, for the models TWA1 (left) and TWA3 (right). This distance is taken as positive in the sense of rotation. Two error bars are overplotted to the l_v points. The blue ones show the root mean square of the errors obtained from Equation 5.4, so they reflect the Poisson noise (low number of particles) and the uncertainty when the velocity ellipsoid is almost circular. The red error bar is simply the error of the mean, that is the standard deviation divided by the square root of the number of regions. It accounts for the spread on l_v at a given angular distance in the radial interval considered. The l_v for TWA1 follows an oscillation from negative values in front of the spiral arm (for phases 0 to $\pi/2$), through null l_v in the interarm region ($\pi/2$), to positive values when approaching the next spiral arm from behind (for phases $\pi/2$ to π). If we compare the l_v oscillation with the one of the overdensity we can conclude that the former is shifted about $\pi/4$ towards to smaller angles. An opposite shift is observed for TWA3. Note also that a small shift is present at 0 phase: l_v is not exactly zero. This shift can be a consequence of the difficulty of finding the density peak properly as it is not a simple sharp peak.

We also point out here that TWA1 and TWA3 models show a clear antisymmetry with respect to interarm region (angular distance from the spiral equal to $\pi/2$). This is a consequence of the symmetries of the potential, similar to what happens in a barred model where there is four-fold symmetry (Fux 2001). In this case, the symmetries are related precisely to the phase with respect to the spiral arm and that is why it appears in this maps.

After our exploration of parameters detailed in Section 5.2.2 we conclude that the behaviour of the l_v presented here is independent of the parameters of the TWA potential and of the initial conditions. We also observe that when imposing lower velocity dispersions in the initial conditions the l_v signatures have a better definition than when we use higher velocity dispersions.

PERLAS spiral arms potential

In Figure 5.8 we show the density (top) and the l_v (bottom) in polar plots of the test particle models where we have imposed the PERLAS spiral arm potential PER2 (left)

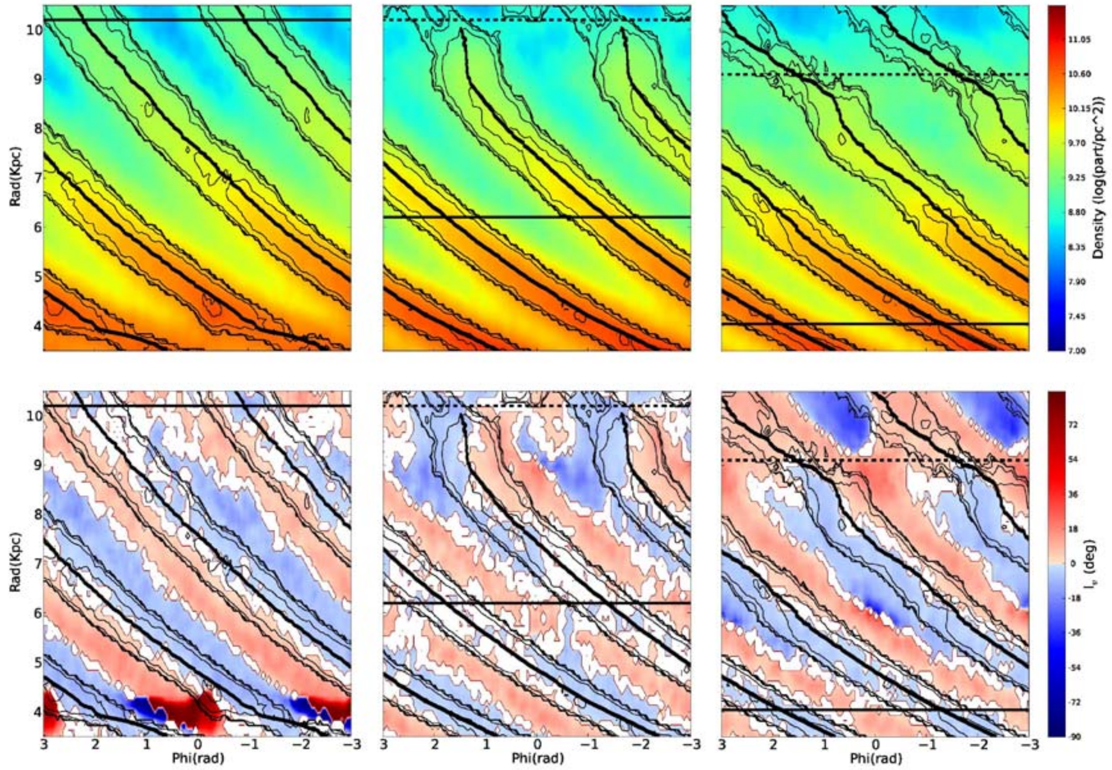

Figure 5.6: Density (top) and I_v (bottom) polar plots for test particle models TWA1 (left), TWA2 (middle) and TWA3 (right) from Table 5.1. The thin black lines show density contours of regions with density above the mean. The thick and dashed horizontal black lines show the position of CR and OLR radius, respectively. The thick black lines show the position of the Fourier m=2 mode locus. White regions in the bottom panels corresponds to regions where the I_v relative error is above 50%.

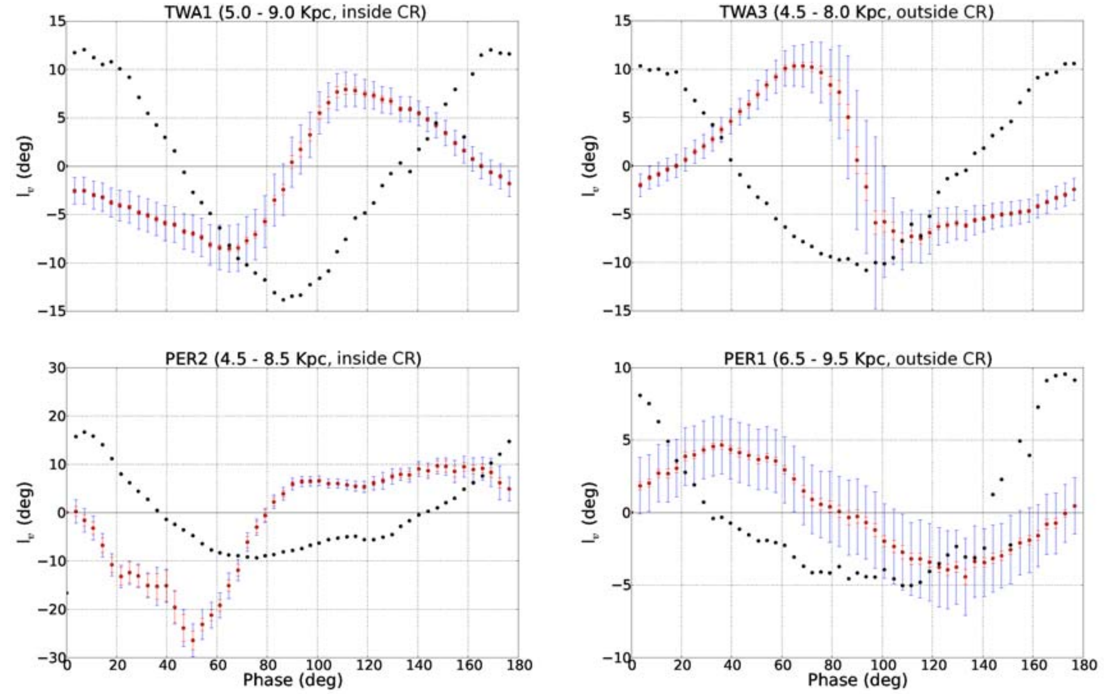

Figure 5.7: Vertex deviation radial mean values with their errors (blue/red error bars) and spiral arm mean overdensity with respect to the mean disk density (black points), as a function of angular distance to the spiral. The phase has been adjusted so that the spiral arm density peak is located at a phase of 0^o while the minimum is at 90^o). Blue error bars correspond to the root mean square of errors computed using Equation 5.4, and the red error bars to the error of the mean. The overdensity values have been normalized to fit in the l_v plot for a better comparison of the curves. Left: Values in regions inside CR (TWA1, top, PER2, bottom). Right: Regions outside CR (TWA3, top, PER1, bottom).

and PER1 (right). This potential is more complex than the cosine expression for the force of the TWA and, as a consequence, the density structures appearing in these models are more complex. One can see, for instance, a bar-like structure in the inner radius for PER1 or the two overdensities outside the spiral arms at radius between 8 and 9 kpc for PER2.

The l_v analysis reveals that, as in the TWA models, there is a clear relation between this parameter and the density structures. In PER1, outside CR we observe the same l_v pattern as in TWA analytical and test particle models in the same region: positive sign in front of spirals and negative sign behind them. Inside CR, however, we do not see a clear behaviour due to the fact that the l_v values are small and that in these regions there are many density substructures. We point out that the presence of these density substructures (apart from the main imposed spiral arms) explains the higher uncertainty that exists around the CR.

For PER2, which is inside CR in the shown range of radius, in general we observe the same l_v behaviour as in the analytical solution and in the TWA models inside CR. Note however, that between 8 and 9 kpc, where additional overdensities showed up, the l_v appears distorted. Note also that the magnitude of the l_v is much smaller for PER1 than for PER2, as correspond to its smaller force amplitude (see Section 5.2.2).

The results for PER models become more clear in Figure 5.7, bottom panels, where we plot l_v values as a function of angular distance to the spiral arm overdensity peak. The general behaviour of the oscillation for PER1 is similar to TWA3 (outside CR), although the magnitude of the l_v is smaller as correspond to a smaller $\mathrm{Q}_t(\mathrm{R})$ (Section 5.2.2). For PER2, the oscillation resembles that of the TWA1 (inside CR) in a first approach. However, the detailed shapes of the curves of models TWA and PER are slightly different. Again this must be due to the differences in the force fields, in particular in the shape of the forces as a function of the position in the disk mentioned in Section 5.2.2. Note also that a comparison between these two different models was done in Antoja et al. (2011) who concluded that, even when models with the same spiral locus, amplitude of the force and pattern speed were used, the obtained velocity field could be significantly different in some parts due to the difference in the force field. As an example, the antisymmetry in the l_v distribution observed in TWA models is clearly broken in the PER2 case. As seen in Pichardo et al. (2003), in the PERLAS model forces are not symmetric with respect to the spiral arm locus, that is the ones in front of the spiral are different from the ones behind.

Ferrers bar potential

Here we analyse spiral arm structures that are produced as a response of a 3D bar potential. In Figure 5.9 we present the density (top) and l_v (bottom) polar maps for a test particle simulation where we imposed a Ferrers bar potential (FBar). The spiral arms generated in this simulation can be observed in the top panel as the diagonal structures. The vertical straight structure between 3 and 4 kpc is the bar whereas a ring-like structure is formed

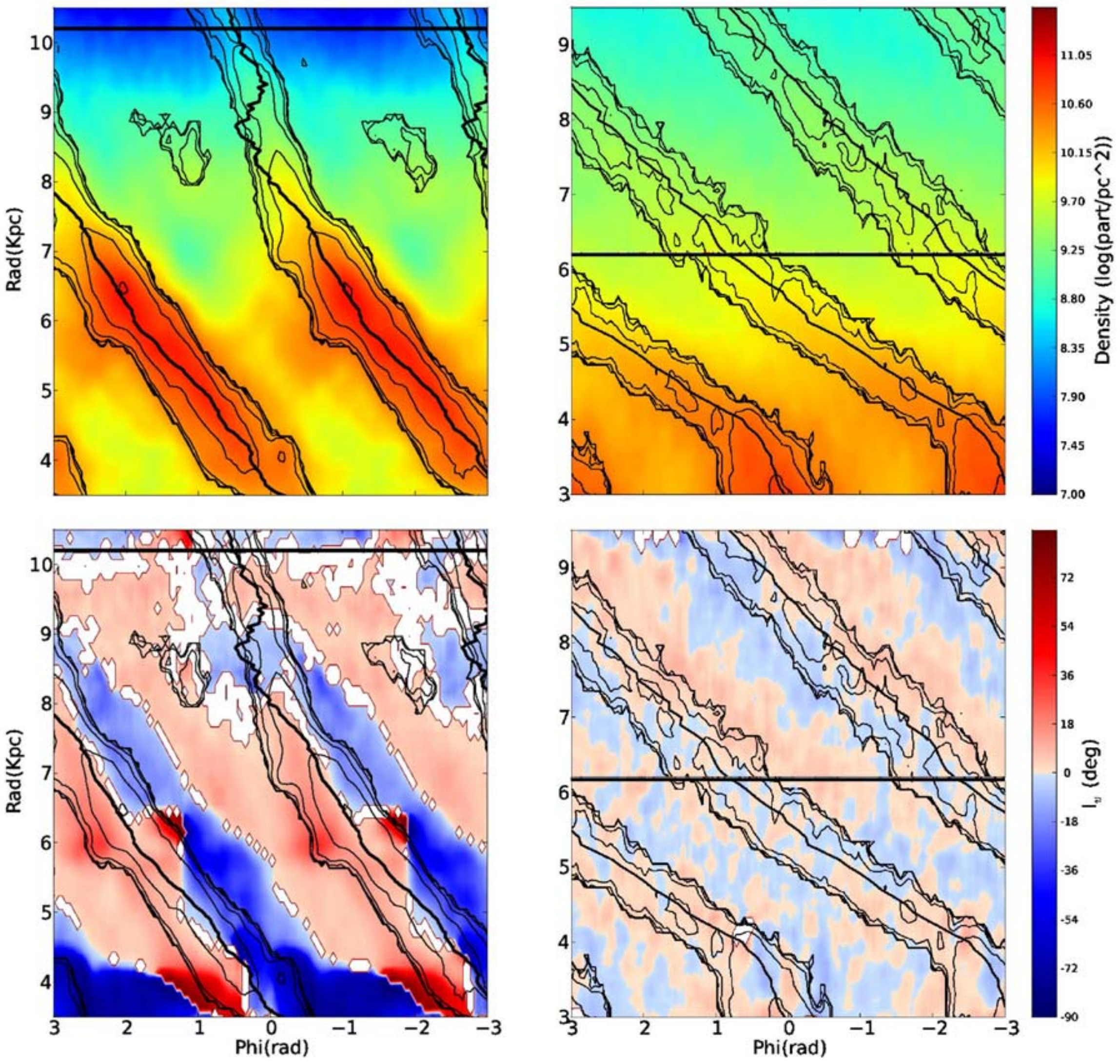

Figure 5.8: Density (top) and l_v (bottom) polar plots for test particle spiral arm models PER2 (left) and PER1 (right) from Table 5.1. See Figure 5.4 for more details on the lines.

between 4 and 6 kpc. As a consequence of its nature, the spirals formed in these models have low amplitude and are placed outside CR.

As can be seen in Figure 5.9 (bottom) the ring region presents a complicated l_v pattern. Out of it, that is at radius > 7.0 kpc the spirals created as a response of the bar are faint (low amplitude) but well defined. In Figure 5.10 we present the oscillating pattern of the l_v and the overdensity induced by these spirals in the radial interval $7 < R < 9$ kpc. We observe positive vertex deviation structures in front of the spirals and negative deviation behind them, with almost null values near the locus $(0,\pi)$ and in the interarm region $(\sim \pi/2)$. This pattern is clearly shifted $\sim \pi/4$ to the density pattern. This behaviour is in agreement with the trend observed in TWA3 and PER1 models (see Figure 5.9 right).

5.3.3 Results from N-body models

In these models we have a more complex scenario as the gravitational potential has not been imposed but it is generated by the system particles themselves. As a consequence, of this self-generation there are several density structures interacting with each other through gravity. Moreover, as discussed in Roca-Fàbrega et al. (2013), these are time dependent structures (e.g. spiral arms are transient), which introduces an additional parameter when analysing the l_v maps.

As mentioned in Section 5.2.3 the B5 N-body simulation develops a strong bar and a dominant bisymmetric spiral arms which rotates roughly as a rigid body (see Figure 5.4). The spirals in this simulation are placed outside CR. In this model we clearly observe that, in agreement with the behaviour found in previous sections, positive values are found in front of the spiral and negative values are found behind (Figure 5.11, left, and Figure 5.12, top). Another interesting feature of this model is the presence of a slow rotating m=2 mode at large galactic radius (R $\sim$ 12-14 kpc) (see Roca-Fàbrega et al. (2013)). This is seen in Figure 5.11, left, where there seem to be a bifurcation in the arms at outer radius or the presence of additional arms that are not in phase with the main ones. These new arms rotate slower than the disk with a frequency of about 8 $\mathrm{kms^{-1}kpc^{-1}}$ and they produce their own signature in l_v: see the additional two red regions at $\phi \sim -0.5$ and $\phi \sim 2.5$ radians and radius of $R \sim 12.5$ kpc. These arms do show the same behaviour as previous arms inside CR, i.e. negative sign in front of the density perturbation and positive behind.

The second model that we analyse here is the U5 simulation. This simulation develops a multiple armed system with Fourier dominant mode being m=4, without a bar, and it corotates with the disk particles. The amplitude in the density of the arms in U5 is much smaller ($A_4/A_0 \sim 0.08$) than in B5 ($A_2/A_0 \sim 0.5$). We present the results for U5 model in Figures 5.11 right, and 5.12 bottom. Although the amplitude of the l_v pattern is small in this case, the small error bars allow us to provide indications that a periodicity is also present. However, in this case, there is no clear relation between the l_v structures and density pattern. This behaviour is completely different from the B5 presented before.

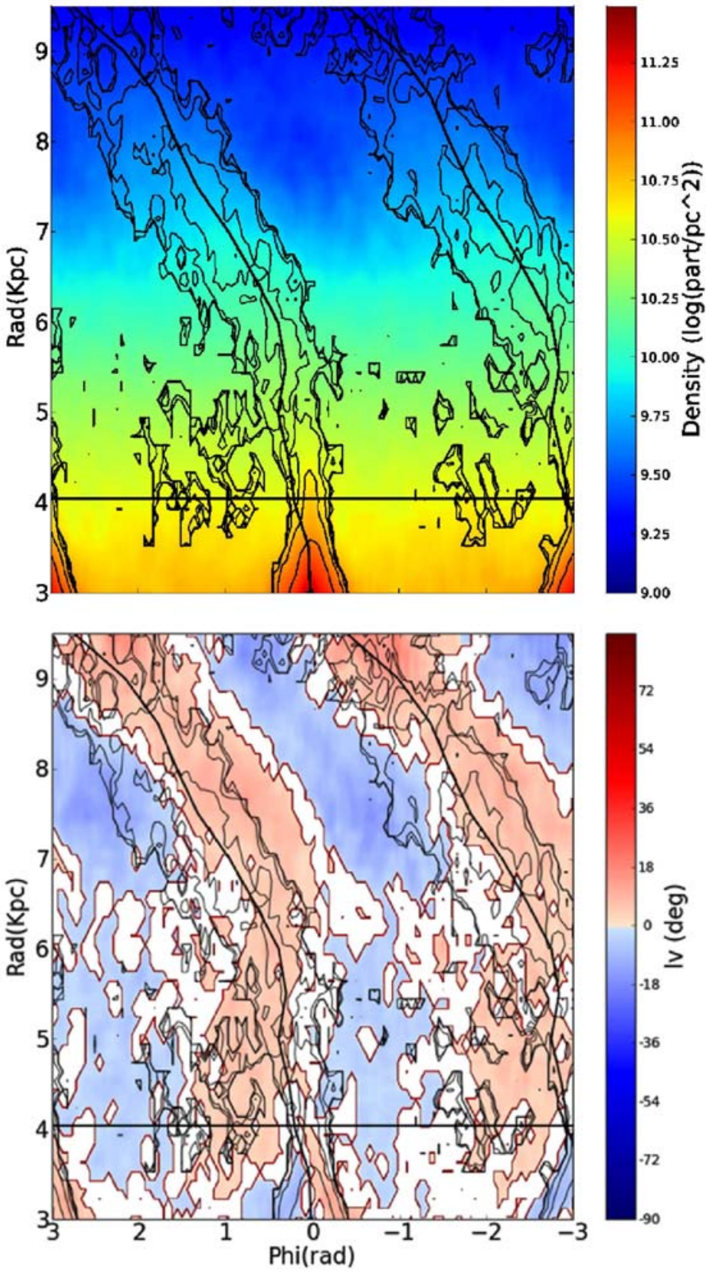

Figure 5.9: Density (top) and l_v (bottom) polar plots for model FBar from Table 5.1. See Figure 4.8 for more details on the lines.

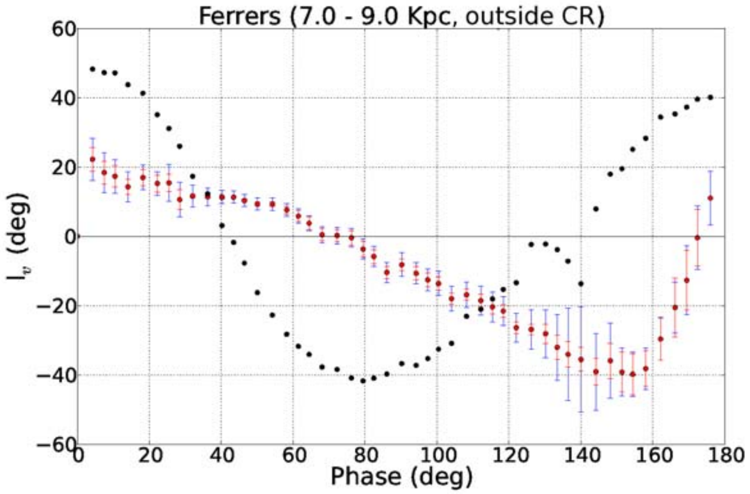

Figure 5.10: Vertex deviation radial mean values with their errors (blue/red points) and spiral arm overdensity (black points) as function of distance to the spiral arms density peak, for the Ferrers bar model i.e. outside CR. For more details see Figure 4.9.

Finally we make a first attempt to analyse the evolution of the l_v behaviour when the density structures evolve in time in our N-body simulations[1]. We find that each density structure generates its own l_v pattern. For model B5 we see that the conclusions presented here are valid when strong spiral arms are present. Otherwise, when complex density structures appear, the relation between them and the l_v is not straightforward. The same stands for model U5, with corotating spirals.

5.4 Conclusions

In this Chapter we have analysed the l_v in simulated galactic disks with spiral structure. We have mapped the l_v all across the disk using a TWA analytical solution, several test particle simulations with imposed spiral or bar potentials and, for the first time, high-resolution N-body simulations. Our main outcomes are:

- We confirm that the l_v is clearly related to the density structure when the spiral arms are non-corotating.
- In all cases with non-corotating spiral arms, the sign of the l_v changes when crossing the density peak of the spiral structure and in the interarm region. When crossing the density peak this change is from negative to positive between CR and OLR radius and the other way around inside CR and outside OLR.

---

[1] See movies in http://www.am.ub.edu/∼sroca/Nbody/movies/.

- When the spiral arms are corotating, there is no clear correlation between the l_v and the overdensity. However also in this case several l_v gradients can be observed.

Using test particle simulations we have exhaustively checked that these conclusions hold both for spiral arm potential (TWA, PERLAS) and spiral arms that are the response to an imposed bar potential (Ferrers, quadrupole). Furthermore, they are independent of the initial parameters, thus on the changes of the pitch angle, the amplitude of the spirals, the velocity dispersion of the population or the total integration time. All these cases consist of a rigid rotating pattern with a well defined CR and ILR and OLR resonances. Moreover, for the first time we show here that our self-consistent high-resolution N-body simulation with a rigid rotating bisymmetric and well defined two armed spiral shows a l_v behaviour with the same main trends as observed in the test particle simulations.

From these models, we conclude that the changes on the sign in l_v when crossing the overdensities and underdensities of the spiral arms give us robust and useful information about the position of the main resonant radii, that is CR and OLR. Measuring the sign of the l_v in front or behind the spiral structure in a certain radius and azimuth would indicate whether that region of the galaxy is inside or outside of CR. A reverse of the sign behaviour at a certain radius would mark the CR, and in turn, give an estimation of the pattern speed of the spiral arms. As the position of spiral arms inside or outside CR is related to their nature (e.g. manifold spiral arms are generated always outside CR), the mapping of the l_v would also trace the nature of the spiral arms in a galaxy.

One may wonder why models with different nature such as the TWA (low amplitude approach), PERLAS (self-gravitating imposed potential), response spirals in test particles barred models or N-body simulations with a well defined spiral pattern (transient structures, self-consistent model) show the same general trends for the l_v. The explanation could come from the fact that the l_v is a first order effect of the velocity field, so its behaviour is successfully reproduced in all our models. We may require N-body simulations with a larger number of particles in order to populate the velocity distribution tails and disentangle the differences between models through higher order momenta. Moreover, second order differences in the shape and magnitude of l_v patterns are observed when comparing all the models analyzed here. These irregularities may be due just to the intrinsic differences among their corresponding force fields.

5.5 Future work and perspectives

The work presented here opens several new questions that will need to be answered in a near future. Here we summarize our perspectives to study and solve them.

5.5.1 Second order effects in l_v maps

As mentioned in Section 5.4, l_v maps show second order differences in the shape and magnitude of l_v patterns when comparing results from models analyzed here. Is one of

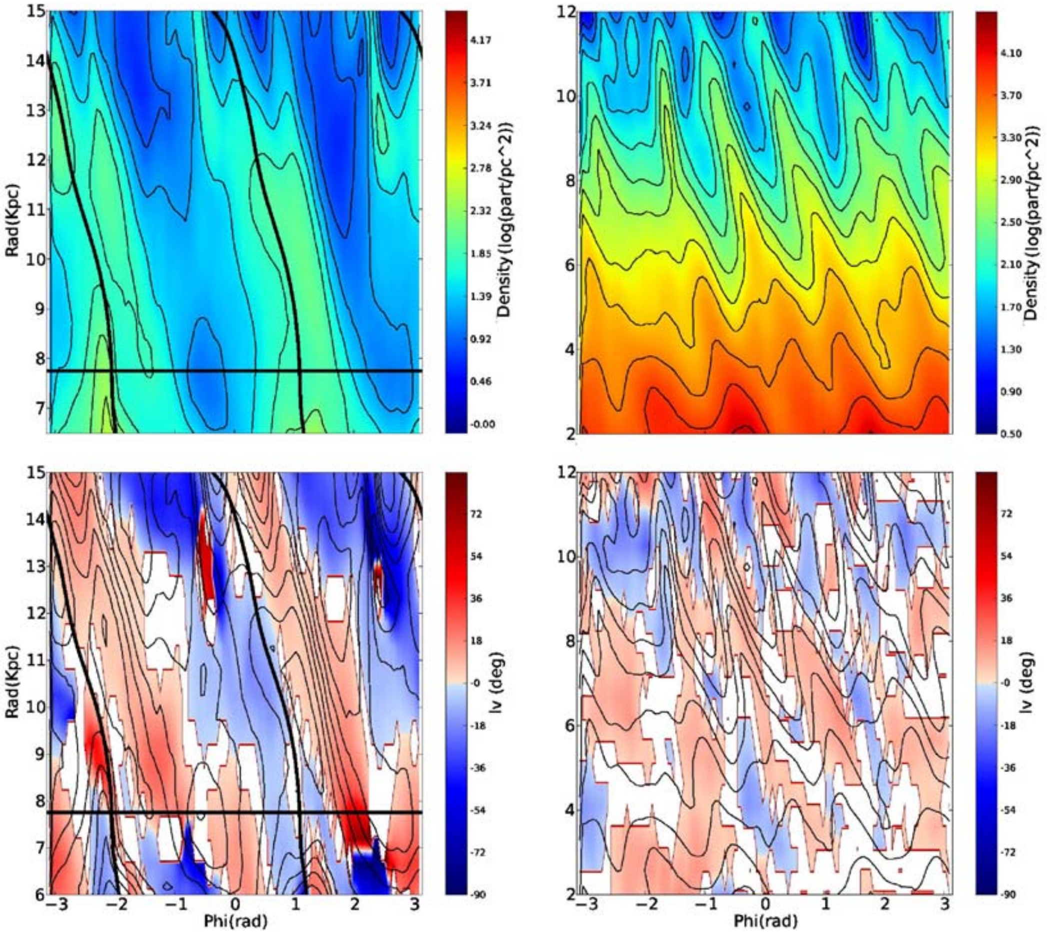

Figure 5.11: Density (top) and I_v (bottom) polar plots for N-body model B5 (left) and U5 (right) at 1.06 Gyrs of evolution. See Figure 5.4 for more details on the lines.

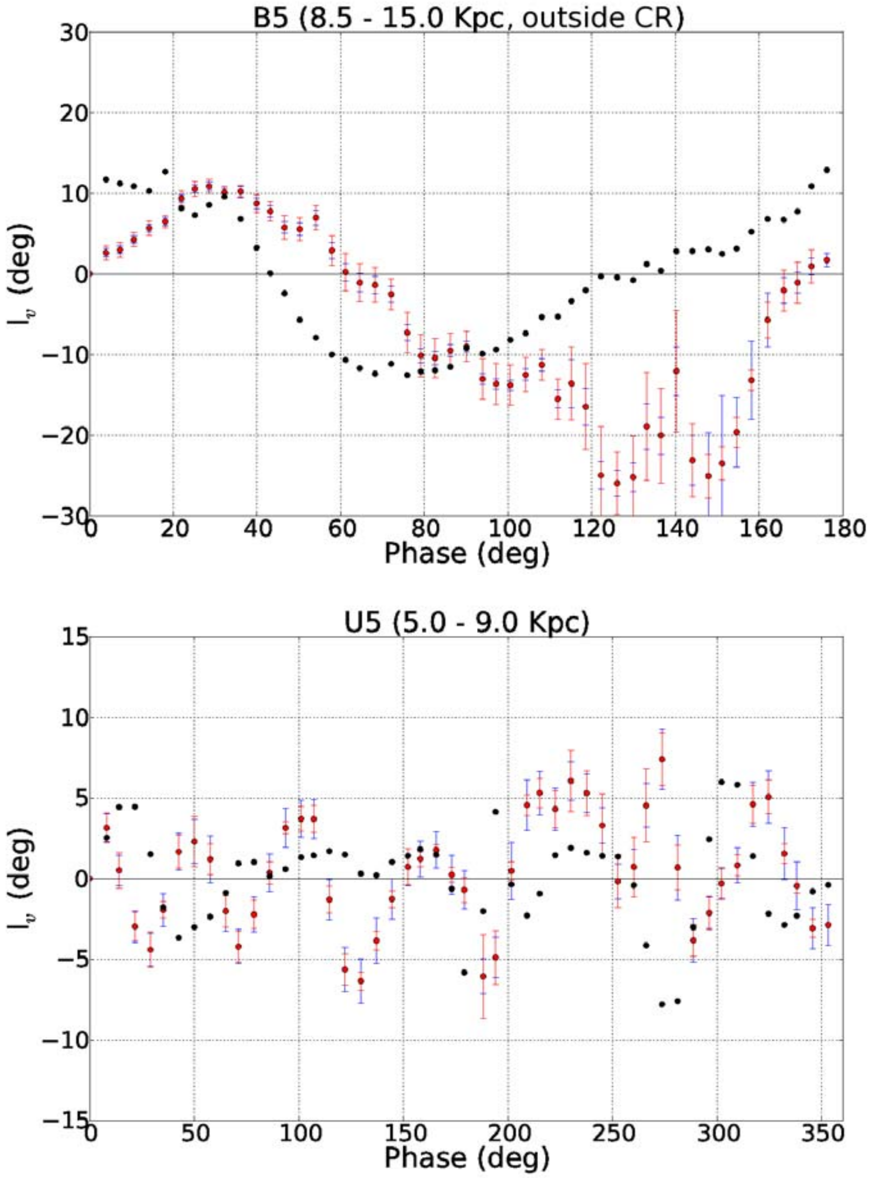

Figure 5.12: Vertex deviation radial mean values with their errors (blue/red points) and spiral arm overdensity (black points). For more details see Figure 5.9. Top: B5 model, i.e. outside CR; values are plotted as a function of the angular distance to the spiral arm density peak. Bottom: U5 model, i.e. corotant structure; values are plotted for all the [0,360] angular distance range, with origin at an arbitrary angle.

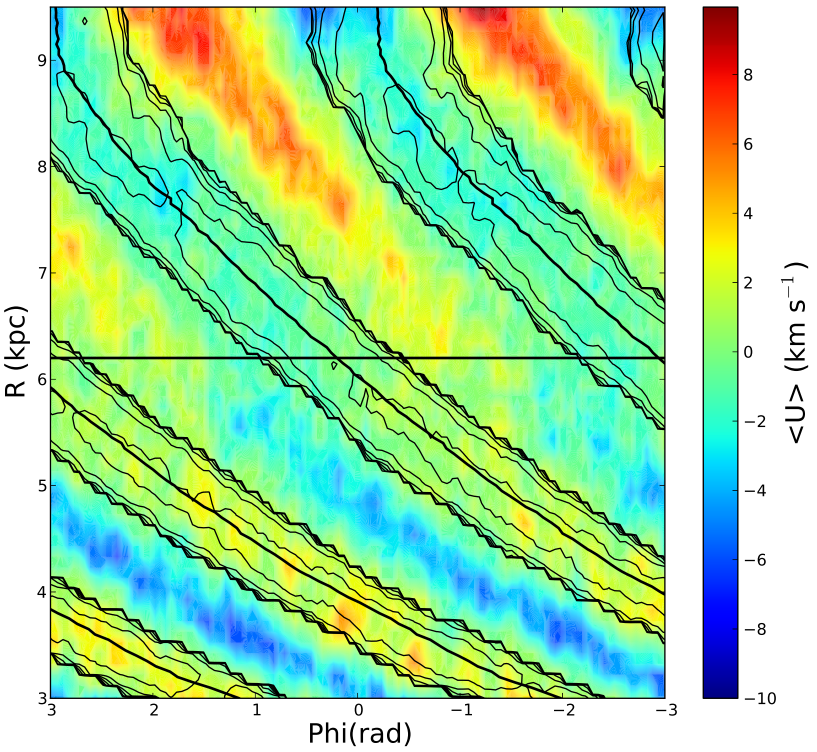

Figure 5.13: Color map of mean U values in model TWA2. Straight black line indicates CR position, diagonal solid lines spiral arms density peak and black contour lines density contours.

our main perspectives to study these irregularities and their possible correlation with the imposed or self-generated force fields. If this correlation exists it will opens the possibility of disentangling between different natures proposed for the non-axisymmetric structures.

5.5.2 Analysis of moments

In this work we have focused our analysis to the l_v parameter. However, as shown in Vorobyov & Theis (2006, 2008), other moments like the means (zero order moments) or the skewness and kurtosis (third order moments) can give us new information about the non-axisymmetric structures. To analyse the second order moments, individually not combined to produce other parameters like the l_v studied here, can also be very interesting. Here we present in Figures 5.13 to 5.17 the first results we have obtained when analysing the first order and second order moments of the TWA2 model.

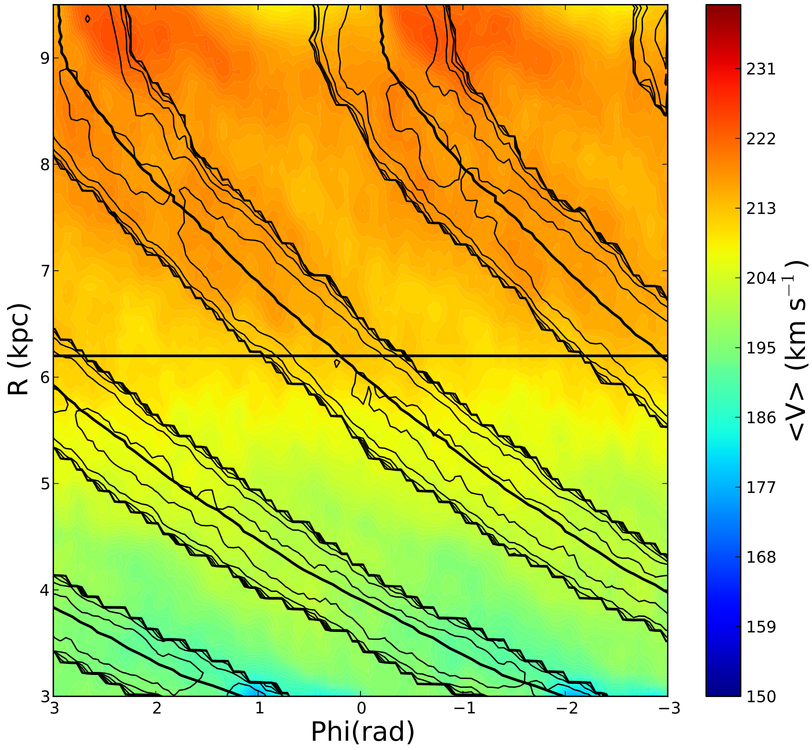

Figure 5.14: Color map of mean V values in model TWA2. For more details on the lines see the caption of Figure 5.13.

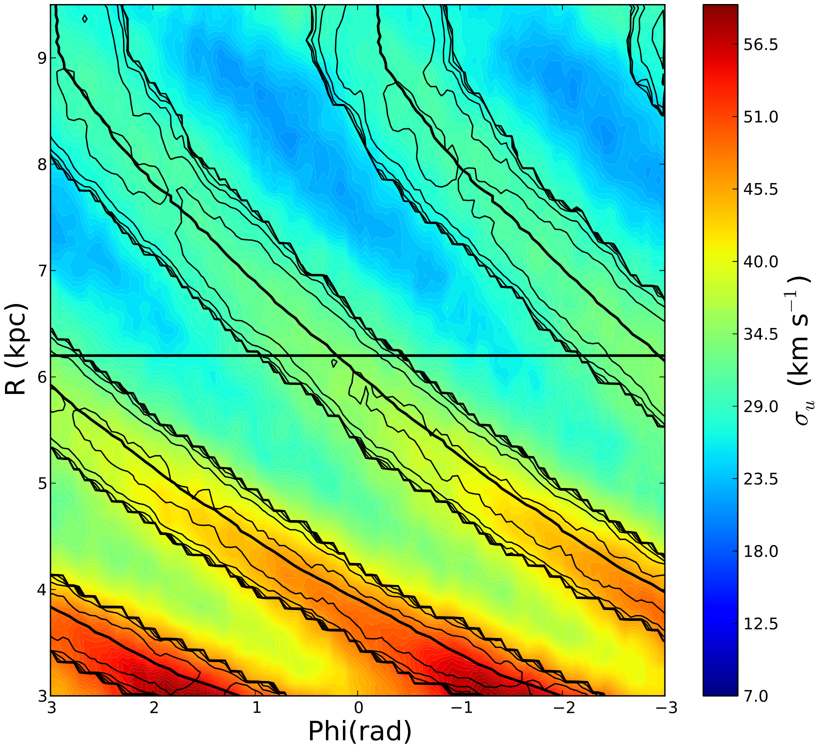

Figure 5.15: Color map of radial velocity dispersion values in model TWA2. For more details on the lines see the caption of Figure 5.13.

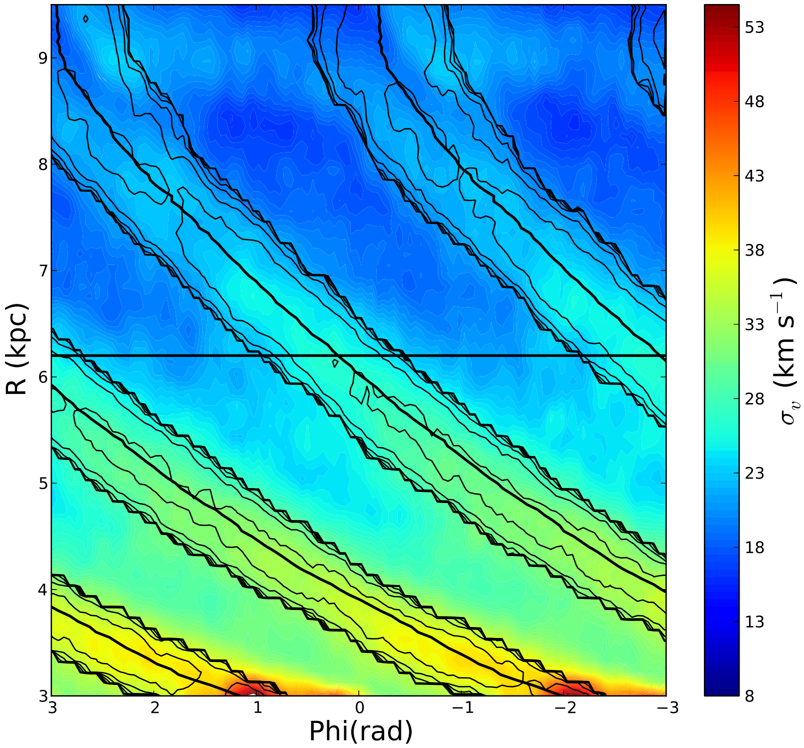

Figure 5.16: Color map of tangential velocity dispersion values in model TWA2. For more details on the lines see the caption of Figure 5.13.

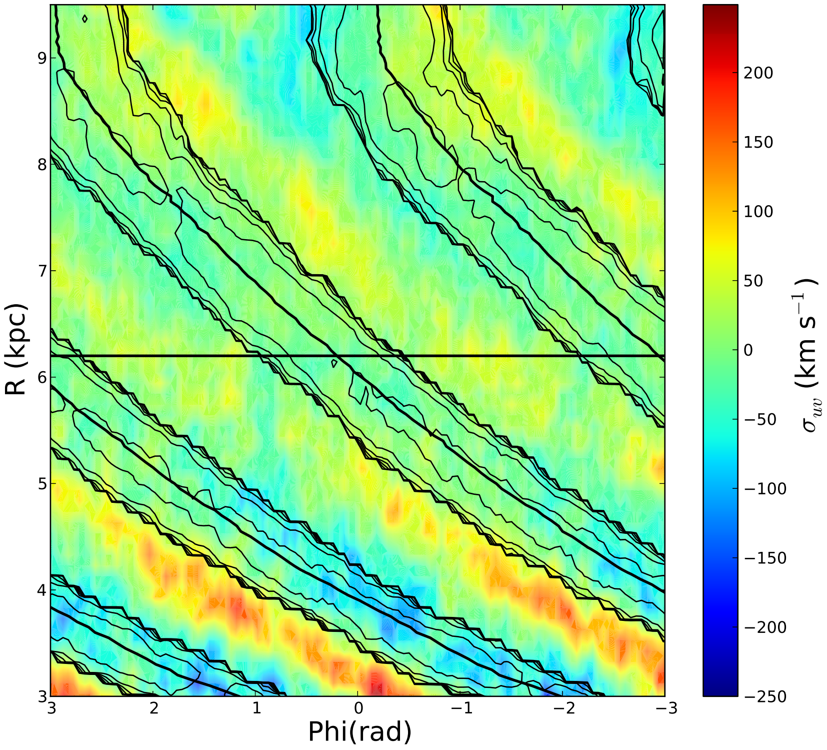

Figure 5.17: Color map of crossed UV second order moment values in model TWA2. For more details on the lines see the caption of Figure 5.13.

5.5.3 Analysis in the vertical component

Another work we plan to undertake in the near future is to make similar analysis as the ones done here in the plane but now in the vertical direction. For that purpose we will need to use 3D models. We plan to analyse both, variations of the vertex deviation and also of equivalent parameters in V-W and U-W planes, in z. Other authors have started these out of plane analysis obtaining interesting results (Monari et al. 2013).

5.5.4 Analysis of more realistic N-body simulations

As we have pointed in the previous Chapter, when using collisionless N-body models some physical processes that can affect the stellar component are not taken into account. One important process that can have an impact in the work presented here is the generation of new stars with low velocity dispersions due to the cold gas inflows. Our perspective is to make the same analysis presented here over the new realistic MW like system presented in the next Chapter.

5.5.5 To apply the method

Another important aspect that should be addressed in the future is to determine under which circumstances the new method presented here can be used to find resonance radius in observational data. An evident caveat when applying the method is that the patterns in the sign of the l_v are degenerate for inside CR and outside OLR. In this case, one would need other kinematic signatures to differentiate between those two cases. Second, when spiral arms coexist with other density structures (i.e. rings, floculent structures, ...), the behaviour of the l_v can be much more complex. In these cases it will be more difficult to apply the method. Finally as it is known that the mean velocities can also be good tracers of the CR (see Binney & Tremaine 2008), it has to be studied in which cases one method is better than the other and how they can be used complementary.

In particular for our own Galaxy, where the spiral structure is one of the main debated features in Galactic studies, it is still pending if the Sun is inside or outside spirals' CR. Measurements of the l_v at several kpc from the Solar neighbourhood are expected with forthcoming large surveys like Gaia (ESA, Perryman et al. 2001), LSST or the APO Galactic Evolution Experiment (APOGEE-SDSS Majewski et al. 2010). The work presented here is offering new strategies to exploit this data. In perspective of the first release of Gaia data in summer 2016, we started to test how the method will be useful when applied. In Figure 5.18 we show first results of this analysis.

For external galaxies, as far as we know, there are no measurements of the l_v. In fact, in studies of the kinematics of external galaxies it is generally assumed that there is alignment of one of the axis of the stellar velocity ellipsoid with the azimuthal coordinate (i.e. there are no l_v) in order to derive properties such as the ratio between radial and azimuthal velocity dispersions from LOS velocity measurements (Gerssen & Shapiro

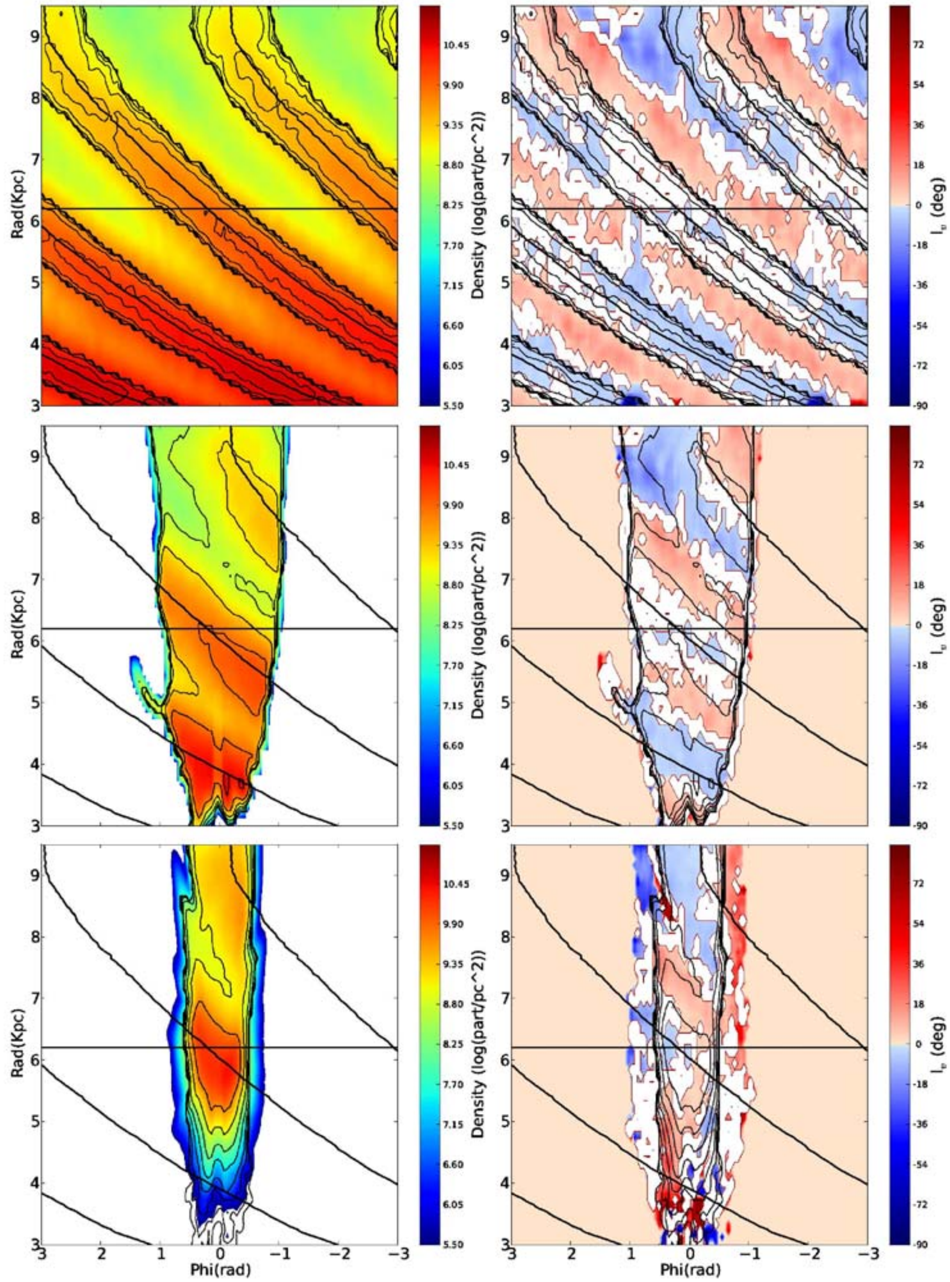

Figure 5.18: Density (left) and vertex deviation (right) polar color maps of model TWA2. Top: All data. Center: Data cut at Gaia magnitude G = 20 after assuming Suns' position at Phi=0 and R=8.0 kpc and applying Drimmels extinction. Bottom: Results obtained from data where Gaia errors have been applied. We made a cut at G= 20 and $\sigma_\pi/\pi < 20\%$. Straight black line indicates CR position, diagonal solid lines spiral arms density peak and black contour lines the density contours.

Griffin 2012; Westfall et al. 2011). Our simulations would allow one to quantify how this assumption could bias their final results. Second, they can be used to establish the level of detection of l_v signals in external galaxies and study which are the observational requirements and perspectives for detecting them with current and future instruments like ELT in its spectroscopic phase or possible nano-arcsecond post-Gaia missions.

Part III

Towards a realistic MW like galaxy

6

Our MW like model

6.1 Introduction

To simulate a system that fits the properties observed for our own Galaxy is not trivial. One of the most challenging problems in ΛCDM cosmological simulations in recent years has been to obtain realistic Milky Way (MW) like systems. It has been specially difficult to get models with extended disks and with a proper stellar age distributions, star formation rates and baryonic fractions that fit within the observations. Nowadays the N-body plus hydrodynamics codes are evolving to a better understanding of physical processes (see discussion on Chapter 3). Important issues have been addressed in he last decade like disk formation or central bulge concentrations. Recently several groups have found the way to simulate systems in which some general properties fit within the MW observed values.

It was long known that disks form when the gas cools and condenses within the dark matter halos (White & Rees 1978; Fall & Efstathiou 1980; Mo et al. 1998) conserving the angular momentum obtained through external torques from neighbouring structures (Hoyle 1953; Peebles 1969). One problem that arose from the first numerical simulations was the lack of angular momentum in disks after the collapse (Navarro & Benz 1991; Navarro & Steinmetz 2000). This angular momentum problem lead to galactic disks be too small and dominated by big and massive bulges. Two major drawbacks were found to be the responsible of this problem. First, artificial losses of angular momentum caused by insufficient resolutions and other numerical effects (Okamoto et al. 2003; Governato et al. 2004; Kaufmann et al. 2007). Second, the dynamical friction that transfers the orbital angular momentum of merging substructures to the outer halo and causes cold baryons to sink to the center of the proto-galaxy, being then consumed at early ages in the formation of an old stellar spheroid rather than in an extended stellar disk, at latter ages (e.g. Maller & Dekel 2002).

Ten years ago, the attempts for obtaining realistic disk galaxies in a ΛCDM universe succeeded as can be seen in Abadi et al. (2003), Governato et al. (2004), Robertson et al. (2004), Okamoto et al. (2005) and Governato et al. (2007). In these simulations the authors used the so called zoom technique to produce individual galactic systems with a high resolution inside cosmological simulations with much less resolution (see Section 3.4). The authors selected halos with masses similar to the ones of the MW, and with a quiet merger histories in the last stages of its formation to be resimulated with high resolution. Several improvements accounting for the success of these models on forming disk galaxies are: better numerical resolutions, the implementation of an efficient supernovae (SNe) feedback and new stellar formation and evolution recipes. These new physical processes implemented in the codes prevent efficient gas cooling and condensation and remove low-angular-momentum material from the central part of galaxies. However, although they obtained realistic disk galaxies none of them was able to produce viable MW like late type spirals.

In the recent years authors like Scannapieco et al. (2009), Stinson et al. (2010), Piontek & Steinmetz (2011), Governato et al. (2010), Agertz et al. (2011), Brooks et al. (2011), Feldmann et al. (2011) and Guedes et al. (2011) among others, obtained realistic rotationally supported disks with the properties of late-type spirals like MW. A new process included in these models is that the gas is acquired through filamentary cold flows that was never shock-heated to the halo virial temperature. This cold gas is the fuel for the late star formation in disks (Kereš et al. 2009; Ceverino et al. 2010). However most of these works have systems with too peaked rotation curves in the center. Agertz et al. (2011) showed that some key parameters to avoid the formation of these peaked systems are the star formation efficiency or the gas density star formation threshold. They argue that to use a proper value for these parameters is necessary to reproduce the subgrid physics of star formation in molecular clouds. As described in Section 3.3.2 a combination of both parameters allow the system to consume the gas in the star formation region fast enough to ensure that the energy provided by SNe is not radiated too fast by the gas cooling. As mentioned this too efficient cooling is known as 'cooling problem' and initially was solved by stopping the cooling in the star formation region for several Myrs after star formation. In recent high resolution simulations this problem has been naturally solved by adding new physical processes like radiation pressure from massive stars (see Section 3.3.2 for more information about the cooling problem).

Simulations in the most recent works have reached very high levels of realism when comparing them with observations for the MW (e.g. Guedes et al. 2011; Aumer et al. 2013; Mollitor et al. 2014). In these works it has been used the Smoothed Particle Hydrodynamics (SPH) and they reached spatial resolutions of hundreds of parsecs.

Realistic MW like simulated systems opens an important window on the study of galaxy formation and evolution. In this chapter we present a set of new realistic MW like models with extended disks and unpeaked slowly decreasing rotation curves. As will be seen, we reach similar or better levels of realism as the most recent presented works but using an Eulerian, AMR approach. These models can be discussed in the context of the most competitive recent collaborative efforts. One of our stronger points is that we have a slightly better spatial resolution (109 pc) so in our models we will be allowed to better analyse processes that occur at smaller scales like spiral arms and bar kinematics.

6.2 Towards a MW like model

Before succeeding into get the MW like model that we present in this chapter we needed to run several other models as a test. The nomenclature used here to name each one of these models is simple: first, we use the 'HART' prefix to indicate that the model have been run using the ART plus hydrodynamics code; next, we add a natural number, starting by 1, to indicate which low resolution initial conditions for the cosmological box have been used; a second natural number, also starting by 1, is added to indicate which DM halo have been selected, into the low resolution run, to be resimulated; finally, a last number, now starting by 0, indicates which simulation of the selected DM halo it is. This last number is necessary as we have several simulations of the same DM halo in where we have changed at least one parameter (e.g. resolution, star formation efficiencies, refinement aggressivity, ...). The main model we present in this thesis is named HART321, following our nomenclature we know that it comes from our third initial conditions generation and that it is the first simulation we have done of the second DM halo we have selected in the low resolution run. Other examples of this nomenclature can be find in Table 6.1.

At the end of this thesis we have used three different cosmological initial conditions and we have selected a total number of 7 halos, 0 for the first initial condition generation, 5 for the second one and 2 for the third one. The total number of high resolution simulations we have made is 12. In the case of the first initial condition generation the result of the low resolution simulation was unrealistic due to problems with the initial parameters. From the second generation we could not find a system that both met all restrictions we impose to the DM halo in the low resolution run (see Section 3.4.2 for more information about the restrictions) and ends in a realistic MW like system after adding baryons and resimulation it at high resolution. It is important to know that when adding baryons, positions and velocities of DM halos in the low resolution run can suffer small changes. These changes are usually translated to an increase of the total mass and rotation curve but they can also affect the distribution of satellites and so the age of the last major merger what can bring the system to a configuration that is far from the one of the MW. Nonetheless, from this second generation we have obtained several non-MW like systems that will be used in future works with other purposes. Finally, from the third initial conditions generation we have been able to find two DM halos that met all imposed restrictions at the low resolution run but only the second one have became a realistic MW like model after adding the baryonic part and resimulating it with high resolution. This last model is the one that we fully describe in the next sections.

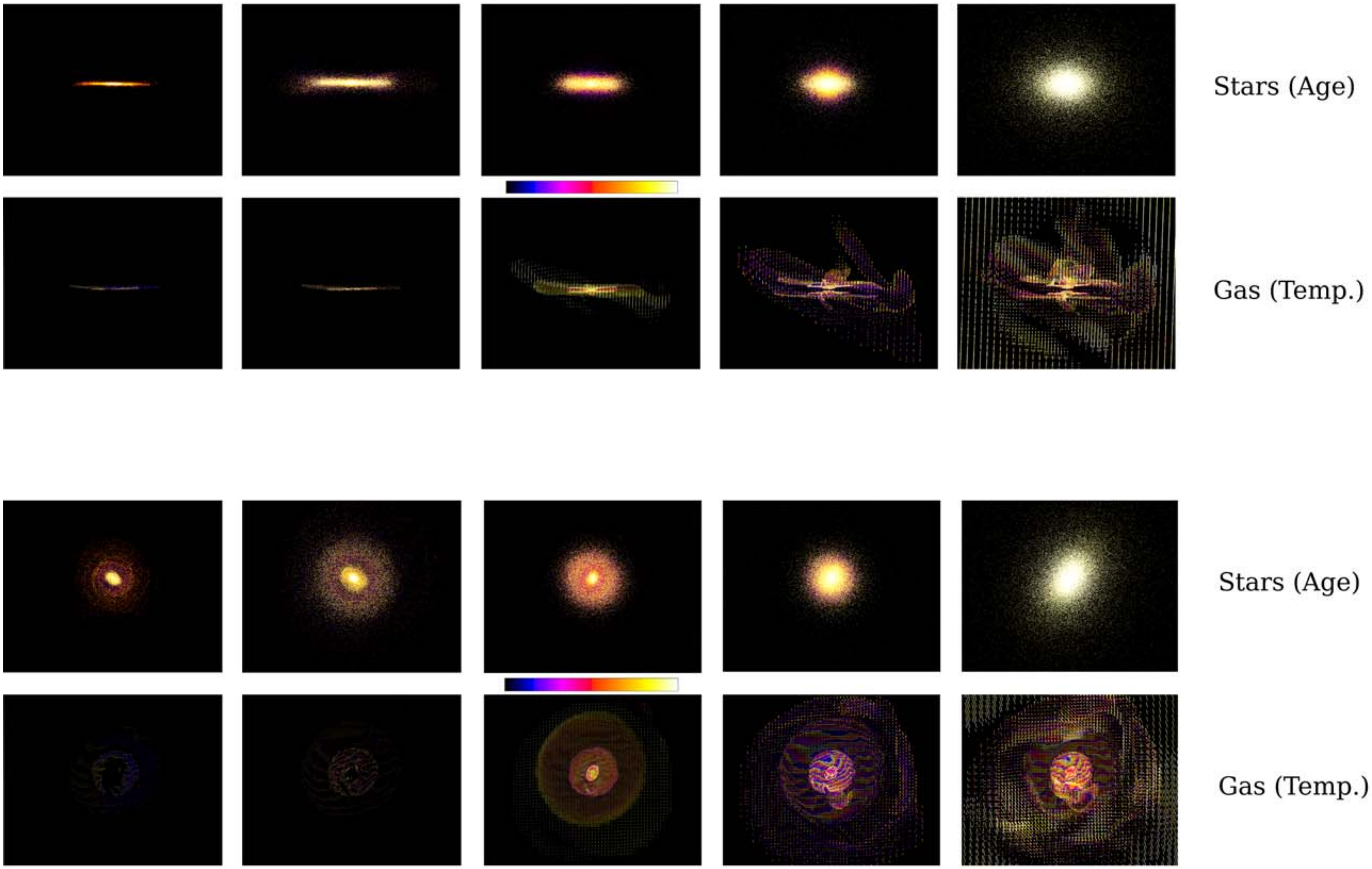

Figure 6.1: Edge on (first two rows) and face on view (last two rows) of stars and gas density in our simulated Milky Way sized galaxy (model HART321). Each column correspond to a different stellar age and gas temperature, respectively. From left to the right, 0-4 Gyrs / 250-1000 K, 4-9 Gyrs / 1000-5000 K, 9-10 Gyrs / 5000-10^4 K, 10-11 / 10^4-10^5 K, 11-13.467 Gyrs / 10^5-10^6 K. All panels span 46 kpc in the vertical direction and 58 in the horizontal. Color code indicates stellar age or gas temperature from the minimum (black) to the maximum (white).

6.3 General properties of the MW like model

In this section we present a set of three models that are identical except for the refinement criteria and that are the ones that best fit the properties of our MW galaxy. Model HART321 is the one with a lightest refinement, HART323 has intermediate conditions and HART322 is the one with hardest refinement conditions (harder means that code splits cells easier).

At z=0 these three models are late type massive spiral galaxies with several non-axisymmetric disk structures such as bars or spirals. Their assembling history is quiet since z=1.5 and the last major merger occurs at z=3. From the major merger at z=3 an old stellar component remains in the form of a long bar, at z=0. In Figure 6.1 we show the edge on (first two rows) and face on (last two rows) views of stars and gas density of our model HART321 for the other two models the main picture is similar but with a larger number of stars. Each column correspond to a different stellar age and gas temperature, respectively (see figure caption).

Here we define the virial radius (R_{vir}) as the one where the sphere of radius R_{vir} encloses a mean density 97 times denser than the critical density (ρ_{crit}) for a flat Universe $\rho_{crit}=3H^2(z)/(8\pi G)$. We have used value 97 as it is the value derived from the spherical top-hat collapse model for ΛCDM at z=0 for our cosmology (Bryan & Norman 1998). This virial radius definition is borrowed from structure growth theory and then its use is not appropriated when one wants to define a physically meaningful halo edge (Cuesta et al. 2008; Zemp 2013). To avoid this problem we also give the properties for another commonly used definition which is R_{200}, the radius that encloses a mean density equal to 200 times ρ_{crit}. Using the first definition we have obtained that the virial radius at z=0 is $R_{vir}=\sim230$ kpc in all our three models and that the mass enclosed in this radius is $M_{vir}=\sim7.45\cdot10^{11}M_\odot$. The total mass enclosed at $R_{200}=175.6$ kpc is $M_{200}=6.84\cdot10^{11}M_\odot$. This total mass is distributed in dark, stellar and gaseous matter as follows: $M_{DM}=6.45\cdot10^{11}M_\odot$, $M_*=6.1\cdot10^{10}M_\odot$ and $M_{gas}=\sim2.0\cdot10^{10}M_\odot$. The baryonic fraction $f_b=\sim0.11$, a 37% smaller than the universal value for the adopted cosmology which is 0.175.

The total rotation curve and its components of our models (black), Klypin et al. (2001) model (blue), Mollitor et al. (2014) model (magenta) and Guedes et al. (2011) ERIS simulation (green) are shown at Figure 6.2, left panel, as solid lines for the total component and long dashed, dotted and short dashed for DM, stellar and gas components, respectively. In Figure 6.2, right panel, we compare the total rotation curve of the models with values from observations of blue horizontal-branch halo stars in the SDSS (Xue et al. 2008) (data points with errorbars), from observations of López-Corredoira (2014) (green dots) and from Sofue et al. (2009) (red dots). We also compare total rotation curves with velocity rotation curves of stars and gas in our models (cyan solid and dashed lines). Changes in the rotation curves of models HART321, HART322 and HART323 are not significant. The peak of circular velocity of our models is reached at R=∼5.69 kpc with a value of

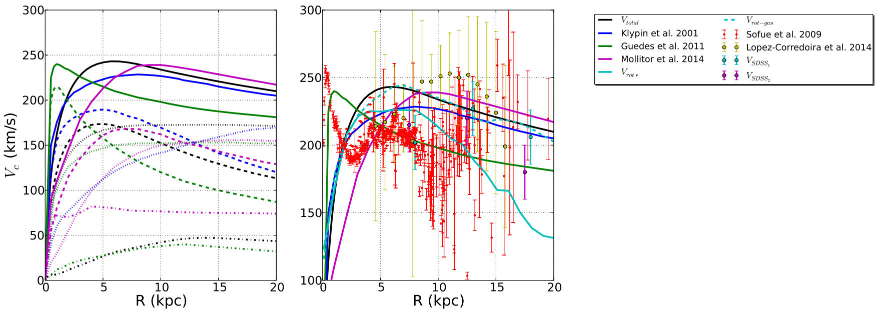

Figure 6.2: Left: Rotation curve of our simulated Milky Way sized galaxy (black), Guedes et al. (2011) (green), Klypin et al. (2001) (blue) and Mollitor et al. (2014) (magenta). The figure shows the contributions to the circular velocity $V_c = \sqrt{GM(<r)/r}$ of the various mass components: dark matter (long dashed curve), stars (dotted), gas (short-dashed) and total mass (solid curve). Right: Total rotation curves of the same models shown at left and data points. Data points come from two realizations of the rotation curve of the Milky Way from observations of blue horizontal-branch halo stars in the SDSS (Xue et al. 2008), in cyan and magenta dots, from López-Corredoira (2014), in green, and from Sofue et al. (2009), in red. The cyan lines show velocity rotation curves of stars and gas in our model.

V_c=~240 km s^{-1}, the value at a standard solar radius ($R_\odot$=8 kpc) is $V_{c\odot}$=~235 km s^{-1}. Also the ratio $V_{2.2}/V_{200}$=~1.9 km s^{-1} is well inside the observational range for the MW, that is $1.67\pm^{+0.31}_{-0.24}$ km s^{-1} (Xue et al. 2008; Dutton et al. 2010). As can be seen in the figure, models presented here resemble the one of Klypin et al. (2001) while they have a bit higher rotation curves than the one of (Guedes et al. 2011). Note that while in works as the one of Guedes et al. (2011) they obtain a peaked rotation curve in the center due to a central mass concentration, in our models this problem do not exist.

For comparison with observations, the recently measured $V_{c\odot}$ and M_{vir} (Koposov et al. 2010; Xue et al. 2008) are $V_{c\odot}$=221±18 km s$^-$1 and $M_{vir}=1.0^{+0.3}_{-0.2}\cdot10^{12}M_\odot$.

The spatial resolution in our models is high, around 109 kpc. Inside R_{vir}, and for the model HART321, we have a total number of particles of $N_{total}=7.52\cdot10^6$, where $N_{DM1sp}=7.12\cdot10^6$ and $N_*=3.94\cdot10^5$ and a total number of gas cells of $2.0\cdot10^6$. For models with a more aggressive refinement we reach values for the number of star particles and cells as high as $5.0\cdot10^7$ and $1.5\cdot10^8$, respectively. All dark matter particles inside virial radius belong to less massive DM specie and have a mass of $9.25\cdot10^4$ $M_\odot$. Star particles have masses between $\sim10^3$ and $1.2\cdot10^6$ $M_\odot$. All these parameters are summarized in Table6.1

Parameter	HART321	HART322 (z=0.14)	HART323	Observations
R_{vir} (kpc)	230.1	230.06	230.06	
M_{vir} ($M_\odot$)	$7.33{\cdot}10^{11}$	$7.29{\cdot}10^{11}$	$7.56{\cdot}10^{11}$	
M_* ($M_\odot$)	$6.1{\cdot}10^{10}$	$6.2{\cdot}10^{10}$	$6.1{\cdot}10^{10}$	$1.0{\pm}0.3{\cdot}10^{12}$
M_{gas} ($M_\odot$)	$2.7{\cdot}10^{10}$	$1.9{\cdot}10^{10}$	$1.73{\cdot}10^{10}$	$4.9\text{-}5.5{\cdot}10^{10}$
M_{hotgas} ($M_\odot$)	$1.2{\cdot}10^{10}$	$1.5{\cdot}10^{10}$	$9.8{\cdot}10^{9}$	
$M_{coldgas}$ ($M_\odot$)	$9.34{\cdot}10^{9}$	$2.10{\cdot}10^{9}$	$1.52{\cdot}10^{9}$	
N_{DM1sp}	$7.12{\cdot}10^{6}$	$6.78{\cdot}10^{6}$	$7.09{\cdot}10^{6}$	
N_*	$3.94{\cdot}10^{5}$	$23.1{\cdot}10^{5}$	$8.62{\cdot}10^{5}$	10^9
N_{gas}	$2.0{\cdot}10^{6}$	$14.3{\cdot}10^{6}$	$5.0{\cdot}10^{6}$	
m_{DM1sp} ($M_\odot$)	$9.25{\cdot}10^{4}$	$8.96{\cdot}10^{4}$	$9.25{\cdot}10^{4}$	
m_{*min} ($M_\odot$)	$2.38{\cdot}10^{3}$	$1.19{\cdot}10^{3}$	$1.18{\cdot}10^{3}$	
m_{*max} ($M_\odot$)	$1.2{\cdot}10^{6}$	$1.2{\cdot}10^{6}$	$1.2{\cdot}10^{6}$	
f_b	0.121	0.111	0.104	0.175
Resolution (pc)	109(1cell)	109(1cell)	109(1cell)	
n_{SF} (cm^{-3})	1	1	1	
T_{SF} (10^3 K)	9	9	9	
ϵ_{SF}	0.65	0.65	0.65	
CPU time (h)	2.5·104	12.5·105	4.3·104	
$c=R_{vir}/R_s$	28.5	26.9	26.8	
R_d (kpc)	2.43 (3.27/1.44)	5.3	3.2 (5.26/2.26)	$2.3{\pm}0.6$
h_{zthin} (kpc)	277-600	295-325	297-355	$300{\pm}60$
h_{zthick} (kpc)	611-1400	802-960	867-913	$600\text{-}1100{\pm}60$
$v_{c\odot}$(R=8 kpc) (km s^{-1})	239.8	219.4	233.6	$221{\pm}18$
v_c(R=2.2R_d) (km s^{-1})	243.0	212.5	236.5	
R_{peak} (kpc)	5.69	6.2	5.69	
$v_c(R_{peak})$ (km s^{-1})	243.8	221.6	237.5	
$V_{2.2}/V_{200}$	1.90	1.70	1.85	$1.67{\pm}^{+0.31}_{-0.24}$
M_X/M_{vir}	0.016	0.02	0.013	
ρ_X(r) powlaw	-0.62	-0.93	-0.83	-0.9
λ'	0.019	0.022	0.017	
$n_{gasT>10^6,R>70kpc}$ (cm^{-3})	$2.83{\cdot}10^{-5}$	$2.84{\cdot}10^{-5}$	$2.83{\cdot}10^{-5}$	$\leq10^{-4}\text{-}10^{-5}$
SFR (z=0) ($M_\odot$ yr^{-1})	0.27	0.41	0.018	0.9-2.2

Table 6.1: Parameters of HART321 and HART323 simulations at z=0 and HART323 at z=0.14. R_{vir} is assumed to be equal to R_{97}. Hot, warm and cold gas is gas at $T>5{\cdot}10^5$K and $5{\cdot}10^5K>T>3{\cdot}10^4K$ and $T<3{\cdot}10^4$K, respectively.

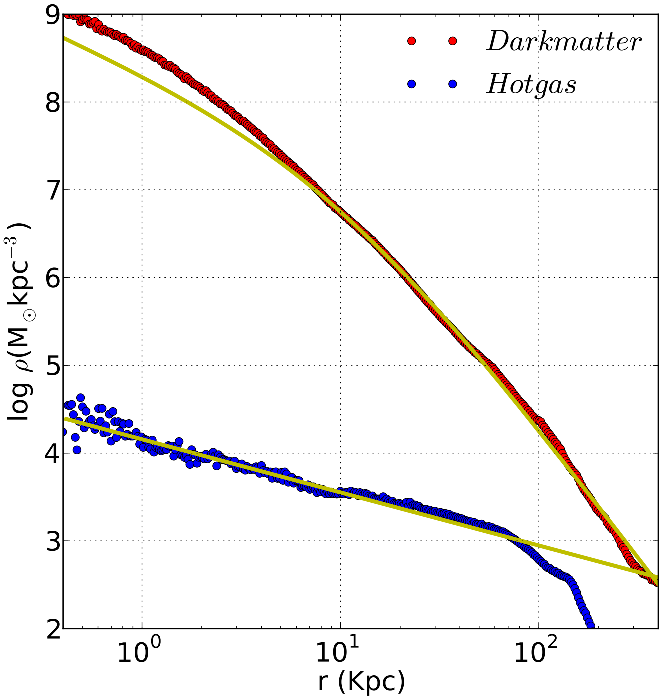

Figure 6.3: Average dark matter (red dots) and hot (T>3·10^5 K) gas (blue dots) density profiles at z=0. The solid yellow lines show the best-fit NFW profile in the range from 5 kpc, outside bar-bulge region, to R_{vir}, for the dark matter (upper curve) and the best-fit power-law profile (with slope -0.62) for the hot gas (lower curve). The best-fit NFW profile is characterized by a large halo concentration parameter c=24 as the dark matter halo contracts in response to the condensation of baryons in its center.

6.4 Component characterization

6.4.1 Dark matter component

As we mentioned in the last section all dark matter particles inside virial radius are particles of the first DM specie, the less massive one. In Figure 6.3 we show the dark matter density distribution as a function of radius (red circles) and the best fit of NFW profile for the model HART321. We avoid the central region to fit the NFW profile as in this region the disk perturbs it. The best fit gives a large value for the halo concentration of $c=R_{vir}/R_s$=28.5, 26.9 and 26.8 for HART321, HART322 and HART323, respectively. These concentration values are large due to that the dark matter halo contracts in response to the condensation of baryons in its center. The halo spin parameter as defined in Bullock et al. (2001) is λ'=0.019, 0.022 and 0.017. The λ' values we obtained falls well inside the range observed by Bullock et al. (2001) after analysing several N-body models that is .

6.4.2 Stellar component

As mentioned in Section 6.3 the total stellar mass in the virial radius of our models is M_*=6.1·$10^{10}M_{\odot}$, that is comparable with values estimated for the Milky Way (4.9-5.5·10^{10}M⊙ (Flynn et al. 2006)). However, if we observe the relation between stellar mass and total mass (see Figure 6.4) and we compare it with the predictions we see that our model fall quite above the M_*/M_{vir} values, as the MW values from observations , do (see shadowed region). This is itself an important result as if theoretical models for the ΛCDM cosmology do not fit with observations and simulations it can only mean that or ΛCDM paradigm is wrong or the galactic stellar mass in both, simulations and observations, is underestimated. In this work we have not studied this result but we deserve it for the future.

To begin with the study of properties of our simulated stellar galactic disk we need to separate stars that belong to it from the ones that belong to spheroidal components such as halo and bulge. To undertake this process we have used an extension of the kinematic decomposition proposed by Scannapieco et al. (2009). Scannapieco et al. (2009) technique uses the ratio between the real stellar angular momentum in the direction perpendicular to the disk plane (j_z) and the value expected in a circular orbit (j_c) to distinguish particles that are rotationally supported (j_z=j_c for disk stars) from ones that are not (spheroid stars). Here we decided to do additional cuts to improve the technique. We do complementary cuts in metallicity, the vertical coordinate $|z|$, the angle between the rotation direction and the vector perpendicular to the plane ($cos(\alpha)$) and finally in radius, being the last cuts we make ones that involve kinematics what will avoid kinematic biases. Some restrictions applied here require from the previous knowledge of the disk plane position. To find this position we used an iterative geometrical approach (pages 9 to 11 in Atanasijevic 1971) that is based on the selection of the plane that minimizes the total distance of all particles to the plane. To find the disk plane we only used young stars inside a sphere of 20 kpc centered to the center of mass of first dark matter specie particles. After the first iteration we start using only stars that fall nearby the plane in the newly defined vertical direction ($|z|$ <5 kpc). We checked that after few iterations we get a plane that coincides with the disk plane defined by young stars and cold gas (see Appendix C for more information about the process).

The final restrictions we imposed to star particles to be selected as disk particles are: j_z/j_c >0.55, $|z|$ <3.5 kpc, [Fe/H]>-0.5, cos(α) >0.7 and R<25 kpc. All particles that do not accomplish one or more of these restrictions are considered spheroid particles. The result of these selection can be seen in Figure 6.5 where we show the stellar mas fraction as a function of j_z/j_c for model HART321, the result is similar for the other models. In this Figure 6.5 it becomes clear that two components are present, one centered at j_z/j_c=1, i.e. rotationally supported, and another at j_z/j_c=0 that is not. The mass of the rotationally supported component (disk) is around M_d=1.82,2.16,2.17·10^{10}M⊙ and the one of spheroidal component M_{sph}=4.29,3.98,3.93·10^{10}M$\odot$ for models HART321, HART322 and HART323 respectively. Comparing this result with previous studies (Guedes et al. 2011) we see that in our models the spheroidal component is much massive than in other works and that the disk is not as massive as the one expected for the MW that is ∼5·10^{10}M$\odot$ (Flynn et al. 2006). When changing the degree of aggressively in the cells refinement criteria we observe that when increasing agressivity the disk component become more massive. This is due to that to make the aggressively in the refinement criteria higher it increases the number of stellar particles that are formed in densest regions (disk regions). Observing results from models presented here one can be concerned about if the massive spheroidal component is a large stellar concentration in the central region, a problem that was common in old cosmological simulations. However, as can be seen in the rotation curves shown in Figure 6.2, this is not the case here. We analyzed the spheroidal component and we detected that it is a dense inner halo, not a massive bulge, and that it was formed in the mayor merger occurred at z=3. We argue that this massive stellar halo will not have a big impact on our analysis of the general properties of the system and their comparisons with the MW, as the rotation curve, disk scale length, amount of gas, etc, are realistic.

After the selection process we have obtained a disk component that is a sample of 2, 18.7, 6·10^5 particles for each one of the models. From the disk component we have computed volume and surface densities in the plane, as function of radius, and we have found that it can be fitted a single or double exponential power low depending on the age of the selected population. In Figure 6.6 we show the total volume density in the plane (black) and the fitted power laws (red and blue) for model HART321. We have obtained that for young population R_d=3.27 kpc in the inner regions and R_d=1.44 kpc in the outer ones. If we fit the whole radial range from 2 to 14.5 kpc we obtain that R_d=2.43 kpc, which is in accordance with values obtained for the MW, that are 2.3±0.6 kpc (Hammer et al. 2007). In Figure 6.7, left, we show the surface density of all stars (not only disk stars) and there the dependence on the population becomes clear: while young populations show a clear two exponential behaviour (blue lines) in the surface density, old populations do not (red and pink lines). We also show, in right panel of Figure 6.7, the mean vertical distance to the plane for each one of the populations. From this figure we see how older populations have a higher mean vertical distance, as expected.

Finally we have computed the scale height (h_z) fitting first a simple exponential and later on an hyperbolic secant to the density, as function of z. In Figure 6.8 we show the density as function of the distance to the plane (z) for young disk population (0-0.5 Gyrs) and old disk population (0.5-4.0 Gyrs). We find that the scale height of young population when fitting a decreasing exponential is h_z=600 pc and h_z=277 pc if we fit a sech. For the old population, following the same procedure, we obtain h_z=1.4 kpc and h_z=611 pc, for an exponential and an sech profile, respectively. These values are compatible with the ones expected for the MW, where in the case of the young population the thin disk has a h_z=300±60 pc (Jurić et al. 2008) and thick disk h_z=600-1100±60 pc

(Du et al. 2006). Our values also follow the relation proposed by Yoachim & Dalcanton (2006) that argue that disk scale height in edge on galaxies increases in disks following $z_0 \sim 2 \cdot h_z = 610(V_c/100)$ km s^{-1}.
The same analysis of the radial and vertical density profiles have been done for models HART322 and HART323 and results can be seen in Table 6.1.

In our simulations HART321, HART322 and HART323 the stars are being formed with SFR=0.27 at z=0, 0.41 at z=0.14 and 0.18 also at z=0, $M_\odot$ yr^{-1}, respectively. These are values smaller than the one inferred by Robitaille & Whitney (2010) using Spitzer data, for the MW, that is SFR=0.68-1.45 $M_\odot$ yr^{-1}. In Figure 6.11 we show the SFR as function of the redshift (top panel) for the total (black), spheroidal (red) and disk (blue) components. In this figure it is easy to see that at slightly higher redshifts than z=0 the SFR fits within the observations for the MW. We also show in bottom panel the stellar mass as function of redshift. Some important results that can be appreciated from this figure are, first, that the spheroidal component is being build at high redshifts while disk starts its formation at around z=2.5, just after the last major merger that was at z=3. Second, it is also important to note that the star formation of spheroidal component decrease quickly after z=2 and became negligible at around z=0.5. The disk SFR also decreases fast in the last time instants, a process that is consequence of a reduction of cold gas available for star formation and that deserves a deeper study.
As we have said it is clear that SFR at z=0 is small due to that the amount of cold gas available for star formation decreases with time. This can be a consequence of, first, cold gas component is consumed at higher redshifts due to a non-realistic implementation of physical parameters that controls star formation. In this first case what we would expect to have a large amount of old stars in the disk. Second, feedback is too efficient and heats the gas inhibiting star formation. In the last scenario we would see an increase of hot gas correlated with the decrease of star formation. Finally it can also be caused by a change in the cold gas inflow due to inhomogeneities in the CGM. In this last case we would observe that our system has no or small cold gas component surrounding it. We deserve the study of the SFR decrease at z=0 for the future.

In the code used to obtain models presented here, a first approach to simulate metallic enrichment by SNe is implemented. In this approach only three species are used, i.e. alpha elements, iron elements and primordial gas (H). With this simple approach we are able to study several processes that involve metalls, in a coarse way. Figures 6.9 and 6.10 show [α/Fe] vs. [Fe/H] and [α/Fe] vs. V_{circ}, respectively, of all stellar particles in the model. From these figures it becomes clear that exists a difference in the chemical composition between disk and halo populations and also when analyzed carefully it is also possible to distinguish a small difference between thick and thin disks particles. In fact, metallicity have been used as a non-kinematical parameter to distinguish between disk and spheroidal components.

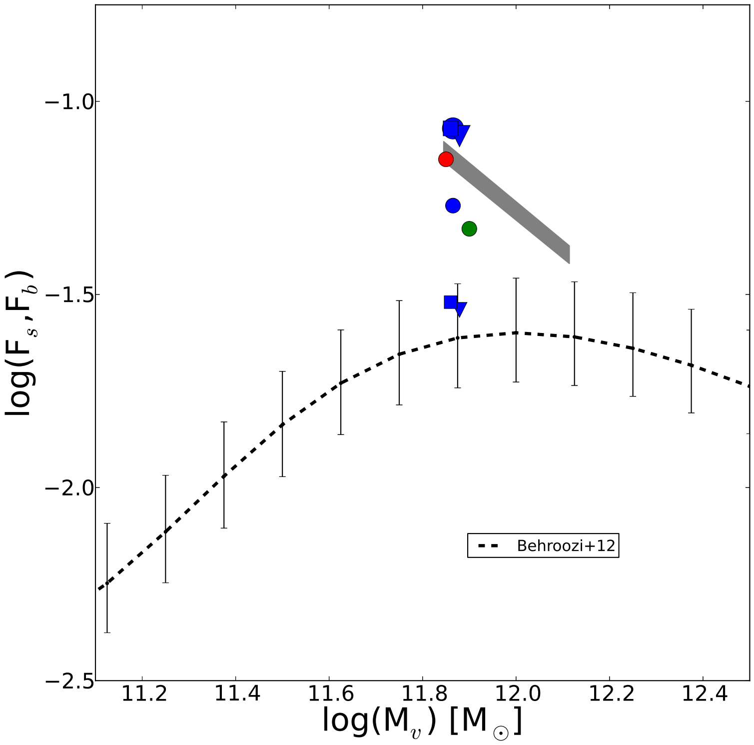

Figure 6.4: M_s/M_h map for our models HART321 (blue circles), HART322 (blue squares) and HART323 (blue triangles), using total stellar mass (large items) and only disk stellar mass (small items). Behroozi et al. (2013) observational curve inferred from observations at z=0.1 with no distinction between blue or red galaxies and its errors is shown as dashed black line, with its errorbars. Expected values for the Milky Way are shown as a grey shadowed region. Finally, red dot show values obtained in model B presented in Mollitor et al. (2014) while green dot shows the ones for ERIS simulation (Guedes et al. 2011).

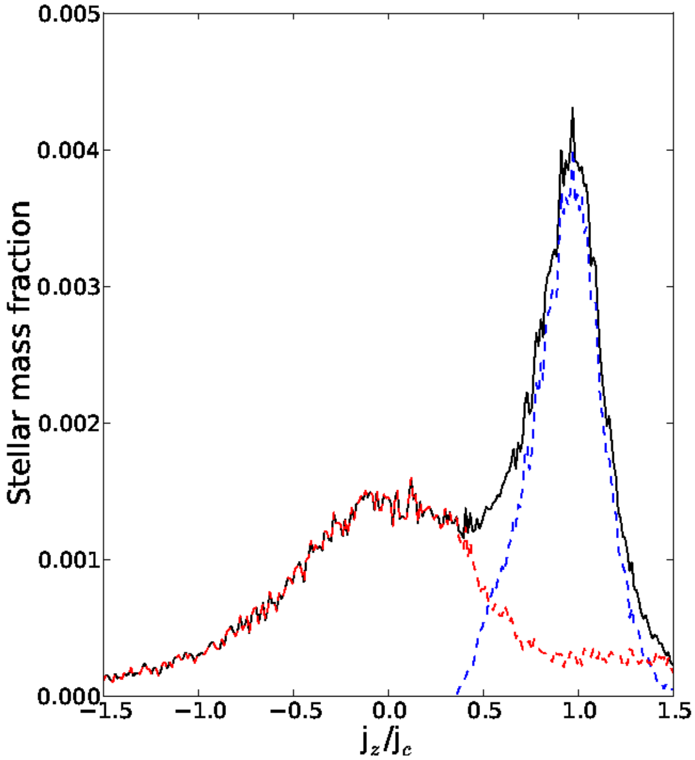

Figure 6.5: Stellar mass as function of the orbital circularity parameter j_z/j_c, describing the degree of rotational support of a given stellar particle at z=0 (black: all particles; red: spheroid; blue: disk). The stars in a centrifugally supported thin disk manifests itself in a sharply peaked distribution about unity. We have used all stellar particles inside disk region ($|z|$ <0.5 kpc and r<15 kpc) of model HART321.

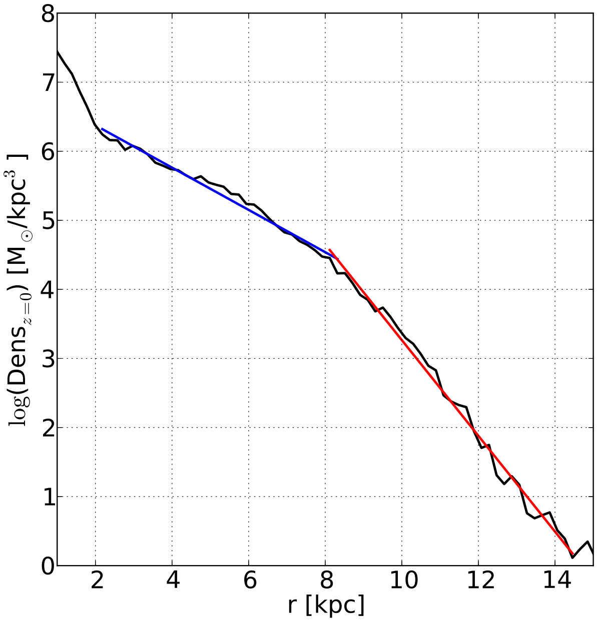

Figure 6.6: Stellar disk density profile at $|z| < 0.5$ kpc (black solid line). The solid blue and red lines show the best-fit power-law profiles to the inner and outer disk components, respectively. The inner component (2-8.5 kpc) has an R$_d$=3.27 kpc and the outer (8.5-14-5 kpc) an R$_d$= 1.44 kpc. If we fit the whole disk density profile from 2 to 14.5 kpc we obtain an R$_d$=2.43 kpc. All results have been obtained analysing model HART321.

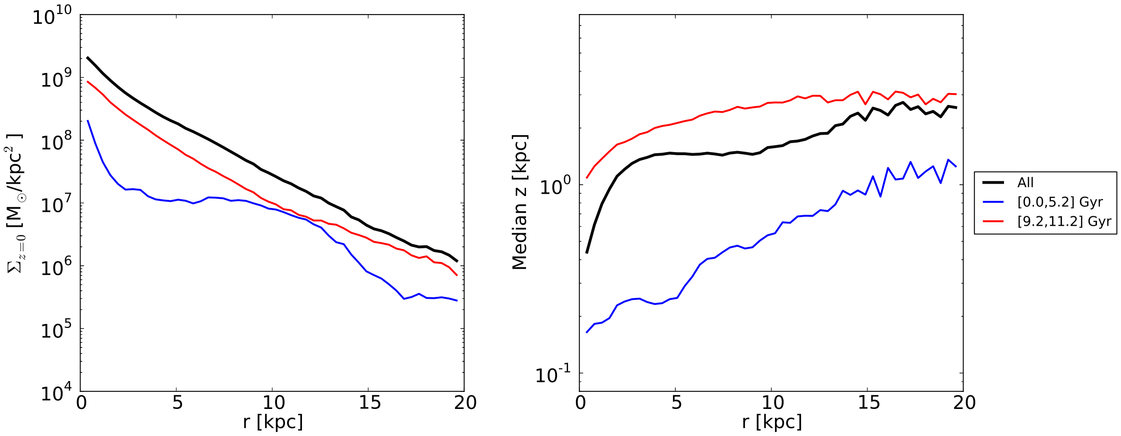

Figure 6.7: Left: Stellar disk surface density profile, in range 7-9 kpc, at redshift 0, for different populations selected by age. Right: Mean vertical distance from the disk plane for different populations selected by age (see the legend for more details). All results have been obtained analysing model HART321.

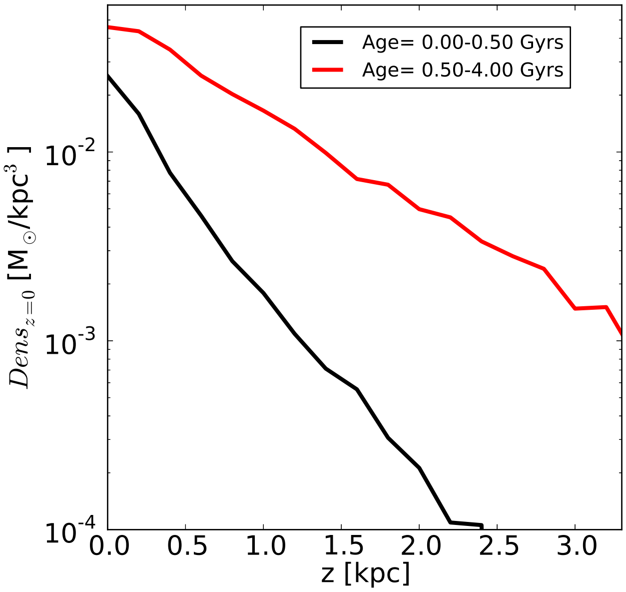

Figure 6.8: Vertical density profile of young disk stars (black) and old disk stars (red) of model HART321.

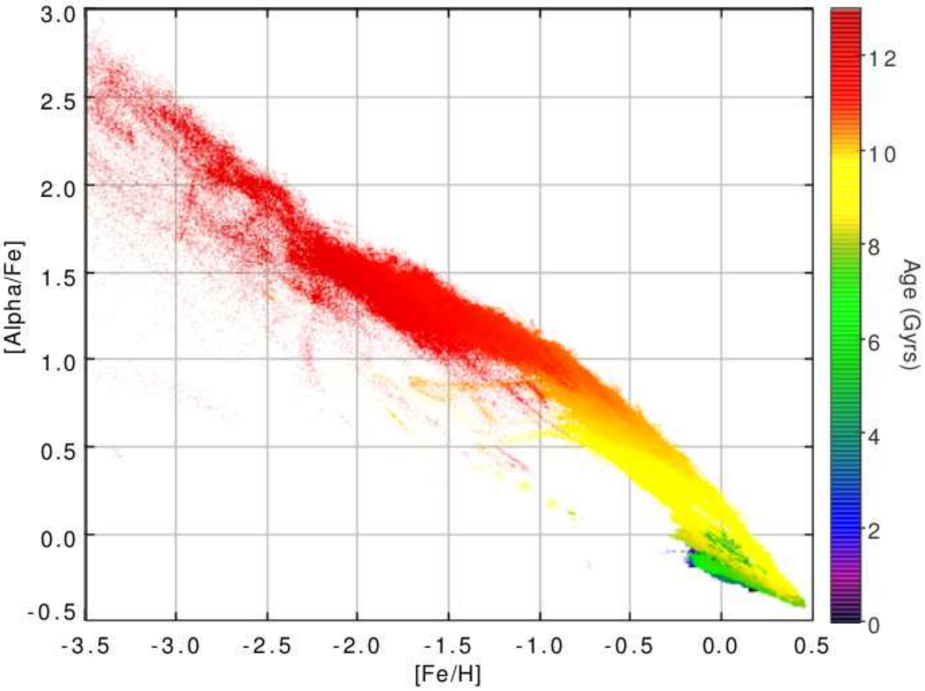

Figure 6.9: Color map of [α/Fe] as function of [Fe/H] of all stellar particles in model HART321. Color shows stellar particles age.

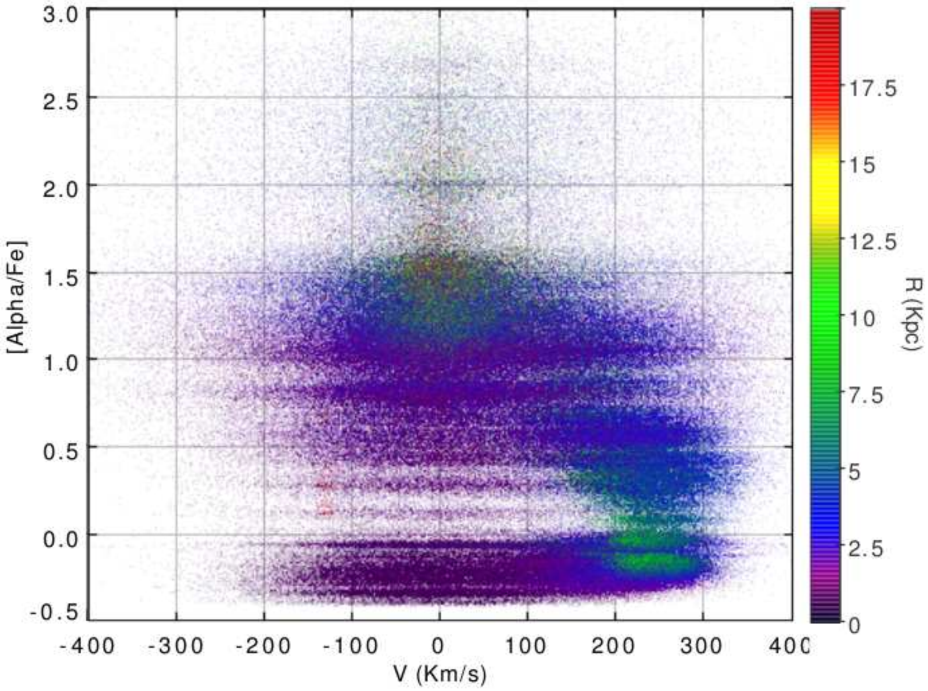

Figure 6.10: Color map of [α/Fe] as function of V$_{circ}$ of all stellar particles in model HART321. Color shows cylindrical radius from the galactic center. Disk particles are identified as having high V$_{circ}$ and low metallicities. Young disk bar can be seen as a group of stars centered at V$_{circ}$ = 0 and with low metallicities.

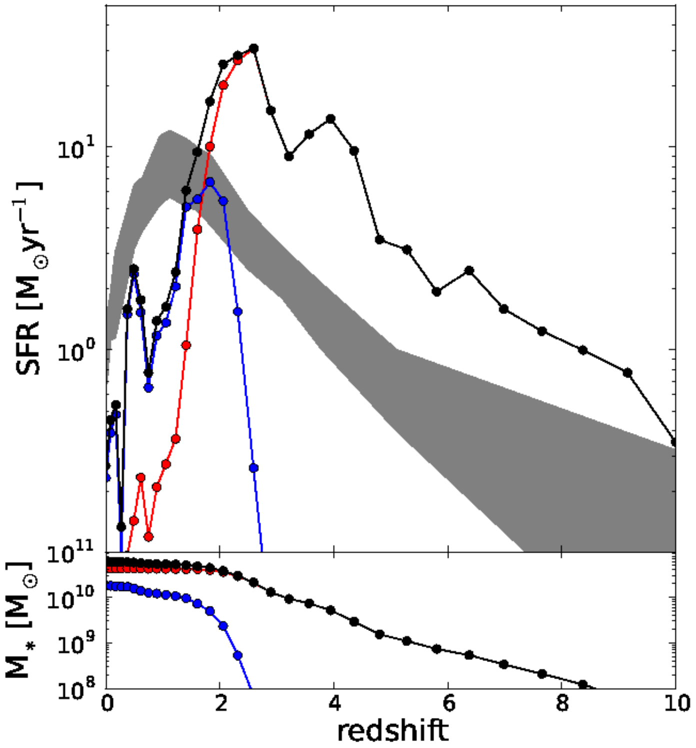

Figure 6.11: Star formation history of all star particles identified within virial radius at z=0 in model HART321. Black filled dots: total star formation rate (top panel) and stellar mass (bottom panel) as a function of redshift. Blue filled dots: same for disk star particles identified at z=0. Red filled dots: same for spheroid star particles identified at z=0. Grey shadowed region represents values estimated for the MW SFR.

6.4.3 Gas component

In our models HART321, HART322 and HART323 the total gas mass inside the virial radius is M_{gas}=2.7, 1.95 and 1.73 $\cdot 10^{1}0 M_{\odot}$. Of this mass about $9.34 \cdot 10^{9} M_{\odot}$ is in cold gas phase ($T<3\cdot10^{4}$ K) in our model HART321 while for models HART322 and HART323 is 2.10 and $1.52\cdot10^{9}M_{\odot}$. For model HART321 the value is comparable to the total mass of the molecular, atomic and warm ionized medium inferred for the MW that is ∼7.3-$9.5\cdot10^{9}M_{\odot}$ in Ferrière (2001). For the rest of models presented here the amount of cold gas is smaller due to the higher gas consumption in star formation in early ages induced by the increase in the refinement criteria agressivity. This increase on the star formation is the only effect we have observed when changing the refinement criteria and it is consequence of resolving a larger number of small dense regions in where the SF criteria is accomplished. As we describe in Section 3.3.1 star formation only occurs in dense cold gas regions, in Figure 6.12 we show the local density distribution of gas as function of radius and temperature and also the density threshold we have imposed in our models. The star formation will only occur in regions with cold gas (blue dots) and above the imposed density threshold, indicated here as a green line. It is interesting to see that these conditions, at z=0, only are being accomplished in a few radius in the inner disk regions.

The hot gas mass ($T>5\cdot10^{5}$ K) is around 1.22, 1.51 and 0.98 $\cdot 10^{1}0 M_{\odot}$ for models HART321, HART322 and HART323, and this is the fraction that is potentially X-ray luminous and then comparable with observations of ionized oxygen. In Figure 6.13 we show the gas distribution as function of temperature in model HART321. Each panel show the distribution of gas at different temperatures (see figure caption). As can be seen in the figure, cold gas is placed in disk region while hotter gas become embedded within the dark matter halo when temperature increases. Contrary to the standard assumption hot gas do not follow the dark matter radial distribution as can be seen in Figure 6.3 where we show in red the dark matter density distribution and in blue the hot gas density distribution. The hot gas density distribution can be fitted as a power law as $\rho_{hg}(r)\propto r^{-a}$ up to r=100 kpc. In Figure 6.3 we also plotted the fit for hot gas density distribution obtaining a scale factor of -0.62, -0.93 and -0.83 for models HART321, HART322 and HART323, respectively, close to values used to fit analytical models o hot gas in dark matter halos (-0.9 in Anderson & Bregman 2010) and in other similar models like ERIS (-1.1 in Guedes et al. 2011). The study of hot gas distribution and comparisons with observations are fully described in Chapter 7.

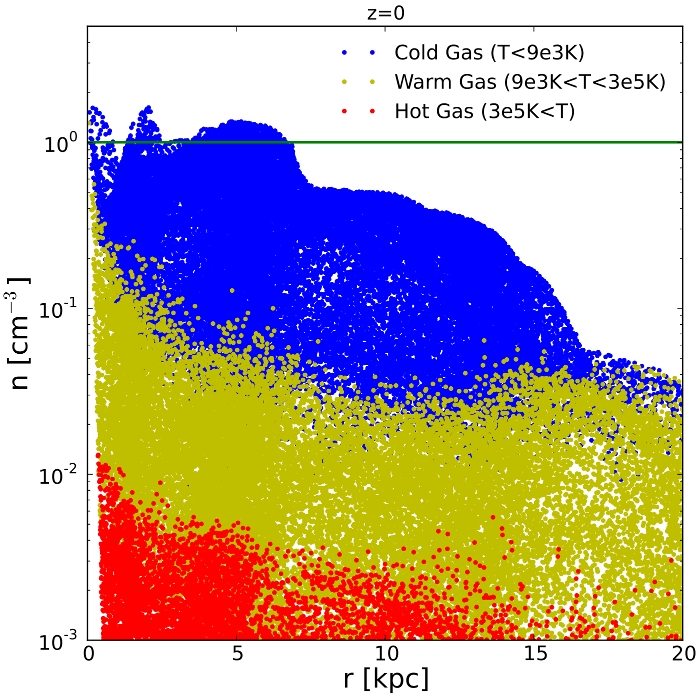

Figure 6.12: Properties of the gas distribution for a star formation threshold of 1 cm^{-3} and at z=0. The local gas density at each point of the gaseous grid is plotted as a function of its radial distance from the galaxy center. Horizontal green line mark the minimum gas density for star formation. The color-coding highlights cold (T ¡ $9{\cdot}10^3$ K, blue), warm ($9{\cdot}10^3$ K ¡ T ¡ $3{\cdot}10^5$ K, yellow) and hot ($3{\cdot}10^5$ K ¡ T , red) gas. Star formation only occurs in blue gas points above the horizontal green line.

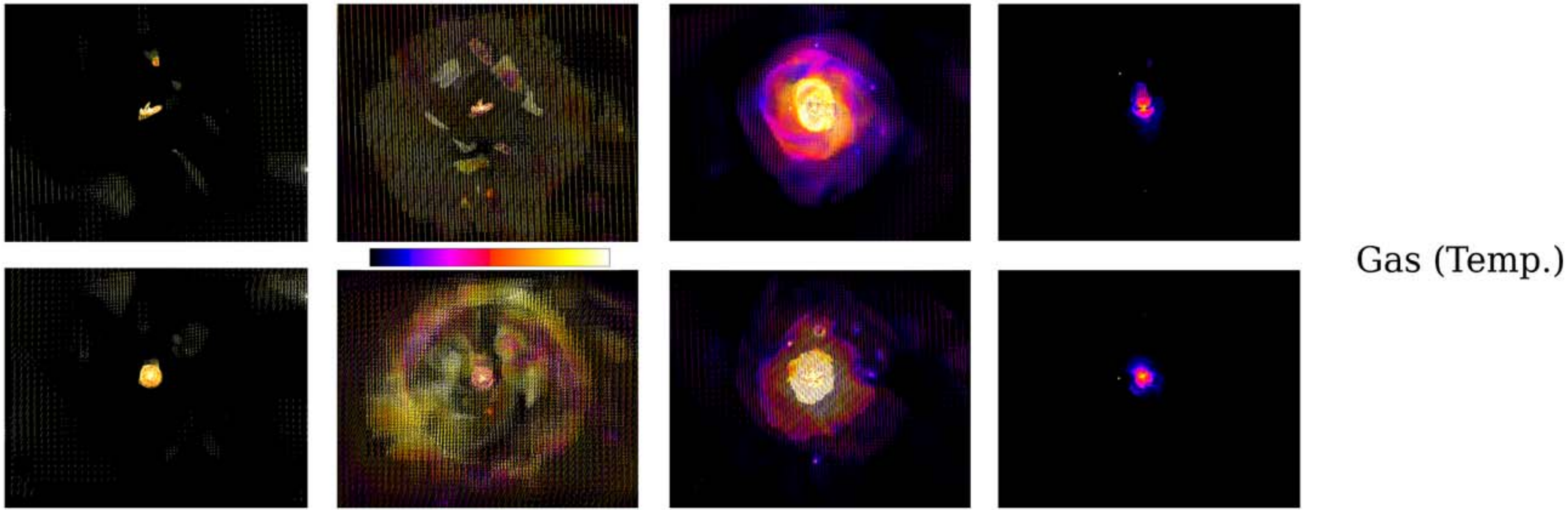

Figure 6.13: Edge on (top) and face on (bottom) gas density plot at different temperature ranges in model HART321. From left to the right, 10^3-10^5 K, 10^5-$3{\cdot}10^5$ K, $3{\cdot}10^5$-10^6 K, 10^6-10^7 K. All panels span 508 kpc in the vertical direction and 640 in the horizontal. Color code indicates gas temperature from the minimum (black) to the maximum (white).

6.5 Conclusions

In this chapter we have presented a new set of MW like cosmological N-body plus hydrodynamics simulations. Most of general parameters we presented here fit within the observational ranges for the real MW. However there are some properties of our model that do not coincide with the ones observed, as for example the SFR at z=0 which is a little bit smaller, or the amount of gas in each range of temperatures. Although these differences exist, the model is sufficiently realistic to study some of the processes observed in the real MW.

Several new models with better conditions are being completed now. We are running models with a higher number of stellar particles, better resolutions and also with new physical processes like the radiation pressure.

7

Unraveling properties of MW like models

7.1 Introduction

7.1.1 Hot gas corona around MW like systems

Apart from stellar components, galaxies also have large gaseous structures which formation and properties are not well understood. This is the case of the X-ray corona. The presence of hot corona in dark matter halos was predicted from structure formation models by White & Rees (1978) and White & Frenk (1991) and it was proposed that it should be detected by its X-ray emission. First detections where done in external galaxies by Forman et al. (1985) and later on several authors get better detections in other systems studying them deeply (e.g. Mathews & Brighenti 2003; Li et al. 2008; Anderson & Bregman 2010; Bogdán & Gilfanov 2011). In these last studies it becomes clear that the X-ray emission can be produced by several processes: low-mass X-ray binaries, active binaries and cataclysmic variables and also from hot gas produced by the SNe in the own galaxy or falling from the intergalactic medium. Bregman & Lloyd-Davies (2007), after studying the hot gas distribution in several directions, found that the large amount of hot gas emission come from gas embedded in the MW Galactic halo not from intergalactic medium. More recently, using Chandra, XMM-Newton, FUSE and other instruments it has been confirmed that a large reservoir of hot gas surrounds our Galaxy and it has been proposed that it can account for a fraction of the so called missing baryons mass. These detections have been done by the analysis of X-ray absorption lines from OVII and OVIII which only exist in environments with temperatures between 10^6 and 10^7 K, the halo has a temperature of about logT=6.1-6.4 (Yao & Wang 2007; Hagihara et al. 2010). The problem

of using this technique is that these X-ray absorption lines can be only observed in the directions of extragalactic luminous sources (QSO, AGN, ...) or galactic X-ray emitters as X-ray binaries and then gives us a limited information about the distribution and the position of this hot gas, inside the Galactic halo or in the intergalactic medium. Due o this limitation to obtain total hot gas masses it is necessary to use a simple hot gas density profile model and fit it with the available data. This process can lead to hot gas mass computations with important biases. Is here where simulations can play an important role as with them we can make full sky maps of this hot gas component and study how results about the gas distribution in halos are biased when using data from only few directions in the sky. Using hydrodynamical simulations, some attempts to reproduce the hot corona have been done. One of the first models was the one presented by Toft et al. (2002). In this model, due to the inefficient feedback, the amount of X-ray luminous components in the halo was too small. More recently, models that account for the SNe feedback and that implement new star formation processes have succeeded in to obtain results that fit better with the observations (Crain et al. 2010, 2013).
Our simulations give also realistic results in the hot gas total mass. In this work we focus the study in the possible scenarios that lead to the formation of the actual MW gas distribution, moreover we know that the feedback and star formation recipes we have used in our simulations can be critical to determine the final configurations.

7.1.2 Missing baryons

The missing baryons problem have been studied for several years without finding any satisfactory solution. The problem arose when the analysis of high precision data obtained by WMAP and Planck showed that the amount of baryons in stars, cold gas and dust components does not fit with what is predicted (e.g. Hoekstra et al. 2005; McGaugh et al. 2007). In fact, the cosmic ratio Ω_b/Ω_M is 3-10 times larger than the one observed for galaxies. This missing baryons problem occurs not only in individual galaxies (e.g., M33 is missing 90% of its baryons Corbelli 2003) but also in clusters of galaxies where it was observed using weak lensing technique (e.g. Gavazzi & Soucail 2007; Parker et al. 2007). Some studies have tried to solve this missing baryon problem proposing that galactic winds, SNe feedback or strong AGN winds ejected part of these baryons to the circumgalactic medium (CGM). Others have proposed that most of the gas never collapsed into the dark matter halos as it was previously heated due to SNe of Population III, this is known as the preheating scenario. In both cases one would expect that a high quantity of hot gas would be found by observations, both in halos and CGM. To find out which one of the proposed theories can solve better the missing baryon problem it is important to measure the amount of warm-hot gas phase present in the CGM and also its metallicity. To know the metalliciy is important as it gives information about the heating mechanism: hot gas with low metallicities is indicative of a Pop III SNe preheating while a more metallic gas suggest that it has been enriched inside disks via disk SNe and stellar winds, before being heated up and ejected.

Supporting the disk origin hypothesis, different authors agree with the idea that the adoption of very strong feedback physics, what drives galactic-scale winds, causes metal-enriched hot gas to be expelled out of the star-forming disk possibly to distances comparable to or beyond the virial radius. This process also lies in the heart of obtaining realistic simulations of disk galaxies (Guedes et al. 2011; Marinacci et al. 2014). By this mechanism gas is temporally placed far from star forming regions delaying the star formation and preventing the formation of an old bulge in the center of the system.

As we describe in Section 7.1.1 from the analysis of OVII and OVIII X-Ray absorption lines in extragalactic sight lines, several authors obtained values for the hot gas distribution in the MW halo (Gupta et al. 2012, 2014) that suggest an important part of missing baryons are in this hot gas phase. In fact they argued that this hot gas component in the halo can account of about 10-50% of these missing baryons. They show that the warm-hot phase of the CGM is extended over a large region around the MW, with a radius over 100 kpc, with a mass around 10^{10} $M_{\odot}$. Also from these observations some authors suggest that this component is in a non isotropic distribution, however as we have pointed in the last section the measures are limited to directions with extragalactic sources (QSO, AGN, ...) and then results are not conclusive. Other studies also suggest that the presence of this hot gas phase can explain part of the isotropic gamma-ray background observed in Fermi Gamma-ray Space Telescope (Feldmann et al. 2013). Also from observations of X-ray diffuse emission in external galaxies several authors have found that large amounts of hot gas are present around most of the galactic halos (Bogdán et al. 2013). However also in the case of external galaxies there is not enough mass to account for the total mass of missing baryons (Strickland et al. 2004; Tüllmann et al. 2006).

Here we check how hot gas in the halo and intergalactic medium of our simulated system can account for the missing baryons in galaxies. We have found that also in simulations it is not enough to account for the total missing mass.

7.2 Hot gas component

7.2.1 Spatial distribution

As introduced in Section 6.4.3 the amount of warm-hot gas in our models is in between M_{hot}=0.98-1.2$\cdot10^{10}M_{\odot}$. This warm-hot gas with a temperature above $5.0\cdot10^{5}$K is embedded in the inner dark matter halo but mostly outside the stellar disk. Here we show several observational measures of hot gas distribution in full sky maps taken as observing from a position at 8 kpc far from the center, resembling the Sun position, and at an arbitrary angle (see Figure 7.2). We have computed values for the hydrogen column density, dispersion measure (DM) and emission measure (EM) (see Equations 7.1, 7.2 and 7.3, ρ_X is the volume density of element X, S is the surface, n_e is the electron density and L the length.)

and we have obtained values well inside the values obtained from observations (see Gupta et al. 2012). From Figure 7.2 we also observe that the distribution of warm-hot gas inferred from all measures is far from isotropic. Gas in this warm-hot phase is concentrated in intermediate latitudes, avoiding disk region, and present but not so concentrated in galactic poles. Another interesting result we get from these figures is that the gas distribution is not symmetric with disk plane what suggest some degree of interaction with extragalactic medium. To study it deeper we have analysed the metallicity and velocities of hot gas cells. In Figure 7.3 and 7.4 we show all sky maps of warm-hot gas metallicity distribution as seen from the Galactic center. What we see is that gas metallicity do not depend on the galactic longitude (l) (Figure 7.3, left panel) while it is clear that it depends on latitude (b) (Figure 7.3, right panel). It is also clear that exists a low metallicity component at positive latitudes that is not present in negative ones, where metallicity is much higher (see Figure 7.4). To put some light to the origin of this bimodality on metallicity we made a set of three colour maps showing the projected metallicity and velocities at each one of the principal planes (see Figures 7.5 and 7.6). Figure 7.5 (X-Y plane) shows how gas follows disk rotation with only some small inhomogeneities. Figure 7.6 show a more complex scenario with several vertical motions and metallicity gradients. In this figure it becomes clear that several low and high metallicity hot gas flows are present in the halo. However the most interesting panel is the one that shows the X-Z plane. This panel shows up clearly the bimodality in metallicity that exists in the vertical direction and also that low-metallic hot gas flow has a mean motion that brings it from outside to inside the system, i.e. is falling from IGM. On the other hand high-metallic hot gas flows observed in the southern hemisphere have the opposite behaviour only in some positions, i.e. in these regions gas is going from inside to outside the system. While it is easy to understand and interpret why low-metallic hot gas is falling inside the system, and why in some cases hot gas departs from it (SN feedback, stellar winds...) it is not so obvious why a part of gas with a high metallicity is behaving differently. We suspect that this high-metallic component is associated with a small gaseous satellite that is passing through the system at z=0 (see Figure 7.7). To confirm this point we have made the same velocity-metallicity maps for several snapshots back to z=0.5 and we have found that the satellite hypothesis is compatible with what we observe. We see that in some instants hot gas with enhanced metalliciy depart from the disk due to feedback of stellar component. We also see that in determinated cases low metal flows appear coming from CGM. Finally at around z=0 we see that a gaseous satellite approaches to the main galaxy perturbing hot gas flows. It is an interesting result that needs for a more detailed study to be confirmed. Finally in therms of metallicity we have also observed that total gas that is inside disk plane have a mean metallicity that is similar to the one of hot gas outside the plane, a value that is around -0.64 dex (except for the high and low metallicity flows discussed here).

A conclusion we obtain from the study of metallicity and mean velocities is that some hot gas is falling from IGM as suggested by some theories, both from low enriched medium

	z	M_{vir} ($10^{11}M_\odot$)	M_{hotgas} ($10^{10}M_\odot$)	ϵ_{SF}	n_{SF} (cm^{-3})	DM_{sp}	n_{ref}
HART321	0.0	7.33	1.20	0.65	1	5	11
HART321	0.48	6.64	0.86	0.65	1	5	11
HART321	0.82	5.97	0.47	0.65	1	5	11
HART321	1.35	4.85	0.32	0.65	1	5	11
HART320	0.0	7.76	1.35	0.60	1	4	11
HART242	0.0	13.9	1.68	0.70	1	4	10
HART242*	0.0	10.8	2.14	0.70	1	4	10
HART240	0.0	13.9	3.06	0.10	1	3	11
HART250	0.0	6.57	0.85	0.70	1	5	11
Observed MW	0.0	6-12	$3.8^{+6.0}_{-0.5}$	-	-	-	-

Table 7.1: * indicates we have analysed a system that is placed in the low resolution region.

and high enriched satellites, but also that the disk is free of hot gas and then that SNe and stellar winds are pushing the hot gas to the inner halo regions.

$$n_X = \int_{los} \rho_X dS \tag{7.1}$$

$$DM = \int_{los} n_e dL \tag{7.2}$$

$$EM = \int_{los} n_e^2 dL \tag{7.3}$$

Also from our simulations we have started to study a weak dependence that exists between the dark matter halo mass and the total amount of hot gas in the galactic systems. Analysing several models both MW like models and other with higher and smaller masses we have found that in general when the dark matter halo mass increases the hot gas mass also increases but at a higher rate. We show our results in Table 7.1. Although it is clear that some kind of relation exists it deserves a deeper investigation. It is important to add that this relation we have observed is evident unless when changing drastically the initial parameters (see model RUN4 vs RUN4.2). If finally confirmed this can be a new method to restrict the virial halo mass in galaxies.

7.2.2 Total hot gas mass: simulations vs. observations

As it is previously pointed out it is difficult to infer the total hot gas mass in the MW as we have information only about few directions. As in simulations we have information about the total mass and its total distribution we have studied how many directions we need to observe to obtain a value for the total mass that is close to the real one.

Target	l (deg)	b (deg)	log(N(OVII)) (cm^-2)	L (Kpc)	$M_{total,baryons}$ ($10^{11}M_\odot$)
Mrk421	179.83	65.03	16.22	239.	10.12
PKS2155-304	17.73	-52.25	16.09	239.	7.53
Mrk290	91.49	47.95	16.14	239.	8.45
Mrk509	35.97	-29.86	16.70	239.	30.73
3C382	289.95	64.36	16.50	239.	19.37
Ark564	92.14	-25.34	15.82	239.	4.05
NGC 3783	287.46	22.95	16.30	239.	12.22
H2106-099	40.27	-34.94	16.23	239.	10.40

Table 7.2: OVII column density values obtained for 8 different directions in Gupta et al. (2012). Assuming L=239 kpc, although the X-ray emitters are much farther away (QSO, ...), we have computed the total baryonic mass. We have assumed an spherically homogeneous gas distribution, a metallicity of $Z=0.2Z\odot$, a ionization factor f_{OVII} of 0.5 and a solar oxygen abundance of $A_O/A_H=8.51\cdot10^{-4}cm^{-3}$.

First of all we have located our mock observer at 8 kpc from the galactic center (i.e. similar to solar position) inside the galactic plane and at a random angle. For comparison we show in Table 7.2 the observations of OVII column densities presented in Gupta et al. (2012) and the total baryonic mass obtained when assuming an spherical uniform gas distribution. In Table 7.3 we show the results we have obtained when making observations at the same directions as the ones in Table 7.2. As in our simulations we have not realistic chemical species like oxygen we have assumed that we are observing all hot gas particles. We have computed, from values at each direction, the total galactic hot gas mass assuming a spherical uniform gas distribution like in Gupta et al. (2012). We find that in all the studied directions we obtain an overestimation of hot gas mass in the system. This happens because most of the hot gas is placed at intermediate latitudes as can be seen in Figure 7.2 and the observations have been done just in mid latitudes to avoid disk emission.

The next step we have done is to plot in an histogram the values of hot gas column density computed for all directions in the sky (see Figure 7.8). From this histogram we observe how the hot gas column density follows a nearly symmetric distribution function peaked $\log(N_H)=-1.4$ but with higher dispersion to higher density region. As to compute the total baryonic mass in real galaxies it is usually used to assume an spherically uniform gas distribution where the density is taken as to be the mean value coming from observations, we have designed a test to determine the number of observations randomly distributed in the sky that are needed to recover a distribution with a median value that fits within the real one. First, we computed the median value of the real distribution (see Table 7.4). The next step has been to make 100 independent experiments in where we have computed the median of the distribution obtained from observing to 5, 10, 50, 100,

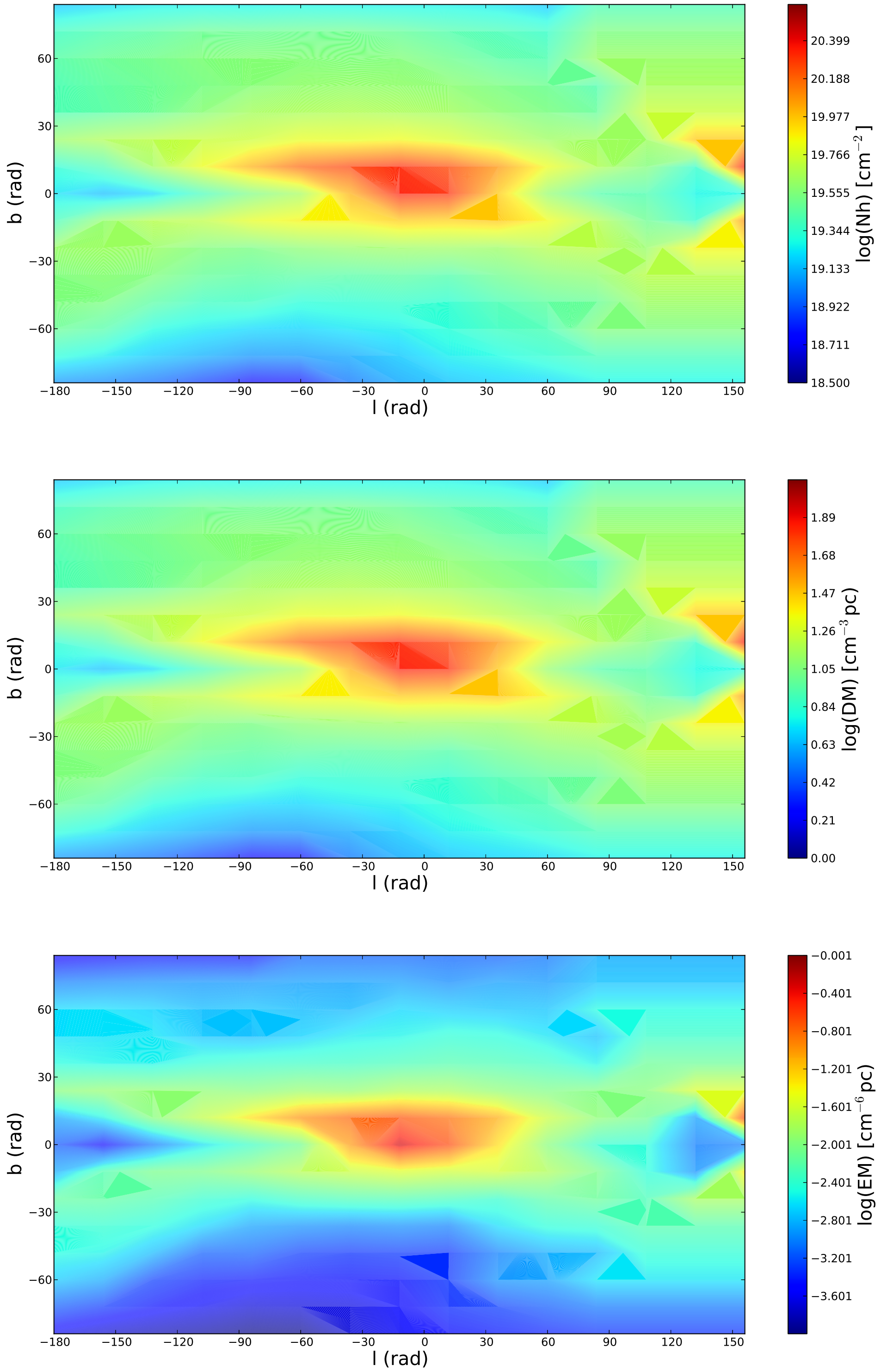

Figure 7.1: Hot gas (T>5·10^5) column density (top), dispersion measure (DM, center) and emission measure (EM, bottom) in a full sky view in galactic coordinates. All values have been computed as observed from R=8kpc and at an arbitrary angle.

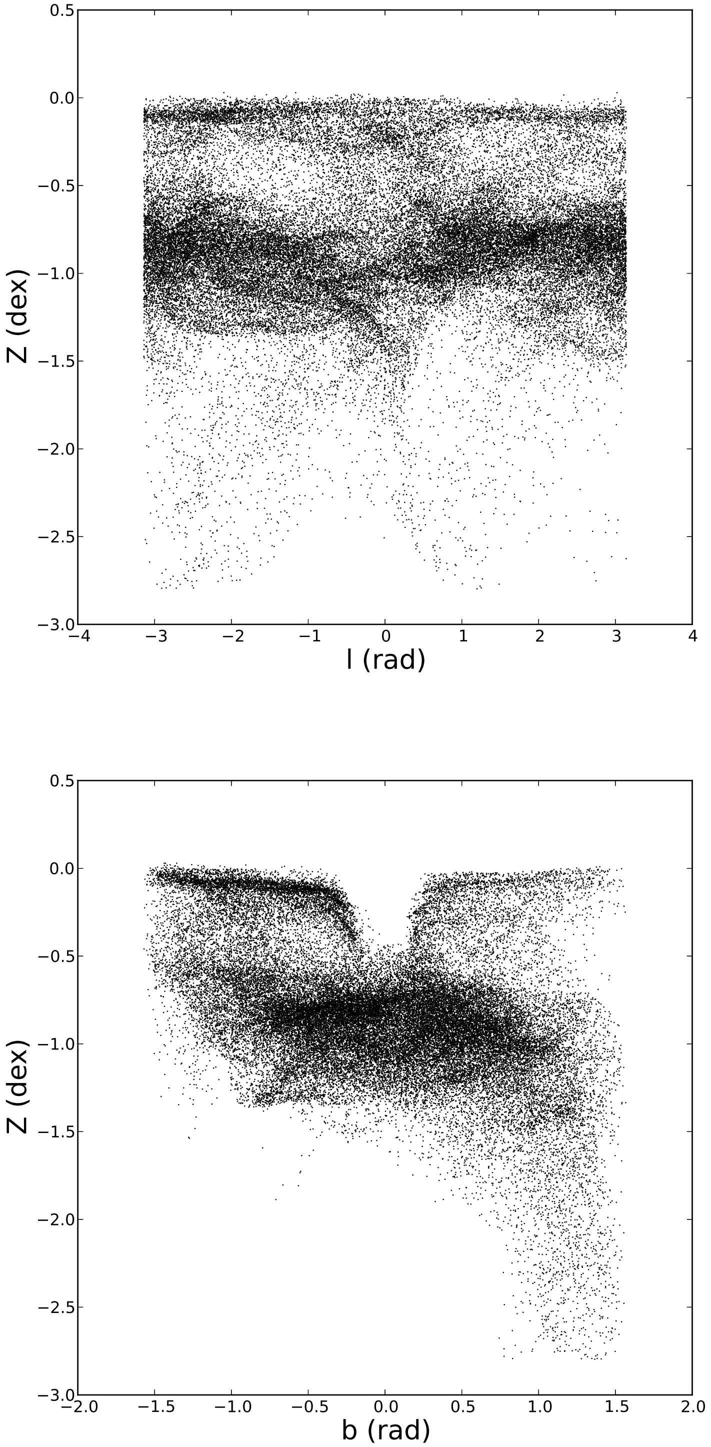

Figure 7.2: Hot gas (T>5·10^5) view in galactic coordinates. Left: metallicity as function of longitude. Right: metallicity as function of latitude. All values have been computed as observed from the galactic center.

	l (deg)	b (deg)	N(H) $(10^{19}\mathrm{cm}^{-}2)$	L (Kpc)	$M_{total,Hotgas}$ $(10^{10}M_{\odot})$
FoV1	179.83	65.03	11.31	230.1	
FoV2	17.73	-52.25	2.02	230.1	
FoV3	91.49	47.95	2.49	230.1	
FoV4	35.97	-29.86	2.68	230.1	
FoV5	289.95	64.36	4.04	230.1	
FoV6	92.14	-25.34	2.33	230.1	
FoV7	287.46	22.95	3.54	230.1	
FoV8	40.27	-34.94	2.59	230.1	

Table 7.3: L set to R_{vir}. Same fields as in Table 7.2. The total hot gas mass in the simulation, up to R_{vir}, is M_{vir}=1.2·10^{10}. We have defined hot gas as gas at T>5·10^5K.

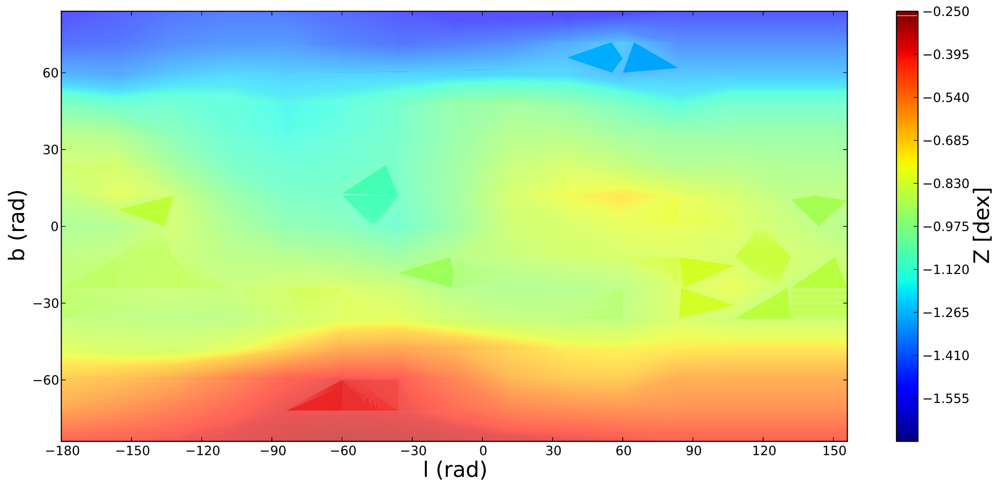

Figure 7.3: Hot gas (T>5·10^5) metallicity ([M/H]) in a full sky view in galactic coordinates. All values have been computed as observed from the galactic center.

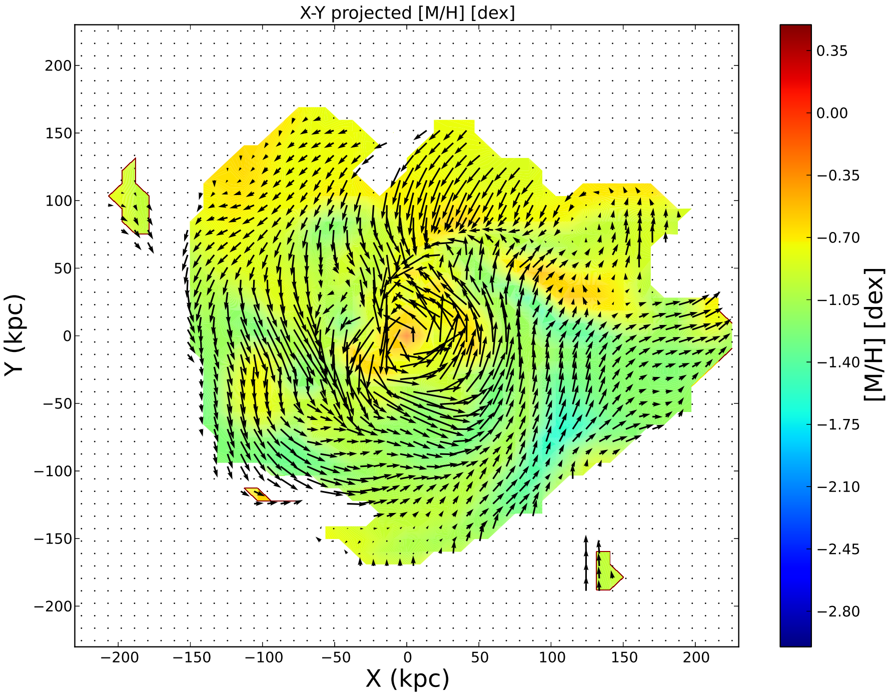

Figure 7.4: Hot gas (T>$5{\cdot}10^5$) projected metallicity (colour map) and velocity (arrows) in the principal plane x-y.

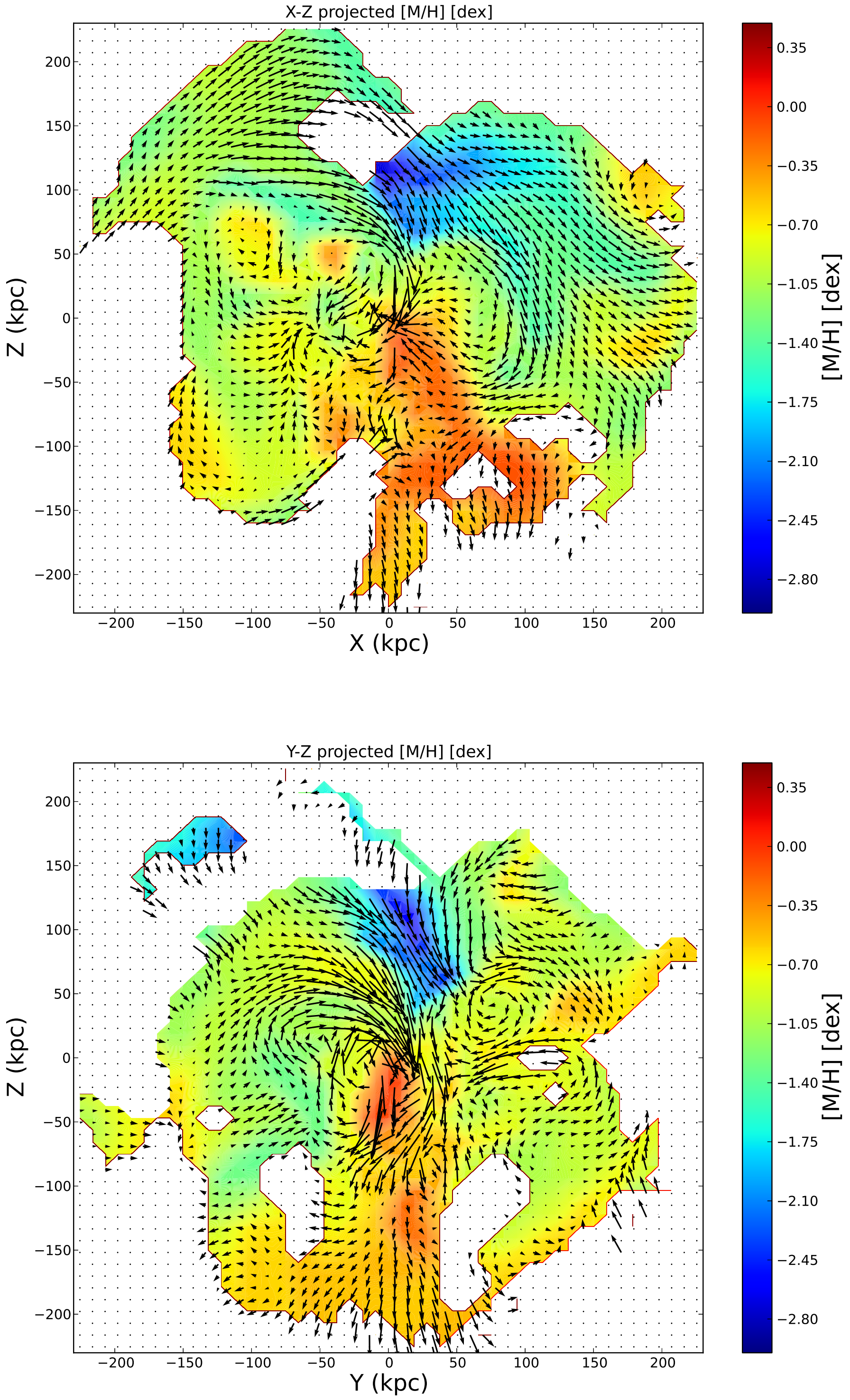

Figure 7.5: Hot gas (T>$5{\cdot}10^5$) projected metallicity (colour map) and velocity (arrows) in two principal planes, x-z (top) and y-z (bottom).

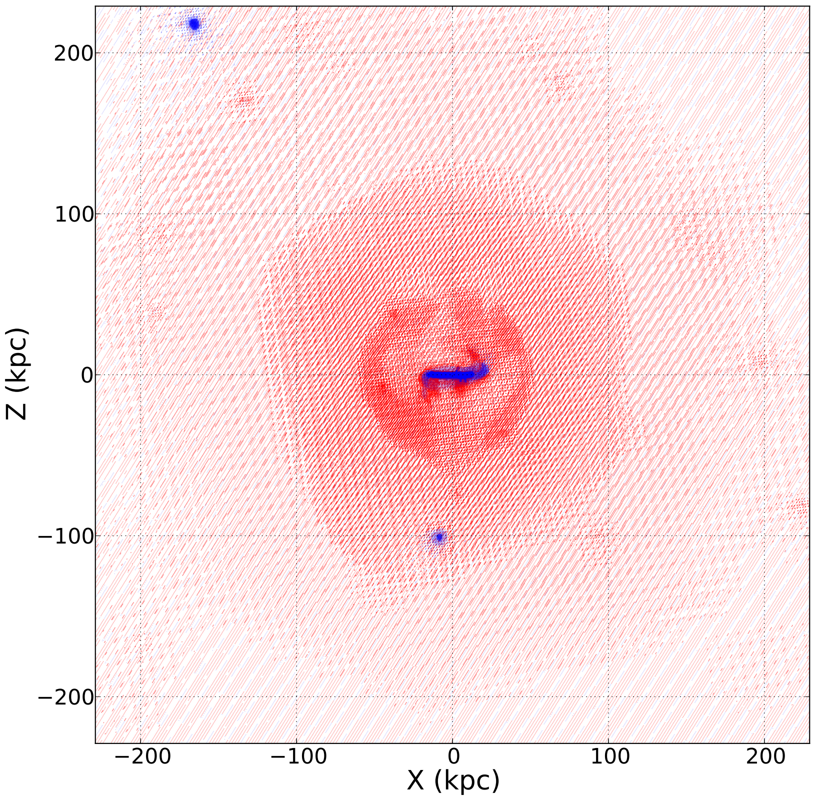

Figure 7.6: Warm-Hot gas (10^6 >T>10^5) in red and cold gas (10^4 >T) in blue for model HART321 at z=0.

200, 500, 1000, 1500 and 2500 Monte Carlo randomly distributed directions each time. We have computed the median value and the standard deviation from the 100 experiments, for each number of randomly distributed directions. Results from this experiment are presented in Table 7.4 where we can clearly see that between 50 and 100 random directions are needed to recover the real median of the distribution with a small dispersion what will give a reasonably good approach to the real baryonic mass in the galaxy. From this work we conclude that the number of observations that are commonly used in the bibliography is not high enough to ensure a good computation of the total baryonic mass in galaxies.

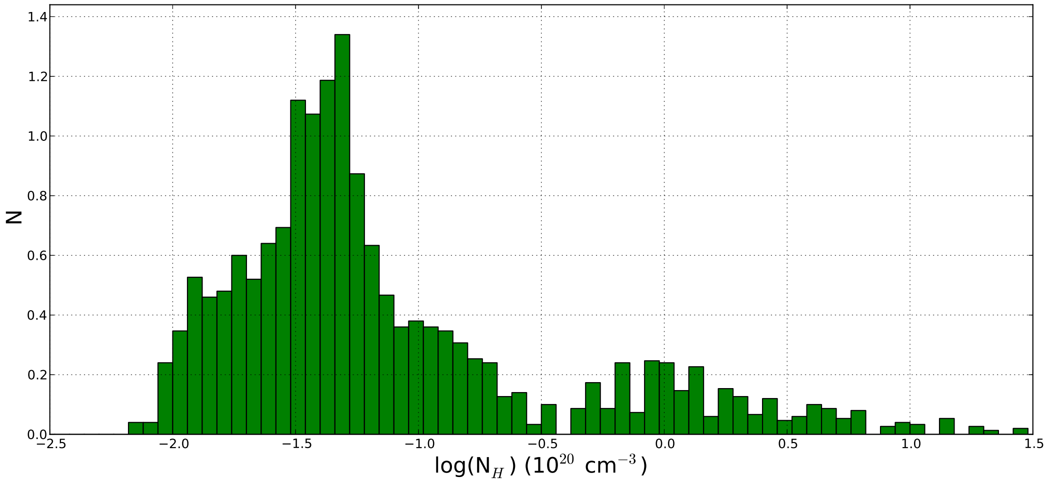

Figure 7.7: Histogram of full sky values for the hydrogen column density in simulation HART321, at z=0.0.

N_{obs}	5	10	50	100	200	500	1000	2500	Total
Median ($\log(N_H)$)	-1.1957	-1.2678	-1.3126	-1.3216	-1.3273	-1.3186	-1.3188	-1.3213	-1.3192
st.dev	0.3714	0.2242	0.0717	0.0372	0.0289	0.0187	0.0127	0.0086	0

Table 7.4: Median and standard deviation of hot gas column density distributions obtained from N observations randomly distributed in the sky.

7.3 Two misaligned bars

The first result we have obtained when analysing the models is the presence of two misaligned stellar bars in the disk region. In Figure 6.1, top panels, this result is evident. First panels, at left, show the distribution of young stars in the disk and in this plots a first bar is present. In the last panels, at right, it is shown the distribution of old stars and there, again, a bar is present but in a complete different orientation. Although Figure 7.1 shows only results for HART321 we state that this structures are also present in the other two models.

We have studied the origin of both structures and we have found that young bar is formed from secular evolution of disk particles in the last 8 Gyrs while old bar has a completely different origin. To study the formation of the old bar we have selected a group of particles that truly belong to the bar at z=0 and we have followed them back in time (see Figure 7.9). It is surprising to see how this component is generated at the last major merger of the system that occurred at z=3. As can be seen in Figure 7.9 most of stellar particles are presents in one of systems involved into the major merger at z=3. From this result we state that old bar is a fossil of this last major merger.

As we have pointed, these two bars are misaligned. Because of this configuration is very rare we were concerned about the stability of such a system with two bars misaligned near 90 degrees. To understand if this system is stable or not and why, we have studied properties of each one of the bars independently. What we have found with these studies is that the young disk bar is much shorter and concentrated that the old spheroidal bar, that is longer and less dense in the central region (see Figure 7.10). On the other hand, the rotation frequency of both bars is similar. These two results suggest that the configuration we observe in our simulation can be stable for a long time as the interaction between both components is small, due to the low density of old bar in young bars' region and to their similar pattern speed. It will be very interesting if such a system exists in nature and under which conditions.

7.4 Conclusions

In this chapter we have presented the first results we have obtained from our MW like models. First, we have analysed the distribution and origin of hot gas in our system. We have seen that hot gas is not distributed homogeneously all around the galactic disk but it is placed away from this region and also not so dense in galactic poles. We have also seen that several hot gas streams are presents in the halo some with low metallicity coming from the IGM others with higher metallicity departing from the disk and others also with high metallicity that can be interpreted as accreted from satellites. Finally, after making mock observations of hot gas observations and applying similar methods to the ones that are used to determine the total baryonic mass inside real galaxies, we conclude that more than 50 observations randomly distributed into the sky are needed to recover the real

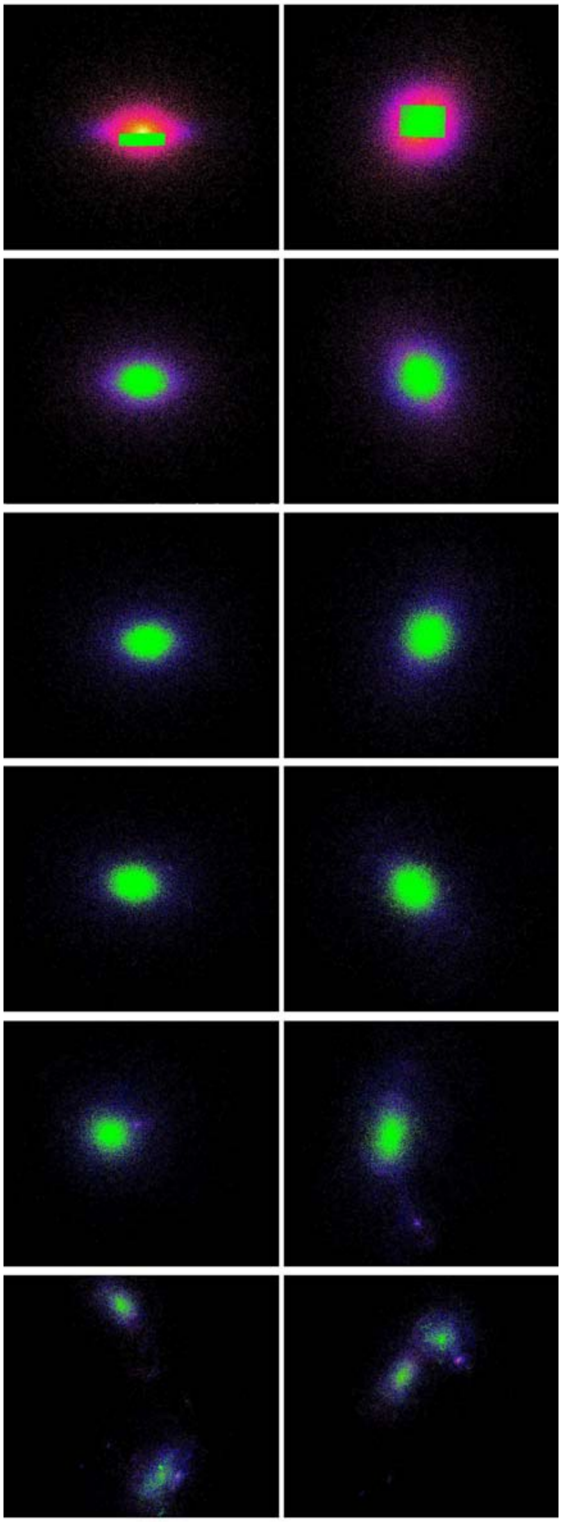

Figure 7.8: Edge on (left) and face on (right) views of the old stellar component of model HART321 at different evolution times. In green, particles that truly belong to the old stellar bar at z=0. From top to the bottom snapshots at z=0, 0.5, 1.0, 1.5, 2.0 and 3.0.

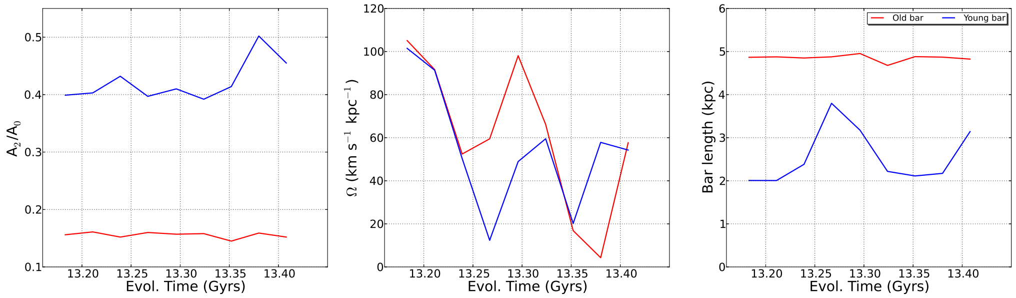

Figure 7.9: Evolution of the amplitude (left), pattern speed (center) and length (right) of old bar, in red, and young bar, in blue, in the model HART321.

mass. This result is important as in the most recent works the used number of directions is the order of 10 or less what make the results not conclusive.

Another important result we have presented is the presence of two misaligned bars, one created by secular evolution from stellar disk particles in the last 8 Gyrs of evolution and another one created in the last major merger of the system at z=3 and then. Both old and young bars rotate at a similar speed and are misaligned at about 90 degrees. The system remains stable due to that the young bar is smaller and concentrated while the old one is much larger and less concentrated in the center, and also to both have similar pattern speed.
Other important result we have found is that it exists a relation between the dark matter halo mass and the amount of hot gas present in the system what, if confirmed will give us a new technique to infer the total mass of galaxies.

7.5 Outcomes and legacies

7.5.1 Analysis of kinematic parameters

In this chapter we have presented a new set of MW like models that include a lot of new physical processes when compared with collisionless N-body presented in Chapters 4 and 5. These new models include from gas physics to the effect of the environment onto the galactic disk evolution and they also have a high resolution compared with previous cosmological models. Such models give us the opportunity of making the same kinematic analysis we have done in Chapters 4 and 5 but in a much more realistic scenario.
After finishing this thesis the work we have planned to undertake first is the study of vertex deviation parameter and spiral arms rotation frequencies in these N-body plus hydrodynamics models.

7.5.2 Study of M_h/M_{hotgas} relation

In Section 7.2 we have purposed that a new method to determine the total virial mass in galaxies may be the determination of their total hot gas mass. We have seen that possibly it exists a correlation between total mass and hot gas mass in galaxies. However it deserves a deeper investigation to be confirmed. We will make a new set of models with different halo masses to confirm that this relation exist and if so, to test how the method can be applied.

7.5.3 Study of the SRF decrease at z=0

In the MW like galaxy model we have presented in this chapter, the parameter that fits worst with that observed for the MW is the SFR at z=0. This problem is also common in other MW like models obtained using different codes and with different implementation of physical processes. Some of these works show SFR too high at z=0 (Mollitor et al. 2014) while others present the opposite situation, as in happens in our models. Several processes can lead to a high variety of results for the SFR at z=0. All of these processes are related with the availability of cold gas in the disk, to form stars. Strong feedback can heat up disk gas, decreasing the amount of cold gas available for star formation. Moreover, weak feedback at high z can lead to a early consumption of cold gas and to an important old stellar population. To study how feedback affects the SFR can be an interesting work but it is not the only process that needs to be taken into account when looking for processes that affect this parameter. For instance it is also important to study the CGM as it is from there that new cold gas can fall over the galactic disk enhancing SFR. An interesting experiment can be to compare two systems with the same feedback strength but differing in the amount of cold gas present in its CGM. In this scenario we expect that the system with a CGM richer in cold gas will have higher SFR than the one poorer in cold gas. We expect this, first, because if feedback is not strong enough to stop it, cold gas flows will be more intense in the former than in the latter case and, second, because the feedback needed to stop a more massive cold gas flow will be more intense. Finally it is obvious that parameters that control the star formation (i.e. star formation efficiency and density threshold for star formation) play an important role in controlling the rate of consumption of the disk cold gas.

As can be seen from the previous discussion the study of SFR in simulations is not trivial and it also deserves much deeper research. As we have mentioned we want to make a new set of models from where we can study the effects of CGM and feedback in the SFR, among others.

7.5.4 Satellite galaxies and stellar streams

The number of particles and the resolution in our models are high enough to ensure that we can undertake a deep analysis of stellar streams and satellite galaxies. Only from the

first look on the satellites we have seen several interesting features, for instance we have found that several of them have more than one stellar population, i.e. they have had more than one star formation burst. Other interesting property of satellites in our models is that some of them have no stellar component at all but only cold gas embedded in a DM halo. It will be very interesting to analyse where the limit is in DM halo mass to contain baryons embedded within them. Finally we also find that some satellites that are too small and too far from the main galaxies to contain stars, they actually have. This last finding is one of the most interesting results we have obtained from our first look into satellites as it suggest that interactions between small dark matter halos can drive to star formation bursts and then to form isolated extremely dwarf galaxies.
Also interesting will be to study the amount of satellites that are orbiting our models and compare the result with the predictions of ΛCDM cosmology.

7.5.5 Warm Dark Matter models

During this thesis we have not only worked in the development of a MW like system under the ΛCDM cosmology but we have also started the process of generating similar systems under WDM cosmologies and with different warmion energies (2 KeV and 3 KeV). We have made the first low resolution simulations and we have selected the MW like halo candidates following the process well described in Section 3.4.2 (see Figures 7.11 and 7.12). Now models are running in several CPUs in the Miztli supercomputer (CADAC-UNAM). We expect that by the end of this year we will have a set of MW like models under this cosmology from where to study differences with classical ΛCDM models, among other studies.

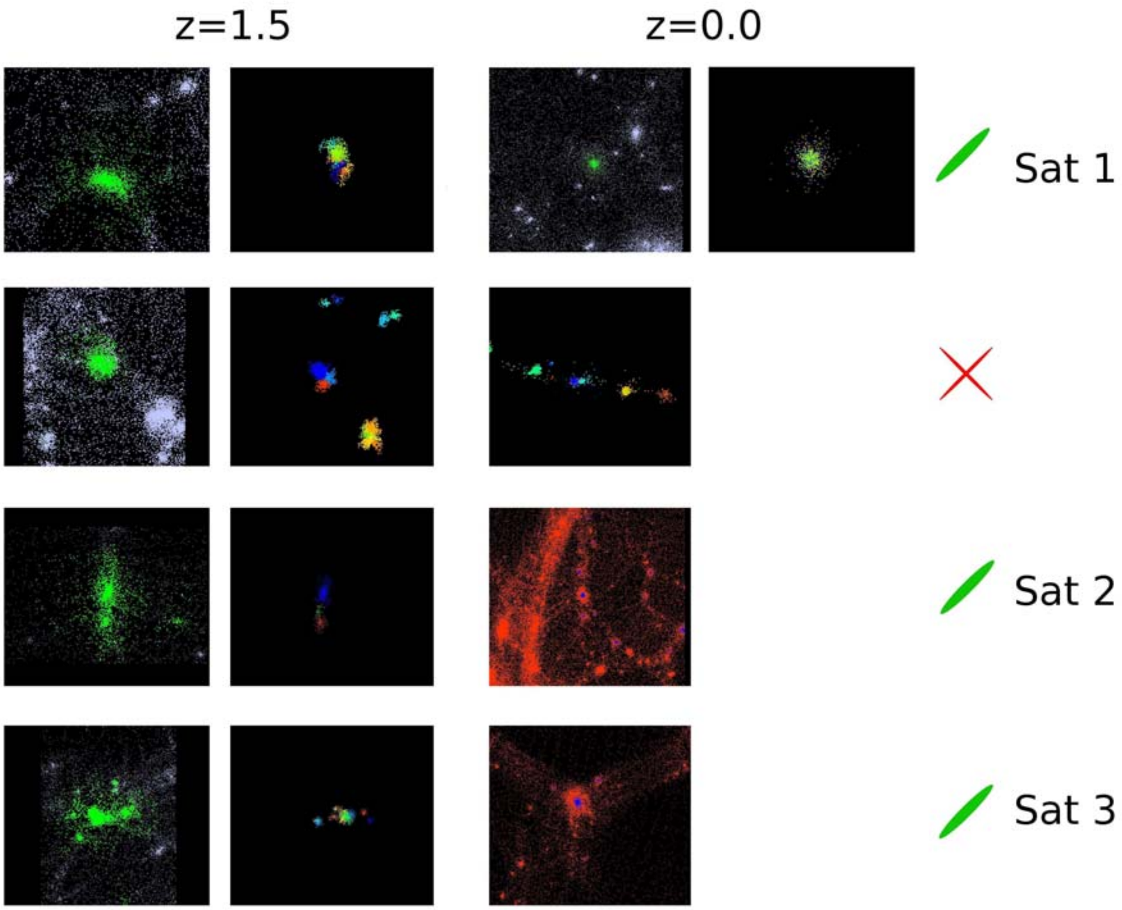

Figure 7.10: MW like halo selection from the low resolution simulation in a WDM cosmology with a warmion energy of 2 KeV. Each row represents a different DM halo selected to have a maximum circular velocity and mass similar to the one of the MW. First two columns show the halo particles (green) back in time to z=1.5. Two last columns show how well mixed is the halo from mergers at z=1.5. Halos that have been finally selected are indicated by a green tick and the ones that not with a red cross.

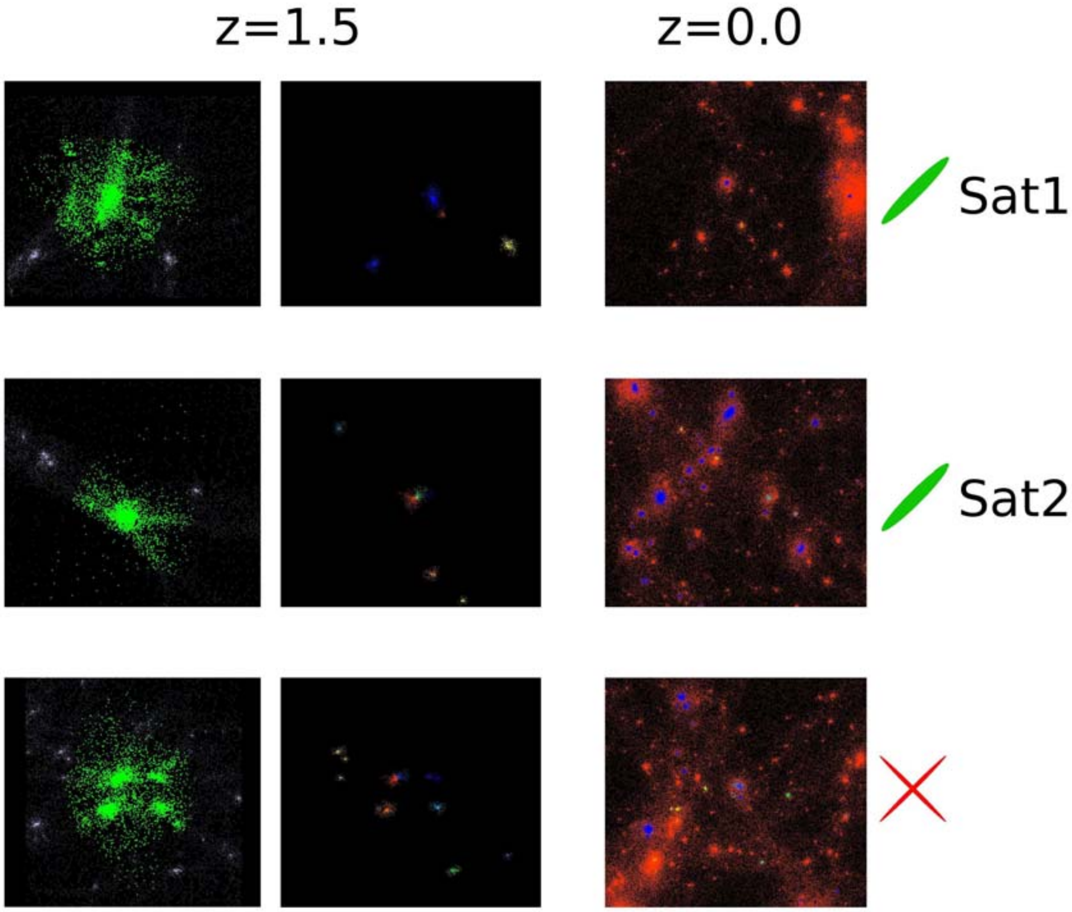

Figure 7.11: Same as in Figure 7.11 but for a WDM cosmology with a warmion energy of 3 KeV.

Part IV

Summary and conclusions

8

General Conclusions

8.1 Summary

In this thesis we have studied kinematics and dynamics of MW like galaxies using different approaches, from analytical models to the most realistic cosmological N-body plus hydrodynamics simulations. Several of the models we have used have been developed by our research group and now are available for a large number and variety of studies. The first simulations we have used are models of isolated MW like galaxies obtained using collisionless N-body codes. We have made several convergence tests to ensure that results from these models are not affected by numerical effects. Later on we have used test particle simulations with imposed spiral arm or bar potentials to undertake other kind of analysis. Finally, after spending the first years of this thesis improving its initial parameters we have succeeded into generating a set of MW like models in a cosmological context and using an N-body plus hydrodynamics code. These last sets of models are much more realistic than the ones we used before and also because of that their analysis is much more complex and takes more time. We have started the first analysis of these new models obtaining interesting results concerning the hot gas distribution and large scale structures presents in the system. Furthermore, much more work is needed to fully understand and to take advantage the most of the model.

8.2 Spiral arms pattern speed

In Chapter 4 we have studied rotation frequencies of spiral arms in different collisionless N-body models of isolated galaxies. We have analysed how this parameter depends on the strength of the bar and also how stellar particles behaves due to the interaction with these spirals. Finally we have made a first attempt to determine the nature of the different spiral arm structures that are presents in our models. The main outcomes of this work are the following:

- The dominant spiral mode in strong barred models is the Fourier mode m=2. This mode is most of the time connected to the bar but suddenly breaks this connection and is disrupted and integrated to the disk. A new m = 2 mode is generated from the bar after the break.

- Dominant spiral mode in strong barred models rotates at the same speed as the bar with a rotation frequency that is near to a solid body rotation.

- The rotation frequency of spirals in barred models departs from solid body rotation with a small decrement with radius when the bar is weak. We have observed that the magnitude of this decrement is correlated with the bar amplitude. Arms can become corotant with disk particles for very weak bars.

- Although the dominant spiral disk mode in barred simulations is the one connected to the bar, other subdominant modes are presents. In this work we have observed that at least exists one subdominant slow and winded mode at large radii.

- In barred models, particles that are placed inside spiral arm density structure move such a way that is compatible with spirals being induced by invariant manifolds. The solid body rotation observed for the spirals is also compatible with the one expected from spirals originated by this invariant manifold process.

- To succeed into obtain systems with a strong bar it is mandatory to use simulations with all density components alive (i.e. not analytical). To use live structures ensures that important physical processes like the angular momentum exchange between the different galactic components into the system are maintained.

- There is not a prominent Fourier mode dominating in unbarred models for a long period of time. In this case several modes are competing, being m=3 and m=4 the ones that have higher amplitude, most of the time.

- In unbarred models the spiral structures are corotating with disk material.

- Motion of particles in unbarred models also support the conclusion that spirals are corotant. Particles selected to be in the spiral arms are winded around the galactic disk due to disk differential rotation, in a small number of rotations.

- Corotant spiral arms induce radial migration.

- Our results are robust to changes in numerical parameters (time step, spatial resolution, number of particles), analysis techniques (SFpFD, Spectrogram, density peak) and also to changes in numerical codes (ART and GADGET3).

It is also important to mention that in the generation of the isolated collisionless N-body galactic models we have learned that it is needed to be very careful when generating initial conditions and when selecting initial parameters to avoid numerical effects. We have also seen that as the systems simulated here are highly non-linear, minor changes in initial parameters can lead to completely different systems, though general parameters remain the same. Finally we add that it is mandatory to control the simulation while it runs and also to make convergence tests when it finishes, to be completely sure that results are non affected by numerical effects.

Simulations presented here are good enough when compared with the best ones that are being used in other galaxy formation and evolution studies. Due to its high resolution they require a lot of CPU time to be simulated. CPU time become, in fact, the real limitation on the resolution that can be reached in these kind of systems.

8.3 Vertex deviation method

Using both, collisionless N-body and test particle simulations of isolated galactic disks we have analysed parameters of the velocity distribution function such as the first and second order moments and also a combination of second order moments that is called vertex deviation. In Chapter 5 we have shown how variations in the l_v, when crossing spiral arm structures, gives us information about the position of CR and OLR resonances. For this analysis we have also used a simplistic analytical approach. The main results of this study are:

- We confirm that non-negative l_v values are clearly related to density structures. We have seen that all non-corotant structures generate gradients in the l_v maps.
- In all cases with non-corotating spiral arms, the sign of the l_v changes when crossing the density peak of the spiral structure and in the interarm region. This result is observed both, in the analytical approach and in test particle and N-body simulations.
- When crossing the density peak of the spiral arms in a non-corotating system the l_v sign changes in a different way depending on its position inside CR, between CR and OLR or outside the OLR. This change is from negative to positive between CR and OLR radius and the other way around inside CR and outside OLR.
- When the spiral arms are corotating, there is no clear correlation between the l_v and the overdensity. However, some correlation survive between density structures and vertex deviation gradients result that deserves a deeper study.

- Using test particle simulations we have exhaustively checked that conclusions we present here hold both for spiral arm potential (TWA, PERLAS) and spiral arms that are the response to an imposed bar potential (Ferrers, quadrupole). Furthermore, we also checked that they are independent of the initial parameters, thus on the changes of the pitch angle, the amplitude of the spirals, the velocity dispersion of the population or the total integration time.

- For the first time we have shown that self-consistent high-resolution N-body simulation with a rigid rotating bisymmetric and well defined two armed spiral shows a l_v behaviour that follows the same main trends than the ones observed in the test particle simulations.

- From all previous conclusions we state that measuring the sign of the l_v in front or behind the spiral structure in a certain radius and azimuth would indicate whether that region of the galaxy is inside or outside of CR. A reverse of the sign behaviour at a certain radius would mark the CR, and in turn, give an estimation of the pattern speed of the spiral arms. As the position of spiral arms inside or outside CR is related to their nature (e.g. manifold spiral arms are generated always outside CR), the mapping of the l_v would also trace the nature of the spiral arms in a galaxy.

- Second order differences in the shape and magnitude of l_v patterns are observed when comparing all the models analyzed here. These irregularities may be due just to intrinsic differences among their corresponding force fields. The study of these irregularities deserves much more investigation as maybe they can be used to constrain spiral potential in real galaxies.

8.4 New MW like model

One of the main goals of this thesis has been to get a realistic MW like model using N-body plus hydrodynamics cosmological simulations. In Chapter 6 we have described the method and initial parameters we have used to undertake this process and how we have succeeded with getting a set of models with several properties that fit within the observed ones for the MW.

Once we have reached this first goal we have started the study of their basic parameters to compare them with observations. We have continued our analysis with studying more complex variables that give us important information about hot topics in the field of galaxy formation and evolution. For instance, we have studied the distribution of gas in the simulated galaxy and its internal structure. Much more work can be done by analysing the models we present here. In fact, in this thesis we only start to take advantage from them. Next we summarise the main conclusions we have reached from Chapter 6:

- To get a galactic system similar to the MW using N-body plus hydrodynamics in a cosmological context is not trivial. Lots of parameters need to be adjusted to describe physical processes such as star formation and stellar feedback properly. These parameters need to be adjusted to mimic the processes that can not be implemented into the code due to their complexity or misunderstanding. The misunderstanding of subgrid physics is an important problem that needs to be solved in the near future to generate systems that are close to real ones in the next generation of very high resolution simulations.

- Once obtained, to analyse galaxy models such ones we have presented here is much more complicated than doing it for less realistic ones as much more processes need to be taken into account. On the other hand much more information can be obtained from this kind of simulations than from the ones used in previous chapters.

- Changes on the aggressiveness of gas and dark matter refinement have no important impact in general parameters such as the presence of disk large scale structures or rotation curves. Otherwise, a more aggressive refinement induces to an increase of cold gas consumption in the star formation at early ages what makes the system to have, at z=0, a lower SFR and smaller total cold gas mass.

- A young bar is present in the disk region of our MW like models. This bar is formed by a secular evolution of disk particles and have been formed 8 Gyrs ago, after the last major merger. It has a scale length that is around 2 kpc.

- Galactic models presented here have had a major merger at z=3. From this major merger an important imprint remains up to the present (z=0) in the form of an old bar. This old bar has a scale length of about 7 kpc and is much less concentrated in the inner regions than the young one.

- Young and old bars are misaligned around 90 degrees and rotate at similar speed. To have similar speed and also the fact that the old one is much less dense in the young bar region makes the system stable for several Gyrs.

- Hot gas distribution around our galactic models is highly anisotropic. This result indicates that if real systems follow similar trends, to infer the total hot gas mass (X-ray luminous) from a small number of line of sight observations can drive to important biases. More than 50 observations at random directions in the sky are needed to ensure that, following the spherically isotropic gas distribution approximation, a proper value for the total baryonic mass is obtained.

- As purposed in previous works hot gas component in the halo is highly turbulent. We observe how low-metallicity components are falling from the CGM while enhanced gas departs from the disk due to stellar feedback. We also purpose that the asymmetry in the metallicity component observed between the northern and the southern hemispheres at z=0 can be driven by the accretion of a small satellite.

- The amount of hot gas in the halo accounts for an important part of the missing baryons but not for all of them. This was also observed both in real galaxies and simulations.
- A relation between the total mass of galaxies and their total hot gas mass have been explored. If confirmed to know the total hot gas mass in galaxies can be a new method to constrain the virial mass of real halos. This result needs for a deeper investigation.
- The implementation of new physical processes such as radiation pressure and of a multi-species environment (in models presented here only iron and alpha elements are simulated) is needed to make our models more realistic.

9
Work in progress and perspectives

In this thesis we have obtained very interesting results that shed some light in the nature of spiral arm structures in galaxies. We have found new methods to distinguish between spirals driven by bars and the ones arising from disk fluctuations and also to trace the position of the main resonances of these structures using kinematic observables. We also have started to analyse structures that arise in fully cosmological N-body plus hydrodynamic simulations with a high resolution, from hot gas distribution to bars in disk galaxies. To get all these results we have developed a large set of simulations both of isolated galactic systems simulated using collisionless N-body codes and cosmological ones using a more realistic code such as N-body plus hydrodynamics. A large amount of new studies can be done analysing these high resolution simulations.

Results presented here can be improved doing new tests both in more realistic simulations and from observational data when available. The former is an easy improvement as just now we dispose of the tools and the models we need to undertake this work. For the later we will need to wait some years until the data from new satellites such as Gaia or APOGEE will be available.

In the process of obtention and analysis of our results several new questions about nature and evolution o spiral arm structures have arisen. For instance to know which is the rotation frequency of spiral arms generated by interaction with external galaxies, which is the process that drives to the breaking of spiral arms from bar structures or how higher or lower order moments of the velocity distribution function can give us information about the total galactic potential. In the following paragraphs we numerate the future work and perspectives that comes out from this thesis.

To begin with, from work presented in Chapter 4:

1. **Spiral-bar breaking.** When observing the evolution of spiral arms in collisionless N-body barred models we see how at some point the spiral arms break their connection with the bar and become disrupted into the disk. Meanwhile this process is happening new spirals appear from the bar. To study the evolution of local disk parameters such as velocity dispersions or Toomre parameter may give us information about these processes. A deeper knowledge about how spiral arms disconnect from the bar and how they fades out into the disk is needed to better understand which is their nature and how they evolve.

2. **Non-linear coupling.** The study of rotation frequencies of spiral arms using Spectrogram technique have given us much more information than the one presented here for the main spiral structure. When analysing Spectrogram from several Fourier modes one can see how different structures from the main one appear with well determined rotation frequencies. In previous works similar structures have been studied. The authors of these studies looked for the presence of a mechanism that generates density structures in disks and that is known as non-linear coupling. We have also started the analysis of Spectrogram results to find possible features that indicate the presence of this mechanism in our simulations. However a deeper analysis is needed to find them.

3. **Same initial conditions, different code.** In this thesis we have generated a large number of simulations. Due to the amount of work that supposes to analyse the data properly and to make all tests to ensure that simulations are not affected by numerical effects, some of these simulations have not been analysed yet. This is the case of a set of simulations that starting from the same initial conditions as the ones that have been used in the models B and U presented here, have been simulated using a different code (GADGET instead of ART). The analysis of this simulations will give us information about the real effect of using a different code to simulate exactly the same system.

4. **Spiral arms in an interacting scenario.** One process that generates spiral arms in disks and that has been well reported from observations is the interaction of galactic disk systems with other galaxies, both with satellites or other main galaxies. It will be very interesting to generate models that reproduce this scenario and to analyse how behave the spiral arms that will be formed. We are deeply interested in to know if great design spirals that arise from this process are corotant or present a similar rotation frequency than the one of our barred models. During this thesis we have had the opportunity of generating a code that let us to introduce a neighbour galaxy into a simulated galactic system, also if it has been evolved for several Gyrs. Now we are studying the properties that the neighbour needs to have to mimic the possible progenitor of Omega Centaurus globular cluster. Once selected the initial conditions for this satellite galaxy we will be able to generate a model of interaction

and disruption of Omega Centaurus satellite into the Milky Way. This new model will be useful, first, to study the process of disruption of a satellite galaxy into a MW like potential. Maybe with this study we will find proofs of the origin of Omega Centaurus globular cluster. And later it will be also useful to study spiral arms generated by an interaction with a satellite.

5. **MW and external galaxies.** From this work in the study of spiral arms pattern speed a natural question arises: Which the situation for the MW and real external galaxies is? Planned and current surveys measuring stellar kinematics and distances inside our Galaxy as Gaia (ESA) or APOGEE (SDSS) will open up the possibility of direct estimation of pattern speeds through methods like the Tremaine-Weinberg (TW) method. For the external galaxies spectroscopic high resolution surveys like CALIFA or MANGA(AS3/SDSSIV) will also contribute to test our predictions using stellar kinematics. We will be waiting for the data releases of these surveys.

From Chapter 5 also several studies showed that need to be undertaken in a near future:

1. **Second order effects in l_v maps.** The study of l_v maps have resulted in a new method to find spiral arm CR and OLR radius in galaxies. We have studied this parameter in several simulations with a different degree of realism and under different initial conditions obtaining the same result in all of them. It is somehow surprising that we have obtained the same results in so different models, however we argue that this means that the effect we have studied here is a first order effect. From this conclusion a new question arises: How can we use kinematics to distinguish between models? In our previous analysis we have found that several second order effects are present in kinematics studied here, i.e. the exact place where l_v sign changes, with respect to the spiral density maximum, is not exactly the same. To find how this second order effects can constrain the spiral arms potential deserves much more investigation.

2. **Analysis of moments.** In this work we have focused our analysis to the l_v parameter. However, other moments like the means (zero order moments) or the skewness and kurtosis (third order moments) can give us new information about the non-axisymmetric structures. To analyse the second order moments, individually not combined to produce other parameters like the l_v studied here, can also be very interesting. We suspect that some of these moments can give us information about the galactic potential and then to distinguish between different spiral arms and bar natures.

3. **Analysis in the vertical component.** Most of the test particle models we have used to study l_v parameter are 2D models. Several recent works show that kinematic

structures in the vertical direction can give us interesting information about non-axisymmetric structures in disks. To undertake this analysis we will need new test particle models that include the 3D component, or to use N-body models that are by definition 3D models. Is our purpose to analyse the tilt of the velocity ellipsoid from W axis, too.

4. **Applying the method to observations.** It will be one of our main goals for the next future to test how useful results for spiral arms rotation frequency and local kinematic parameters we have obtained here, are, to constrain properties of real large scale structures in galaxies, when applied to real data. An evident caveat when applying the l_v method will be that patterns in the sign of the l_v are degenerate for inside CR and outside OLR. In this case, it will be needed to find other kinematic signatures that help to differentiate between those two cases. Another problem we will find when applying this l_v method to real data is that when spiral arms coexist with other density structures (i.e. rings, floculent structures, ...), the behaviour of the l_v can be difficult to interpret. It will be necessary to study in which cases mean velocities, that showed to be good tracers of the CR, can be used complementary. Moreover to start all these analysis we will need real data:

   - Nowadays the available data from stars in our MW galaxy lets us to compute l_v values only for the solar neighbourhood. The method in this case can not be applied.
   - New surveys like LSST or the APO Galactic Evolution Experiment (APOGEE) will provide us with data that will let us to measure l_v at several kpc from the Solar neighbourhood.
   - Also Gaia will publish his first release at about summer 2016.
   - For external galaxies, as far as we know, there are no measurements of the l_v yet. In fact, in studies of the kinematics of external galaxies it is generally assumed that there is alignment of one of the axis of the stellar velocity ellipsoid with the azimuthal coordinate (i.e. there are no l_v) in order to derive properties such as the ratio between radial and azimuthal velocity dispersions from LOS velocity measurements.
   - In the case of kinematic studies of external galaxies we can only establish the level of detection of l_v signals and study which are the observational requirements and perspectives for detecting them with current and future instruments like ELT in its spectroscopic phase or possible nano-arcsecond post-Gaia missions.

   As data is not available yet, we have started to test if with Gaia data we will be allowed or not to use the method.

The last results we have obtained in this thesis are the ones presented in Chapter 6 and also from them arise lot of new work and analysis to be done. We summarize the main future work that comes out from the generation of our new MW like model in the next paragraphs:

1. **Analysis of kinematic parameters.** The force that drives the formation and evolution of galaxies is mainly the gravity. However, gas physics plays an important role in some of the processes of that formation and evolution. Our first results in the study of kinematics and dynamics of large scale structures in galaxies have been obtained here from systems where only gravity acts. We do not expect great changes when including the gas component as the processes we have studied are mainly driven by gravitational interactions, moreover it is interesting to see in which degree and in what direction our results change when adding these components. With our new MW like models in a cosmological context simulated with a N-body plus hydrodynamics code all the analysis we have done in Chapters 4 and 5 of this thesis can be reproduced in a more realistic frame.

2. **Deeper analysis of hot gas component and large scale structures.** To better understand the evolution and the distribution of hot gas in our new models, as so the formation and evolution of bars and spirals in them, we need to study models much deeper than what we have done. Comparisons with observations and other works will be necessary to better understand our results, too.

3. **$\mathbf{M}_h/\mathbf{M}_{hotgas}$ relation.** The total mass of our galaxy and also of external galaxies is not well constrained at all. Different techniques lead to slightly different results without converging to a single value. The total hot gas mass parameters has shown to be a possible tracer of the total mass in galaxies. If confirmed, the study of hot gas component would become a new technique to better constrain this parameter.

4. **SRF decrease at z=0.** One parameter in our models that is not fitting within the observed values for the MW is the SFR at z=0. This discrepancy between the value we obtain from simulations and the one that is inferred from observations can come be a consequence of several different processes all of them related with the process of consumption of cold gas available for star formation. The study of all these processes will give us information about the mechanisms that inhibits star formation in galaxies and also about the realism of the recent implementations of star formation and stellar feedback physics in MW like models.

5. **Satellite galaxies and stellar streams.** The study of satellite galaxies in cosmological simulations have been long used to test cosmological theories. These studies look for the number of satellite galaxies or small dark matter halos that fall around main galactic systems. Among much other studies it is also interesting to study the mass threshold for isolated halos to form stars. Here, as in our models the resolution

is high enough we can undertake a new kind of studies, we can study the satellite galaxies' inner structure. Furthermore as our models are good enough to study low density structures, we can also study the disruption of satellite galaxies in the main galactic halo and then try to constrain the galactic potential.

6. **More realistic models.** The N-body plus hydrodynamics code we have used to generate the set of MW like models we present in this thesis can be improved adding new physics. We are in the process of generating new models with a slightly modified code that includes radiation pressure, among others. These new models will be more realistic and will let us to analyse new physical properties.

7. **Warm Dark Matter models.** Several scenarios have been proposed to fix the mismatches that have been found between observations and theoretical predictions. It is well know that some observations are not well fitted by a ΛCDM scenario. We have started to make a new set of models under a WDM cosmology with different warmion energies. It is of our interest to study the structures that arise from these models and compare them with the ones under the classical ΛCDM cosmology. We want to find if exist some parameter that can help us to distinguish between both in the real universe and if WDM can solve some of the problems that faces ΛCDM theory.

A
Appendix 1

A.1 Tests of spatial Fourier method in synthetic models

To test in which situations the spatial Fourier method has problems in finding the density structures we developed a simple generator of synthetic bar and spiral arms generator. This generator is a FORTRAN code that retrieves x,y positions of several thousands of particles according to a selected spiral arms and bar configuration. We used a Monte Carlo sampling to obtain particles positions. In these simple models galactic structures have been generated as Gaussian distributions with a constant dispersion. The code let us to select the dispersion of the Gaussian distribution and also parameters of the structures such as:

- Bar length
- Angle of the bar, computed from x axis.
- Bisymmetric spiral arm starting angle (that lets us to have a spiral connected or not to the bar).
- Presence of an external bisymmetric spiral arms component. The same component can be placed in the inner region to obtain a 4-armed system.
- Starting angle of the external new spiral arms.
- The radii interval where the external and internal spirals are being overlapped.

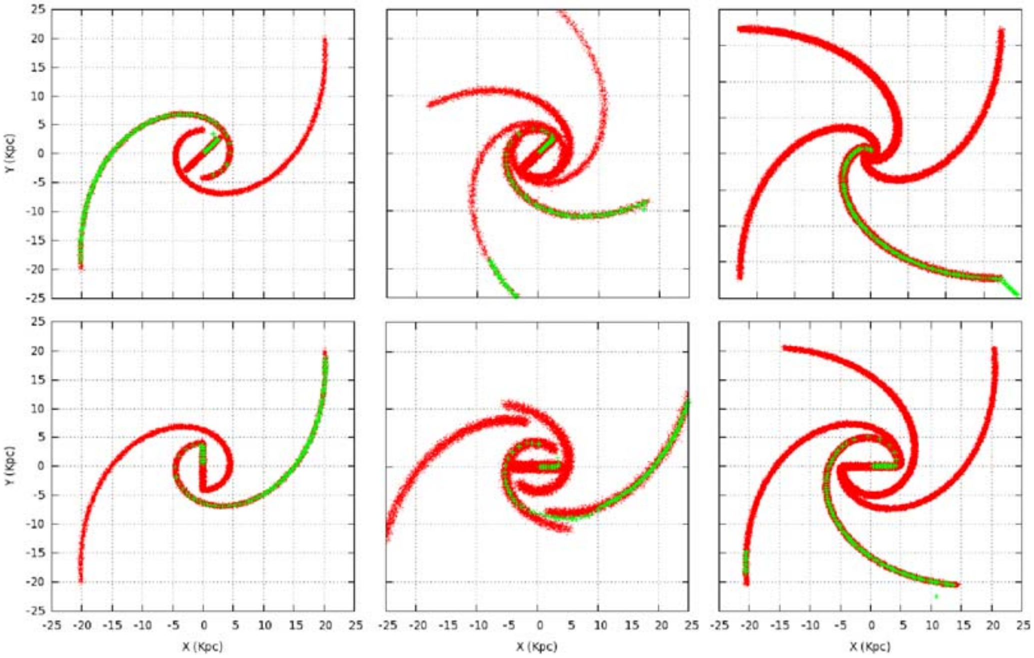

Figure A.1: In black synthetic particles, in red, results obtained applying the Fourier mode analysis code.

In Figure A.1 we show the results of applying the spatial Fourier method to several synthetic models. The main conclusions we subtract from these tests are:

- The program find without any problem the bisymmetric structures (i.e. bars and spirals).
- The method has some problems to find the density structures when the spiral structure is not connected to the bar and both start at the same radius.
- If in the system two structures overlap at any radius, for instance two spirals coexisting, the method gives the mean angle between structures.
- The method is able to find the position of m=4 structures as well as m=2.

A.2 Tests of Spectrogram method using synthetic models

In this appendix we present a new FORTRAN code based in the one proposed in Appendix A.1 that have been written to test the limitations of Spectrogram method.
Here synthetic models are generated as the ones in Appendix A.1 but adding temporal evolution. The code generates the desired number of snapshots of the rotating structure with the temporal periodicity needed for the analysis (remember Nyquist limitation presented

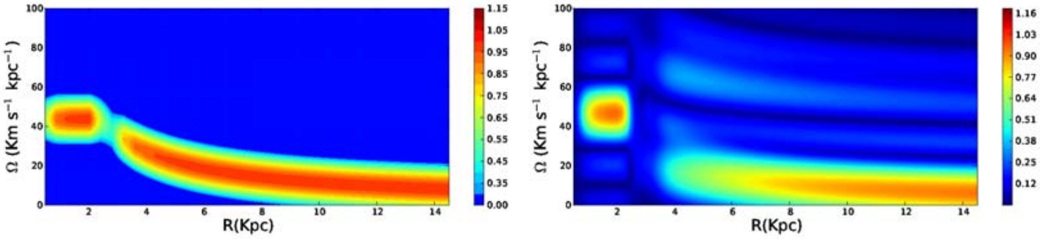

Figure A.2: Results from applying Spectrogram method to two synthetic models. Left: single m=2 long-lived corotating structure. Right: two m=2 transient corotating structures with an amplitude in phase opposition.

in Section 4.2.2). The density structure can be one of the ones proposed in Section A.1. The code also includes several possibilities for the rotation curve of this structure:

- Permanent structure with rigid rotation.
- Permanent structure with a disk like rotation curve (corotant). A simple rotation curve ($150 \cdot r^{\frac{1}{16}}$) is used.
- Transient, rigid or corotant, structure. The period of the transience can be changed.
- Two transient, rigid or corotant, structures, with opposed amplitude phase, i.e. one becomes strong just when the other fades out.

To simulate the transience we used a sinusoidal function that regulates the formation and destruction of structures. The period of formation/destruction can be changed.
In Figure A.2 we show results of applying Spectrogram method to a single m=2 long-lived corotating structure (right) and to a system of two m=2 transient corotating structures that have their amplitude phase in opposition (left). Here we sow only two examples of how the method is able to find the proper rotation frequencies. It is important to mention that we only obtained positive results when the number of snapshots and the time interval between them was well above Nyquist frequency, otherwise the method is unable to detect the real rotation frequencies.

B

Appendix 2

In this appendix we describe the calculations we made to obtain the analytical expression for the vertex deviation (l_v).

B.1 Notation

The notation we use in next sections is the one that follows:

Ψ = Total velocity distribution function,
Ψ_0 = Schwarzschild velocity distribution function,
σ_*^0 = Non-perturbed surface density [$\mathrm{M}_\odot$ kpc^{-2}],
σ_* = Total surface density [$\mathrm{M}_\odot$ kpc^{-2}],
m_* = Stellar mass. We assume it is the same for all stars [$\mathrm{M}_\odot$],
ϖ = Distance to the galactic center in the disk plane [kpc],
θ = Azimuthal angle in the disk plane [rad.],
θ = Time [s],
Ω = Angular velocity of a particle in a circular orbit in the axisymmetric averaged potential of the galactic disk [km s^{-1} kpc^{-1}],

(B.1)

Θ = Radial velocity [km s^{-1}],

Π = Azimuthal velocity [km s^{-1}],

Z = Vertical velocity [km s^{-1}],

c_ϖ = Θ: Radial residual velocity [km s^{-1}],

c_θ = $\Pi - \varpi\Omega$: Azimuthal residual velocity [km s^{-1}],

c_z = Z: Vertical residual velocity [km s^{-1}],

V_ϖ, V_θ = Radial and azimuthal mean systematic movements [km s^{-1}],

σ_ϖ = $\sqrt{\mu_{200}^{(0)}}$: Dispersion of the non-perturbed radial residual velocities [km s^{-1}],

l_v = Vertex deviation [rad.],

κ = $2\Omega\sqrt{1+\frac{\varpi}{2\Omega}\frac{d\Omega}{d\varpi}}$: Epicyclic frequency [km s^{-1} kpc^{-1}],

γ = $\frac{2\Omega}{\kappa}$

i = Pitch angle of the spiral [rad.],

m = Number of spiral arms,

ω = Rotation frequency of the spiral [km s^{-1} kpc^{-1}],

Ω_p = $Re(\omega)/m$Angular velocity of the spiral arm pattern [km s^{-1} kpc^{-1}],

R_0 = Initial radius for the spiral perturbation [kpc],

Φ = $-\frac{2}{\tan i}\ln\left(\frac{\varpi}{R_0}\right)$: Spiral arm locus,

K = $\frac{d\Phi}{d\varpi}$: Wave number [kpc^{-1}],

A_{sp} = Spiral arms potential amplitude normalization [km^2 s^{-2} kpc^{-1}],

R_Σ = Spiral arms radial scale length [kpc],

A = $-A_{sp}\varpi\exp^{-\varpi/R_\Sigma}$: Amplitude of the spiral arms potential [km^2 s^{-2}],

ϑ_1 = $A\exp^{i(\omega t-2\theta+\Phi(\varpi))}$: Spiral arm potential [km^2 s^{-2}],

x = $K^2\frac{\sigma_\varpi^2}{\kappa^2}$: Toomre number,

ν = $\frac{m\left(\Omega_p-\Omega\right)}{\kappa}$; $V_1 = \frac{(2\Omega)(\varpi\Omega)}{\kappa}$; $a = \frac{(K\varpi)\left(2\Omega^2\right)}{\kappa^2}$; $\mu_0 = \frac{V_1^2}{\sigma_\varpi^2}$

ξ = $\frac{c_\varpi}{V_1}$; $\eta = \frac{c_\theta}{\varpi\Omega}$: Dimensionless velocities referred to local values,

$\langle f\rangle$ = $\frac{m_*}{\sigma_*^0}\int\int\int f\Psi_0 dc_\varpi dc_\theta dc_z$: Weighed average with respect to Ψ_0

B.2 Velocity distribution function

To compute the moments we used the velocity distribution function first presented in Lin et al. (1969). This function (Equation B.2) is a direct summation of a classical Schwarzschild distribution (Ψ_o) and a small perturbation due to the presence of a tightly wound spiral (Ψ_1). For details on the derivation of Ψ_1 see Appendix A in Lin et al. (1969).

$$\begin{aligned}
\Psi &= \Psi_0 + \Psi_1 \\
\Psi_0 &= P_0(\varpi)\exp^{-\frac{\mu_0}{2}(\xi^2+\eta^2)} \\
\Psi_1 &= \frac{-\vartheta_1}{\sigma_\varpi^2}\cdot\Psi_0\cdot(1-q) \qquad \text{(B.2)} \\
\text{where:}& \\
q &= \frac{\nu\pi}{\sin(\nu\pi)}\cdot\frac{1}{2\pi}\int_{-\pi}^{\pi}\exp^{i[\nu\alpha - a\cdot\xi\sin\alpha + a\cdot\eta(1+\cos\alpha)]}\,d\alpha
\end{aligned}$$

B.3 Computation of the moments

The equations presented in this section have been obtained imposing the perturbed velocity distribution function (Equation B.2) to the general expression for the moments, Equation 5.1. To get the final expressions shown here we used the relations proposed in Section B.8 and also that the first order moments and the crossed second order moments of a non-perturbed Schwarzschild velocity distribution function are 0 ($\mu_{100}^{(0)} = \mu_{010}^{(0)} = \mu_{110}^{(0)} = 0$). The epicyclic approximation was used to link the second order moments of the non-perturbed Schwarzschild velocity distribution function ($\mu_{020}^{(0)} = \mu_{200}^{(0)}(2\Omega/\kappa)^{-2}$). A detailed example of how we obtain the final expressions can be seen in Equations B.4 and B.5.

B.4 Zero order moments:

To obtain the expressions for the zero order moments we used the Equation B.13.

$$\sigma_*^0 = \mu_{000}^{(0)} = m_* \int\int\int \Psi_0 dc_\varpi dc_\theta dc_z \tag{B.3}$$

$$\begin{aligned} \sigma_* = \mu_{000}\ m_* = m_* \int\int\int \Psi dc_\varpi dc_\theta dc_z = m_* \int\int\int \Psi_0 + \Psi_0 \frac{-\vartheta_1}{\sigma_\varpi^2}(1-q) dc_\varpi dc_\theta dc_z = \\ = \sigma_*^0 \left(1 - \frac{\vartheta_1}{\sigma_\varpi^2}\langle(1-q)\rangle\right) = \sigma_*^0 \left[1 - \frac{\vartheta_1}{\sigma_\varpi^2}\left(1 - \frac{\nu\pi}{\sin(\nu\pi)}\frac{1}{2\pi}\int_{-\pi}^{\pi} \cos(\nu\alpha) \exp^{-\frac{\alpha^2}{\mu_0}(1+\cos\alpha)} d\alpha\right)\right] \end{aligned} \tag{B.4}$$

B.5 First order moments:

We obtained the expressions for the first order moments using Equations B.14 and B.15, after changing the residual velocities (c_ϖ, c_θ) for the dimensionless velocities referred to local values (ξ, η). We also used that $\mu_{100}^{(0)} = \mu_{010}^{(0)} = 0$.

$$\begin{aligned} V_\varpi = \frac{m_*}{\sigma_*}\int\int\int c_\varpi \Psi dc_\varpi dc_\theta dc_z = \mu_{100} = \frac{\sigma_*^0}{\sigma_*}[\frac{m_*}{\sigma_*^0}\int dc_z \int\int c_\varpi \Psi_0 dc_\varpi dc_\theta - \frac{\sigma_*^0}{\sigma_*}\frac{\vartheta_1}{\sigma_\varpi^2}\frac{m_*}{\sigma_*^0}\int dc_z \int\int c_\varpi \Psi_0 (1-q) dc_\varpi dc_\theta = \\ = -\frac{\sigma_*^0}{\sigma_*}\frac{\vartheta_1}{\sigma_\varpi^2}\frac{2\Omega(\varpi\Omega)}{\kappa}\langle\xi(1-q)\rangle = \frac{\sigma_*^0}{\sigma_*}\frac{\vartheta_1 K}{\kappa}\frac{\nu\pi}{\sin(\nu\pi)}\frac{1}{2\pi}\int_{-\pi}^{\pi}\sin(\nu\alpha)\sin\alpha \exp^{-\frac{\alpha^2}{\mu_0}(1+\cos\alpha)} d\alpha \end{aligned} \tag{B.5}$$

$$V_\theta = \frac{m_*}{\sigma_*}\int\int\int c_\theta \Psi dc_\varpi dc_\theta dc_z = \mu_{010} = -i\frac{\sigma_*^0}{\sigma_*}\frac{\vartheta_1 K}{2\Omega}\frac{\nu\pi}{\sin(\nu\pi)}\frac{1}{2\pi}\int_{-\pi}^{\pi}(1+\cos\alpha)\cos(\nu\alpha)\exp^{-\frac{\alpha^2}{\mu_0}(1+\cos\alpha)} d\alpha \tag{B.6}$$

B.6 Second order moments:

Here we obtained the expressions for the second order moments using Equations B.16, B.17 and B.18, after changing the residual velocities (c_ϖ, c_θ) for the dimensionless velocities referred to local values (ξ, η). We also used that $\mu_{110}^{(0)} = 0$ and $\mu_{020}^{(0)} = \mu_{200}^{(0)}(2\Omega/\kappa)^{-2}$.

$$\begin{aligned}\mu_{110} &= \frac{m_*}{\sigma_*}\int\int\int \Psi c_\theta c_\varpi dc_\varpi dc_\theta dc_z = \frac{\sigma_*^0}{\sigma_*}\left(\mu_{110}^0 - \frac{\vartheta_1}{\sigma_\varpi^2}\frac{2\Omega}{\kappa}\left(\varpi\Omega\right)^2\left\langle\xi\eta(1-q)\right\rangle\right) = \\ &= \frac{\sigma_*^0}{\sigma_*}\frac{\vartheta_1\kappa}{2\Omega}\frac{a^2}{\mu_0}\frac{\nu\pi}{\sin\left(\nu\pi\right)}\frac{i}{2\pi}\int_{-\pi}^{\pi}\sin\left(\nu\alpha\right)\sin\alpha\left(1+\cos\alpha\right)\exp^{-\frac{a^2}{\mu_0}(1+\cos\alpha)}d\alpha \end{aligned} \tag{B.7}$$

$$\begin{aligned}\mu_{200} &= \frac{m_*}{\sigma_*}\int\int\int \Psi c_\varpi^2 dc_\varpi dc_\theta dc_z = \frac{\sigma_*^0}{\sigma_*}\left(\mu_{200}^0 - \frac{\vartheta_1}{\sigma_\varpi^2}\left(\frac{2\Omega}{\kappa}\right)^2\left(\varpi\Omega\right)^2\left\langle\xi^2(1-q)\right\rangle\right) = \\ &= \frac{\sigma_*^0}{\sigma_*}\left(\frac{\kappa}{2\Omega}\right)^2\left(\sigma_\varpi^2 - \vartheta_1\left[1 - \frac{\nu\pi}{\sin\left(\nu\pi\right)}\frac{1}{2\pi}\int_{-\pi}^{\pi}\left(1-\frac{a^2}{\mu_0}-2\frac{a^2}{\mu_0}\cos\alpha-\frac{a^2}{\mu_0}\cos^2\alpha\right)\cos\left(\nu\alpha\right)\exp^{-\frac{a^2}{\mu_0}(1+\cos\alpha)}d\alpha\right]\right) \end{aligned} \tag{B.8}$$

$$\begin{aligned}\mu_{020} &= \frac{m_*}{\sigma_*}\int\int\int \Psi c_\theta^2 dc_\varpi dc_\theta dc_z = \frac{\sigma_*^0}{\sigma_*}\left(\mu_{020}^0 - \frac{\vartheta_1}{\sigma_\varpi^2}\left(\varpi\Omega\right)^2\left\langle\eta^2(1-q)\right\rangle\right) \\ &= \frac{\sigma_*^0}{\sigma_*}\left(\frac{\kappa}{2\Omega}\right)^2\left(\sigma_\varpi^2 - \vartheta_1\left[1 - \frac{\nu\pi}{\sin\left(\nu\pi\right)}\frac{1}{2\pi}\int_{-\pi}^{\pi}\left(1-\frac{a^2}{\mu_0}-2\frac{a^2}{\mu_0}\cos\alpha-\frac{a^2}{\mu_0}\cos^2\alpha\right)\cos\left(\nu\alpha\right)\exp^{-\frac{a^2}{\mu_0}(1+\cos\alpha)}d\alpha\right]\right) \end{aligned} \tag{B.9}$$

B.7 Centered second order moments:

Expressions for the centered second order moments have been obtained using the equations obtained in the previous sections (B.3 to B.9).

$$
\begin{aligned}
\tilde{\mu}_{110} &= \frac{m_*}{\sigma_*}\int\int\int \Psi\left(c_\theta - V_\theta\right)\left(c_\varpi - V_\varpi\right) dc_\varpi dc_\theta dc_z = \\
&= \frac{m_*}{\sigma_*}\left(\int dc_z \int\int \Psi c_\theta c_\varpi dc_\varpi dc_\theta - V_\theta \int dc_z \int\int \Psi c_\varpi dc_\varpi dc_\theta - V_\varpi \int dc_z \int\int \Psi c_\theta dc_\varpi dc_\theta + V_\theta V_\varpi \sigma_*\right) = \\
&= \frac{\sigma_*^0}{\sigma_*}\left(\frac{\vartheta_1 \kappa}{2\Omega}\frac{a^2}{\mu_0}\frac{\nu\pi}{\sin\left(\nu\pi\right)}\frac{i}{2\pi}\int_{-\pi}^{\pi}\sin\left(\nu\alpha\right)\sin\alpha\left(1+\cos\alpha\right)\exp^{-\frac{a^2}{\mu_0}\left(1+\cos\alpha\right)} d\alpha - V_\theta V_\varpi \frac{\sigma_*}{\sigma_*^0}\right)
\end{aligned}
\tag{B.10}
$$

$$
\begin{aligned}
\tilde{\mu}_{200} &= \frac{m_*}{\sigma_*}\int\int\int \Psi\left(c_\varpi - V_\varpi\right)^2 dc_\varpi dc_\theta dc_z = \\
&= \frac{m_*}{\sigma_*}\left(\int dc_z \int\int \Psi c_\varpi^2 dc_\varpi dc_\theta + V_\varpi^2 \sigma_* - 2V_\varpi \int dc_z \int\int \Psi c_\varpi dc_\varpi dc_\theta\right) = \\
&= \frac{\sigma_*^0}{\sigma_*}\left(\sigma_\varpi^2 - \vartheta_1\left[1 - \frac{\nu\pi}{\sin\left(\nu\pi\right)}\frac{1}{2\pi}\int_{-\pi}^{\pi}\left(1 - \frac{a^2}{\mu_0}\sin^2\alpha\right)\cos\left(\nu\alpha\right)\exp^{-\frac{a^2}{\mu_0}\left(1+\cos\alpha\right)} d\alpha\right] - V_\varpi^2 \frac{\sigma_*}{\sigma_*^0}\right)
\end{aligned}
\tag{B.11}
$$

$$
\begin{aligned}
\tilde{\mu}_{020} &= \frac{m_*}{\sigma_*}\int\int\int \Psi\left(c_\theta - V_\theta\right)^2 dc_\varpi dc_\theta dc_z = \\
&= \frac{m_*}{\sigma_*}\left(\int dc_z \int\int \Psi c_\theta^2 dc_\varpi dc_\theta + V_\theta^2 \sigma_* - 2V_\theta \int dc_z \int\int \Psi c_\theta dc_\varpi dc_\theta\right) = \\
&= \frac{\sigma_*^0}{\sigma_*}\left(\frac{\kappa}{2\Omega}\right)^2\left(\sigma_\varpi^2 - \vartheta_1\left[1 - \frac{\nu\pi}{\sin\left(\nu\pi\right)}\frac{1}{2\pi}\int_{-\pi}^{\pi}\left(1 - \frac{a^2}{\mu_0} - 2\frac{a^2}{\mu_0}\cos\alpha - \frac{a^2}{\mu_0}\cos^2\alpha\right)\cos\left(\nu\alpha\right)\exp^{-\frac{a^2}{\mu_0}\left(1+\cos\alpha\right)} d\alpha\right] - V_\theta^2 \frac{\sigma_*}{\sigma_*^0}\right)
\end{aligned}
\tag{B.12}
$$

B.8 Useful weighed averages with respect to Ψ_0

Next we present some useful relations that can be easily obtained using the expression for the weighed averages with respect to Ψ_0 presented in Section B.1, $\langle \mathrm{f} \rangle$, and the Schwarzschild velocity distribution function (Ψ_0 in Equation B.2):

$$\langle (1-q) \rangle = 1 - \frac{\nu\pi}{\sin(\nu\pi)} \frac{1}{2\pi} \int_{-\pi}^{\pi} \cos(\nu\alpha) \exp^{-\frac{a^2}{\mu_0}(1+\cos\alpha)} \, d\alpha \tag{B.13}$$

$$\langle \xi(1-q) \rangle = -\frac{a}{\mu_0} \frac{\nu\pi}{\sin(\nu\pi)} \frac{1}{2\pi} \int_{-\pi}^{\pi} \sin(\nu\alpha) \sin\alpha \exp^{-\frac{a^2}{\mu_0}(1+\cos\alpha)} \, d\alpha \tag{B.14}$$

$$\langle \eta(1-q) \rangle = \frac{ia}{\mu_0} \frac{\nu\pi}{\sin(\nu\pi)} \frac{1}{2\pi} \int_{-\pi}^{\pi} \cos(\nu\alpha) (1+\cos\alpha) \exp^{-\frac{a^2}{\mu_0}(1+\cos\alpha)} \, d\alpha \tag{B.15}$$

$$\left\langle \xi^2(1-q) \right\rangle = \frac{\sigma_{\varpi}^2}{V_1^2} - \frac{1}{\mu_0} \frac{\nu\pi}{\sin(\nu\pi)} \frac{1}{2\pi} \int_{-\pi}^{\pi} \cos(\nu\alpha) \left(1 - \frac{a^2}{\mu_0} \sin^2\alpha\right) \exp^{-\frac{a^2}{\mu_0}(1+\cos\alpha)} \, d\alpha \tag{B.16}$$

$$\left\langle \eta^2(1-q) \right\rangle = \left(\frac{\kappa}{2\Omega}\right)^2 \frac{\sigma_{\varpi}^2}{(\varpi\Omega)^2} - \frac{1}{\mu_0} \frac{\nu\pi}{\sin(\nu\pi)} \frac{1}{2\pi} \int_{-\pi}^{\pi} \cos(\nu\alpha) \left(1 - \frac{a^2}{\mu_0} - 2\frac{a^2}{\mu_0}\cos\alpha - \frac{a^2}{\mu_0}\cos^2\alpha\right) \exp^{-\frac{a^2}{\mu_0}(1+\cos\alpha)} \, d\alpha \tag{B.17}$$

$$\langle \xi\eta(1-q) \rangle = -\frac{a^2}{\mu_0^2} \frac{\nu\pi}{\sin(\nu\pi)} \frac{i}{2\pi} \int_{-\pi}^{\pi} \sin(\nu\alpha) \sin\alpha (1+\cos\alpha) \exp^{-\frac{a^2}{\mu_0}(1+\cos\alpha)} \, d\alpha \tag{B.18}$$

B.9 Analytical expression for vertex deviation

Using the expressions we obtained for the centered second order moments (Section B.7), we find the analytical formula for the l$_v$ we present here.

$$\frac{1}{2}\tan\left(2\cdot l_v\right) = \frac{\tilde{\mu}_{110}}{\tilde{\mu}_{200}-\tilde{\mu}_{020}} = \frac{\frac{Re(i\vartheta_1)}{\gamma}D_\nu^{(1)}(x) - V_\varpi V_\theta \frac{\sigma_*}{\sigma_*^0}}{\left(\sigma_\varpi^2 - Re(\vartheta_1)\right)\left(1-\frac{1}{\gamma^2}\right) + Re(\vartheta_1)\left(D_\nu^{(2)} - \frac{D_\nu^{(3)}}{\gamma}\right) - \left(V_\varpi^2 - V_\theta^2\right)\frac{\sigma_*}{\sigma_*^0}} \tag{B.19}$$

where:

$$\begin{aligned}
D_\nu^{(1)}(x) &= x\frac{\nu\pi}{\sin\left(\nu\pi\right)}\frac{1}{2\pi}\int_{-\pi}^{\pi}\sin\left(\nu\alpha\right)\sin\alpha\left(1+\cos\alpha\right)\exp^{-x(1+\cos\alpha)}\,d\alpha\\
D_\nu^{(2)}(x) &= \frac{\nu\pi}{\sin\left(\nu\pi\right)}\frac{1}{2\pi}\int_{-\pi}^{\pi}\cos\left(\nu\alpha\right)\left(1-x\sin^2\alpha\right)\exp^{-x(1+\cos\alpha)}\,d\alpha\\
D_\nu^{(3)}(x) &= \frac{\nu\pi}{\sin\left(\nu\pi\right)}\frac{1}{2\pi}\int_{-\pi}^{\pi}\cos\left(\nu\alpha\right)\left(1-x-2x\cos\alpha-x\cos\alpha^2\right)\exp^{-x(1+\cos\alpha)}\,d\alpha
\end{aligned}$$

C
Appendix 4

In this appendix we describe the method we have used to find the center of the re-simulated system that is inside the full cosmological box used in the simulation. Next, we also describe how we set the x-y axis of the model as being the ones of the main simulated systems' disk plane.

C.1 Finding the galactic center

To find the center of the galactic system we have re-simulated, and which has the higher resolution, we have used only positions of the first species of dark matter, the ones that have lower masses. The steps we have followed using these positions are:
We used the following steps:

1. Compute the mean position of all 1rst specie DM particles in the full simulated box (28 Mpc).

2. Compute the new positions of all particles according to the new origin of coordinates that is the mean position computed in the previous step.

3. Define a sphere with a radius that depends on the iteration number as R = 400 kpc/N_{steps}, centered at the origin of coordinates.

4. Compute the mean position of all 1rst specie DM particles inside the defined sphere.

5. Redo all steps from step 2, until getting R = 1 kpc.

6. Check that the main system have been centered correctly, if not, change initial sphere radius and redo all the process.

To compute the velocity of the galaxy with respect to the initial cosmological box, we computed the mean velocity of all dark matter particles inside a sphere of 400 kpc centered at the galactic center.
Once found these velocities we subtract them from the velocity of all particles in the system to obtain the velocity with respect to the galactic center.
It is important to note that here we are finding the center of DMs' potential that can be or not the same as the center of the stellar component or the center of the gas component.

C.2 Finding the plane

To find the galactic plane of our simulated disk galaxy is not trivial. First we need to define if we want to find stellar or gaseous disk. In he work we have presented here we have used stellar disk. Second, there are, at least, two approaches to find it: 1- To use the angular momentum, 2- To use the geometry. Here we have decided to use the geometrical approach as it is independent on the kinetic parameters we want to investigate. The geometrical approach works as follows:

1. Define the initial coordinates.
    - For defining a plane that goes through the origin of coordinates we need two variables, here we use two angles: declination and right ascension.
    - It is also needed to define an initial plane. Here we use the x-y plane (z=0), and then in this case the planes' normal vector will be the z axis.
    - The origin of the right ascensions is defined as the x axis.
2. Define planes' equations:
    - $lx + my + nz - p = 0$
    - If the plane goes through the (0,0,0), then: $lx + my + nz = 0$
        - It is important to know which origin of coordinates we will use, as it is different to use the center defined by dark matter particles, by the gas component or by the stars. Here we will use the center defined by the stars in a spherical shell between 2 and 20 kpc as we are looking for stellar plane.
    - $l^2 + m^2 + n^2 = 1$
    - $cos\delta_p cos\alpha_p = l$, $cos\delta_p sin\alpha_p = m$, $sin\delta_p = n$.
    - The distance of any point to the plane is $d_i = lx_i + my_i + nz_i$.
3. Find the galactic plane:

- The plane defined by galactic particles will be the one that minimize the sum of squared distances of all particles in the system (here we use only stellar particles with 2 kpc < R < 20 kpc and after the first iteration also z < 2.5 kpc.
- To accomplish the previous condition the derivatives with respect to l, m and n have to be equal to 0.
- The condition $l^2 + m^2 + n^2 - 1 = 0$ also needs to be preserved.
- We use the Lagranges' method of indeterminate multipliers to find when the system has real solutions.
- $\sum Dist - \lambda(l^2 + m^2 + n^2 - 1) = 0$
- The previous system of equations has solution (apart from the trivial l=m=n=0) if its' determinant is equal to 0. Using this condition we can find the λs' value (Lagrange's multiplier).
- After computing the determinant we need to solve a third order equation to find λ (pages 9 to 11 in Atanasijevic 1971).
- We can solve the third order equation using the analytical formulae or an iterative process (Newton-Raphson). We implemented both methods in the code.
- Once found λ we solve the system and we find the values of l,m,n.
- l, m and n define the new plane and with them we can compute the declination and the right ascension of its normal vector.

4. Define the new plane
    - We rotate the system to define the new plane as the z=0 one. To do that we need to make two rotations, the first one in y (declination) and the last in z (right ascension).
    - We apply the new Cartesian coordinates to all particles in the system.
5. Iterate
    - We iterate until get convergence to l = m = 0 and n = 1 with a discrepancy lower than 10^{-6}. We usually need around 10 iterations to converge.
6. Define new velocities
    - We define the Cartesian velocities of all particles with respect to the new coordinates systems.

In Figures 6.1 and 6.13 we show how this technique lets us to find the galactic plane very efficiently.

References

Abadi M. G., Navarro J. F., Steinmetz M., Eke V. R., 2003, ApJ, 591, 499

Agertz O., Moore B., Stadel J., et al. 2007, MNRAS, 380, 963

Agertz O., Teyssier R., Moore B., 2011, MNRAS, 410, 1391

Allen C., Santillan A., 1991, RMxAA, 22, 255

Anderson M. E., Bregman J. N., 2010, ApJ, 714, 320

Andrews B. H., Thompson T. A., 2011, ApJ, 727, 97

Angulo R. E., Springel V., White S. D. M., Jenkins A., Baugh C. M., Frenk C. S., 2012, MNRAS, 426, 2046

Anninos P., Norman M. L., Clarke D. A., 1994, ApJ, 436, 11

Antoja T., Figueras F., Romero-Gómez M., Pichardo B., Valenzuela O., Moreno E., 2011, MNRAS, 418, 1423

Antoja T., Helmi A., et al. D., 2013, ArXiv e-prints

Antoja T., Helmi H., Bienayme O., et al. 2012, MNRAS, 426, L1

Antoja T., Valenzuela O., Pichardo B., Moreno E., Figueras F., Fernández D., 2009, ApJ, 700, 78

Atanasijevic I., ed. 1971, Selected exercises in galactic astronomy Vol. 26 of Astrophysics and Space Science Library

Athanassoula E., 1980, A&A, 88, 184

Athanassoula E., ed. 1984, The spiral structure of galaxies

Athanassoula E., 1996, in Buta R., Crocker D. A., Elmegreen B. G., eds, IAU Colloq. 157: Barred Galaxies Vol. 91 of Astronomical Society of the Pacific Conference Series, Evolution of Bars in Isolated and in Interacting Disk Galaxies. p. 309

Athanassoula E., 2002, ApJl, 569, L83

Athanassoula E., 2012, MNRAS, 426, L46

Athanassoula E., Lambert J. C., Dehnen W., 2005, MNRAS, 363, 496

Aumer M., Binney J. J., 2009, MNRAS, 397, 1286

Aumer M., White S. D. M., Naab T., Scannapieco C., 2013, MNRAS, 434, 3142

Avila-Reese V., Carrillo A., Valenzuela O., Klypin A., 2005, MNRAS, 361, 997

Avila-Reese V., Colín P., González-Samaniego A., Valenzuela O., Firmani C., Velázquez H., Ceverino D., 2011, ApJ, 736, 134

Baba J., Saitoh T. R., Wada K., 2013, ApJ, 763, 14

Barnes J., Hut P., 1986, Nature, 324, 446

Baugh C. M., Cole S., Frenk C. S., 1996, MNRAS, 283, 1361

Behroozi P. S., Wechsler R. H., Conroy C., 2013, ApJ, 770, 57

Bertin G., Lin C. C., 1996, Cambridge, MA MIT Press

Binney J., Tremaine S., 2008, Galactic Dynamics: Second Edition

Bird J. C., Kazantzidis S., Weinberg D. H., 2012, MNRAS, 420, 913

Bird J. C., Kazantzidis S., Weinberg D. H., Guedes J., Callegari S., Mayer L., Madau P., 2013, ApJ, 773, 43

Bogdán Á., Forman W. R., Kraft R. P., Jones C., 2013, ApJ, 772, 98

Bogdán Á., Gilfanov M., 2011, MNRAS, 418, 1901

Bovy J., Allende Prieto C., Beers T. C., et al. 2012, ApJ, 759, 131

Boylan-Kolchin M., Bullock J. S., Sohn S. T., Besla G., van der Marel R. P., 2013, ApJ, 768, 140

Boylan-Kolchin M., Springel V., White S. D. M., Jenkins A., Lemson G., 2009, MNRAS, 398, 1150

Bregman J. N., Lloyd-Davies E. J., 2007, ApJ, 669, 990

Brook C. B., Stinson G., Gibson B. K., Roškar R., Wadsley J., Quinn T., 2012, MNRAS, 419, 771

Brooks A. M., Solomon A. R., Governato F., McCleary J., MacArthur L. A., Brook C. B. A., Jonsson P., Quinn T. R., Wadsley J., 2011, ApJ, 728, 51

Bryan G. L., Norman M. L., 1998, ApJ, 495, 80

Bullock J. S., Dekel A., Kolatt T. S., Kravtsov A. V., Klypin A. A., Porciani C., Primack J. R., 2001, ApJ, 555, 240

Busha M. T., Marshall P. J., Wechsler R. H., Klypin A., Primack J., 2011, ApJ, 743, 40

Buta R. J., Byrd G., Freeman T., 2004, AJ, 127, 1982

Buta R. J., Laurikainen E., Salo H., Block D. L., Knapen J. H. R., 2005, AAS, 37, 1481

Buta R. J., Shang X., 2011, MSAIS, 18, 13

Byrd R., Freeman T., Buta R. J., 2006, AJ, 131, 1377

Calura F., Gibson B. K., Michel-Dansac L., Stinson G. S., Cignoni M., Dotter A., Pilkington K., House E. L., Brook C. B., Few C. G., Bailin J., Couchman H. M. P., Wadsley J., 2012, MNRAS, 427, 1401

Canzian B., 1993, ApJ, 414, 487

Ceverino D., Dekel A., Bournaud F., 2010, MNRAS, 404, 2151

Ceverino D., Klypin A., Klimek E. S., Trujillo-Gomez S., Churchill C. W., Primack J., Dekel A., 2014, MNRAS, 442, 1545

Chakrabarty D., 2007, A&Ap, 467, 145

Christensen C., Quinn T., Governato F., Stilp A., Shen S., Wadsley J., 2012, MNRAS, 425, 3058

Clemens D. P., Sanders D. B., Scoville N. Z., 1988, ApJ, 327, 139

Colín P., Avila-Reese V., Valenzuela O., Firmani C., 2003, in Avila-Reese V., Firmani C., Frenk C. S., Allen C., eds, Revista Mexicana de Astronomia y Astrofisica Conference Series Vol. 17 of Revista Mexicana de Astronomia y Astrofisica Conference Series, The structure of halos in Self-Interacting Cold Dark Matter models. pp 19–21

Colín P., Avila-Reese V., Vázquez-Semadeni E., Valenzuela O., Ceverino D., 2010, ApJ, 713, 535

Colín P., Valenzuela O., Klypin A., 2006, ApJ, 644, 687

Combes F., Sanders R. H., 1981, A&A, 96, 164

Comparetta J., Quillen A. C., 2012, ArXiv e-prints (arXiv:1207.5753)

Corbelli E., 2003, MNRAS, 342, 199

Crain R. A., McCarthy I. G., Frenk C. S., Theuns T., Schaye J., 2010, MNRAS, 407, 1403

Crain R. A., McCarthy I. G., Schaye J., Theuns T., Frenk C. S., 2013, MNRAS, 432, 3005

Cuesta A. J., Prada F., Klypin A., Moles M., 2008, MNRAS, 389, 385

Dalla Vecchia C., Schaye J., 2012, MNRAS, 426, 140

Deason A. J., Belokurov V., Evans N. W., An J., 2012, MNRAS, 424, L44

Debattista V. P., Sellwood J. A., 2000, ApJ, 543, 704

Dehnen W., 2000, AJ, 119, 800

Dehnen W., Binney J. J., 1998, MNRAS, 298, 387

Di Matteo P., Haywood M., Combes F., Semelin B., Snaith O. N., 2013, ArXiv e-prints (arXiv:1301.2545)

D'Onghia E., Springel V., Hernquist L., Keres D., 2010, ApJ, 709, 1138

D'Onghia E., Vogelsberger M., Hernquist L., 2013, ApJ, 766, 34

Du C., Ma J., Wu Z., Zhou X., 2006, MNRAS, 372, 1304

Dubinski J., Berentzen I., Shlosman I., 2009, ApJ, 697, 293

Dutton A. A., Conroy C., van den Bosch F. C., Prada F., More S., 2010, MNRAS, 407, 2

Fall S. M., Efstathiou G., 1980, MNRAS, 193, 189

Feldmann R., Carollo C. M., Mayer L., 2011, ApJ, 736, 88

Feldmann R., Hooper D., Gnedin N. Y., 2013, ApJ, 763, 21

Ferland G. J., Korista K. T., Verner D. A., Ferguson J. W., Kingdon J. B., Verner E. M., 1998, PASP, 110, 761

Fernández D., Figueras F., Torra J., 2001, A&Ap, 372, 833

Ferreras I., Cropper M., Kawata D., Page M. Erik A., 2012, MNRAS, 424, 1636

Ferrière K. M., 2001, Reviews of Modern Physics, 73, 1031

Flynn C., Holmberg J., Portinari L., Fuchs B., Jahreiß H., 2006, MNRAS, 372, 1149

Font J., Beckman J. E., Epinat B., Fathi K., Gutiérrez L., Hernandez O., 2011, ApJl, 741, L14

Forman W., Jones C., Tucker W., 1985, ApJ, 293, 102

Foyle K., Rix H. W., Doobs C. L., Leroy A. K., Walter F., 2011, ApJ, 735, 101

Friedli D., Benz W., 1993, A&A, 268, 65

Fuchs B., Dettbarn C., Rix H.-W., et al. 2009, AJ, 137, 4149

Fux R., 2001, A&Ap, 373, 511

Gauthier J.-R., Dubinski J., Widrow L. M., 2006, ApJ, 653, 1180

Gavazzi R., Soucail G., 2007, A&Ap, 462, 459

Gerhard ., 2011, MSAIS, 18, 185

Gerssen J., Shapiro Griffin K., 2012, MNRAS, 423, 2726

Goldreich P., Lynden-Bell D., 1965, MNRAS, 130, 125

Gottlöber S., Yepes G., Khalatyan A., Sevilla R., Turchaninov V., 2006, in Manoz C., Yepes G., eds, The Dark Side of the Universe Vol. 878 of American Institute of Physics Conference Series, Dark and baryonic matter in the MareNostrum Universe. pp 3–9

Governato F., Brook C., Mayer L., et al. 2010, Nature, 463, 203

Governato F., Mayer L., Wadsley J., Gardner J. P., Willman B., Hayashi E., Quinn T., Stadel J., Lake G., 2004, ApJ, 607, 688

Governato F., Willman B., Mayer L., Brooks A., Stinson G., Valenzuela O., Wadsley J., Quinn T., 2007, MNRAS, 374, 1479

Governato F., Zolotov A., Pontzen A., Christensen C., Oh S. H., Brooks A. M., Quinn T., Shen S., Wadsley J., 2012, MNRAS, 422, 1231

Grand R. J. J., Kawata D., Cropper M., 2012a, MNRAS, 426, 167

Grand R. J. J., Kawata D., Cropper M., 2012b, MNRAS, 421, 1529

Guedes J., Callegari S., Madau P., Mayer L., 2011, ApJ, 742, 76

Gupta A., Mathur S., Galeazzi M., Krongold Y., 2014, APSS

Gupta A., Mathur S., Krongold Y., Nicastro F., Galeazzi M., 2012, ApJl, 756, L8

Haardt F., Madau P., 1996, ApJ, 461, 20

Hagihara T., Yao Y., Yamasaki N. Y., Mitsuda K., Wang Q. D., Takei Y., Yoshino T., McCammon D., 2010, PASJ, 62, 723

Hahn O., Abel T., 2011, MNRAS, 415, 2101

Hammer F., Puech M., Chemin L., Flores H., Lehnert M. D., 2007, ApJ, 662, 322

Hernquist L., 1993, ApJS, 86, 389

Hilton J. L., Bash R., 1982, ApJ, 255, 217

Hockney R. W., Eastwood J. W., 1981, Computer Simulation Using Particles

Hoekstra H., Hsieh B. C., Yee H. K. C., Lin H., Gladders M. D., 2005, ApJ, 635, 73

Hohl F., 1971, ApJ, 168, 343

Hohl F., Zang T. A., 1979, AJ, 84, 585

Holmberg E., 1941, ApJ, 94, 385

Hopkins P. F., Kereš D., Murray N., Quataert E., Hernquist L., 2012, MNRAS, 427, 968

Hopkins P. F., Quataert E., Murray N., 2011, MNRAS, 417, 950

Hoyle F., 1953, ApJ, 118, 513

Hummels C. B., Bryan G. L., 2012, ApJ, 749, 140

Jarvis B. J., Freeman K. C., 1985, ApJ, 295, 314

Jessop C., Duncan M., Chau W. Y., 1994, Journal of Computational Physics, 115, 339

Julian W. H., Toomre A., 1966, ApJ, 146, 810

Jurić M., Ivezić Ž., Brooks e. a., 2008, ApJ, 673, 864

Kafle P. R., Sharma S., Lewis G. F., Bland-Hawthorn J., 2012, ApJ, 761, 98

Kaufmann T., Mayer L., Wadsley J., Stadel J., Moore B., 2007, MNRAS, 375, 53

Kawamura A., Mizuno Y., Minamidani T., Filipović M. D., Staveley-Smith L., Kim S., Mizuno N., Onishi T., Mizuno A., Fukui Y., 2009, ApJS, 184, 1

Kawata D., Gibson B. K., 2003, MNRAS, 340, 908

Kawata D., Okamoto T., Gibson B. K., Barnes D. J., Cen R., 2013, MNRAS, 428, 1968

Kereš D., Katz N., Fardal M., Davé R., Weinberg D. H., 2009, MNRAS, 395, 160

Klypin A., Holtzman J., 1997, ArXiv Astrophysics e-prints

Klypin A., Kravtsov A. V., Bullock J. S., Primack J. R., 2001, ApJ, 554, 903

Klypin A. A., Trujillo-Gomez S., Primack J., 2011, ApJ, 740, 102

Klypin A. A., Valenzuela O., Colín P., Quinn T., 2009, MNRAS, 398, 1027

Klypin A. A., Zhao H., Somerville R. S., 2002, ApJ, 573, 597

Koposov S. E., Rix H.-W., Hogg D. W., 2010, ApJ, 712, 260

Kravtsov A. V., 1999, PhD thesis, NEW MEXICO STATE UNIVERSITY

Kravtsov A. V., 2003, ApJ, 590, L1

Kravtsov A. V., Klypin A. A., Khokhlov A. M., 1997, ApJS, 111, 73

Kravtsov A. V., Nagai D., Vikhlinin A. A., 2005, ApJ, 625, 588

Krumholz M. R., Matzner C. D., 2009, ApJ, 703, 1352

Krumholz M. R., Tan J. C., 2007, ApJ, 654, 304

Krumholz M. R., Thompson T. A., 2012, ApJ, 760, 155

Kuijken K., Tremaine S., 1994, ApJ, 421, 178

Lada C. J., Forbrich J., Lombardi M., Alves J. F., 2012, ApJ, 745, 190

Lada C. J., Lombardi M., Alves J. F., 2010, ApJ, 724, 687

Li J.-T., Li Z., Wang Q. D., Irwin J. A., Rossa J., 2008, MNRAS, 390, 59

Lin C. C., Shu F. H., 1964, ApJ, 140, 646

Lin C. C., Yuan C., Shu F. H., 1969, A&A, 155, 721

Lopez L. A., Krumholz M. R., Bolatto A. D., Prochaska J. X., Ramirez-Ruiz E., 2011, ApJ, 731, 91

López-Corredoira M., 2014, A&A, 563, A128

Machacek M. E., Bryan G. L., Abel T., 2001, ApJ, 548, 509

Majewski S. R., Wilson J. C., Hearty F., Schiavon R. R., Skrutskie M. F., 2010, in Cunha K., Spite M., Barbuy B., eds, IAU Symposium Vol. 265 of IAU Symposium, The Apache Point Observatory Galactic Evolution Experiment (APOGEE) in Sloan Digital

Sky Survey III (SDSS-III). p. 480

Maller A. H., Dekel A., 2002, MNRAS, 335, 487

Marinacci F., Pakmor R., Springel V., 2014, MNRAS, 437, 1750

Martínez-García E. E., González-Lópezlira R. A., Bruzual G., 2009, ApJ, 694, 512

Martos M., Hernández X., Yáñez M., Moreno E., Pichardo B., 2004, MNRAS, 350, 47

Masset F., Tagger M., 1997, A&A, 322, 442

Mathews W. G., Brighenti F., 2003, ARA&A, 41, 191

Mayor M., 1970, A&A, 6, 60

McGaugh S. S., de Blok W. J. G., Schombert J. M., Kuzio de Naray R., Kim J. H., 2007, ApJ, 659, 149

Meidt S. E., Rand R. J., Merrifield M. R., 2009, ApJ, 702, 277

Meidt S. E., Rand R. J., Merrifield M. R., Shetty R., Vogel S. N., 2008, ApJ, 688, 224

Miller G. E., Scalo J. M., 1979, ApJS, 41, 513

Miller R. H., Prendergast K. H., Quirk W. J., 1970, ApJ, 161, 903

Miller R. H., Smith B. F., 1979, ApJ, 227, 785

Minchev I., Famaey B., Quillen A. C., Di Matteo P., Combes F., Vlajić M., Erwin P., Bland-Hawthorn J., 2012, A&A, 548, 126

Mo H. J., Mao S., White S. D. M., 1998, MNRAS, 295, 319

Mollitor P., Nezri E., Teyssier R., 2014, ArXiv e-prints

Monari G., Antoja T., Helmi A., 2013, ArXiv e-prints

Monari G., Helmi A., Antoja T., Steinmetz M., 2014, ArXiv e-prints

Moster B. P., Naab T., White S. D. M., 2013, MNRAS, 428, 3121

Muhlbauer G., Dehnen W., 2003, A&A, 401, 975

Munshi F., 2013, PhD thesis, University of Washington

Murray N., 2011, ApJ, 729, 133

Murray N., Quataert E., Thompson T. A., 2010, ApJ, 709, 191

Navarro J. F., Benz W., 1991, ApJ, 380, 320

Navarro J. F., Frenk C. S., White S. D. M., 1997, ApJ, 490, 493

Navarro J. F., Steinmetz M., 2000, ApJ, 528, 607

Nunez J., Torra J., 1982, A&Ap, 110, 95

Okamoto T., Eke V. R., Frenk C. S., Jenkins A., 2005, MNRAS, 363, 1299

Okamoto T., Jenkins A., Eke V. R., Quilis V., Frenk C. S., 2003, MNRAS, 345, 429

Ostriker J. P., Peebles P. J. E., 1973, ApJ, 186, 467

Parker L. C., Hoekstra H., Hudson M. J., van Waerbeke L., Mellier Y., 2007, ApJ, 669, 21

Peebles P. J. E., 1969, ApJ, 155, 393

Peebles P. J. E., 1980, The large-scale structure of the universe

Pellegrini E. W., Baldwin J. A., Ferland G. J., 2011, ApJ, 738, 34

Perryman M. A. C., de Boer K. S., Gilmore G., Høg E., Lattanzi M. G., Lindegren L., Luri X., Mignard F., Pace O., de Zeeuw P. T., 2001, A&Ap, 369, 339

Pichardo B., Martos M., Moreno E., Espresate J., 2003, ApJ, 582, 230

Pifﬂ T., Scannapieco C., Binney J., et al. 2014, a&a, 562, A91

Piontek F., Steinmetz M., 2011, MNRAS, 410, 2625

Press W. H., Teukolsky S. A., Vetterling W. T., Flannery B. P., 1992, Numerical recipes in FORTRAN. The art of scientific computing

Purcell C. W., Kazantzidis S., Bullock J. S., 2009, ApJl, 694, L98

Quillen A. C., Dougherty J., Bagley M. B., Minchev I., Comparetta J., 2011, MNRAS, 417, 762

Quinn T., Katz N., Stadel J., Lake G., 1997, ArXiv Astrophysics e-prints

Rasera Y., Corasaniti P.-S., Alimi J.-M., Bouillot V., Reverdy V., Balmès I., 2014, MNRAS, 440, 1420

Rautiainen P., Salo H., 1999, A&A, 348, 737

Rautiainen P., Salo H., Laurikainen E., 2008, MNRAS, 388, 1803

Robertson B., Yoshida N., Springel V., Hernquist L., 2004, ApJ, 606, 32

Robin A., Creze M., 1986, A&Ap, 157, 71

Robitaille T. P., Whitney B. A., 2010, ApJl, 710, L11

Roca-Fàbrega S., Antoja T., Figueras F., Valenzuela O., Romero-Gómez M., Pichardo B., 2014, MNRAS, 440, 1950

Roca-Fàbrega S., Valenzuela O., Figueras F., Romero-Gómez M., Velázquez H., Antoja T., Pichardo B., 2013, MNRAS, 432, 2878

Romero-Gómez M., Athanassoula E., Antoja T., Figueras F., 2011, MNRAS, 418, 1176

Romero-Gómez M., Athanassoula E., Masdemont J. J., García-Gómez C., 2007, A&A, 472, 63

Roskar R., Debattista V. P., Loebman S. R., Ivezić Z., Quinn T. R., 2011, ASPC, 448, 371

Roskar R., Debattista V. P., Quinn T. R., Stinson G. S., Wadsley J., 2008, ApJl, 684, 79

Rubin V. C., Thonnard N., Ford Jr. W. K., 1978, ApJL, 225, L107

Sánchez S. F., Kennicutt R. C., Gil de Paz A., et al. 2012, A&Ap, 538, A8

Sanders R. H., Huntley J. M., 1976, ApJ, 209, 53

Scannapieco C., Wadepuhl M., Parry O. H., et al. 2012, MNRAS, 423, 1726

Scannapieco C., White S. D. M., Springel V., Tissera P. B., 2009, MNRAS, 396, 696

Schönrich R., Binney J., 2009, MNRAS, 396, 203

Sellwood J., 2013, in AAS/Division of Dynamical Astronomy Meeting Vol. 44 of AAS/Division of Dynamical Astronomy Meeting, Spiral Structure in Galaxies. p. 104.01

Sellwood J. A., 1980, A&A, 89, 296

Sellwood J. A., 2000, Ap&SS, 272, 31

Sellwood J. A., Athanassoula E., 1986, MNRAS, 221, 195

Sellwood J. A., Binney J. J., 2002, MNRAS, 336, 785

Sellwood J. A., Carlberg R. G., 1984, ApJ, 282, 61

Sellwood J. A., Carlberg R. G., 2014, ApJ, 785, 137

Sellwood J. A., Debattista V. P., 2009, MNRAS, 398, 1279

Sellwood J. A., Sparke L. S., 1988, MNRAS, 231, 25

Sheth R. K., Rossi G., 2010, MNRAS, 403, 2137

Sofue Y., Honma M., Omodaka T., 2009, PASJ, 61, 227

Sommer-Larsen J., Götz M., Portinari L., 2003, ApJ, 596, 47

Speights J. C., Westpfahl D. J., 2012, ApJ, 752, 52

Spergel D. N., Bean R., Doré O., et al. 2007, ApJS, 170, 377

Springel V., 2005, MNRAS, 364, 1105

Springel V., Wang J., Vogelsberger M., Ludlow A., Jenkins A., Helmi A., Navarro J. F., Frenk C. S., White S. D. M., 2008, MNRAS, 391, 1685

Springel V., White S. D. M., Jenkins A., et al. 2005, Nature, 435, 629

Springel V., Yoshida N., White S. D. M., 2001, NA, 6, 79

Stinson G., Seth A., Katz N., Wadsley J., Governato F., Quinn T., 2006, MNRAS, 373, 1074

Stinson G. S., Bailin J., Couchman H., Wadsley J., Shen S., Nickerson S., Brook C., Quinn T., 2010, MNRAS, 408, 812

Strickland D. K., Heckman T. M., Colbert E. J. M., Hoopes C. G., Weaver K. A., 2004, ApJS, 151, 193

Strömberg G., 1946, ApJ, 104, 12

Sygnet J. F., Tagger M., Athanassoula E., Pellat R., 1988, MNRAS, 232, 733

Tasker E. J., Brunino R., Mitchell N. L., et al. 2008, MNRAS, 390, 1267

Toft S., Rasmussen J., Sommer-Larsen J., Pedersen K., 2002, MNRAS, 335, 799

Toomre A., 1977, ARA&A, 15, 437

Toomre A., 1990, International Conference on Dynamics and Interactions of Galaxies, p. 292

Toomre A., Kalnajs A. J., 1991, in Sundelius B., ed., Dynamics of Disc Galaxies Spiral Chaos in an Orbiting Patch. p. 341

Tremaine S., Weinberg M. D., 1984, ApJl, 282, 5

Tsoutsis P., Kalapotharakos C., Efthymiopoulos C., Contopoulos G., 2009, A&A, 495, 743

Tüllmann R., Pietsch W., Rossa J., Breitschwerdt D., Dettmar R. J., 2006, A&Ap, 448, 43

Valenzuela O., Klypin A. A., 2003, MNRAS, 345, 406

von Hoerner S., 1960, ZA, 50, 184

von Roos O., 1960, Physical Review, 119, 1174

Vorobyov E. I., Theis C., 2006, MNRAS, 373, 197

Vorobyov E. I., Theis C., 2008, MNRAS, 383, 817

Westfall K. B., Bershady M. A., Verheijen M. A. W., 2011, APJS, 193, 21

White S. D. M., Frenk C. S., 1991, ApJ, 379, 52

White S. D. M., Rees M. J., 1978, MNRAS, 183, 341

Widrow L. M., Dubinski J., 2005, ApJ, 631, 838

Wielen R., Fuchs B., Dettbarn C., 1996, A&A, 314, 438

Woolley R., 1970, in Becker W., Kontopoulos G. I., eds, The Spiral Structure of our Galaxy Vol. 38 of IAU Symposium, Deviation of the Vertex of teh Velocity Ellipse of Young Stars and its Connection with Spiral Structure. p. 423

Xue X. X., Rix H. W., Zhao G., Re Fiorentin P., Naab T., Steinmetz M., van den Bosch F. C., Beers T. C., Lee Y. S., Bell E. F., Rockosi C., Yanny B., Newberg H., Wilhelm R., Kang X., Smith M. C., Schneider D. P., 2008, ApJ, 684, 1143

Yao Y., Wang Q. D., 2007, ApJ, 658, 1088

Yoachim P., Dalcanton J. J., 2006, AJ, 131, 226

Yoshida H., 1993, Celestial Mechanics and Dynamical Astronomy, 56, 27

Zemp M., 2013, ArXiv e-prints

Zhang X., Buta R. J., 2007, AJ, 133, 2584

List of Figures

List of Tables